

BIOLOGICAL AND PHYSICAL PROCESSES CONTROLLING
THE SPRING PHYTOPLANKTON BLOOM DYNAMICS ON GEORGES BANK

by

RUBAO JI

(Under the direction of Changsheng Chen)

ABSTRACT

A lower trophic level food web model was developed to examine the biological and physical processes controlling the spring phytoplankton bloom dynamics on Georges Bank. It is a 9-component nutrients-phytoplankton-zooplankton-detritus model including 3 nutrients (nitrate, ammonia and silicate), 2 phytoplankton (large- and small-size groups), 2 zooplankton (large- and small-size groups), 1 detrital-organic nitrogen and 1 detrital silicon. This biological model was coupled with state of the art structured- and unstructured-grid coastal ocean models (ECOM-si and FVCOM) and was used to examine impacts of physical processes on the ecosystem dynamics on Georges Bank.

To distinguish the roles of light intensity and light attenuation, current advection, tidal mixing/rectification, wind-induced mixing/advection, and buoyancy fronts as well as remote inflow in the formation of the spring phytoplankton bloom on Georges Bank, numerical experiments were conducted through 1-dimensional (1-D), 2-dimensional (2-D), and 3-dimensional (3-D) approaches. The 1-D experiments were performed for a fixed location at which all biological and physical variables were assumed to be uniform in the horizontal but not in the vertical. The 2-D

experiments featured a transect across Georges Bank in which the along-isobath variation for all the variables were ignored. The 3-D experiments were focused on the influence of the “cross-over” event through the Northeast Channel in the Scotian Shelf on the formation of the dense spring bloom over the southeastern edge of Georges Bank.

The 1-D model results clearly suggest that the biological and physical mechanism for the spring phytoplankton bloom significantly differs between the shallow and deeper regions of Georges Bank. In the shallow, well-mixed central bank, the timing and duration of the spring bloom are determined by light intensity and its downward penetration while the bloom intensity is regulated by initial nutrient concentration and zooplankton grazing pressure. In deeper water (> 60 m), given the same conditions of light intensity/attenuation, initial nutrient concentration and zooplankton grazing pressure as those in the shallow, well-mixed region, the timing of the spring bloom is closely linked to the seasonal development of stratification. The dense phytoplankton biomass forms as the seasonal vertical stratification develops.

The 2-D model results show that the biological and physical processes governing the spring phytoplankton bloom in the well-mixed region remain the same as in the 1-D case. However, in deeper water, the timing, location, and duration of the bloom are influenced strongly by on-bank nutrient supply over the flanks of Georges Bank. In particular, once the tidal mixing front is established, a “second bloom” can form near the front as a result of the up-frontal nutrient flux driven by the secondary flow.

A 3-D model experiment detected that the 1999 March bloom event captured in SeaWiFS images on the southeastern flank of Georges Bank was typical of features driven by strongly coupled biological and physical processes. It was influenced by (1) transport of the Scotian Shelf Water, (2) wind- and tidal-induced vertical mixing and surface cooling, and (3) on-bank intrusion of the salinity-dominated shelf break

front. With a sufficient supply of nutrients from the slope, the bloom could occur due to rapid *in situ* growth of phytoplankton near the shelf break front. This experiment also suggests that an accurate simulation of the spatial distribution of water temperature and salinity (in particular, the location of the shelf break front) and “cross-over” water transport is a prerequisite to capture the spring bloom over the southeastern and southern edges of Georges Bank.

INDEX WORDS: Georges Bank, spring phytoplankton bloom, food web, numerical modeling, biological-physical coupling

BIOLOGICAL AND PHYSICAL PROCESSES CONTROLLING
THE SPRING PHYTOPLANKTON BLOOM DYNAMICS ON GEORGES BANK

by

RUBAO JI

M.Sc., Ocean University of Qingdao, China 1994

M.Sc., The University of Georgia, 2002

A Dissertation Submitted to the Graduate Faculty
of The University of Georgia in Partial Fulfillment
of the

Requirements for the Degree

DOCTOR OF PHILOSOPHY

ATHENS, GEORGIA

2003

© 2003

Rubao Ji

All Rights Reserved

BIOLOGICAL AND PHYSICAL PROCESSES CONTROLLING
THE SPRING PHYTOPLANKTON BLOOM DYNAMICS ON GEORGES BANK

by

RUBAO JI

Approved:

Major Professor: Changsheng Chen

Committee: Brian J. Binder
James T. Hollibaugh
Randal L. Walker
Patricia L. Yager

Electronic Version Approved:

Maureen Grasso
Dean of the Graduate School
The University of Georgia
December 2003

ACKNOWLEDGMENTS

First of all, I would like to thank my advisor, Dr. Changsheng Chen, for his patient guidance and encouragement, for his constructive criticism of this work and for his financial support throughout my graduate studies. Dr. Chen has spent a significant amount of time with me to revise this thesis. His deep insight into coastal physical processes and biological-physical interactions benefited my research greatly. I owe him a great deal of thanks.

I also would like to thank my co-advisor Dr. Brian Binder, for willing to serve as my major advisor after Dr. Chen departed to the University of Massachusetts. His advice, encouragement and support proved invaluable to my thesis study.

I greatly appreciate all the help and support from my thesis committee members: Drs. Tim Hollibaugh, Randal Walker, and Patricia Yager. They have been very generous with their time and expertise, and have been a continuous source of encouragement. Thanks for their time, criticisms and insights during my thesis work.

I cannot forget the encouragement and support from Dr. Mac Rawson. I have worked under the supervision of Dr. Rawson during the US-China Living Marine Resources project and during the interface development of management tool for water quality model in Satilla River, GA. He has given me invaluable advices and suggestions on numerous occasions, which have directly benefited my research work.

Dr. Peter Franks has given me strong support and great encouragement during my thesis research. He was so patient to go through biological model together with me, and provided me with his insight about modeling and thesis writing during the GLOBEC/GB workshop at the UNH. His advice has been greatly appreciated.

Dr. David Townsend was very kind to provide me his biological survey data when I started working on the development of this model. I engaged in a very productive discussion with him on the design of the model when we met at the US GLOBEC Phase IV PIs meeting. His deep insight into nutrients and phytoplankton dynamics on GB directly benefited me in this thesis study.

I will always remember my discussion with Dr. Greg Lough when he visited our lab. He gave me an informal lecture about zooplankton dynamics and made many constructive suggestions on my proposed research to perform modeling studies of the ecosystem dynamics on GB. His support was greatly appreciated.

Drs. Edward Durbin and Karen Wishner gave me great support when I started working on my Ph.D. thesis proposal. Both of them provided me with a complete set of their zooplankton data taken on GB. Discussion with Dr. Durbin on zooplankton population dynamics has enriched my understanding of the ecosystem on GB. Although their data were not included in the final version of my thesis due to a shift of thesis focus, their support was greatly appreciated.

Dr. Jamie Pringle is a very open-minded scientist who is always willing to share his innovative ideas with me. He suggested that I used his climatologic heat flux data for my 1-D experiments. Although I did not have enough time to incorporate his data, the discussion with him has greatly benefited my thesis research.

Special thanks go to Dr. Robert Beardsley. He has been collaborating with Dr. Chen on the application of FVCOM to the Gulf of Maine/GB region. I can always sense Dr. Beardsley's valuable suggestions and guidance through Dr. Chen. His deep insight into physical processes has provided direction to the development of coupled physical and biological model.

As a part of U.S. GLOBEC/GB Program Phase IV Project, most of the data used in this study was downloaded directly from the program's online database. The

excellent database provided by scientist and maintained by GLOBEC/GB program managers facilitated my modeling efforts directly.

This study was only possible with support from my teammates, past and present, from Dr. Chen's lab. They have helped me in a million various ways. Specifically I want to mention Professor Qichun Xu, Drs. Hedong Liu, Geoffrey Cowles, Haosheng Huang, Liuzhi Zhao and Jianhua Qi, and Mr. Song Hu. Their friendship and help on hydrodynamic modeling and data analysis have proven extremely valuable.

I want to thank Drs. Brian Rothschild and Joseph Deck at SMAST, who have kindly provided a comfortable working environment for me. Their support was greatly appreciated. My friend Mr. Glenn Strout taught me how to process the satellite-derived SST image data. Mrs. Susan Monahan helped me solve many difficult technical issues involved in computer's software and hardware. Their friendship and help was also greatly appreciated. I cannot forget one of my best friends Dirk Koopmans for mucking through my very first version of this thesis and making it readable.

Special thanks go to Professor Mingyuan Zhu at First Institute of Oceanography, State Oceanic Administration, China. He was and will always be my mentor. Five years ago, it was he who encouraged me to go abroad to continue my education and pursuit my career in marine sciences.

Last, but certainly not least, I wish to express my sincere thanks to my wife Jianjun for her patient support and continuous love. It is she and my darling daughter who made me realized that there are things much more precious than research work.

This research was supported by the US GLOBEC/GB IV Program through the National Science Foundation under OCE0227679, OCE0234545 and NOAA Coastal Ocean Science Program under NA160P2323 as well as by the Georgia Sea Grant College Program under NA06RG0029.

TABLE OF CONTENTS

	Page
ACKNOWLEDGMENTS	iv
LIST OF FIGURES	x
LIST OF TABLES	xxii
 CHAPTER	
1 INTRODUCTION	1
1.1 GEORGES BANK	1
1.2 PHYSICAL PROCESSES IN GOM/GB	3
1.3 BIOLOGICAL PROCESSES ON GB	7
1.4 MODELING OF PHYTOPLANKTON DYNAMICS ON GB	12
1.5 OBJECTIVE, HYPOTHESIS AND APPROACH OF THIS STUDY	17
1.6 REFERENCES	20
2 THE COUPLED BIOLOGICAL AND PHYSICAL MODELS	30
2.1 INTRODUCTION	30
2.2 THE BIOLOGICAL MODEL	32
2.3 PHYSICAL MODELS	47
2.4 REFERENCES	54
3 LOWER TROPHIC LEVEL FOOD WEB DYNAMICS ON GEORGES BANK: 1-D EXPERIMENTS	59
3.1 ABSTRACT	60

3.2	INTRODUCTION	60
3.3	RECENTLY OBSERVED FEATURES OF NUTRIENTS AND PHY- TOPLANKTON ON GB	64
3.4	DESIGN OF NUMERICAL EXPERIMENTS	72
3.5	MODEL RESULTS	74
3.6	DISCUSSION	85
3.7	SUMMARY	98
3.8	REFERENCES	99
4	EFFECTS OF STRATIFICATION AND FRONTAL SYSTEM ON SPRING BLOOM: 2-D MODEL EXPERIMENTS	103
4.1	ABSTRACT	104
4.2	INTRODUCTION	104
4.3	MODELING APPROACH	109
4.4	MODEL RESULTS	111
4.5	DISCUSSION	118
4.6	SUMMARY	152
4.7	REFERENCES	153
5	THE IMPACT OF SCOTIAN SHELF WATER “CROSS-OVER” ON THE PLANKTON DYNAMICS ON GEORGES BANK: A 3-D EXPERIMENT FOR THE 1999 SPRING BLOOM	156
5.1	ABSTRACT	157
5.2	INTRODUCTION	157
5.3	OBSERVED BIOLOGICAL FEATURES ASSOCIATED WITH SSW “CROSS-OVER”	162
5.4	MODELING APPROACH	168
5.5	MODEL RESULTS	173

5.6	DISCUSSION	189
5.7	SUMMARY	195
5.8	REFERENCES	196
6	SUMMARY AND SUGGESTIONS FOR FUTURE STUDY	200

APPENDIX

A	BIOLOGICAL MODEL	204
A.1	EQUATIONS FOR EACH FLUX TERM	205
A.2	MODEL PARAMETERS	206
B	SENSITIVITY OF BIOLOGICAL PARAMETER	208
B.1	REFERENCES	210
C	TIME SERIES DATA OF SURFACE WIND AND HEAT FLUX IN 1995	211

LIST OF FIGURES

1.1 The general circulation in GOM/GB region during stratification condition (May-September). From *Beardsley et al.* [1997]. 2

1.2 Schematic of fronts around Georges Bank and generalized distribution of cod/haddock eggs (1), larvae (2,3), and pelagic juveniles (4,5) during their first 3-4 months of life in the clockwise circulation over Georges Bank. The year-round shelf-break front (blue curve) is located along the 100-m isobath; and the tidal mixing front (brown curves) is located near the 40-m isobath on the northern flank and around the 50- to 60-m isobath on the southern flank during later spring and summer. Adapted from *Lough and Manning* [2001]. 5

1.3 Schematic of possible sources of *Calanus finmarchicus* resupply to Georges Bank and succession of generations in GOM/GB region. G0: the generation ascending from diapause; G1: the first generation reproduced from G0; G2: the second generation reproduced from G0. See the text for detail. 10

1.4 The approximate spatial and temporal ranges for a variety of oceanic phenomena, along with estimated observational capabilities of various research platforms. Three basic trophic levels (phytoplankton, zooplankton, and fish) and three physical phenomena (tidal mixing, storms and oceanic fronts) are shown. Observations using aircraft, ships and satellites are suitable for different spatial and temporal scales. 14

2.1	Schematic of the lower trophic level food web model in GOM/GB region. The model consists 9 components including nitrate (NO_3^-), ammonia (NH_4^+), silicate (Si), small phytoplankton (P_S), large phytoplankton (P_L), small zooplankton (Z_S), large zooplankton (Z_L), detrital organic nitrogen (D_N) and detrital organic silicon (D_{Si}). Arrows represent flux between different components.	34
2.2	Another version of Figure 2.1 with labeled number for each process.	35
2.3	The photosynthesis versus irradiance relationship. Datasets are from Dr. David Townsend's field measurements in Massachusetts Bay during February, 1990 (blue diamonds), and August, 1990 (red filled circles). Photosynthesis rate is normalized to the maximum rate. Three functions are applied to fit the data. The orange line is a function from <i>Jassby and Platt</i> [1976], blue line from <i>Eilers and Peeters</i> [1988], and black line from <i>Steele</i> [1962].	39
2.4	The unstructured grid for the finite-volume model.	53
3.1	The U.S. GLOBEC/GB Program broad-scale sampling station plan for 1998 and 1999. Station 39 was added in 1996 based on 38 stations used in 1995, Station 40 was added in 1997, and Station 41 was added in 1998. The intermediate stations added in each individual year are omitted here.	65
3.2	Areal contour plots of surface chlorophyll <i>a</i> for 1997 (left column), 1998 (middle column) and 1999 (right column) from January to June. Black dots represent sampling stations. No data available for January, 1998.	67

3.3	Cell densities of 3 phytoplankton groups (diatom, dinoflagellates and other flagellates) at Station 3, 12, 20 and 32 on GB from January to June 1999. This figure is adapted from <i>Townsend and Thomas</i> [2002].	68
3.4	Areal contour plots of surface nitrate + nitrite for 1997 (left column), 1998 (middle column) and 1999 (right column) from January to June. Black dots represent sampling stations. No data available for January and June, 1997 and January 1998.	70
3.5	Areal contour plots of surface silicate for 1997 (left column), 1998 (middle column) and 1999 (right column) from January to June. Black dots represent sampling stations. No data available for January and June 1997 and January 1998.	71
3.6	One-dimension model grid showing the 5x5 grid structure and computational point.	73
3.7	Time sequence of the vertical distribution of model-predicted temperature in Site A from January to June.	76
3.8	Time sequence of the vertical distribution of model-predicted nitrate (NO_3^-), ammonia (NH_4^+), silicate(Si), small phytoplankton (P_S), and large phytoplankton (P_L) in Site A from January to June.	77
3.9	Time sequence of the vertical distribution of model-predicted small zooplankton (Z_S), large zooplankton (Z_L), detrital organic nitrogen (D_N) and detrital organic silicon (D_{Si}) in Site A from January to June.	80
3.10	Time sequence of the vertical distribution of model-predicted temperature in Site B from January to June.	81
3.11	Time sequence of the vertical distribution of model-predicted nitrate (NO_3^-), ammonia (NH_4^+), silicate(Si), small phytoplankton (P_S), and large phytoplankton (P_L) in Site B from January to June.	82

3.12	Time sequence of the vertical distribution of model-predicted small zooplankton (Z_S), large zooplankton (Z_L), detrital organic nitrogen (D_N) and detrital organic silicon (D_{Si}) in Site B from January to June.	84
3.13	Comparisons between the model-predicted and observed depth-averaged phytoplankton (top), nitrate (NO_3) (middle), ammonia (NH_4) (middle), and silicate (Si) (bottom) in Site A from January to June.	86
3.14	Comparisons between the model-predicted and observed depth-averaged phytoplankton (top), nitrate (NO_3) (middle), ammonia (NH_4) (middle), and silicate (Si) (bottom) in Site B from January to June.	88
3.15	Time series of short-wave radiation from February 1 to June 30, 1995.	89
3.16	Comparison of days with wind speed over 10 m/s for each month in 1997, 1998 and 1999.	91
3.17	Effects of light attenuation coefficient (K_{ext}) on the seasonal variation of large phytoplankton (PL). The case labeled with “ K_{ext} varied” means K_{ext} is 0.15 m^{-1} for January, February and March, 0.12 m^{-1} for April, and 0.10 m^{-1} for May and June.	91
3.18	Effects of different P-I functions on the seasonal variation of large phytoplankton (PL).	92
3.19	Effects of silicate initial concentration ($[\text{Si}]_{init}$) on the seasonal variation of large phytoplankton (PL).	93
3.20	Seasonal variation of large phytoplankton (PL) and small phytoplankton (Ps) (top) when ratio of nitrogen and silicon (Rns) in large phytoplankton is 1.5. Bottom shows a synchronized depletion of nitrate (NO_3) and silicate (Si) during later March.	94

3.21	Seasonal variation of large phytoplankton (Pl) and small phytoplankton (Ps) (top) when ratio of nitrogen and silicon (Rns) in large phytoplankton is 0.8. Bottom shows an asynchronized depletion of nitrate (NO ₃) and silicate (Si), with silicate being depleted about 1 month earlier than nitrate.	94
3.22	Effects of decomposition rate (Edn) of detrital organic nitrogen on the seasonal variation of small phytoplankton (Ps) (top), large phytoplankton (Pl) (middle), and ammonia (NH ₄) (bottom). The dashed line represents the case with Edn of 0.1 and solid line with Edn of 0.06.	96
3.23	Effects of maximum grazing rate of large zooplankton on large phytoplankton (Rzl) on the seasonal variation of large phytoplankton (PL).	97
4.1	A schematic view of interaction between biological and physical factors along the section. Upper figure represents an un-stratified case and bottom one represents a stratified case. TMF stands form tidal mixing front. The critical depth changes with light intensity and water turbidity.	107
4.2	Numerical model grid, plotted every five points in the vertical and every three in the horizontal. Horizontal resolution is 500 m near and across the bank and increase linearly over an interval of 30 grid points to 11.96 km away from the region of interest. A uniform grid is used in σ , with vertical resolution $\Delta\sigma = 0.0196$	110
4.3	Model-computed cross-isobath distribution of tidally averaged temperature (T), and cross-bank (U: positive on-bank), along-bank (V: positive out of the paper) and vertical (W: positive upward) velocities on the southern flank of GB on February 15, 1995.	112

4.4	Model-computed cross-isobath distribution of tidally averaged temperature (T), and cross-bank (U: positive on-bank), along-bank (V: positive out of the paper) and vertical (W: positive upward) velocities on the southern flank of GB on April 15, 1995.	113
4.5	Model-computed cross-isobath distribution of tidally averaged temperature (T), and cross-bank (U: positive on-bank), along-bank (V: positive out of the paper) and vertical (W: positive upward) velocities on the southern flank of GB on June 15, 1995.	114
4.6	Model-computed cross-isobath distribution of tidally averaged nitrate (NO ₃), silicate (Si), small phytoplankton (Ps), large phytoplankton (Pl), and small zooplankton (Zs) on the southern flank of GB on February 15, 1995.	116
4.7	Model-computed cross-isobath distribution of tidally averaged large zooplankton (Zl), detrital organic nitrogen (Dn), detrital organic silicon (Dsi), and ammonia (NH ₄) on the southern flank of GB on February 15, 1995.	117
4.8	Model-computed cross-isobath distribution of tidally averaged nitrate (NO ₃), silicate (Si), small phytoplankton (Ps), large phytoplankton (Pl), and small zooplankton (Zs) on the southern flank of GB on April 15, 1995.	119
4.9	Model-computed cross-isobath distribution of tidally averaged large zooplankton (Zl), detrital organic nitrogen (Dn), detrital organic silicon (Dsi), and ammonia (NH ₄) on the southern flank of GB on April 15, 1995.	120

4.10	Model-computed cross-isobath distribution of tidally averaged nitrate (NO ₃), silicate (Si), small phytoplankton (Ps), large phytoplankton (Pl), and small zooplankton (Zs) on the southern flank of GB on June 15, 1995.	121
4.11	Model-computed cross-isobath distribution of tidally averaged large zooplankton (Zl), detrital organic nitrogen (Dn), detrital organic silicon (Dsi), and ammonia (NH ₄) on the southern flank of GB on June 15, 1995.	122
4.12	Time series of wind and surface heatflux for the 2-D model experiments (Top two), and model-computed cross-isobath distribution of tidally averaged temperature (T) and vertical turbulence mixing coefficient (Km) on the southern flank of GB on April 21, 1995 (bottom two).	124
4.13	Time series of wind and surface heatflux for the 2-D model experiments (Top two), and model-computed cross-isobath distribution of tidally averaged temperature (T) and vertical turbulence mixing coefficient (Km) on the southern flank of GB on April 29, 1995 (bottom two).	125
4.14	Time series of wind and surface heatflux for the 2-D model experiments (Top two), and model-computed cross-isobath distribution of tidally averaged temperature (T) and vertical turbulence mixing coefficient (Km) on the southern flank of GB on May 2, 1995 (bottom two).	126
4.15	Model-computed cross-isobath distribution of tidally averaged nitrate (NO ₃), silicate (Si) and large phytoplankton (PL) on the southern flank of GB on April 21, 1995.	127

4.16	Model-computed cross-isobath distribution of tidally averaged nitrate (NO ₃), silicate (Si) and large phytoplankton (PL) on the southern flank of GB on April 29, 1995.	128
4.17	Model-computed cross-isobath distribution of tidally averaged nitrate (NO ₃), silicate (Si) and large phytoplankton (PL) on the southern flank of GB on May 2, 1995.	129
4.18	Time sequence of the vertical distribution of model-predicted temperature gradient ($\delta T/\delta Z$), vertical turbulence mixing coefficient (Km), and large phytoplankton (Pl). The vertical section is located in at the distance of 20 km in 2-D model domain.	131
4.19	Time sequence of the vertical distribution of model-predicted temperature gradient ($\delta T/\delta Z$), and large phytoplankton (Pl) with 30% less of surface heat flux. The vertical section is located in at the distance of 20 km in 2-D model domain.	132
4.20	Model-computed cross-isobath distribution of tidally averaged nitrate (NO ₃), silicate (Si) and large phytoplankton (PL) on the southern flank of GB on April 29, 1995 with low initial silicate concentration (1 $\mu\text{mol/l}$) in the deeper region (water depth >60 m).	133
4.21	Model-computed cross-isobath distribution of tidally averaged nitrate (NO ₃), silicate (Si) and large phytoplankton (PL) on the southern flank of GB on June 12, 1995, showing the stratification in the deeper region with nutrients being depleted in the surface layer (top two) and a subsurface maximum of large phytoplankton (bottom).	135
4.22	Fluorescence profile for representative station in the stratified areas of the southern flank of GB. This figure is from Mountain and Taylor (1996).	136
4.23	Chlorophyll <i>a</i> profile for station 15 during June of 1998 and 1999. . .	137

4.24	Initial distribution of tracer along the cross-isobath section, with concentration of tracer below the 10 °C isothermal line is 1 unit/l and 0 unit/l in the rest of the area.	138
4.25	Model computed distribution of tracer along the cross-isobath section after one tidal cycle with tidal forcing plus realistic wind stress. . . .	139
4.26	Model computed distribution of tracer along the cross-isobath section after ten tidal cycle with tidal forcing plus realistic wind stress. . . .	140
4.27	Model computed distribution of tracer along the cross-isobath section after ten tidal cycle with tidal only.	141
4.28	Schematic of formation of phytoplankton maximum area (PMA) in the transition between shallow and deep areas. See the text for detailed explanation.	143
4.29	Example of a phytoplankton maximum area (PMA) in the transition between shallow and deep areas along the cross-isobath section during April 1997.	144
4.30	Cross-isobath distribution of chlorophyll <i>a</i> during the broad-scale survey for the U.S. GLOBEC/GB Program in 1999.	146
4.31	A cross-isobath section used to plot the vertical distribution of chlorophyll <i>a</i> , silicate, nitrate, temperature and salinity during the broad scale survey for the U.S. GLOBEC/GB Program in 1999.	147
4.32	Cross-isobath distribution of silicate during the broad-scale survey for the U.S. GLOBEC/GB Program in 1999.	148
4.33	Cross-isobath distribution of nitrate during the broad-scale survey for the U.S. GLOBEC/GB Program in 1999.	149
4.34	Cross-isobath distribution of temperature during the broad- scale survey for the U.S. GLOBEC/GB Program in 1999.	150

4.35	Cross-isobath distribution of salinity during the broad-scale survey for the U.S. GLOBEC/GB Program in 1999.	151
5.1	Monthly composite SeaWiFS image of GB and surrounding area during March 1999. Image is adapted from Dr. Andrew Thomas's website at the School of Marine Sciences, University of Maine.	160
5.2	Schematic of possible source of water on the southern flank of GB. GOMW: Gulf of Maine Water; SSW: Scotian Shelf Water; GB: Georges Bank; WCR: Warm Core Ring.	161
5.3	Eight-day composite SeaWiFS image of GB and surrounding area during March 1999. Image is adapted from Dr. Andrew Thomas's website at the School of Marine Sciences, University of Maine.	163
5.4	Selected Sea Surface Temperature (SST) images of GB and surrounding area during March 1999. Data is downloaded from NOAA's AVHRR (Advanced Very High Resolution Radiometer) website. White circles highlight SSW intrusion.	165
5.5	The U.S. GLOBEC/GB Program broad-scale sampling station plan for 1998 and 1999. CTD and water sample data at stations along the connected arrows are present later.	166
5.6	Vertical profile of fluorescence (green lines), salinity (blue lines) and temperature (black lines) along the stations as shown in Figure 5.5 during March 1999.	167
5.7	Vertical profile of chlorophyll <i>a</i> (green dots), nitrate (blue dots) and silicate (black dots) along the stations as shown in Figure 5.5 during March 1999.	169
5.8	Unstructured numerical model grid for GOM/GB region.	171
5.9	Wind field of selected days in March 1999 as the MM5 model output.	174

5.10	Model-computed subtidal currents on GB and surrounding region in day 66. upper: surface subtidal currents; bottom: subtidal currents at 20-m water depth.	175
5.11	Model-computed subtidal currents on GB and surrounding region in day 76. upper: surface subtidal currents; bottom: subtidal currents at 20-m water depth.	176
5.12	Model-computed subtidal currents on GB and surrounding region in day 81. upper: surface subtidal currents; bottom: subtidal currents at 20-m water depth.	177
5.13	Selected snapshots of Lagrange particle trajectory. Particles were released at the surface near Browns Bank region at day 63.	180
5.14	Selected snapshots of Lagrange particle trajectory. Particles were released at the sub-surface (30-40 m below the surface) near Browns Bank region at day 63.	181
5.15	Selected snapshots of Lagrange particle trajectory. Particles were released at the surface on the central portion of GB at day 63.	182
5.16	Selected snapshots of Lagrange particle trajectory. Particles were released at the sub-surface (20-30 m below the surface) on the central portion of GB at day 63.	183
5.17	Selected snapshots of tracer experiment results. Tracer were released at the surface layer (<30 m) near the Browns Bank region at day 63.	185
5.18	Selected snapshots of tracer experiment results. Tracer was released at the surface layer (<30 m) near the Browns Bank region at day 63. The vertical mixing coefficient in the water column below 30 m is one order smaller than the standard model run as shown in Figure 5.17 .	186
5.19	Time series of vertically integrated tracer concentration in the entire model domain.	187

5.20	Selected snapshots of tracer experiment results. Tracer were released homogenously in the entire water column of the central portion of GB at day 63.	188
5.21	Selected snapshots of coupled biological-physical model experiment results. The large phytoplankton at the surface layer (< 30 m) near the Browns Bank region was set to be 3 $\mu\text{mol/l}$ at day 63.	190
5.22	Eight-day composite SeaWiFS image of GB and surrounding area during March 1998. Image is adapted from Dr. Andrew Thomas's website at the School of Marine Sciences, University of Maine.	192
5.23	Vertical profile of fluorescence (green lines), salinity (blue lines) and temperature (black lines) along the stations as shown in Figure 5.5 during March 1998.	193
B.1	Result of sensitivity analysis for 1-D model experiment as described in Chapter 3.	209
C.1	Time series of wind stress and surface heat flux on the southern Georges Bank in February 1995	212
C.2	Time series of wind stress and surface heat flux on the southern Georges Bank in March 1995	213
C.3	Time series of wind stress and surface heat flux on the southern Georges Bank in April 1995	214
C.4	Time series of wind stress and surface heat flux on the southern Georges Bank in May 1995	215
C.5	Time series of wind stress and surface heat flux on the southern Georges Bank in June 1995	216

LIST OF TABLES

2.1	Definitions of the flux terms in the food web	36
3.1	Definition of code used in Table 3.2 for site A.	75
3.2	Design of model run matrix for site A.	75
A.1	Parameters used for the biological model	207

CHAPTER 1

INTRODUCTION

It is believed that in the ocean, the basic features of an ecosystem in a particular region are determined by its physical attributes [*Mann and Lazier, 1996; Robinson et al., 2002*]. This is certainly the case on Georges Bank (GB), where the combination of proper light condition, steep bottom topography, vertical stratification, tidal mixing and shelf break fronts as well as the remote “cross-over” water transport and on-bank intrusion of warm-core rings promotes the growth of phytoplankton and zooplankton populations. As a result, high primary and secondary production establish the biological foundation of the ecosystem that supports the high fish production on the bank [*GLOBEC, 1992; Wiebe et al., 2002*].

1.1 GEORGES BANK

Georges Bank is a shallow submarine bank lying along the outer continental shelf about 180 km east of Cape Cod, Massachusetts (Figure 1.1). As defined by the 100 m isobath, GB is approximately 280 km long by 150 km wide with an area of about 33,700 km² [*Uchupi and Austin, 1987*]. The cross-bank bottom topography rises steeply, with a slope of about 0.01, from 1000 m on the upper slope to 100 m at the shelf break connecting to the North Atlantic Ocean. Afterward, it increases slowly, with a slope of roughly 0.0005, toward the crest of the bank; and then decreases rapidly, with a slope of about 0.03, to a depth of 300 m in the deep basin off the northern edge of the bank. Over the crest, within the 60-m isobath, are a complex

General Circulation During Stratified Season

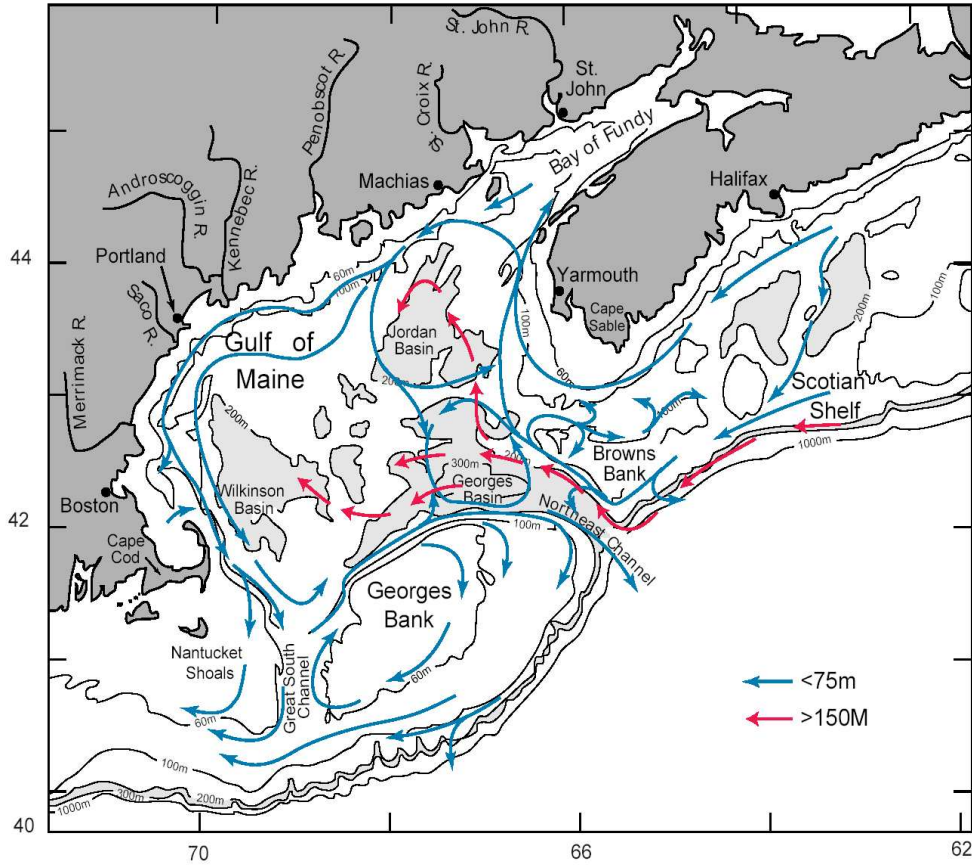


Figure 1.1: The general circulation in GOM/GB region during stratification condition (May-September). From *Beardsley et al.* [1997].

series of shoals and overlying sand waves that rise, in some places, to within a few meters of the surface. This terrain is shifting with time due to storm- or strong tide-induced sediment resuspension and deposition in submarine sand dunes [*Twichell et al.*, 1987; *Uchupi and Austin*, 1987]

1.2 PHYSICAL PROCESSES IN GOM/GB

From a large-scale point of view, GB water is part of a coastal current system, originating from the Newfoundland Shelf, inflowing from the Scotian Shelf (SS) and across the Northeast Channel (NEC), moving westward along the slope of the Mid-Atlantic Bight and then outflowing to the New England Shelf (NES) (Figure 1.1 [Chapman and Beardsley, 1989]). Water in GOM/GB is a mixture of cool/low salinity near-surface water flowing from SS and local coastal rivers and warm/high salinity slope water inflowing through the NEC (Figure 1.1) [Bigelow, 1927; Smith, 1983; Ramp *et al.*, 1985]. The SS water enters the GOM through two paths: one flows along the inner shelf, turns northward around Cape Sable, and enters the Bay of Fundy. This water joins the local freshwater discharge waters to form a westward coastal current along the northern inner shelf of the GOM. The other flows offshore around Halifax, enters the shelf break of SS, moves westward along the 200-m isobath on the slope, and turns clockwise into the NEC. This water tends to either enter Georges Basin or episodically flows onto GB through the NEC as a result of so-called “cross-over” events. The deep water in the GOM mainly originates from the slope water entering in the deep region of the NEC [Ramp *et al.*, 1985]. The baroclinic geostrophic currents constructed from hydrographic survey data suggest that the water entering the Georges Basin from the NEC tends to split northeastward into the Jordan Basin and northwestward into the Wilkinson Basin [Brown and Beardsley, 1978].

GB is characterized with strong M_2 tidal currents [Moody *et al.*, 1984]. Tidal currents are about 30 cm/s around the 100-m isobath near the shelf break on the southern flank and about 100 cm/s at the edge of the northern flank. Nonlinear interaction of tidal currents over steep bottom topography across the bank generates a permanent clockwise residual circulation gyre around GB, with a strong eastward current jet at the edge of the northern flank and a weak recirculation covering a

broad area on the southern flank [Loder, 1980; Butman *et al.*, 1982; Chen *et al.*, 1995]. This gyre intensifies with season due to the development of stratification. In winter, the maximum velocity is about 20-25 cm/s on the northern flank and about 3-5 cm/s over the southern flank [Butman *et al.*, 1982]. In summer, the residual current is enhanced to 30-40 cm/s on the northern flank and about 5-10 cm/s on the southern flank [Loder and Platt, 1985; Chen, 1992; Naimie *et al.*, 1994; Chen *et al.*, 1995].

The shear of strong tidal currents across this finite-amplitude, asymmetric bank produces energetic turbulent mixing, which varies temporally and spatially over topography [Loder *et al.*, 1992; Chen *et al.*, 1995; Horne *et al.*, 1996; Yoshida and Oakey, 1996; Chen and Beardsley, 1998]. Tidal mixing creates a well defined tidally mixed front closed around the shallow cap of GB (Figure 1.2). During late spring through summer, this front is located near the 40-m isobath on the northern flank and about the 50-60-m isobath on the southern flank [Flagg, 1987]. During winter, the front disappears over the southern flank after the water is homogenized by strong wind mixing and surface cooling [Chen *et al.*, 1995].

There is another buoyancy front located at the shelf break, which is usually called the shelf break front (Figure 1.2). The physical mechanism for the formation of the shelf break front is unclear, but the intensity and variation of this front is related to (1) the slope current flowing from the Scotian Shelf, (2) the “cross-over” buoyancy flux through the NEC, and (3) the clockwise buoyancy flow recirculated from the slope of the northern flank of GB, (4) intrusion of the slope water from the North Atlantic Ocean, and (5) seasonal variation of surface heating/cooling. During winter, the shelf break front is located around the 100-m isobath and characterized with sharp gradients of water temperature and salinity. During summer, it tends to migrate onbank to the 70-80 m isobath and is distinguished by sharp gradient of salinity only [Gawarkiewicz and Chapman, 1992]. The existence of the shelf break

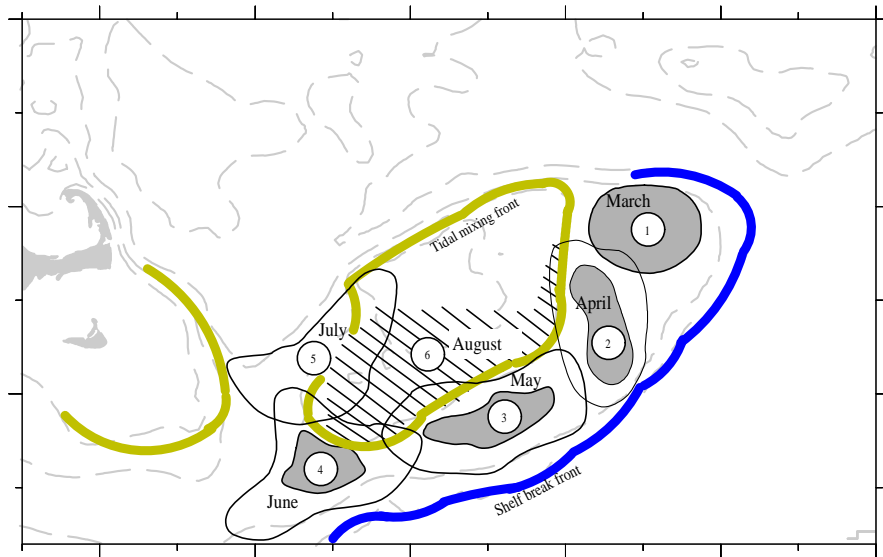


Figure 1.2: Schematic of fronts around Georges Bank and generalized distribution of cod/haddock eggs (1), larvae (2,3), and pelagic juveniles (4,5) during their first 3-4 months of life in the clockwise circulation over Georges Bank. The year-round shelf-break front (blue curve) is located along the 100-m isobath; and the tidal mixing front (brown curves) is located near the 40-m isobath on the northern flank and around the 50- to 60-m isobath on the southern flank during later spring and summer. Adapted from *Lough and Manning* [2001].

leads to a permanent westward subtidal flow around the shelf break of the southern flank of GB. This current is about 10 cm/s in winter and can increase to 15-20 cm/s in summer as the front is intensified [*Chen et al.*, 2003].

The two fronts on GB make this submarine area a unique region for a productive ecosystem. The tidal mixing front acts like a barrier separating well-mixed water on the cap of the bank from stratified water on the flanks. The shelf break front adds a second wall at the outer edge of GB to form a stratified retention zone over the southern flank [*Naimie*, 1996; *Chen et al.*, 2003]. Lagrangian model experiments suggest that the near-bottom water tends to converge toward the tidal mixing and shelf break fronts to form a divergence zone between these two fronts [*Chen et al.*, 2003]. This model result was recently detected in the dye experiments injected near the bottom on the southern flank in late spring and summer of 1999 [*Houghton*, 2002].

GB is also influenced episodically by (1) the low-salinity water inflowing through the NEC on the eastern side [*Ramp et al.*, 1985] and across the northern Great South Channel (GSC) on the western side [*Chen et al.*, 1995b]; (2) onbank intrusion of warm core rings [*Ramp*, 1986; *Garfield and Evans*, 1987; *Ryan et al.*, 2001] and (3) meso-scale variable wind field and seasonal surface heating/cooling [*Brink et al.*, 2003]. Water exchange over GB is controlled mainly by varying winds [*Chen et al.*, 2003b], asymmetric tidal mixing [*Chen and Beardsley*, 1998; *Pringle and Franks*, 2001], strong nonlinear tidal current interaction [*Loder et al.*, 1997] and chaotic mixing [*Chen and Beardsley*, 2002] as well as entrainment of warm core rings [*Ramp*, 1986; *Garfield and Evans*, 1987; *Ryan et al.*, 2001]. In winter, the water on GB could be washed out due to strong wind-induced off-bank transport. In summer, winds are generally too weak to alter the general pattern of tidal-induced clockwise residual circulation on the bank and buoyancy-induced westward flow at the shelf break.

1.3 BIOLOGICAL PROCESSES ON GB

Recent interdisciplinary field and modeling studies in the GB/GOM clearly demonstrate that physical processes can strongly influence key biological processes of phytoplankton blooms, zooplankton distribution and abundance, larval pathways and distributions, fish distribution and recruitment. Phytoplankton blooms are events of rapid production and accumulation of phytoplankton biomass that are usually responses to various physical forcings. Since climatic or hydrologic conditions vary over a broad spectrum of time scales and can be exceptional, the algal bloom can be a short-term episodic event, or a recurrent seasonal phenomena, or a rare event [Cloern, 1996]. On GB, for example, the spring phytoplankton bloom is a recurrent seasonal event, which usually occurs in February or March in the well-mixed region (< 60 m) and in April in deeper water (60-100 m) and declines in late April or early May [Gran and Braarud, 1935; Lillick, 1940]. The bloom usually re-occurs again near the tidal mixing frontal zone in June. The primary productivity varies with space and time on GB, with a maximum value of over $400 \text{ gC m}^{-2} \text{ yr}^{-1}$ observed on the crest of the bank [O'Reilly *et al.*, 1987].

Regarding the species composition, biomass and timing, the property of the phytoplankton blooms on GB significantly differs in well-mixed shallow and stratified deep regions. In the well-mixed shallow region, diatoms remain dominant, no matter when the bloom occurs. In the stratified deep region, the species are usually dominated by dinoflagellates during summer and fall, with maximum abundance occurring near the seasonal pycnocline [O'Reilly *et al.*, 1987]. *Chaetoceros* (e.g. *C. debile* and *C. decipens*) are the dominant species in the well-mixed region [Sears, 1941], while *Thalassiosira spp.* is usually abundant and occasionally dominant in the stratified region. Observations also found that *Navicula sp.* and *Phaeocystis pouchetti* might occasionally be abundant in the well mixed region [Falkowski and

[Von Bock, 1979; Cura, 1982]. This species composition in the bloom on GB was evident in either water samples collected in recent phytoplankton survey [Campbell *et al.*, 2001; Townsend and Thomas, 2002] or images gained from a video plankton recorder [Davis *et al.*, 1996; Ashjian *et al.*, 2001].

Both field measurements and modeling studies suggest that the spatial distribution and temporal variability of phytoplankton biomass on GB are controlled by coupled biological and physical processes. The biological process mainly refers to an *in situ* change of the phytoplankton population that is caused by (1) growth, (2) mortality, and (3) grazing loss. The physical processes are (1) advection, (2) mixing/diffusion, (3) sinking and (4) bottom flux due to resuspension via sedimentation. These processes tend to re-distribute the phytoplankton biomass in space and time and provide the source of species from an external region. On GB, the closed nature of tidal mixing front makes the water in the well-mixed region relatively shelf-contained, so that the phytoplankton is dominantly controlled by the biological process. In the stratified deep region, however, the phytoplankton is significantly influenced by the seasonal variability of stratification due to surface heating/cooling, inflows from remote areas (e.g. “cross-over” water through the NEC from the SS), and frontward upwelling caused by cross-isobath secondary flow [Townsend and Thomas, 2002; Franks and Chen, 1996, 2001].

On GB, zooplankton are dominant in both number and biomass by the copepods *Calanus finmarchicus*, *Pseudocalanus newmanii*, *Pseudocalanus moultoni*, *Centropages typicus*, *Centropages hamatus*, *Paracalanus parvus*, and *Oithona similis* [Davis, 1987]. They are dominated by *Calanus finmarchicus* and *Pseudocalanus* sp. from winter through the spring, and by *Centropages typicus*, *Centropages hamatus* and *Paracalanus parvus* from late summer through the fall [Davis, 1987]. *Oithona similis* is a year-round abundant species. Regarding the recruitment of fishes on GB, *Calanus finmarchicus* and *Pseudocalanus* sp.

are two target species since they are the most important prey sources for early life stages of cod and haddock [Sherman *et al.*, 1981; Kane, 1984; Buckley and Lough, 1987].

There is a dynamic linkage between phytoplankton and target zooplankton species in the GOM/GB region. *Calanus finmarchicus* in GOM, for example, usually begin to emerge from diapause stage (dominated by copepodites fifth-C5) in deep basins in late December. Maturation occurs during the ascent with males first appearing and then females. These adults are called the zero generation of *Calanus finmarchicus* (termed G0). The reproduction of G0 begins in January-February each year. Adults of G0 and young naupli of the first generation (G1) are upwelled and advected onto GB from deep basins in the GOM and the SS water through the NEC (Figure 1.3). Once these populations reach the bank and carried into the northeastern and southern flanks, retention areas on the GB side of the shelf break front, they appear to be in a rich food-environment [Davis, 1984]. Consequently, second generation (G2) of *Calanus finmarchicus* is produced and becomes abundant in spring during a westward journey of G1 [Durbin *et al.*, 2000a]. The large peak in abundance of *Calanus finmarchicus* occurring on the southern flank of GB in March and April appears to be the combination of both early members of the G2 and late members of the G1 [Durbin *et al.*, 2000a].

Although GB is recognized as a region with high primary production that is favorable to maximal copepod production rates [Davis, 1984], the growth and reproduction of *Calanus finmarchicus* in late spring and early summer are significantly affected by food limitation [Durbin *et al.*, 1995a,b]. More direct evidence of food limitation was reported on the southern flank of the bank in April 1997 [Campbell *et al.*, 2001]. In that cruise, samples of *Calanus finmarchicus* were collected at a shallow, well-mixed site on the central Bank and a stratified site south of the tidal mixing front on the southern flank, respectively. Chlorophyll *a* concentration was high at

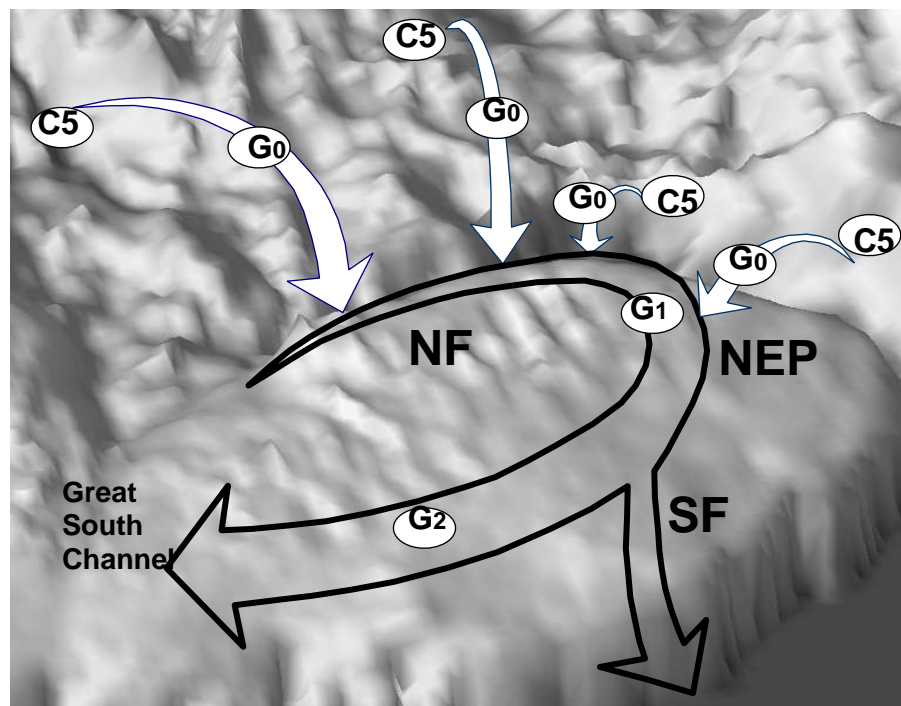


Figure 1.3: Schematic of possible sources of *Calanus finmarchicus* resupply to Georges Bank and succession of generations in GOM/GB region. G0: the generation ascending from diapause; G1: the first generation reproduced from G0; G2: the second generation reproduced from G0. See the text for detail.

the well-mixed site but low at the stratified site. Indices of *Calanus finmarchicus* production, which refer to size, condition, RNA/DNA ratio, and the rates of molting, growth, and egg production, were significantly lower at the stratified site with low food concentration than at the well-mixed site with high food concentration. This fact suggests that food limitation functions spatially on GB, and can be more severe in naupliar and early copepodite stages of *Calanus finmarchicus*.

The absence of diel vertical migration for *Calanus finmarchicus* on GB provides an additional indirect evidence of food limitation [Durbin *et al.*, 1995c, 2000a,b; Ashjian *et al.*, 2001]. The diel vertical migration of copepod is usually a result of two competing factors: (1) food availability and (2) visual predator pressure. Under a low food resource situation, copepods may stop diel vertical migration and remain near the surface both day and night to conserve their energy [Huntley and Brooks, 1982; Durbin *et al.*, 1995c]. However, since most of the evidence was based on measurements from cruise surveys conducted in limited areas and during short time periods, it remains unclear whether food limitation is an isolated and localized incident or it recurs over a broad area every year. It appears that the timing and magnitude of the spring bloom can have a significant impact on the zooplankton population [Durbin *et al.*, 1995c]. An early spring bloom may mismatch *Calanus finmarchicus* cohort development and cause the “waste” of food. As a result, much of the spring bloom phytoplankton would settle to the bottom and enter benthic food chains [Townsend and Cammen, 1988]. On the other hand, late occurrence of spring bloom may also mismatch the first generation of *Calanus finmarchicus* that are abundant on GB during spring, which may lead to less success in recruitment for that year.

The cod and haddock are the most commercially valued fish species found in abundance on GB [GLOBEC, 1992]. Both cod and haddock spend much of their early life stages (from egg to demersal stages) within the shelf waters covering the

bank from winter through summer (Figure 1.2). Generally, they spawn on the north-east flank of Georges Bank in late winter and early spring [*Smith and Baker, 1985*]. Their eggs and young larvae drift southwestward following the clockwise residual circulation gyre and arrive on the southern flank in late April and May. A high abundance of cod and haddock larvae usually occur in the stratified region between tidal and shelf break fronts [*Lough, 1984; Townsend and Pettigrew, 1996; Lough and Mountain, 1996*]. These larval fishes continue to move westward and northeastward following the recirculation and shelf break front-guided westward buoyancy current, and then grow to pelagic juveniles on the western flank in late spring. The transition from pelagic to demersal life normally occurs in mid-summer, when they migrate to and reside in the mixed region of the central Bank [*Lough et al., 1989*].

The survival of larval fishes is significantly controlled by physical processes of the water exchange over GB from winter to summer. In winter through spring, the weather on GB is characterized by episodic cold atmospheric frontal passages with a period of 5 to 7 days or strong winter or spring storms. As a storm passes by GB, the larval fishes can be “washed out” off the bank and die in the open ocean over a short time period. This scenario could also occur during a cold atmospheric frontal passage, in which the northerly wind tends to produce an offbank Ekman transport and push larval fishes off the bank [*Chen et al., 2003b*]. It is no doubt that these wind events directly affect the recruitment of cod and haddock on GB.

1.4 MODELING OF PHYTOPLANKTON DYNAMICS ON GB

The dynamics of phytoplankton on GB is controlled by complex interactions of trophic levels and biological-physical processes over different time and space scales. As pointed out by *Esaias [1981]* (Figure 1.4), for example, phytoplankton usually features biological production over a time scale of less than 10 days and a space

scale of less than 10 km. The life cycle and patch pattern of zooplankton are usually one order of magnitude greater than phytoplankton, while the time and space scales of fishes are one order further greater than zooplankton. Since these plankton and animals live in the coastal ocean physical environment, they are influenced or controlled by various physical processes such as tidal mixing, strong storms, and oceanic fronts. These physical processes occur over a large range of temporal scales from hours to months and spatial scales from a few meters to 1000 km. Since biological and physical processes are nonlinearly coupled with each other, the current newly developed field measurement technology, such as remote sensing, acoustic and video plankton recording systems, is limited in its ability to capture a continuous view of the temporal variation and spatial distribution of the ecosystem on GB. A satellite can provide a nice image of surface chlorophyll *a* concentration during clear skies. However, it fails to accurately resolve pigments due to cloud cover or non-chlorophyll suspended materials during storm events or cold atmospheric frontal passages. Similarly, although acoustic and video systems are able to provide a continuous time series of plankton biomass, they are still limited in their abilities to instantaneously cover a broad region.

Coupled biological-physical models have become scientifically-sound tools for the study of ecosystem dynamics over the last several decades. The biological component of these models can be divided into three categories: (1) theoretical models, (2) heuristic models, and (3) predictive models [*Franks, 1995*]. The theoretical models are usually used to explore general principles of biological-physical processes and to predict potential outcomes based on idealized scenarios. Typically, these models are built on certain assumptions, so they are useful to explore the driving mechanism under specific conditions. The best example of this kind of model is *Sverdrup [1953]*'s theory from which the occurrence spring phytoplankton bloom event in a moderate marine condition can be predicted based on the ratio of critical depth to the thickness

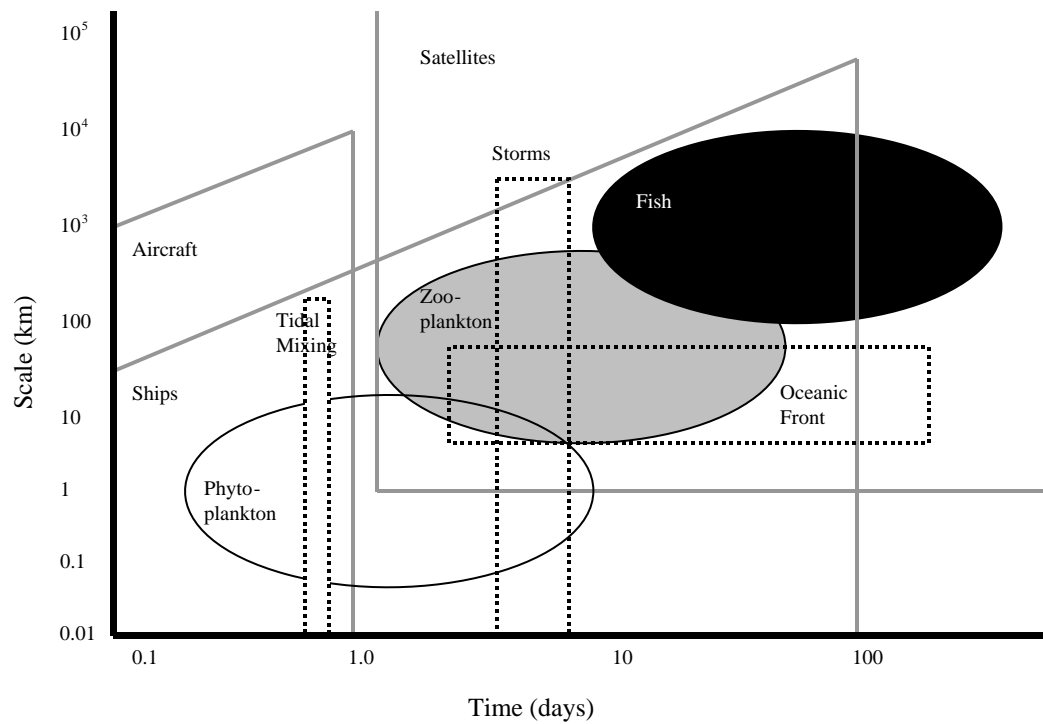


Figure 1.4: The approximate spatial and temporal ranges for a variety of oceanic phenomena, along with estimated observational capabilities of various research platforms. Three basic trophic levels (phytoplankton, zooplankton, and fish) and three physical phenomena (tidal mixing, storms and oceanic fronts) are shown. Observations using aircraft, ships and satellites are suitable for different spatial and temporal scales.

of the surface mixed layer. Heuristic models are formulated and parameterized based on evidences from field measurements or laboratory experiments. These models are mainly used to interpret the retrospective data sets and to explore how a particular scenario occurs. Good examples of this type of model are process-oriented biological models such as Nutrients-Phytoplankton (NP) or Nutrient-Phytoplankton-Zooplankton (NPZ) model that are used to study the biological and physical processes controlling the spatial distribution of the phytoplankton patch at density fronts or tidal mixing fronts [*Steele, 1974; Franks and Chen, 1996*]. Predictive models refer to statistical or dynamical models that are well- tested or calibrated by long-term measurement data, to render them capable of predicting the behavior of the ecosystem beyond the constraints of available data. The current understanding of the complex interactions between physical and biological processes which drive the marine ecosystem resides at a basic level. For this reason, there is no predictive model that is capable of accurately capturing the temporal variation and spatial distributions of ecosystem variables in coastal regions and estuaries. The “predictive models” currently in use can only provide a certain level of statistical meaning in the trends of the primary ecosystem variables with a large range of uncertainty.

The coupled biological and physical models for GB that have been published to date are heuristic models with relatively simple food web structures. *Klein [1987]* coupled an NPZ model with an idealized steady circulation gyre and used it to study the roles of retention, loss, and *in situ* productivity in the spring bloom. His results suggest that the tidal mixing and shelf break fronts must be taken into account since they can have a significant impact on the spring bloom on GB. *Lewis et al. [1994]* coupled the same type of NPZ model with a fully-nonlinear, primitive, semi-spectral ocean model (SPEM, *Haidvogel et al., 1991*) and used it to examine the effects of winds on the “wash out” events of phytoplankton or zooplankton on an idealized circular bank. Although the model didn’t represent the realistic physical condition

of GB due to the lack of tidal motion, his studies clearly show that the “wash out” events can happen during a winter storm. Tidal motion was included in the recent modeling study the effect of wind on the spatial and temporal variation of plankton on GB conducted by *Lewis et al.* [2001]. Their results clearly show that the spatial distribution of plankton is significantly influenced by a varying wind field. The patch structure of plankton under physical environment with a realistically varying wind field can considerably differ from that obtained with a climatologically averaged wind field.

Franks and Chen [1996] were the first to couple an NPZ model with a fully nonlinear, primitive equation, turbulence-closure model (ECOM-si, *Blumberg and Mellor*, 1987). They applied it to the exploration of the impact of tidal mixing, internal tidal waves, and stratified tidal rectification on the summertime cross-bank distribution of nutrients and phytoplankton on a 2-D section of GB. The model shows that the secondary current was characterized with a double cell circulation: converging toward the front at the surface and bottom, upwelling from the bottom and downwelling from the surface, merging near the bottom of the thermocline and then re-circulating back along the thermocline to the deep region. This secondary current tends to advect nutrients from the deep region to the eutrophic layer and support the growth of phytoplankton near the front. In addition, asymmetric variation of tidal mixing over a tidal cycle generated an onbank current near the bottom, which directly contributed to a near-bottom, cross-frontal transport of nutrients [*Chen and Beardsley*, 1998; *Pringle and Franks*, 2001]. Following their 1996 work, *Franks and Chen* [2001] extended their coupled NPZ/ECOM-si model to a 3-D, realistic GB topography. Driven by tidal forcing, this model captured plankton patterns on GB which agreed reasonably well with observations taken during summertime cruises and satellite-derived chlorophyll *a* images. *Franks and Chen* [2001]’s model

experiments suggest that the summertime patterns of phytoplankton on GB are primarily controlled by tidal mixing and the associated front.

1.5 OBJECTIVE, HYPOTHESIS AND APPROACH OF THIS STUDY

Although there have been many modeling effort made to understanding the dynamics of phytoplankton on GB, there is no model that is capable of capturing the recurrent phytoplankton blooms over a seasonal time scale in that region. Recent field measurements taken by *Townsend and Thomas* [2001, 2002] clearly show that nutrient limitation to primary productivity is not only time-dependent but also spatial-dependent. The recurrent phytoplankton bloom events during spring and early summer are directly related to silica limitation in addition to nitrogen. As a result of silica limitation, species of phytoplankton also significantly differ in the well-mixed and stratified regions. The species are dominated by diatoms in the well-mixed shallow region during spring when silica is a key limiting factor, and by dinoflagellates during summer and fall when nitrogen is a key limiting factor. These facts suggest that in order to capture a seasonal pattern of phytoplankton on GB, it is necessary to develop a model including multiple nutrient limiting processes. For this reason, the current *Franks and Chen* [1996]'s model can not be used to simulate the seasonal variability of phytoplankton on GB.

The objective of my Ph.D. thesis work is to examine the biological and physical interaction processes controlling the spring phytoplankton bloom dynamics on GB. To achieve this goal, a 9-compartment nutrients-phytoplankton-zooplankton-detritus model has been developed, including 3 nutrients (nitrate, ammonia and silicate), 2 phytoplankton (large- and small-size groups), 2 zooplankton (large- and small-size groups), 1 detrital-organic nitrogen and 1 detrital silicon. This biological model is driven by state of the art structured- and unstructured-grid coastal ocean models

(ECOM-si and FVCOM) with biological parameters specified using retrospective field measurements and existing literature.

Modeling experiments were aimed at testing three hypotheses regarding the formation and distribution of the spring bloom observed on GB. These hypotheses are described in detail as follows.

Hypothesis I:

According to observed features and processes controlling the low trophic level food web dynamics, GB can be divided into three dynamic zones: (1) the central bank in which water is shallow, vertically well-mixed, and relatively self-contained; (2) the mid- bank region characterized by a seasonal tidal mixing front; and (3) the outer-flank between the seasonal tidal mixing front and the permanent shelf break front in which wind- and buoyancy-induced advection processes are dominant. In the shallow, well-mixed central bank, the timing and duration of the spring bloom are controlled by a 1-D dynamical process associated with light intensity and its downward penetration, while in the deeper mid- and outer-flank, the timing of the spring bloom is closely linked to the seasonal development of stratification. The dense phytoplankton biomass can form as seasonal vertical stratification develops.

Hypothesis II:

The early spring bloom occurring in the central bank is mainly controlled by biological process associated with light intensity, but the recurrent bloom event during late spring and summer is mainly driven by the seasonal tidal mixing front. The timing of the bloom on the southern flank is determined by (1) timing of the formation of the tidal mixing front and onset of vertical stratification, and (2) forward nutrient flux from the deeper region.

Hypothesis III:

The spring bloom occurring on the outer southeastern or the southern flank of GB is a typical biological and physical coupling event associated with cross-frontal water

exchange and “cross-over” water transport from the SS through the NEC. Vertical mixing tends to reduce the “cross-over” water transport and thus phytoplankton transport onto the GB. With a sufficient supply of nutrients from the slope, the bloom occurs as a result of combined advective transport from the SS and rapid in situ growth of phytoplankton near the shelf break front. The structure of the phytoplankton patch is directly controlled by the location of the shelf break front, which could significantly differ year to year due to onbank migration of the shelf break front.

These three hypotheses were tested using 1-D, 2-D and 3-D numerical experiments. The 1-D experiments were conducted in a fixed location at which all biological and physical variables were assumed to be uniform in the horizontal but not in the vertical. The 2-D experiments featured a transect across GB in which the along-isobath variation for all the variables were ignored. The 3-D experiments were focused on the influence of the “cross-over” event through the NEC in the SS on the formation of the dense spring bloom over the southeastern edge of GB. The biological model is the same for all the experiments. For the physical model, ECOM-si was used for 1-D and 2-D experiments while the finite-volume coastal ocean model (FVCOM) developed by *Chen et al.* [2003] was used for 3-D experiments.

The remaining chapters of this thesis are organized as follows. In chapter 2, the coupled biological and physical model approach is introduced. In chapter 3, the 9-compartment food web model is tested in a 1-D model domain. Chapter 4 and 5 are aimed at discussing the model findings from 2-D, and 3-D experiments. Finally, a summary is given in chapter 6. To shorten the text of the thesis, appendices have been included for the description of the biological model, sensitivity study of biological parameters, and meteorological forcing data.

1.6 REFERENCES

- Ashjian, C. J., C. S. Davis, S. M. Gallager, and P. Alatalo, Distribution of plankton, particles, and hydrographic features across Georges Bank described using the video plankton recorder, *Deep Sea Research II*, 48(1-3), 245–282, 2001.
- Beardsley, R. C., B. Butman, W. R. Geyer, and P. Smith, Physical oceanography of the gulf of maine: an update, in *Proceedings of the Gulf of Maine Ecosystem Dynamics Scientific Symposium and Workshop*, pp. 39–52, 1997.
- Bigelow, H. B., Physical oceanography of the Gulf of Maine, *Bulletin of the United States Bureau of Fisheries*, 40, 511–1027, 1927.
- Blumberg, A. F., and G. L. Mellor, A description of a three-dimensional coastal ocean circulation model, in *Three-Dimensional Coastal Ocean Models, Coastal and Estuarine Science*, vol. 4, edited by N. S. Heaps, pp. 1–16, 1987.
- Brink, K. H., R. Limeburner, and R. C. Beardsley, Properties of flow and pressure over Georges Bank as observed with near-surface drifters, *Journal of Geophysical Research*, In press, 2003.
- Brown, W. S., and R. C. Beardsley, Winter circulation in the western Gulf of Maine. Part I: Cooling and water mass formation., *Journal of Physical Oceanography*, 8, 265–277, 1978.
- Buckley, L. J., and R. G. Lough, Recent growth, biochemical composition, and prey field of larval haddock (*Melanogrammus aeglefnus*) and Atlantic cod (*Gadus morhua*) on Georges Bank, *Canadian Journal of Fisheries and Aquatic Sciences*, 44(1), 14–25, 1987.

- Butman, B., R. C. Beardsley, B. Magnell, D. Frye, J. A. Vermersch, R. S. R. Limeburner, W. R. Wright, and M. A. Noble, Recent observations of the mean circulation on Georges Bank, *Journal of Physical Oceanography*, *12*, 569–591, 1982.
- Campbell, R. G., J. A. Runge, and E. G. Durbin, Evidence for food limitation of *Calanus finmarchicus* production rates on the southern flank of Georges Bank during April, 1997, *Deep Sea Research II*, *48*, 531–550, 2001.
- Chapman, D. C., and R. C. Beardsley, On the origin of shelf water in the Middle Atlantic Bight, *Journal of Physical Oceanography*, *19*, 384–391, 1989.
- Chen, C., Variability of currents in Great South Channel and over Georges Bank: observation and modeling, Ph.D. thesis, MIT/WHOI Joint Program, Woods Hole, Massachusetts, 1992.
- Chen, C., and R. Beardsley, Tidal mixing and cross-frontal particle exchange over a finite amplitude asymmetric bank: A model study with application to Georges Bank, *Journal of Marine Research*, *56*, 1163–1201, 1998.
- Chen, C., and R. Beardsley, Cross-frontal water exchange on Georges Bank: modeling exploration of the US GLOBEC/Georges Bank phase III study, *Journal of Oceanography*, *58*, 403–420, 2002.
- Chen, C., R. C. Beardsley, and R. Limeburner, Numerical study of stratified tidal rectification over finite-amplitude banks. Part II: Georges Bank, *Journal of Physical Oceanography*, *25*, 2111–2128, 1995a.
- Chen, C., R. C. Beardsley, and R. Limeburner, Variability of water properties in late spring in the northern Great South Channel, *Continental Shelf Research*, *15*, 415–431, 1995b.

- Chen, C., R. Beardsley, P. J. S. Franks, and J. V. Keuren, Wind-induced cross-frontal water transport on the southern flank of Georges Bank: A physical mechanism for the cross-frontal fish larval transport in early summer, *Journal of Geophysical Research*, In press, 2003a.
- Chen, C., H. Liu, and R. C. Beardsley, An unstructured, finite-volume, three-dimensional, primitive equation ocean model: application to coastal ocean and estuaries, *Journal of Atmospheric and Oceanic Technology*, 20, 159–186, 2003b.
- Chen, C., Q. Xu, R. C. Beardsley, and P. J. S. Franks, Model study of the cross-frontal water exchange on Georges Bank: A three-dimensional Lagrangian experiment, *Journal of Geophysical Research*, p. In press, 2003c.
- Cloern, J. E., Phytoplankton bloom dynamics in coastal systems: A review with some general lessons from sustained investigation of San Francisco Bay, California, *Reviews of Geophysics*, 34(2), 127–168, 1996.
- Cura, J. J., Nutrients and productivity, *Tech. Rep. EGS G 82-B4*, U.S. Department of Interior, Bureau of Land Management, 1982.
- Davis, C. S., Interaction of a copepod population with the mean circulation on Georges Bank, *Journal of Marine Research*, 42, 573–590, 1984.
- Davis, C. S., Zooplankton life cycles, in *Georges Bank*, edited by R. H. Backus and D. W. Bourne, pp. 256–267, MIT Press, Cambridge, Massachusetts, 1987.
- Davis, C. S., S. M. Gallagher, M. Marra, and W. K. Stewart, Rapid visualization of plankton abundance and taxonomic composition using the Video Plankton Recorder, *Deep Sea Research II*, 43, 1946–1970, 1996.

- Durbin, E. G., R. G. Campbell, S. L. Gilman, and A. G. Durbin, Diel feeding behavior and ingestion rate of *Calanus finmarchicus* in the southern Gulf of Maine during late spring, *Continental Shelf Research*, *15*, 539–570, 1995a.
- Durbin, E. G., R. G. Campbell, S. L. Gilman, and A. G. Durbin, Abundance, biomass, vertical migration and estimated development rate of *Calanus finmarchicus* in the southern Gulf of Maine during late spring, *Continental Shelf Research*, *15*, 571–591, 1995b.
- Durbin, E. G., A. G. Durbin, and R. C. Beardsley, Springtime nutrient and chlorophyll *a* concentrations in the southwestern Gulf of Maine, *Continental Shelf Research*, *15*, 433–450, 1995c.
- Durbin, E. G., P. R. Garrahan, and M. C. Casas, Abundance and distribution of *Calanus finmarchicus* on the Georges Bank during 1995 and 1996, *ICES Journal of Marine Science*, *57*, 1664–1685, 2000a.
- Durbin, E. G., P. R. Garrahan, and M. C. Casas, Depth distribution of *Calanus finmarchicus* nauplii on the Georges Bank during 1995 and 1996, *ICES Journal of Marine Science*, *57*, 1686–1693, 2000b.
- Esaias, W. E., Remote sensing in biological oceanography, *Oceanus*, *24*, 32–38, 1981.
- Falkowski, P., and K. Von Bock, Atlantic coastal experiment. Phytoplankton species composition, *Tech. Rep. BNL-26335*, Brookhaven National Laboratory Associated University, Inc., 1979.
- Flagg, C. N., Hydrographic structure and variability, in *Georges Bank*, edited by R. H. Backus and D. W. Bourne, pp. 108–124, MIT Press, Cambridge, Massachusetts, 1987.

- Franks, P. J. S., Coupled physical-biological models in oceanography. U.S. National Report to International Union of Geodesy and Geophysics 1991-94, *Reviews of Geophysics, Supplement*, 1177–1187, 1995.
- Franks, P. J. S., and C. Chen, Plankton production in tidal fronts: A model of Georges Bank in summer, *Journal of Marine Research*, 54, 631–651, 1996.
- Franks, P. J. S., and C. Chen, A 3-d prognostic numerical model study of the Georges Bank ecosystem. Part II: biological-physical model, *Deep Sea Research II*, 48, 457–482, 2001.
- Garfield, N., and D. L. Evans, Shelf water entrainment by Gulf Stream warm-core rings, *Journal of Geophysical Research*, 92, 13,003–13,012, 1987.
- Gawarkiewicz, G. G., and D. C. Chapman, The role of stratification in the formation and maintenance of shelf-break fronts, *Journal of Physical Oceanography*, 22, 753–772, 1992.
- GLOBEC, Northwest Atlantic Implementation Plan, *U.S. Global Ocean Ecosystem Dynamics Report*, 6, 1992.
- Gran, H. H., and T. Braarud, A quantitative study of the phytoplankton in the Bay of Fundy and the Gulf of Maine (including observation on hydrography, chemistry and turbidity), *Journal of the Biological Board of Canada*, 1, 279–467, 1935.
- Haidvogel, D., J. Wilkin, and R. Young, A semi-spectral primitive equation ocean circulation model using vertical sigma and orthogonal curvilinear coordinates, *Journal of Computational Physics*, 94, 151–185, 1991.
- Horne, E. P. W., J. W. Loder, C. E. Naimie, and N. S. Oakey, Turbulence dissipation rates and nitrate supply in the upper water column on Georges Bank, *Deep Sea Research II*, 43, 1683–1712, 1996.

- Houghton, R. W., Diapycnal flow through a tidal front: a dye tracer study on Georges Bank, *Journal of Marine Systems*, *37*, 31–46, 2002.
- Huntley, M., and E. R. Brooks, Effects of age and food availability on diel vertical migration of *Calanus finmarchicus*, *Marine Biology*, *71*, 23–31, 1982.
- Kane, J., The feeding habits of co-occurring cod and haddock larvae from Georges Bank, *Marine Ecology Progress Series*, *16*, 9–20, 1984.
- Klein, P., A simulation of some physical and biological interactions, in *Georges Bank*, edited by R. H. Backus and D. W. Bourne, pp. 395–402, MIT Press, Cambridge, Massachusetts, 1987.
- Lewis, C. V., C. S. Davis, and G. Gawarkiewicz, Wind-forced biological-physical interactions on an isolated off-shore bank, *Deep Sea Research II*, *41*, 51–73, 1994.
- Lewis, C. V. W., C. Chen, and C. S. Davis, Effect of winter wind variability on plankton transport over Georges Bank, *Deep Sea Research II*, *48*, 137–158, 2001.
- Lillick, L. C., Phytoplankton and planktonic protozoa of the offshore waters of the Gulf of Maine: part 1, numerical distribution, *Transactions of the American Philosophical Society*, *31*, 193–237, 1940.
- Loder, J. W., Topographic rectification of tidal currents on the sides of Georges Bank, *Journal of Physical Oceanography*, *10*, 1399–1416, 1980.
- Loder, J. W., and T. Platt, Physical controls on phytoplankton production at tidal fronts, in *Proceedings of the Nineteenth European Marine Biology Symposium*, edited by P. E. Gibbs, pp. 3–21, Cambridge University Press, 1985.
- Loder, J. W., D. Brickman, and P. W. Horne, Detailed structure of currents and hydrography on the northern side of Georges Bank, *Journal of Geophysical Research*, *97*, 14,331–14,352, 1992.

- Loder, J. W., Y. Shen, and H. Ridderinkhof, Characterization of three-dimensional Lagrangian circulation associated with tidal rectification over a submarine bank, *Journal of Physical Oceanography*, *27*, 1729–1742, 1997.
- Lough, R. G., Larval fish trophodynamic studies on Georges Bank: sampling strategy and initial results, in *Flodevingen rapportster*, vol. 1, edited by E. Dahl, D. S. Danielssen, E. Moksness, and P. Solemdal, chap. The Propagation of cod *Gadhus morhua* L., pp. 395–434, 1984.
- Lough, R. G., and J. P. Manning, Tidal-front entrainment and retention of fish larvae on the southern flank of Georges Bank, *Deep Sea Research II*, *48*, 631–644, 2001.
- Lough, R. G., and D. G. Mountain, Effect of small-scale turbulence on feeding rates of larval cod and haddock in stratified waters on Georges Bank, *Deep Sea Research II*, *43*, 1745–1772, 1996.
- Lough, R. G., P. C. Valentine, D. C. Potter, P. J. Auditore, G. R. Bolz, J. D. Neilsonand, and R. I. Perry, Ecology and distribution of juvenile cod and haddock in relation to sediment type and bottom currents on eastern Georges Bank, *Marine Ecology Progress Series*, *56*, 1–12, 1989.
- Mann, K. H., and J. R. N. Lazier, *Dynamics of Marine Ecosystems: Biological-Physical Interactions in the Oceans*, second ed., 400 pp., Blackwell Science, Cambridge, Massachusetts and Oxford, U.K., 1996.
- Moody, J. A., B. Butman, R. C. Beardsley, W. S. Brown, P. Daifuku, J. D. Irish, D. A. Mayer, H. O. Mofjelf, B. Petrie, S. Ramp, P. Simith, and W. R. Wright, Atlas of tidal elevation and current observations on the northeast American continental shelf and slope, *US Geological Survey Bulletin*, *1611*, 1984.

- Naimie, C. E., Georges Bank residual circulation during weak and strong stratification periods: prognostic numerical model results, *Journal of Geophysical Research*, *101*(C3), 6469–6486, 1996.
- Naimie, C. E., J. W. Loder, and D. R. Lynch, Seasonal variation of the three-dimensional residual circulation on Georges Bank, *Journal of Geophysical Research*, *99*(C8), 15,967–15,989, 1994.
- O'Reilly, J. E., C. E. Evans-Zetlin, and D. A. Busch, Primary production, in *Georges Bank*, edited by R. H. Backus and D. W. Bourne, pp. 220–233, MIT Press, Cambridge, Massachusetts, 1987.
- Pringle, J. M., and P. J. S. Franks, Asymmetric mixing transport: A horizontal transport mechanism for sinking plankton and sediment in tidal flows, *Limnology and Oceanography*, *46*(2), 381–391, 2001.
- Ramp, S., R. Schlitz, and W. Wright, The deep flow through the Northeast Channel, Gulf of Maine, *Journal of Physical Oceanography*, *15*, 1790–1808, 1985.
- Ramp, S. R., The interaction of warm core rings with the shelf water and shelf-slope front south of New England, Ph.D. thesis, University of Rhode Island, Narragansett, Rhode Island, 1986.
- Robinson, A. R., B. J. Rothschild, and J. J. McCarthy (Eds.), *The Sea: Biological-physical interactions in the ocean*, 640 pp., Wiley, John & Sons, New York, New York, 2002.
- Ryan, J. P., J. A. Yoder, and D. W. Townsend, Influence of a Gulf Stream warm-core ring on water mass and chlorophyll distributions along the southern flank of Georges Bank, *Deep Sea Research II*, *48*, 159–178, 2001.

- Sears, M., Notes on phytoplankton on Georges Bank in 1940, *Journal of Marine Research*, 4, 247–257, 1941.
- Sherman, K. R. L., W. Richards, and A. W. Kendall Jr., Relationship between larval fish communities and zooplankton prey species in an offshore spawning ground, *Rapports et Proces-Verbaux des Reunions*, 178, 289–294, 1981.
- Smith, P. C., The mean seasonal circulation off southwest Nova Scotia, *Journal of Physical Oceanography*, 13, 1034–1054, 1983.
- Smith, R. C., and K. S. Baker, Spatial and temporal patterns in pigment biomass in Gulf Stream warm-core ring 82B and its environs, *Journal of Geophysical Research*, 90, 8859–8870, 1985.
- Steele, J. H., *The Structure of Marine Ecosystem*, 128 pp., Harvard University Press, Cambridge, Massachusetts, 1974.
- Sverdrup, H. U., On conditions for the vernal blooming of phytoplankton, *Journal du Conseil International pour l'Exploration de la Mer*, 18, 287–295, 1953.
- Townsend, D. W., and L. M. Cammen, Potential importance of the timing of spring plankton blooms to benthic pelagic coupling and recruitment of juvenile demersal fishes, *Biological Oceanography*, 5, 215–229, 1988.
- Townsend, D. W., and N. R. Pettigrew, The role of frontal currents in larval fish transport on Georges Bank, *Deep Sea Research II*, 43, 1773–1792, 1996.
- Townsend, D. W., and A. C. Thomas, Winter-spring transition of phytoplankton chlorophyll and inorganic nutrients on Georges Bank, *Deep Sea Research II*, 48, 199–214, 2001.
- Townsend, D. W., and M. Thomas, Springtime nutrient and phytoplankton dynamics on Georges Bank, *Marine Ecology Progress Series*, 228, 57–74, 2002.

- Twichell, D. C., B. Butman, and R. S. Lewis, Shallow structure, surficial geology, and the processes currently shaping the bank, in *Georges Bank*, edited by R. H. Backus and D. W. Bourne, pp. 31–37, MIT Press, Cambridge, Massachusetts, 1987.
- Uchupi, E., and J. A. Austin Jr., Morphology, in *Georges Bank*, edited by R. H. Backus and D. W. Bourne, pp. 25–30, MIT Press, Cambridge, Massachusetts, 1987.
- Wiebe, P., R. Beardsley, D. Mountain, and A. Bucklin, U.S. GLOBEC Northwest Atlantic/Georges Bank Program, *Oceanography*, 15(2), 13–29, 2002.
- Yoshida, J., and N. S. Oakey, Characterization of vertical mixing at a tidal-front on Georges Bank, *Deep Sea Research II*, 43, 1713–1744, 1996.

CHAPTER 2

THE COUPLED BIOLOGICAL AND PHYSICAL MODELS

2.1 INTRODUCTION

The ecosystem in the Gulf of Maine (GOM)/Georges Bank (GB) is dynamically coupled with the physical environment through advection, mixing, and heat fluxes. As generally recognized, a regional coupled physical and biological model can offer the promise of a better understanding of the complexity of marine ecosystems. This modeling system can also be used to examine the impact of climate change, extreme natural forcing, pollution and other external stressors on the coastal ecosystem.

Unlike physical processes that are governed by the momentum, temperature, salinity, continuity, and density equations, there is not a unique ecosystem model that can function universally for all coastal oceans and estuaries. Since biological processes can widely vary in different environments, a biological model must be developed based on the observed features of the local ecosystem. The general development strategy is to keep the biological model as simple as possible, because adding one variable would generate 4-7 additional parameters that are unknown or must be specified from limited resources. The 3-compartment nutrient-phytoplankton-zooplankton (NPZ) model is one of the least complicated biological models, yet it still contains 7 unknown biological parameters which are associated with nutrient uptake, maximum zooplankton grazing, grazing efficiency, phytoplankton and zooplankton mortality rates, half-saturation constant for nutrient uptake, and assimilation efficiency coefficient of zooplankton grazing on phytoplankton [*Franks et al.*,

1986]. As another example, an 8-component lower trophic level food web model contains about 30 biological parameters that need to be specified from either field measurement data or laboratory experiments. From a point of view of statistics and stability, increasing biological variables would dramatically increase degrees of freedom and thus reduce the model reliability and stability.

The NPZ model has proven successful in capturing the summertime cross-bank distribution of nutrients and phytoplankton on GB [*Franks and Chen, 1996, 2001*]. This simple model has demonstrated that the patch structure of the phytoplankton observed on GB in summer is controlled directly by the frontal dynamics, and is not sensitive to biological parameters chosen in the NPZ model. Although the NPZ model is a scientifically sound tool for process-oriented studies of the nitrogen-limiting phytoplankton dynamics on GB, it fails to resolve the diatom-dominant spring bloom that occurs in late winter or early spring with possible multiple limiting nutrients.

Townsend and Thomas [2002] suggested that the seasonal pattern of the phytoplankton on GB is governed by a multiple nutrient limiting process including both nitrogen and silicate. Also the species of the phytoplankton differ significantly spatially between the well-mixed shallow region and the seasonal stratified deep region and temporally between winter-early spring and summer. To capture this seasonal pattern, one must consider at least two major nutrients (nitrogen and silicate), two distinct phytoplankton species (silicate-consuming diatoms and non-silicate-consuming flagellates), and two zooplankton species. In order to distinguish recycling of nutrients through remineralization from organic matter, detritus must be also included in the food web loop. From the point of view of ecosystem modeling dynamics, it is risky to develop complex multiple species nutrients-phytoplankton-zooplankton-detritus (NPZD) model. However, it is necessary to increase the complexity in order to develop a workable model based on observed features.

A 9-compartment lower trophic level food web model was developed based on features observed in the year-round US GLOBEC/GB field program in 1997-1999. This relatively complex model was built on the previous accomplishments of the NPZ model on GB and also was tested carefully with sensitivity studies. Intense 1-D experiments were conducted to provide an objective view of the reliability, stability, and capability of the new NPZD model for the study of the phytoplankton dynamics on GB. The 2-D and 3-D experiments were also performed with an understanding of the limitation and uncertainty due to model parameterization. This new NPZD model is expected to be used to simulate the seasonal pattern of phytoplankton on GB after all sensitive parameters can be better estimated from the field measurements or laboratory experiments.

The remaining sections are organized as follows. In section 2.2, the NPZD model is introduced and some critical issues regarding model parameterization are discussed. In section 2.3, two state of the art physical models are briefly described, and in section 2.4, a conclusion is presented.

2.2 THE BIOLOGICAL MODEL

The lower trophic level food web model developed in this thesis work is a 9-compartment nutrients-phytoplankton-zooplankton-detritus (NPZD) model containing 3 nutrients (nitrate, ammonia and silicate), 2 phytoplankton (large and small size groups), 2 zooplankton (large and small size groups), 1 detrital organic nitrogen and 1 detrital organic silicon. The schematic of the model is given in Figure 2.1 . Due to the complexity of the mathematic expressions of biological process terms in the equations, a flux diagram is shown in Figure 2.2 to depict the food web loop.

The governing equations of this 9-compartment model are as follows:

$$\frac{dP_S}{dt} - \frac{\partial}{\partial z} \left(A_h \frac{\partial P_S}{\partial z} \right) = F3 + F4 - F5 - F6 \quad (2.1)$$

$$\frac{dP_L}{dt} - \frac{\partial}{\partial z} \left(A_h \frac{\partial P_L}{\partial z} \right) = F1 + F2 - F11 - F14 \quad (2.2)$$

$$\frac{dZ_S}{dt} - \frac{\partial}{\partial z} \left(A_h \frac{\partial Z_S}{\partial z} \right) = F5a + F9 - F7 - F8 \quad (2.3)$$

$$\frac{dZ_L}{dt} - \frac{\partial}{\partial z} \left(A_h \frac{\partial Z_L}{\partial z} \right) = F8a + F14b - F12 \quad (2.4)$$

$$\frac{dNO_3}{dt} - \frac{\partial}{\partial z} \left(A_h \frac{\partial NO_3}{\partial z} \right) = -F1 - F3 \quad (2.5)$$

$$\frac{dNH_4}{dt} - \frac{\partial}{\partial z} \left(A_h \frac{\partial NH_4}{\partial z} \right) = F10 - F2 - F4 \quad (2.6)$$

$$\begin{aligned} \frac{dD_N}{dt} - \frac{\partial}{\partial z} \left(A_h \frac{\partial D_N}{\partial z} \right) &= F5b + F6 + F7 + F8b + F11 \\ &+ F12 + F14a - F9 - F10 \end{aligned} \quad (2.7)$$

$$\frac{dSi}{dt} - \frac{\partial}{\partial z} \left(A_h \frac{\partial Si}{\partial z} \right) = F17 - F13 \quad (2.8)$$

$$\frac{dD_{Si}}{dt} - \frac{\partial}{\partial z} \left(A_h \frac{\partial D_{Si}}{\partial z} \right) = F15 + F16 - F17 \quad (2.9)$$

where P_S : small-phytoplankton biomass ($\mu\text{mol N/l}$); P_L : large- phytoplankton biomass ($\mu\text{mol N/l}$); Z_S : small-zooplankton biomass ($\mu\text{mol N/l}$); Z_L : large-zooplankton biomass ($\mu\text{mol N/l}$); NO_3 : nitrate concentration ($\mu\text{mol N/l}$), NH_4 : ammonium concentration ($\mu\text{mol N/l}$); D_N : particulate organic nitrogen concentration ($\mu\text{mol N/l}$); Si : silicate concentration ($\mu\text{mol Si/l}$); D_{si} : particulate organic silica concentration ($\mu\text{mol Si/l}$). F1 to F17 are the flux terms for the food web. The definitions of these terms are shown in Table 2.1; their mathematic descriptions are given in Appendix A.

On the left side of each of the above equations, A_h is the thermal diffusion coefficient that is calculated using the Mellor and Yamada level 2.5 turbulent closure scheme incorporated in the physical model; $\frac{d}{dt} = \frac{\partial}{\partial t} + u \frac{\partial}{\partial x} + v \frac{\partial}{\partial y} + w \frac{\partial}{\partial z}$ is the derivative operator; x , y and z are the eastward, northward, and vertical axes of the Cartesian coordinate; and u , v , and w are the x , y , and z components of the velocity.

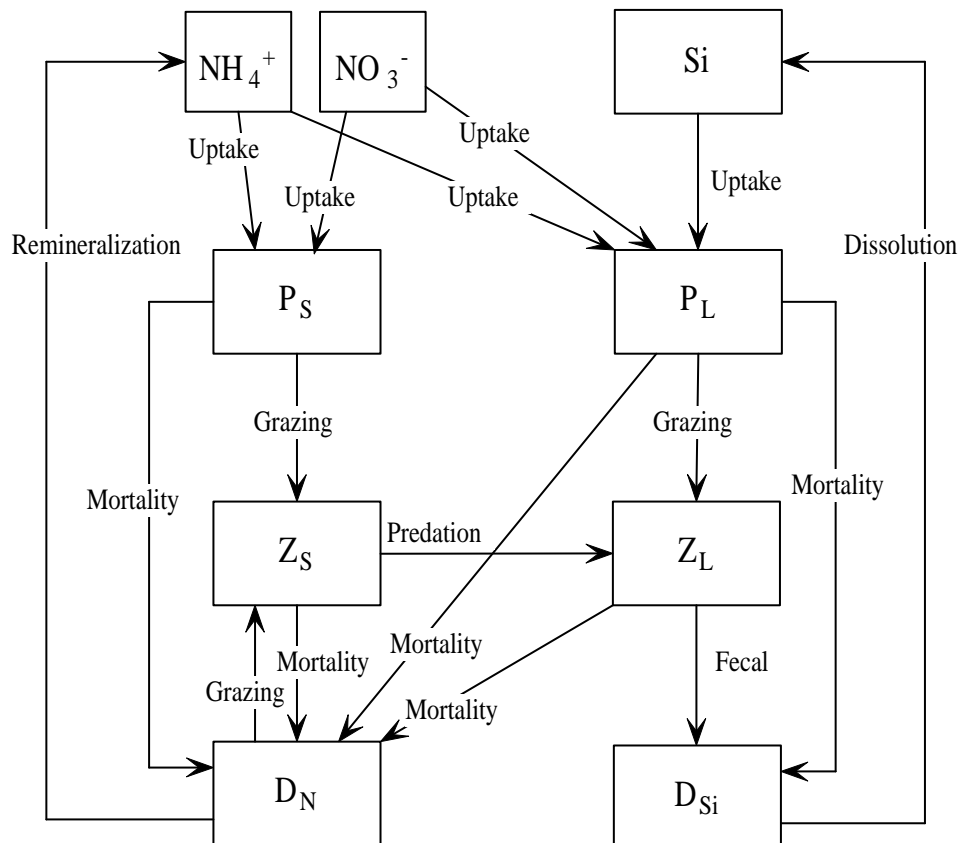


Figure 2.1: Schematic of the lower trophic level food web model in GOM/GB region. The model consists 9 components including nitrate (NO_3^-), ammonia (NH_4^+), silicate (Si), small phytoplankton (P_S), large phytoplankton (P_L), small zooplankton (Z_S), large zooplankton (Z_L), detrital organic nitrogen (D_N) and detrital organic silicon (D_{Si}). Arrows represent flux between different components.

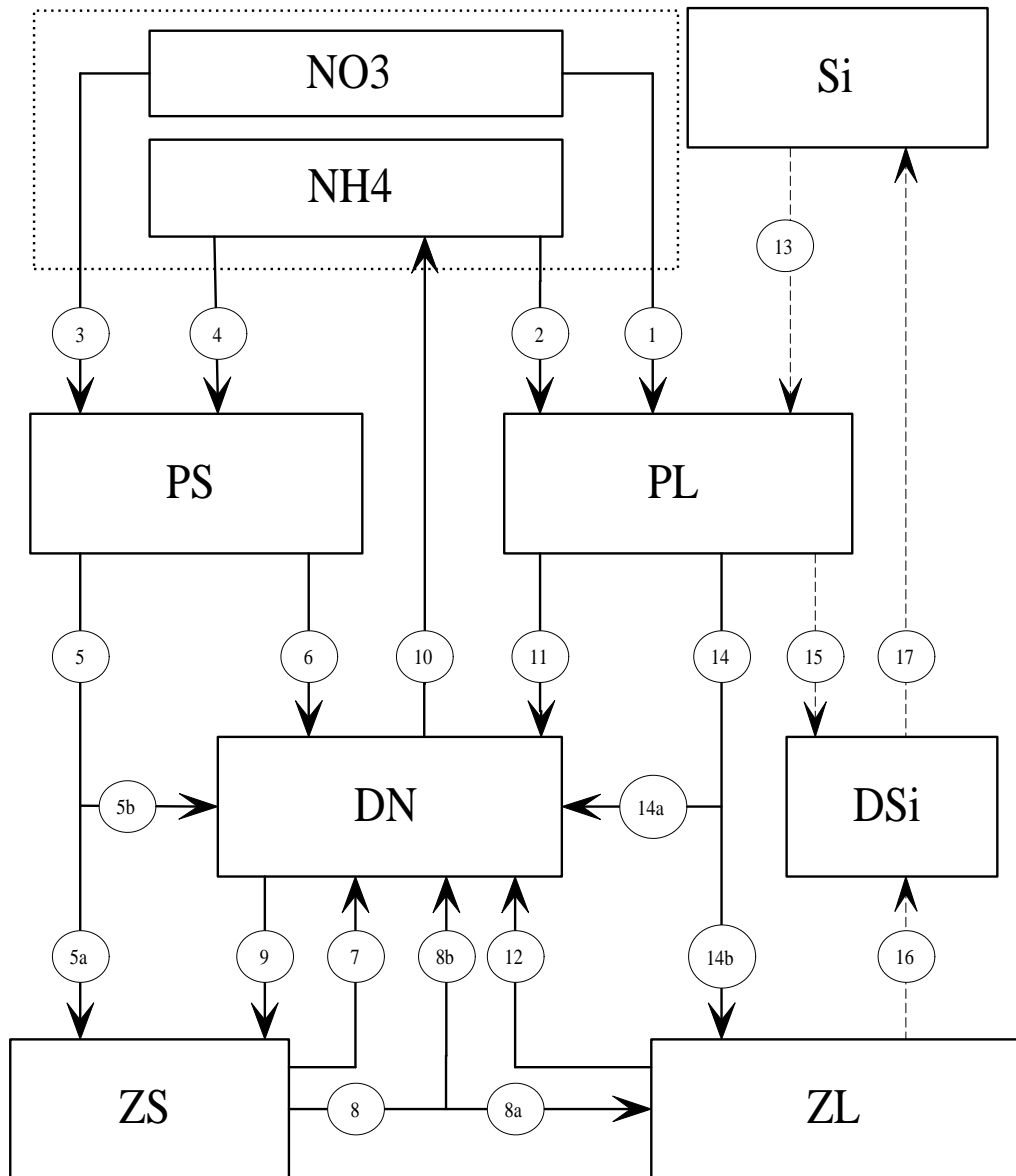


Figure 2.2: Another version of Figure 2.1 with labeled number for each process.

Table 2.1: Definitions of the flux terms in the food web

<i>Flux</i>	<i>Definition</i>
F1	Uptake of nitrate by large phytoplankton ($\mu\text{mol N l}^{-1}\text{day}^{-1}$)
F2	Uptake of ammonia by large phytoplankton ($\mu\text{mol N l}^{-1}\text{day}^{-1}$)
F3	Uptake of nitrate by small phytoplankton ($\mu\text{mol N l}^{-1}\text{day}^{-1}$)
F4	Uptake of ammonia by small phytoplankton ($\mu\text{mol N l}^{-1}\text{day}^{-1}$)
F5	Small zooplankton grazing on small phytoplankton ($\mu\text{mol N l}^{-1}\text{day}^{-1}$)
F5a	Assimilated part of F5 ($\mu\text{mol N l}^{-1}\text{day}^{-1}$)
F5b	Un-assimilated part of F5 ($\mu\text{mol N l}^{-1}\text{day}^{-1}$)
F6	Mortality of small phytoplankton ($\mu\text{mol N l}^{-1}\text{day}^{-1}$)
F7	Mortality of large phytoplankton ($\mu\text{mol N l}^{-1}\text{day}^{-1}$)
F8	Large zooplankton grazing on small zooplankton ($\mu\text{mol N l}^{-1}\text{day}^{-1}$)
F8a	Assimilated part of F8 ($\mu\text{mol N l}^{-1}\text{day}^{-1}$)
F8b	Un-assimilated part of F8 ($\mu\text{mol N l}^{-1}\text{day}^{-1}$)
F9	Small zooplankton grazing on detritus nitrogen ($\mu\text{mol N l}^{-1}\text{day}^{-1}$)
F10	Remineralization of particulate organic nitrogen ($\mu\text{mol N l}^{-1}\text{day}^{-1}$)
F11	Mortality of large phytoplankton (in term of N) ($\mu\text{mol N l}^{-1}\text{day}^{-1}$)
F12	Mortality of large zooplankton ($\mu\text{mol N l}^{-1}\text{day}^{-1}$)
F13	Uptake of silicate by large phytoplankton ($\mu\text{mol Si l}^{-1}\text{day}^{-1}$)
F14	Large zooplankton grazing on large phytoplankton ($\mu\text{mol N l}^{-1}\text{day}^{-1}$)
F14a	Assimilated part of F14 ($\mu\text{mol N l}^{-1}\text{day}^{-1}$)
F14b	Un-assimilated part of F14 ($\mu\text{mol N l}^{-1}\text{day}^{-1}$)
F15	Mortality of large phytoplankton (in term of Si) ($\mu\text{mol Si l}^{-1}\text{day}^{-1}$)
F16	Silica rejected from large zooplankton ($\mu\text{mol Si l}^{-1}\text{day}^{-1}$)
F17	Dissolution of particulate organic silica ($\mu\text{mol Si l}^{-1}\text{day}^{-1}$)

The surface and bottom boundary conditions for biological variables are given by

$$\frac{\partial}{\partial \sigma}(Z_S, Z_L, NO_3, NH_4, Si) = 0, \quad \text{at } \sigma = 0, -1 \quad (2.10)$$

$$\frac{\partial P_L}{\partial \sigma} = \frac{D}{A_h} w_{P_L} P_L; \quad \frac{\partial P_S}{\partial \sigma} = \frac{D}{A_h} w_{P_S} P_S, \quad \text{at } \sigma = 0, -1 \quad (2.11)$$

$$\frac{\partial D_N}{\partial \sigma} = \frac{D}{A_h} w_{D_N} D_N; \quad \frac{\partial D_{Si}}{\partial \sigma} = \frac{D}{A_h} w_{D_{Si}} D_{Si}, \quad \text{at } \sigma = 0, -1 \quad (2.12)$$

where w_x represents sinking velocity of biological component x .

In the model, the small-size phytoplankton group represents nano- and pico-sized phytoplankton, which are usually flagellates. The growth of small phytoplankton is limited by nitrogen and light. The large phytoplankton size group is explicitly modeled as diatoms, and the growth of this group is limited by nitrogen, silicon and light. The zooplankton on GB and in the surrounding region are dominated in abundance and biomass by the copepods *Calanus finmarchicus*, *Pseudocalanus sp.*, *Paracalanus parvus*, *Centropages typicus*, *Centropages hamatus*, and *Olithona similes*. At any given time of the year, these six species collectively make up over 80% of total zooplankton abundance [Davis, 1987]. Because the main focus of the present study was the winter-spring phytoplankton bloom, the large zooplankton in the model represents the dominant species of *Calanus* and *Pseudocalanus*. The small zooplankton refers to micro-zooplankton with size much smaller than large zooplankton. It is somewhat ambiguous to make a definition of large and small zooplankton in terms of species, because young stages of *Calanus* and *Pseudocalanus* could be considered to be small zooplankton in terms of size. Also, some heterotrophic protozoans are catalogued into the small size zooplankton group. It should be pointed out that because of the lack of higher trophic level regulation on zooplankton, the model-estimated zooplankton biomass is difficult to validate. From the point of view of the food web dynamics, the large and small zooplankton function like flux balancing terms to maintain the stability of the lower trophic level food web.

Equations 2.1-2.9 describe a complex lower trophic web system with internal fluxes consisting of the major physical and biological components. A detailed description and discussion of the primary variables in this system are given below.

2.2.1 LIGHT LIMITATION

It has been recognized that the growth of phytoplankton is sensitive to the photosynthesis-irradiance (P/I) relationship. Many empirical or semi-empirical formulas are widely used in biological modelling to represent this relationship [e.g., *Steele*, 1962; *Jassby and Platt*, 1976; *Platt et al.*, 1980; *Falkowski and Wirick*, 1981; *Mergard et al.*, 1984; *Eilers and Peeters*, 1988; *Pahl-Wostl and Imboden*, 1990; *Janowitz and Kamykowski*, 1991]. Since the P/I relationship varies significantly with time and space in different environments and there have been relatively few measurements made to determine it, it is usually difficult to derive an exact function to describe the P/I relationship in the real coastal ocean. For example, it seems that the only available data for the P/I relationship in the vicinity of GB are the field measurements carried out in the Massachusetts Bay in February and August 1990 (personal communication with Dr. Townsend). The P/I relationship constructed from these two seasons clearly showed that photo-inhibition is more likely to occur in winter than in summer (Figure 2.3) (note: these data were provided by Dr. Townsend). The data also show that there is a significant vertical variation of the P/I relationship with greater photo-inhibition in the deep layer than in the upper layer.

Efforts have been made to fit the observational data obtained in the Massachusetts Bay. Three functions were used here. The first is a hyperbolic tangent function proposed by *Jassby and Platt* [1976], which is given as

$$P^B = P_{\max}^B \tanh(\alpha I / P_{\max}^B), \quad (2.13)$$

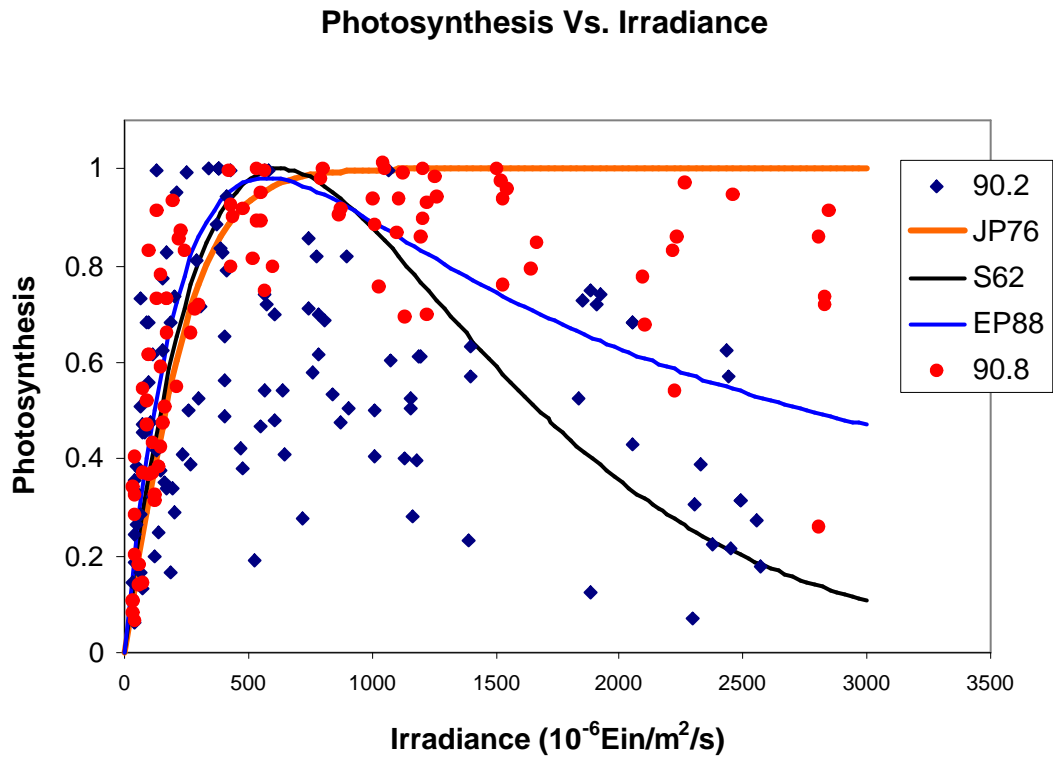


Figure 2.3: The photosynthesis versus irradiance relationship. Datasets are from Dr. David Townsend's field measurements in Massachusetts Bay during February, 1990 (blue diamonds), and August, 1990 (red filled circles). Photosynthesis rate is normalized to the maximum rate. Three functions are applied to fit the data. The orange line is a function from *Jassby and Platt* [1976], blue line from *Eilers and Peeters* [1988], and black line from *Steele* [1962].

where α is the initial slope of the photosynthesis-irradiance curve. P^B is the instantaneous production rate and P_{max}^B is the specific production rate at optimal light intensity. P^B and P_{max}^B are normalized to the chlorophyll biomass B . I is the available light intensity. The second is the Steele's function given as

$$P^B = \alpha I e^{(-\alpha I / P_{max}^B)}, \quad (2.14)$$

where the definitions of the terms are the same as those described in Equation 2.13. The third is the function proposed by *Eilers and Peeters* [1988], which is given as

$$P^B = \frac{I}{aI^2 + bI + c}, \quad (2.15)$$

where a , b and c are parameters related to optimal light intensity and maximum photosynthesis rate.

Equation 2.13 is valid for the case of no light photo-inhibition. This function has good agreement with the data collected in August 1990. Equation 2.14 is suitable for the case of strong light photo-inhibition. This function seems to provide a reasonable fit to the data collected in February 1990. The curve corresponding to Equation 2.15 lies between the curve corresponding to Equations 2.13 and 2.14, and seems to represent the averaged structure of P/I between February and August.

Because there were no comprehensive P/I data available for GB, it was assumed that the P/I relationship shown in the Massachusetts Bay could be applied to GB due to the proximity of these two regions. Since the main interest of this work was the spring bloom which occurs in March or April, it was decided to use the P/I relationship fitted by Equation 2.15, with a profile varying between winter and summer extremes. This selection was made with the understanding that some uncertainty must be taken into account when the model results are interpreted.

2.2.2 NUTRIENTS

There are two different approaches to including the limiting effects of multiple nutrients. The first is to multiply them together and the other is to select the nutrient that is most limiting. The first method is built on the assumption that the relative contribution of an individual factor is determined by its own saturation level; but the combined contribution of these factors satisfies a nonlinear relationship with their products. Theoretically speaking, when these three limiting nutrients are all at saturation level, the combined factor reaches 1. However, when these factors are not at saturation level, the product of factors would be significantly less than the minimum value of factors. This method is perfectly correct for the saturation case, but is questionable in the realistic conditions where factors are lower than saturation level. The second method is built on a competitive theory in which the growth of phytoplankton is always controlled by the minimum value of all factors. Similar to the first method, the limiting factor reaches 1 when all factors are at saturation level. When any of these factors is below saturation level, however, the growth of phytoplankton is always limited to a maximum level. In the real world, the limiting of multiple nutrients not only exhibits a nonlinear linkage, but also varies with space and time. It is difficult to say which method is better.

The second method was chosen for this thesis work in the formulation of the combined limiting factor of multiple nutrients for the growth of large phytoplankton. The growth of phytoplankton is limited by the Liebig's "law of the minimum" expressed as

$$f(N) = \min\{(L_{NO_3} + L_{NH_4}), L_{Si}\}, \quad (2.16)$$

For the growth of small phytoplankton, only nitrogen limitation is considered, so that the combined limiting factors is equal to the sum of L_{NO_3} and L_{NH_4} .

Nitrogen uptake is partitioned between ammonium and nitrate. Instead of using the standard Michaelis-Menten equation that is widely used in the simple NPZ model, the inhibiting effect of ammonium concentration on nitrate uptake has been taken into consideration by using the equation proposed by *Frost and Franzen* [1992], in which L_{NO_3} is expressed as

$$L_{NO_3} = \frac{NO_3}{(K_{NO_3} + NO_3)(1 + \frac{NH_4}{\beta})}, \quad (2.17)$$

where K_{NO_3} is the half-saturation constant of NO_3 uptake, and β is the ammonium inhibition coefficient [*Dortch*, 1990; *Wheeler and Kokkinakis*, 1990; *Hurtt and Armstrong*, 1996; *Chen*, 2003].

The limiting factors for ammonium and silicate follows the standard Michaelis-Menten equations given as

$$L_{NH_4} = \frac{NH_4}{(K_{NH_4} + NH_4)} \quad (2.18)$$

and

$$L_{Si} = \frac{Si}{(K_{Si} + Si)}, \quad (2.19)$$

where K_{NH_4} , and K_{Si} are half saturation constants for phytoplankton uptake on NO_3 and NH_4 .

2.2.3 PHYTOPLANKTON

The local change of the phytoplankton biomass is controlled by growth, physiological or non-grazing mortality and grazing, as well as advection and diffusion. The growth of phytoplankton is estimated by the specific growth rate, which is parameterized by a maximum growth rate modulated by nutrients and light limitation. The measurement on GB showed a dominance of the large phytoplankton in spring-early summer. Different maximum growth rates of 3.0 day^{-1} and 2.4 day^{-1} were specified for large and small phytoplankton, respectively in the model. Although there are

not sufficient measurement data to prove the accuracy of these two constant rates, they seemed reasonable for the diatom-dominated system in the highly energetic biological system of GB.

Phytoplankton mortality is defined as physiological death and subsequent lysis of phytoplanktonic cells, caused by a number of factors, including parasitic attack by viruses, bacteria and fungi or exposure to physiological extremes of light, temperature, nutrient concentration, and toxic substances [e.g., *Reynolds*, 1984]. It is difficult to determine this parameter from field measurements or laboratory experiments because it varies with time and space as well as the physiological condition. In this work, a constant mortality rate of phytoplankton is used in order to compare properly with other modeling studies done on GB. The specified rate was 0.1 day^{-1} for the large phytoplankton and 0.2 day^{-1} for small phytoplankton. This assumption suggests that for a given biomass, the small phytoplankton died at twice the rate as the large phytoplankton, which represents a faster recycling process for the small phytoplankton.

A detailed discussion on the parameterization of the grazing rate of zooplankton is given below. The diffusion of phytoplankton biomass was estimated from a turbulence closure model in which the vertical diffusion coefficient of the phytoplankton was assumed to be the same as the thermal diffusion coefficient used for temperature and salinity. The advection currents were directly determined by the physical model, which is described in detail in the next section.

2.2.4 ZOOPLANKTON

The total change of zooplankton biomass is controlled by grazing and mortality. For large zooplankton, both small zooplankton and large phytoplankton are prey. Based on a personal communication with Gifford and Sieracki, *Townsend and Thomas* [2002] pointed out that large zooplankton may prefer small zooplankton

(heterotrophic protozoans) rather than large phytoplankton on GB during winter-spring time. Since there are no sufficient data to parameterize the feeding preference of zooplankton, this is not taken into account in the zooplankton equation in this work. Trial model runs also suggest that the model-predicted biomass of small zooplankton is very low during winter-spring time, which suggested that the feeding preference might not play an essential role in the temporal variation of large zooplankton on GB.

The grazing of large zooplankton on large phytoplankton, small zooplankton on small phytoplankton, and large zooplankton on small zooplankton in this model follow the Ivlev function [Ivlev, 1961], which is parameterized by the maximum grazing rate, the Ivlev's constant, the efficiency of grazing and a constant assimilated fraction of the ingested food. The assimilated food was directly converted to biomass, while the non-assimilated fraction was rejected into detrital organic matters. To distinguish the silicon source in the detrital pool, it is assumed that the large zooplankton (primarily copepods) do not digest the diatom frustulae when they graze on large phytoplankton, so that the silica parts of diatoms are directly deposited into the detrital pool [Scavia *et al.*, 1988; Chen *et al.*, 2002].

As was the case for phytoplankton, there are significant uncertainties in the parameterization of zooplankton mortality. Steele and Henderson [1992] proposed a quadratic form in which the mortality rate is a linear function of biomass. This treatment tends to reduce the oscillation inherent to the model system. Chen *et al.* [2002] and Ji *et al.* [2002] introduced this empirical formula into a 9-component lower trophic level food web model for Lake Michigan. It seemed to work well regarding the stability of zooplankton biomass.

2.2.5 DETRITUS

The detrital component plays a “buffer” role in the NZPD model. All the dead material from phytoplankton and zooplankton, as well as the egesta from grazing processes, drop to the detrital pool. These detrital components are remineralized through bacterial breakdown and regenerated nutrients then flow back into the system. Since the ratio of nitrogen to silicon in a detrital pool varies with multiple factors related to the mortality of phytoplankton and zooplankton and the assimilated rate of zooplankton, it is impossible to use a constant ratio of nitrogen to silicon to separate nitrogen from silicon dynamically in the detrital pool. For example, the growth of large phytoplankton is limited by both nitrogen and silicon, while no silicon is needed for small phytoplankton (non-diatoms). Therefore, dead diatoms contain both nitrogen and silicon, while dead small phytoplankton have only nitrogen. Similar processes occur for the grazing of large and small zooplankton, in which the unassimilated part of large zooplankton contributes to both nitrogen and silicon pools, but that of the small zooplankton contributes to nitrogen only. In order to resolve the ratio of nitrogen to silicon from the total concentration of detritus, the detrital pool in this study has been divided into two components: detrital nitrogen and detrital silicon. This treatment was adapted directly from the 9-component biological model developed by *Chen et al.* [2002].

Ammonia is modeled as a recycled nutrient, which is supplied internally only through detrital nitrogen. This is far more simplistic than the real situation, where some processes, such as zooplankton excretion, can produce ammonia instantaneously. The advantage of this simplification is that it allows the regeneration process to be parameterized into one single temperature-dependent rate, without detailing bacterial processes and other various chemical steps.

Including a complete microbial food web would make the model structure too complicated to be easily validated. For this reason, the impact of microbial processes has been considered by allowing the small zooplankton to graze directly on detrital nitrogen. This treatment only considers the net flux from the microbial food web to microzooplankton with the assumption that the detailed chemical and biological processes in that web are not important to this lower trophic level food web system on GB, with the exception of the net output.

Dissolved organic matter is not considered in this model. There are two reasons for this. Firstly, the dissolved organic matter has already been included implicitly in the model through a linkage between phytoplankton exudation, zooplankton excretion and egestion, and detritus. Secondly, it is difficult to distinguish chemical and biological processes that control the concentration of dissolved organic matter in the model. For example, labile compounds of dissolved organic matter can be degraded by bacteria and be transferred to a higher trophic level via the microbial food web; while more refractory compounds are remineralized over time scales ranging from months to centuries [Druffel *et al.*, 1992].

2.2.6 BIOLOGICAL PARAMETERS AND RATIOS

The most difficult element of biological model development is the determination of the biological parameters. Due to the complex nature of biological processes, most of the parameters used in the biological model are derived from either limited observational data or literature with lack of theoretical support. Some parameters are determined by an optimal fitting of the model results with the observed biomass or internal fluxes among the food web estimated from the observational data. A detailed list of parameters is given in Appendix A.

There are two “currencies” coexisting in this model, nitrogen and silicon. Large phytoplankton (diatoms) involves both nitrogen and silicon, while small phyto-

plankton (non-diatoms) are controlled only by nitrogen. The exchange of these two “currencies” is via a constant N:Si ratio in diatoms. In reality, this ratio varies with species composition and light conditions. The average value is close to 1.0 with a variation factor of 3 [Brzezinski, 1985]. A value of 1.5 was initially used for these model experiments and a series of studies were conducted later to examine the sensitivity of the model results to this ratio.

Phytoplankton biomass is usually measured in the field as chlorophyll *a* concentration. To convert between nitrogen and chlorophyll *a* concentration, two ratios (C:N and C:Chl-*a* ratios) need to be determined. The C:N ratio is assumed to be the Redfield value, 6.6 (atom:atom). The C:Chl-*a* ratio for phytoplankton varies over a wide range. For a healthy, nutrient-sufficient diatom community, the ratio ranges from 21.5 to 46.6 (weight ratio) [Gallegos and Vant, 1996]. Early studies [Strickland, 1960; Parsons *et al.*, 1984] showed that the C:Chl-*a* ratio ranged from 23 to 79 during a diatom bloom. These studies recommended an average value of 30. However, this ratio is significantly influenced by both nutrient supply and light regime. An average C:Chl-*a* ratio of 40 is used in our model experiments. Combining these two ratios gives an N(mmols):Chl-*a*(mg) ratio of 0.5.

2.3 PHYSICAL MODELS

Two types of physical models were used in this study: 1) the Estuarine-Coastal Ocean Model-semi-implicit version (called ECOM-si) developed originally by *Blumberg* [1994] and 2) the Finite Volume Coastal Ocean Model (called FVCOM) developed by *Chen et al.* [2003]. Both ECOM-si and FVCOM consist of 7 primitive ocean governing equations (three for momentum, one for incompressible continuity, two for temperature and salinity, and one for density) [Blumberg and Mellor, 1987; *Chen et al.*, 2003]. These equations include a free surface and are closed using Mellor and

Yamada level-2.5 (MY-2.5) turbulent closure scheme for vertical mixing [*Mellor and Yamada*, 1982; *Galperin et al.*, 1988]. A σ -transformation is used in the vertical to convert irregular bottom topography into a rectangular computational domain for a simple numerical approach.

The difference between ECOM-si and FVCOM is in their numerical approaches. ECOM-si is a structured grid model solved numerically by the finite-difference method, while FVCOM is an unstructured grid model solved numerically by the finite-volume method. The ECOM-si was modified to include short-wave radiation, a gravity open boundary condition and non-orthogonal transformation by *Chen and Beardsley* [1995], *Chen et al.* [2001], and *Chen et al.* [2003]. FVCOM was first introduced in the ocean community in *Chen et al.* [2003]. This model has been significantly improved in the last two years by the Marine Ecosystem Dynamics Modeling Laboratory at the University of Massachusetts-Dartmouth. A series of numerical experiments have been conducted to validate FVCOM and to compare FVCOM with ECOM-si and POM (see *Chen et al.*, 2003c). The updated version of FVCOM includes the data-assimilation method and is parallelized for computing with multiple processors.. Detailed descriptions of ECOM-si and FVCOM were given by *Blumberg* [1994] and *Chen et al.* [2003], respectively. Governing equations and numerical approaches for ECOM-si and FVCOM are repeated below to provide readers with some brief information about these two models.

The governing equations for motion, temperature, salinity and density are given as

$$\begin{aligned} & \frac{\partial uD}{\partial t} + \frac{\partial u^2D}{\partial x} + \frac{\partial uvD}{\partial y} + \frac{\partial u\omega}{\partial \sigma} - fvD \\ = & -gD\frac{\partial \zeta}{\partial x} - \frac{gD}{\rho_o} \left[\frac{\partial}{\partial x} \left(D \int_{\sigma}^0 \rho' d\sigma' \right) + \sigma \rho' \frac{\partial D}{\partial x} \right] + \frac{1}{D} \frac{\partial}{\partial \sigma} \left(K_m \frac{\partial u}{\partial \sigma} \right) + DF_x \end{aligned} \quad (2.20)$$

$$\begin{aligned} & \frac{\partial vD}{\partial t} + \frac{\partial uvD}{\partial x} + \frac{\partial v^2D}{\partial y} + \frac{\partial v\omega}{\partial \sigma} + fuD \\ = & -gD\frac{\partial \zeta}{\partial y} - \frac{gD}{\rho_o} \left[\frac{\partial}{\partial y} \left(D \int_{\sigma}^0 \rho' d\sigma' \right) + \sigma \rho' \frac{\partial D}{\partial y} \right] + \frac{1}{D} \frac{\partial}{\partial \sigma} \left(K_m \frac{\partial v}{\partial \sigma} \right) + DF_y \end{aligned} \quad (2.21)$$

$$\frac{\partial TD}{\partial t} + \frac{\partial TuD}{\partial x} + \frac{\partial TvD}{\partial y} + \frac{\partial T\omega}{\partial \sigma} = \frac{1}{D} \frac{\partial}{\partial \sigma} \left(K_h \frac{\partial T}{\partial \sigma} \right) + D\hat{H} + DF_T \quad (2.22)$$

$$\frac{\partial SD}{\partial t} + \frac{\partial SuD}{\partial x} + \frac{\partial SvD}{\partial y} + \frac{\partial S\omega}{\partial \sigma} = \frac{1}{D} \frac{\partial}{\partial \sigma} \left(K_h \frac{\partial S}{\partial \sigma} \right) + DF_S \quad (2.23)$$

$$\rho = \rho(T, S) \quad (2.24)$$

where x , y , and σ are the east, north, and vertical axes; u , v , and ω are the x , y , σ velocity components; D is the total depth as a sum of mean depth H and surface elevation ζ ; T is the temperature; S is the salinity; ρ is the total density as a sum of perturbation density ρ' and reference density ρ_0 ; f is the Coriolis parameter; g is the gravitational acceleration; K_m is the vertical eddy viscosity coefficient; K_h is the thermal vertical eddy diffusion coefficient; F_u , F_v , F_T , and F_S represent the horizontal momentum, thermal, and salt diffusion terms; \hat{H} is the absorption of downward short-wave irradiance. K_m and K_h are parameterized using the MY-2.5 turbulent submodel, and horizontal diffusion coefficients are determined using a Smagorinsky eddy parameterization method [Smagorinsky, 1963].

The surface and bottom boundary conditions for u , v , and w are specified as

$$\left(\frac{\partial u}{\partial \sigma}, \frac{\partial v}{\partial \sigma} \right) = \frac{D}{\rho_o K_m} (\tau_{sx}, \tau_{sy}), \quad \omega = 0, \quad \text{at } \sigma = 0 \quad (2.25)$$

and

$$\left(\frac{\partial u}{\partial \sigma}, \frac{\partial v}{\partial \sigma}\right) = \frac{D}{\rho_o K_m}(\tau_{bx}, \tau_{by}), \quad \omega = 0, \quad \text{at } \sigma = -1 \quad (2.26)$$

where (τ_{sx}, τ_{sy}) and $(\tau_{bx}, \tau_{by}) = C_d \sqrt{u^2 + v^2}(u, v)$ are the x and y components of surface wind and bottom stresses. The drag coefficient C_d is determined by matching a logarithmic bottom layer to the model at a height Z_{ab} above the bottom, *i.e.*,

$$C_d = \max\left(k^2 / \ln\left(\frac{z_{ab}}{z_o}\right)^2, 0.0025\right), \quad (2.27)$$

where $k = 0.4$ is the von Karman's constant and Z_0 is the bottom roughness parameter.

The surface and bottom boundary conditions for temperature are:

$$\frac{\partial T}{\partial \sigma} = \frac{D}{\rho c_p K_h} [Q_n(x, y, t) - Q_s(x, y, 0, t)], \quad \text{at } \sigma = 0 \quad (2.28)$$

$$\frac{\partial T}{\partial \sigma} = \frac{A_H D \tan \alpha}{K_h - A_H \tan^2 \alpha} \frac{\partial T}{\partial n}, \quad \text{at } \sigma = -1 \quad (2.29)$$

where $Q_n(x, y, t)$ is the surface net heat flux consisting of four components: downward shortwave, net air-sea longwave radiation, sensible, and latent fluxes. c_p is the specific heat of seawater. A_H is the horizontal thermal diffusivity. n is the horizontal coordinate on the σ surface. The bottom condition of temperature is specified to satisfy a condition of no-flux normal to the slope. This condition was first introduced into the primitive equation model by *Chen et al.* [2003a], who not only derived this condition, but also validated it by comparing the model results for the shelf break front. $Q_s(x, y, 0, t)$ is the incident shortwave flux at the sea surface given as

$$Q_s(x, y, z, t) = Q_s(x, y, 0, t) [Re^{\frac{z}{a}} + (1 - R)e^{\frac{z}{b}}], \quad (2.30)$$

where a and b are attenuation lengths for longer and shorter (blue-green) wavelength components of the shortwave irradiance, and R is the percent of the total flux associated with the longer wavelength irradiance [*Chen et al.*, 2003a]. The absorption of

downward irradiance is included in the temperature (heat) equation in the form of

$$\hat{H}(x, y, z, t) = \frac{\partial Q_s(x, y, \sigma, t)}{D\partial\sigma} = \frac{Q_s(x, y, 0, t)}{D\rho c_p} \left[\frac{R}{a} e^{\frac{\sigma D + \zeta}{a}} + \frac{1 - R}{b} e^{\frac{\sigma D + \zeta}{b}} \right], \quad (2.31)$$

The surface and bottom boundary conditions for salinity are:

$$\frac{\partial S}{\partial\sigma} = 0, \quad \text{at } \sigma = 0 \quad (2.32)$$

$$\frac{\partial S}{\partial\sigma} = \frac{A_H D \tan \alpha}{K_h - A_H \tan^2 \alpha} \frac{\partial S}{\partial n}, \quad \text{at } \sigma = -1 \quad (2.33)$$

where \hat{P} and \hat{E} are precipitation and evaporation rates, respectively. The bottom boundary condition of the salinity has the same form for the temperature.

ECOM-si is a modified version of the Princeton Ocean Model (POM) [Blumberg, 1994]. This model is solved numerically using state of the art finite-difference method with a single time step Δt . The semi-implicit numerical method used in the ECOM-si leads to a linear symmetrical diagonal algebra system at each time step, which can be solved efficiently by a preconditioned conjugate method with no sacrifice in computational time [Casulli, 1990]. In ECOM-si, Δt is constrained by $\min(\Delta x, \Delta y) / \sqrt{u^2 + v^2}$, which could be one order of magnitude larger than that chosen in POM regarding the requirement for numerical stability. However, enlarging Δt necessarily results in sacrifice of energy conservation because of the energy decay nature of semi-implicit schemes.

FVCOM is a new unstructured grid, finite-volume, 3-D primitive equation coastal ocean model [Chen *et al.*, 2003]. Like POM, FVCOM is composed of external and internal modes that are computed separately using two split time steps. Distinct difference is that FVCOM is solved numerically by flux calculation in the integral form of the equations 2.20-2.24 over non-overlapping, unstructured triangular grids. Flux calculation not only ensures the conservation of total mass over the whole computational domain but also on individual meshes used to compute currents and water

properties. The finite-volume numerical approach takes the advantages of finite-element methods for geometric flexibility and finite-difference methods for simple structures of the discrete code and computational efficiency. A detailed comparison between POM and FVCOM is described by *Chen et al.* [2003c].

FVCOM subdivides the horizontal numerical computational domain into a set of non-overlapping unstructured triangular cells. An unstructured triangle is comprised of three nodes, a centroid, and three sides (Figure 2.4), on which u and v are placed at centroids and all scalar variables are placed at nodes. A second-order accuracy upwind finite-difference scheme is used for flux calculation in the integral form of advective terms [*Kobayashi et al.*, 1999; *Hubbard*, 1999], and the modified fourth-order Runge-Kutta time-stepping scheme is used for time integration. Similar to ECOM-si, no temporal and spatial smoothing is needed for numerical stability.

In this study, ECOM-si was used for 1-D and 2-D experiments and FVCOM for 3-D experiments. Since the 1-D and 2-D cases feature a single point or a transect across GB, ECOM-si and FVCOM shows no differences, except for the sloping bottom boundary conditions of temperature and salinity. There are three reasons for choosing FVCOM for the 3-D model experiments in the present study. Firstly, the finite-difference model has difficulty in resolving the steep bottom topography on GB and also fails to capture the near-resonance nature of M_2 tidal waves in the GOM, while FVCOM has shown promises with regard to these two issues. Secondly, FVCOM has been well validated for the real-time simulation and assimilation for the GOM/GB. Thirdly, the biological model developed in this study will be eventually used to simulate the ecosystem in the GOM/GB. It seems that FVCOM is the only physical model validated for a long-term simulation and assimilation of tidal/subtidal currents and water temperatures, and is capable of solving major numerical difficulties over the steep bottom topography, mass conservation, and bottom mixing.

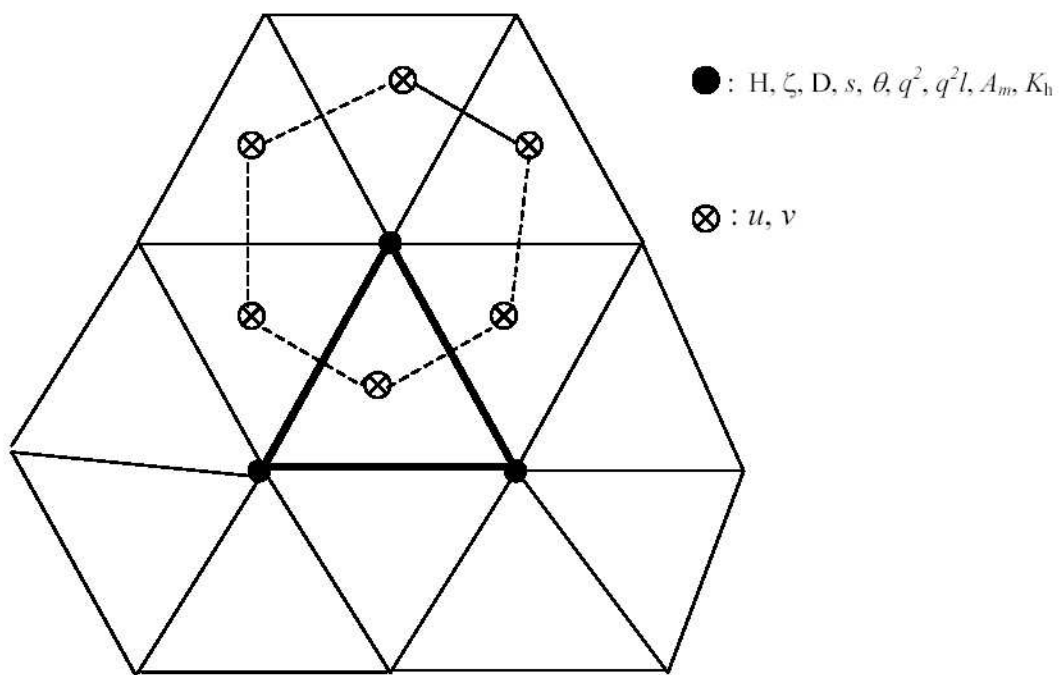


Figure 2.4: The unstructured grid for the finite-volume model.

Coupling this biological model directly with FVCOM would accelerate the development of the ecosystem modeling system for the GOM/GB.

2.4 REFERENCES

- Blumberg, A. F., A primer of ECOM3D-si, *Tech. rep.*, HydroQual, Inc., Mahwah, NJ, 1994.
- Blumberg, A. F., and G. L. Mellor, A description of a three-dimensional coastal ocean circulation model, in *Three-Dimensional Coastal Ocean Models, Coastal and Estuarine Science*, vol. 4, edited by N. S. Heaps, pp. 1–16, 1987.
- Brzezinski, M. A., The silicon:carbon:nitrogen ratio of marine diatoms: interspecific variability and the effect of some environmental variables, *Journal of Phycology*, 1985.
- Casulli, V., Semi-implicit finite-difference methods for the two-dimensional shallow water equations., *Journal of Computational Physics*, 86, 56–74, 1990.
- Chen, C., *Marine Ecosystem dynamics and modeling*, 404 pp., Higher Education Press, Beijing, China, 2003.
- Chen, C., and R. C. Beardsley, Numerical study of stratified tidal rectification over finite-amplitude banks. Part I: Symmetric Banks, *Journal of Physical Oceanography*, 25, 2090–2210, 1995.
- Chen, C., R. C. Beardsley, and P. J. S. Franks, A 3-d prognostic model study of the ecosystem over Georges Bank and adjacent coastal regions. Part I: physical model, *Deep Sea Research II*, 48, 419–456, 2001.
- Chen, C., R. Ji, D. J. Schwab, D. Beletsky, G. L. Fahnenstiel, M. Jiang, T. H. Johengen, H. Vanderploeg, B. Eadie, J. W. Budd, M. H. Bundy, W. Gardner,

- J. Cotner, and P. J. Lavrentyev, A model study of the coupled biological and physical dynamics in Lake Michigan, *Ecological Modelling*, *152*, 145–168, 2002.
- Chen, C., R. Beardsley, P. J. S. Franks, and J. V. Keuren, Influences of diurnal varying heat flux on circulation and stratification over Georges Bank: a 3-D prognostic model experiment, *Journal of Geophysical Research*, In press, 2003a.
- Chen, C., H. Liu, and R. C. Beardsley, An unstructured, finite-volume, three-dimensional, primitive equation ocean model: application to coastal ocean and estuaries, *Journal of Atmospheric and Oceanic Technology*, *20*, 159–186, 2003b.
- Chen, C., H. Liu, R. C. Beardsley, L. Wang, and Q. Xu, A finite-volume numerical approach for coastal ocean studies: comparisons with the finite-difference models, *Journal of Physical Oceanography*, *submitted*, 2003c.
- Chen, C., Q. Xu, R. C. Beardsley, and P. J. S. Franks, Model study of the cross-frontal water exchange on Georges Bank: A three-dimensional Lagrangian experiment, *Journal of Geophysical Research*, p. In press, 2003d.
- Davis, C. S., Zooplankton life cycles, in *Georges Bank*, edited by R. H. Backus and D. W. Bourne, pp. 256–267, MIT Press, Cambridge, Massachusetts, 1987.
- Dortch, Q., The interaction between ammonium and nitrate uptake in phytoplankton, *Marine Ecology Progress Series*, *61*, 138–201, 1990.
- Druffel, E. R. M., P. M. Williams, J. E. Bauer, and J. R. Ertel, Cycling of dissolved and particulate organic matter in the open ocean, *Journal of Geophysical Research*, *97*, 15,639–15,659, 1992.
- Eilers, P. H. C., and J. C. H. Peeters, A model for the relationship between light intensity and the rate of photosynthesis in phytoplankton, *Ecological Modelling*, *42*, 199–215, 1988.

- Falkowski, P. G., and C. D. Wirick, A simulation model of the effects of vertical mixing on primary productivity, *Marine Biology*, 65, 69–75, 1981.
- Franks, P. J. S., and C. Chen, Plankton production in tidal fronts: A model of Georges Bank in summer, *Journal of Marine Research*, 54, 631–651, 1996.
- Franks, P. J. S., and C. Chen, A 3-d prognostic numerical model study of the Georges Bank ecosystem. Part II: biological-physical model, *Deep Sea Research II*, 48, 457–482, 2001.
- Franks, P. J. S., J. S. Wroblewski, and G. R. Flierl, Behavior of a simple plankton model with food-level acclimation by herbivores, *Marine Biology*, 91, 121–129, 1986.
- Frost, B. W., and N. C. Franzen, Grazing and iron limitation in the control of phytoplankton stock and nutrient concentration: a chemostat analog of the Pacific equatorial upwelling zone, *Marine Ecology Progress Series*, 83, 291–303, 1992.
- Gallegos, C. L., and W. N. Vant, An incubation procedure for estimating carbon-to-chlorophyll ratios and growth irradiance relationships of estuarine phytoplankton, *Marine Ecology Progress Series*, 138, 275–291, 1996.
- Galperin, B., L. H. Kantha, S. Hassid, and A. Rosati, A quasi-equilibrium turbulent energy model for geophysical flows, *Journal of Atmospheric Sciences*, 45, 55–62, 1988.
- Hubbard, M. E., Multidimensional slope limiters for muscl-type finite volume schemes on unstructured grids, *Journal of Computational Physics*, 155, 54–74, 1999.
- Hurtt, G. C., and R. A. Armstrong, A pelagic ecosystem model calibrated with BATS data, *Deep Sea Research II*, 43(2-3), 653–683, 1996.
- Ivlev, V. S., *Experimental Ecology of the Feeding of Fishes*, Yale University Press, New Haven, Connecticut, 1961.

- Janowitz, G. S., and D. Kamykowski, An Eulerian model of phytoplankton photosynthetic response in the upper mixed layer, *Journal of Plankton Research*, *13*(5), 988–1002, 1991.
- Jassby, A. D., and T. Platt, Mathematical formulation of the relationship between photosynthesis and light for phytoplankton, *Limnology and Oceanography*, *21*(4), 540–547, 1976.
- Ji, R., C. Chen, J. W. Budd, D. J. Schwab, D. Beletsky, G. L. Fahnenstiel, T. H. Johengen, H. Vanderploeg, B. Eadie, M. Bundy, W. Gardner, and J. Cotner, Influences of suspended sediments on the ecosystem in Lake Michigan: a 3-D coupled bio-physical modeling experiment, *Ecological Modelling*, *152*, 169–190, 2002.
- Kobayashi, M. H., J. M. C. Pereira, and J. C. F. Pereira, A conservative finite-volume second-order-accurate projection method on hybrid unstructured grids, *Journal of Computational Physics*, *150*, 40–45, 1999.
- Mellor, G. L., and T. Yamada, Development of a turbulence closure model for geophysical fluid problems, *Reviews of Geophysics and Space Physics*, *20*, 851–875, 1982.
- Mergard, R. O., D. W. Tonkyo, and W. H. Senft, Kinetics of oxygenic photosynthesis in planktonic algae, *Journal of Plankton Research*, *6*(2), 325–337, 1984.
- Pahl-Wostl, C., and D. M. Imboden, DYPHORA - a dynamic model for the rate of photosynthesis of algae, *Journal of Plankton Research*, *12*, 1207–1221, 1990.
- Parsons, T. R., M. Takahashi, and B. Hargrave, *Biological Oceanographic Processes*, third ed., Pergamon Press, New York, New York, 1984.

- Platt, T., C. L. Gallegos, and W. G. Harrison, Photoinhibition of photosynthesis in natural assemblages of marine phytoplankton, *Journal of Marine Research*, 38, 687–701, 1980.
- Reynolds, C. S., *The Ecology of Freshwater Phytoplankton*, Cambridge University Press, Cambridge, Massachusetts, 1984.
- Scavia, D., G. A. Lang, and J. F. Kitchell, Dynamics of Lake Michigan plankton: a model evaluation of nutrient loading, competition, and predation, *Canadian Journal of Fisheries and Aquatic Sciences*, 45, 165–177, 1988.
- Smagorinsky, J., General circulation experiments with the primitive equations, I. the basic experiment, *Monthly Weather Review*, 91, 99–164, 1963.
- Steele, J. H., Environmental control of photosynthesis in the sea, *Limnology and Oceanography*, 7, 137–150, 1962.
- Steele, J. H., and E. W. Henderson, The role of predation in plankton models, *Journal of Plankton Research*, 14, 157–172, 1992.
- Strickland, J. D. H., Measuring the production of marine phytoplankton, *Bulletin of the Fisheries Research Board of Canada*, 122, 1–172, 1960.
- Townsend, D. W., and M. Thomas, Springtime nutrient and phytoplankton dynamics on Georges Bank, *Marine Ecology Progress Series*, 228, 57–74, 2002.
- Wheeler, P. A., and S. A. Kokkinakis, Ammonium recycling limits nitrate use in the oceanic subarctic Pacific, *Limnology and Oceanography*, 35, 1267–1278, 1990.

CHAPTER 3

LOWER TROPHIC LEVEL FOOD WEB DYNAMICS ON GEORGES BANK: 1-D EXPERIMENTS¹

¹R. Ji. Will be submitted to *Journal of Geophysical Research*. 2003.12.

3.1 ABSTRACT

A one-dimensional coupled biological-physical model was used to examine the biological and physical factors controlling the timing and magnitude of the spring bloom on GB. The 1-D experiment results show that the controlling mechanism for spring bloom dynamics differs between the central Bank and the flank area. In the shallow, well-mixed central bank, the timing and duration of the spring bloom are determined by light intensity and its downward penetration, while the bloom intensity is regulated by initial nutrient concentration and zooplankton grazing pressure. In deeper water (> 60 m), given the same conditions of light intensity/attenuation, initial nutrient concentration and zooplankton grazing pressure as those in the shallow, well-mixed region, the timing of the spring bloom is closely linked to the seasonal development of stratification. The 1-D model captures the basic seasonal pattern of the nutrients and phytoplankton dynamics in the shallow, well-mixed central bank, but not in the deeper flank area, suggesting that frontal dynamics and advective processes have significant impacts on the phytoplankton dynamics in the seasonally stratified region of GB.

3.2 INTRODUCTION

Spring and early summer are critical seasons to biological productivity on Georges Bank (GB). As discussed in chapter 1, the recruitment of two commercially important fish species - cod and haddock - is strongly linked to zooplankton population dynamics, which is further associated with nutrients and phytoplankton dynamics. It is essential to examine the biological and physical processes controlling lower trophic level food web dynamics, because these processes can have significant impacts on biological production and fish recruitment on GB.

Our previous understanding of the spring bloom and associated nutrients and phytoplankton dynamics on GB is mainly based on limited historic data summarized by *Cura* [1987] and *O'Reilly et al.* [1987]. According to these historic scenarios observed on GB, in general, the spring bloom occurs in late winter and early spring in a well-mixed shallow region (< 60 m), mainly in March. The spring bloom can also occur during April in the deeper area of GB (60-100 m) where the water is seasonally stratified. The blooms usually decline rapidly by late April and/or early May as nutrients become depleted. The blooms can re-occur in autumn as a result of the increase of nutrient supply due to enhanced vertical mixing. Patches of relatively high phytoplankton biomass can also be observed near the surface close to the seasonal tidal mixing front or in the subsurface near thermoclines during summer as stratification develops. These high biomass phytoplankton patches are sometimes referred to as the secondary summertime bloom.

The seasonal pattern of the spring bloom described above was challenged by recent observational evidence found during the U.S. GLOBEC/GB multi-year interdisciplinary survey [*Townsend and Thomas*, 2002]. These observations clearly show an interannual variation of the timing, duration, and location of the spring bloom. In 1997, for example, a strong bloom occurred in May, which is about two months later than the general pattern. In 1998, no bloom occurred in the well-mixed shallow central bank until April, when a high concentration patch of phytoplankton was found in the southwestern region with depths of 40-60 m over GB. In 1999, the bloom started in February, continued to intensify until April, decreased in May, and then reoccurred in the mid-bank region between 40- and 70- m isobaths.

It has been believed that seasonal and interannual variations of the spring bloom are related to availability of nutrients in the water column since the timing of nitrate depletion coincides well with the spring bloom [*O'Reilly et al.*, 1987]. The concentration of nitrogen is usually high ($> 6 \mu\text{mol/l}$) in both shallow central bank and deep

flank areas before the bloom occurred and then depleted rapidly over the bank during the bloom event, except in the lower water column in the deep flank areas. On GB, the nutrients are mainly maintained or supplied through advective processes associated with upwelling due to cross-bank secondary circulation and transport from the remote areas from the Gulf of Maine (GOM), Scotian Shelf (SS), and Great South Channel (GSC). As the vertical stratification develops, a tidal mixing front forms in a mid-bank region between the 40- and 60-m isobath, which separates the well-mixed water in the central bank from the stratified water on the flank area. The existence of the tidal mixing front acts like a barrier to limit the on-bank flux of nutrients. Similarly, the formation of a thermocline in the stratified side of the front can also restrict the vertical exchange of nutrients between the upper and lower water column of the deep flank area. Primary production on the central GB remains high throughout the summer and fall, with daily production rates of 1-2 g C m⁻²day⁻¹ [O'Reilly *et al.*, 1987]. This high production in the central bank is mainly supported by recycled nitrogen [Loder and Platt, 1985; O'Reilly *et al.*, 1987; Walsh *et al.*, 1987] and on-bank fluxes of “new” nitrate along the edges of the bank [Dugdale and Goering, 1967; Eppley and Peterson, 1979; Pastuszak *et al.*, 1982; Townsend and Pettigrew, 1997; Chen and Beardsley, 1998; Franks and Chen, 2001; Houghton, 2002].

There is no question that nitrogen is a limiting factor that can impact the formation and duration of spring bloom on GB. Recent studies, however, have revealed that the timing and duration of the spring bloom are also related to the availability of silicon in the water column [Townsend and Thomas, 2001, 2002]. It is difficult to estimate the ratio of nitrogen to silicon (N/Si) in diatom cells in the field since this ratio may vary with species composition, physiologic conditions and light environment. The average value is close to 1.0 with a variation range of 3 [Brzezinski, 1985]. The relative importance of nitrogen and silicon limitation to the spring bloom might also be related to N/Si. Although these factors have been recognized by biologist,

to date no process-oriented modeling studies have been conducted to address these questions on GB. Previous biological modeling studies [e.g., *Klein, 1987; Lewis et al., 1994; Franks and Chen, 1996, 2001*] are all based on the assumption that nitrogen is the primary limiting nutrient for the growth of phytoplankton on GB. This assumption appears valid only for summertime, but definitely not suitable for the simulation of the seasonal nutrients and phytoplankton dynamics on GB.

The objective of this study is to examine the biological and physical processes controlling the spring bloom dynamics on GB. 1-D modeling approach is probably a good start in order to distinguish the relative importance of biological and physical processes. Firstly, the light intensity can be assumed to be uniform over the bank as a first order approximation [*Chen et al., 2003a*]. Therefore, the impact of light intensity and downward light attenuation on the spring bloom can be examined in a 1-D domain. Secondly, nutrients supply on GB is affected by complex physical processes associated with upwelling, advection, and inflow from remote regions. By excluding these 3-D physical processes in a 1-D model, the relative importance of the locally available nutrient sources to the growth of phytoplankton on GB can be identified. Thirdly, the biological model involves numerous parameters. Since these parameters have a wide range of uncertainty, a sensitivity study must be conducted to validate the reliability and stability of the food web system constructed in the model. Driving the 1-D biological model with simple physical forcings can help us to provide quantitative estimation of parameter sensitivity. Finally, the 1-D model can be run with a high computational efficiency. For example, with a single Xeon/533 2.8GHz processor PC, the half-year simulation takes less than 2 minutes with a time step of 0.46 hr. This efficiency allows us to focus on the process studies with no sacrifice of our model efforts due to computing resources.

The remaining sections of this chapter are organized as follows. In Section 3.3, a brief overview of three-year GLOBEC/GB broad-scale survey data is described.

These data were directly downloaded from Dr. Townsend's research group website at University of Maine (<http://grampus.umeoce.maine.edu/globec/globec.html>). Data analyses were carried out as one component of the U.S. GLOBEC/GB Program modeling studies with collaboration of Dr. Townsend. The design of numerical modeling experiments for hypothesis testing is described in Section 3.4. The base model-run results, with standard parameters, are given in Section 3.5, followed with the discussion in Section 3.6. Finally, conclusions are summarized in Section 3.7

3.3 RECENTLY OBSERVED FEATURES OF NUTRIENTS AND PHYTOPLANKTON ON GB

The general features of nutrient and phytoplankton dynamics on GB have been summarized in *Backus and Bourne* [1987]. However, neither details of the seasonal cycle of primary production nor the dynamics of the spring bloom on GB are well understood. As one component of US GLOBEC/GB interdisciplinary field programs, broad-scale surveys were conducted on GB during 1997-1999. The survey area covered the whole of GB with most of stations inside the 200-m isobath (Figure 3.1). Biological samples and hydrographic measurements were made on a monthly basis from January to June in 1997, 1998 and 1999, respectively. Biological data included chlorophyll *a*, nitrate + nitrite, silicate, phosphate and ammonium, and physical data included water temperature and salinity. All the data were posted on Dr. Townsend's research group website at <http://grampus.umeoce.maine.edu/globec/globec.html>. The data used in this section were directly downloaded from this web site and reviews were also based on the published papers by *Townsend and Thomas* [2001] and *Townsend and Thomas* [2002].

The surface chlorophyll *a* distribution (Figure 3.2) shows that the timing and duration of spring bloom on GB varied from year to year. The significant spring

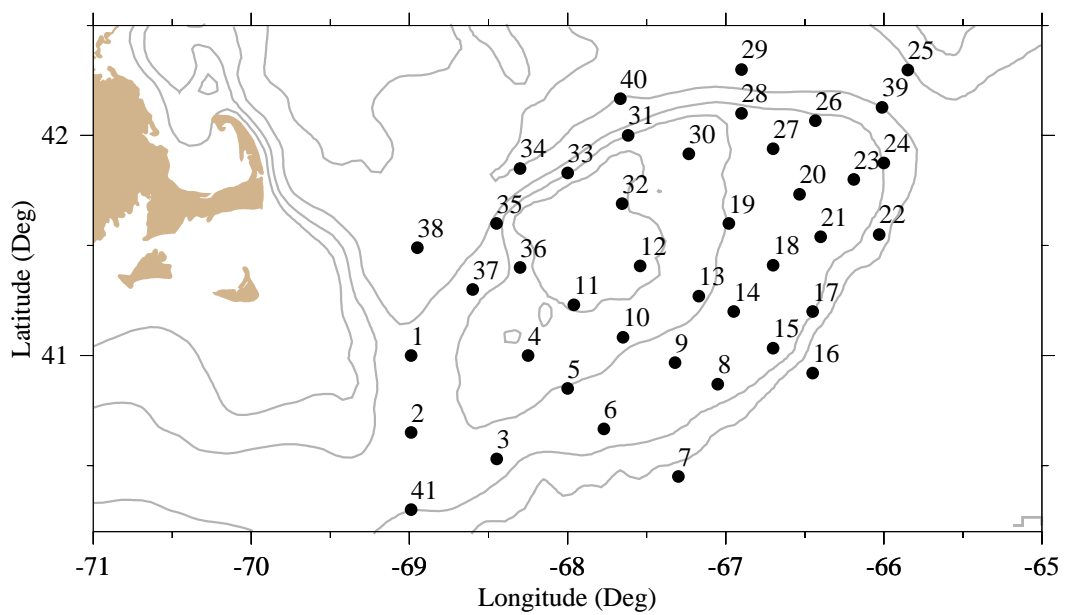


Figure 3.1: The U.S. GLOBEC/GB Program broad-scale sampling station plan for 1998 and 1999. Station 39 was added in 1996 based on 38 stations used in 1995, Station 40 was added in 1997, and Station 41 was added in 1998. The intermediate stations added in each individual year are omitted here.

bloom occurred in May in 1997, while it occurred in April 1998 and in February 1999. In May 1997 the bloom was located in the northeastern and southwestern area between the 40- to 60-m isobath, respectively, with a relatively low concentration in the central bank. The 1998 bloom started along the northwestern edge of the bank in March, but the maximum biomass occurred in the southwestern area between the 40- to 100-m isobath. The 1999 bloom, which occurred in February, almost covered the entire region of the central bank, and intensified with time until April. Both 1998 and 1999 showed a clear second bloom in a less extensive area of the bank. For June 1997, due to the poor data coverage, it is hard to say whether the second bloom existed on the bank. The concentration of chlorophyll *a* was about 1 $\mu\text{g}/\text{l}$ at most stations during January, while it exceeded 6 $\mu\text{g}/\text{l}$ during the bloom events. In some stations, the concentration exceeded 10 $\mu\text{g}/\text{l}$.

Samples of species were collected in the 1999 survey. According to cell densities counted from samples, the phytoplankton assemblage was comprised almost exclusively of diatoms from January to April (Figure 3.3). The cell density of diatoms in March and April reached as high as ca. 450 cells/ml. The density of dinoflagellates and nanoflagellates was low (<10 cells/ml) from January to April, but increased to nearly 300 cells/ml on the central bank in May and June. These findings were slightly different from those summarized by *O'Reilly et al.* [1987], who reported that nanoplankton accounted for 20-30% of total chlorophyll *a* concentration over the shallow area of the bank from in May and June.

The distribution and availability of nutrients on GB also differed significantly from year to year. In 1997 and 1998, the bloom occurred in May and April, respectively, so that the concentration of nitrate + nitrite remained high (>4 μM) over the entire bank from January to February (Figure 3.4). In 1999, however, an early bloom started appearing on the southern part of the bank in January, which caused a significant depletion of nitrate and nitrite in that area. In all three years, the sur-

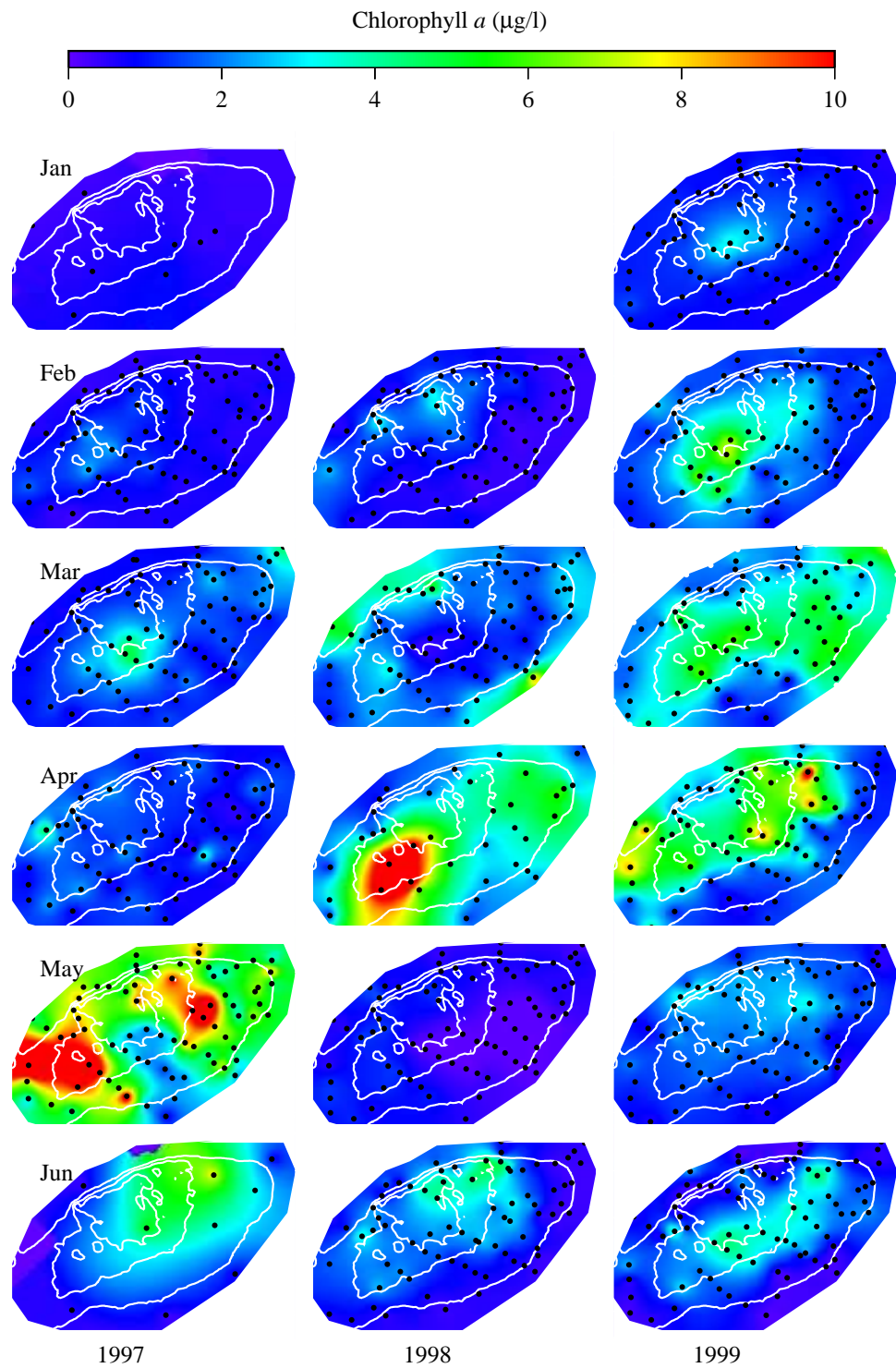


Figure 3.2: Areal contour plots of surface chlorophyll *a* for 1997 (left column), 1998 (middle column) and 1999 (right column) from January to June. Black dots represent sampling stations. No data available for January, 1998.

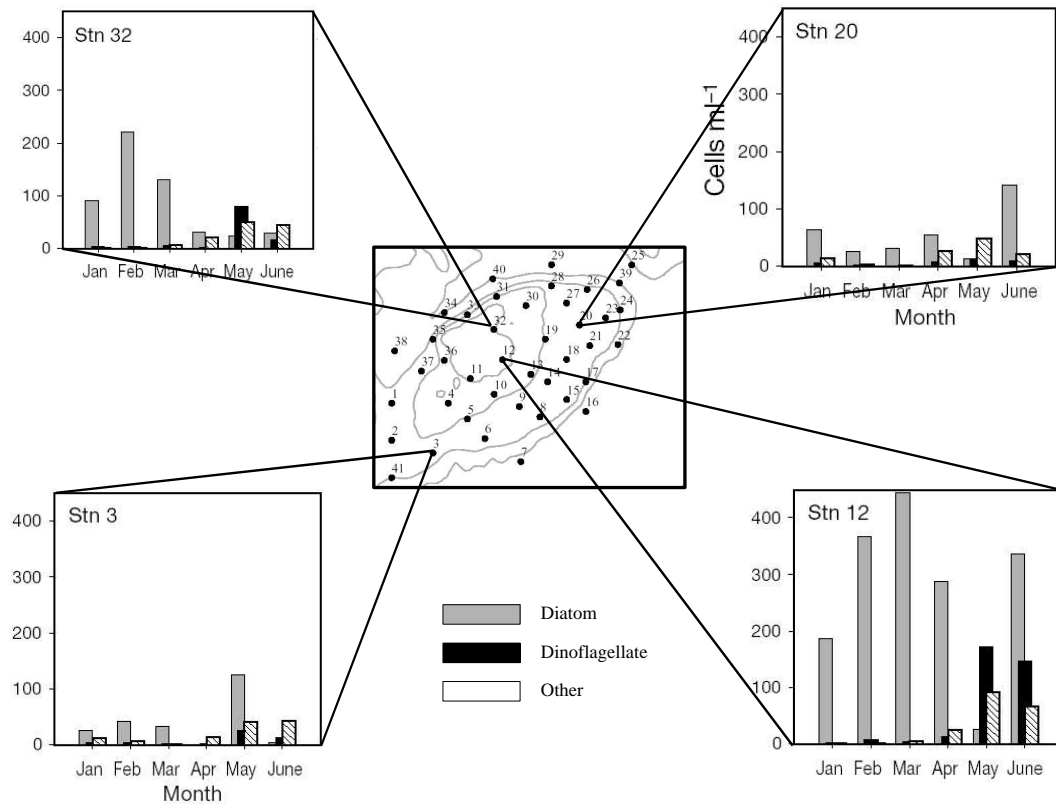


Figure 3.3: Cell densities of 3 phytoplankton groups (diatom, dinoflagellates and other flagellates) at Station 3, 12, 20 and 32 on GB from January to June 1999. This figure is adapted from *Townsend and Thomas* [2002].

face concentration of nitrate + nitrite significantly decreased over the entire bank in April, with the lowest concentration of $< 2 \mu\text{M}$ at the central portion of the bank. The surface concentration of nitrate and nitrite over almost the entire GB dropped to an un-detectible level in May and June.

Silicate, an equivalently important nutrient as nitrogen, also showed a coherent response to the temporal variation of phytoplankton on GB. In all three years of 1997, 1998, and 1999, the central bank was characterized by a low concentration of silicate in February, with the lowest in 1999 (Figure 3.5). The average value of silicate concentration in the central bank in February was about $3 \mu\text{M}$, while it dropped below $2 \mu\text{M}$ in 1998 and 1999. The half saturation constant for diatoms has been estimated to be in a range of $2\text{-}4 \mu\text{M}$ [Paasch, 1973]. This implies that silicate had become a limiting factor for the growth of diatoms on GB as early as February, prior to the onset of nitrogen limitation. The concentration of silicate continued to decrease through March and April. During May, a significant recovery of silicate was found at the northern edge of the bank in 1997 and on the southwestern flank in 1998. In 1999, the recovery of silicate occurred at the northern part of the bank in June, about one month later than previous years. *Townsend and Thomas* [2002] suggested that the recurrence of relatively high silicate found in May or June was due to the increased silicate regeneration on the bank as the water getting warmer. They argued that it was unlikely to be produced by upwelling-induced silicate flux from deep water on the flanks of the bank, because neither colder and saltier water nor high nitrate + nitrite concentrations were observed in the area with a higher concentration of silicate.

These data raised some fundamental dynamical questions regarding the formation of the spring bloom on GB. Firstly, although it is clear that there is interannual variability of nutrients and phytoplankton on GB, the major biological or physical processes controlling this variability remain unclear. Secondly, if silicate started lim-

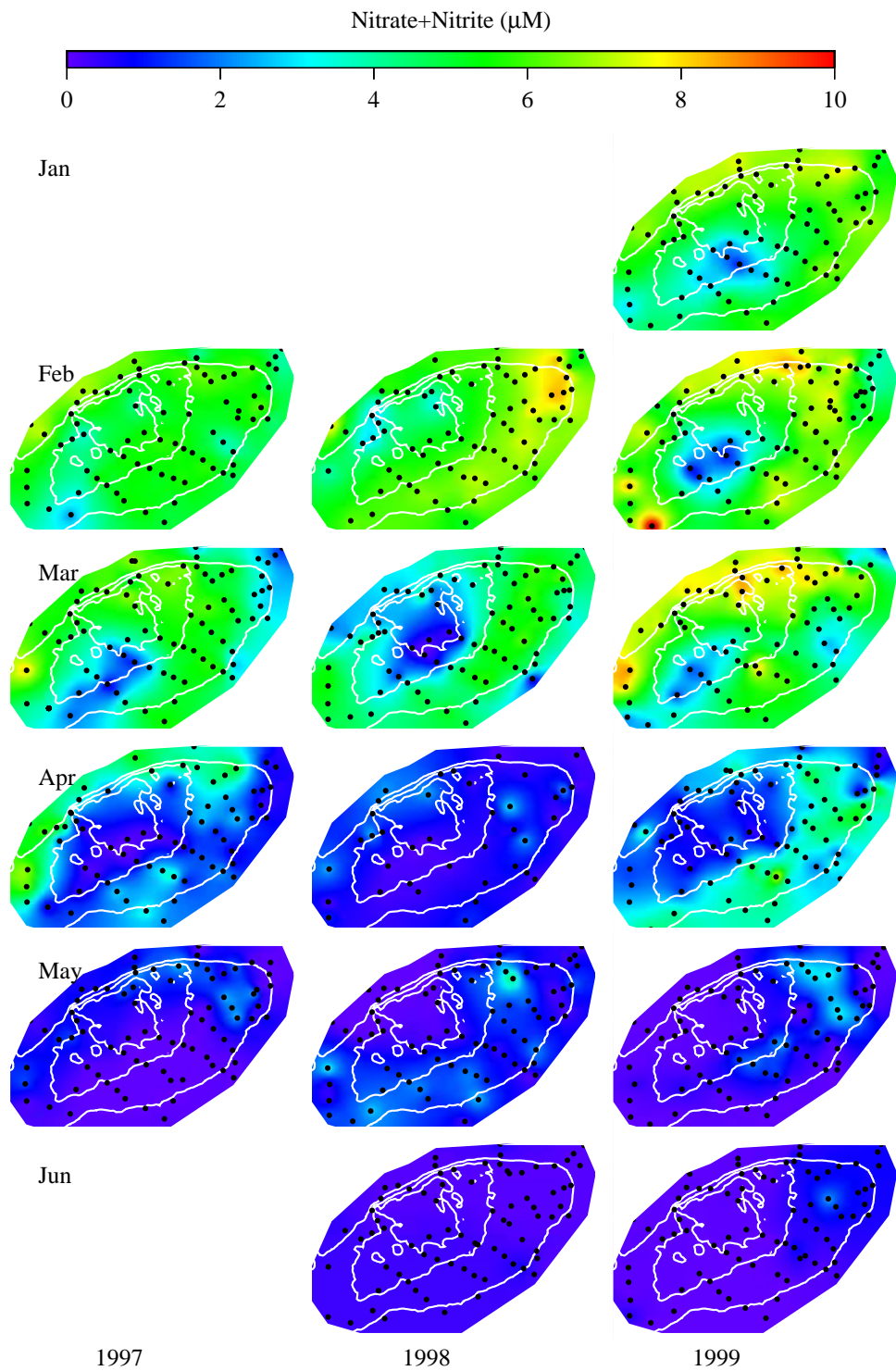


Figure 3.4: Areal contour plots of surface nitrate + nitrite for 1997 (left column), 1998 (middle column) and 1999 (right column) from January to June. Black dots represent sampling stations. No data available for January and June, 1997 and January 1998.

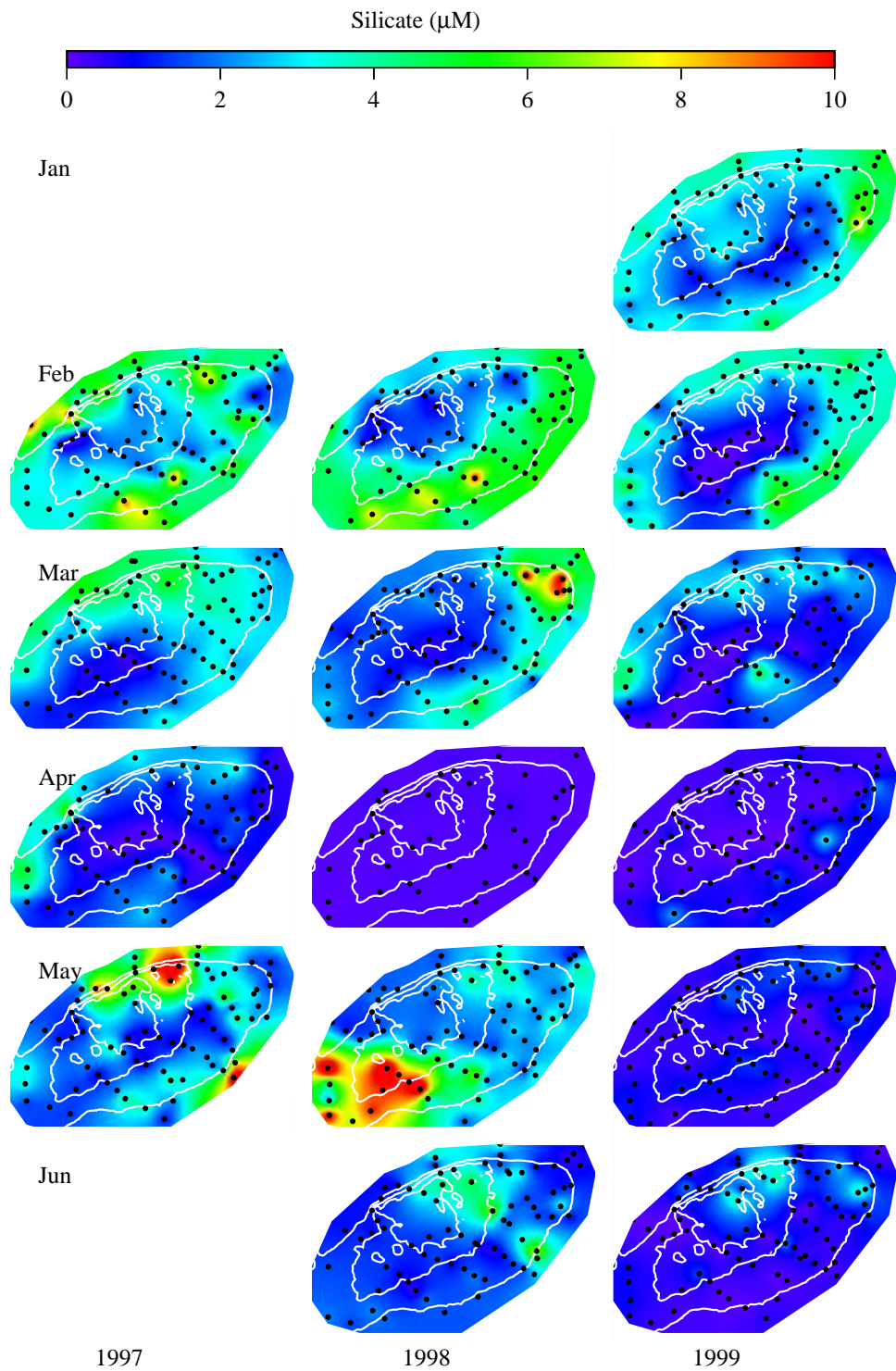


Figure 3.5: Areal contour plots of surface silicate for 1997 (left column), 1998 (middle column) and 1999 (right column) from January to June. Black dots represent sampling stations. No data available for January and June 1997 and January 1998.

iting the growth of phytoplankton as early as February, how could a spring bloom last 2 months, and reach its maximum in April? Thirdly, because a high concentration of silicate occurred in May or June, can the recycling of silicate catch up with the phytoplankton bloom occurring in June? What are the biological and physical processes controlling the occurrence of the second bloom? What is the role of the seasonal development of stratification in the growth of phytoplankton on GB? Fourthly, was the growth of phytoplankton on GB controlled dominantly by bottom-up (nutrients and light availability) or top-down (zooplankton grazing) processes? Finally, were the bloom events observed on GB in these three years just a local event or were they influenced significantly by the advection of either nutrients or plankton from surrounding waters?

3.4 DESIGN OF NUMERICAL EXPERIMENTS

The one-dimensional physical sub-model is adapted from *Chen et al.* [2002]. It is a spatially simplified ECOM-si 3-D model with 5×5 model grids horizontally (Figure 3.6), in which all the biological and physical variables are made uniform. Vertically, the uniform grid is used in σ coordinates, with a resolution of $\Delta\sigma = 0.0196$ (51 points in the vertical). Two sites with different water depths are modeled. The site with 40-m depth (Site A) represents the well-mixed area; and the site with 100-m depth (Site B), the stratified area. *Mellor and Yamada* [1982] 2.5 turbulence closure scheme is used for turbulent mixing of momentum and tracers. Considering the difference of tidal mixing over the shallow and deep area of the bank, 10^{-3} and $10^{-4} \text{ m}^2\text{s}^{-1}$ background mixing coefficient is used for Site A and B, respectively.

Surface heat and wind data observed on southern GB during 1995 are used in this model (see Appendix C). This is the first comprehensive set of *in situ* data available which allows the direct estimation of surface heat and moisture fluxes [*Beardsley*

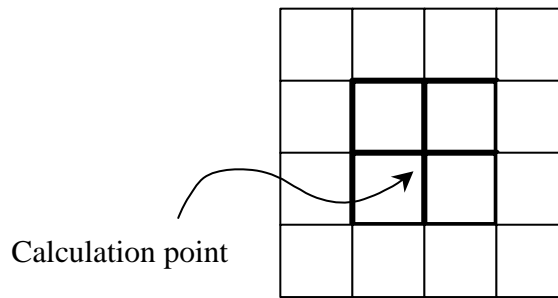


Figure 3.6: One-dimension model grid showing the 5x5 grid structure and computational point.

et al., 2003]. It serves as a standard meteorological forcing for both 1D and 2D model experiments.

The standard model run starts from January 1, and ends on June 30. The concentration of the biological variables are initiated homogenously vertically, in which nitrate was set to $5.0 \mu\text{mol N/l}$; ammonia $0.1 \mu\text{mol N/l}$; silicate $5.0 \mu\text{mol Si/l}$; small phytoplankton $0.1 \mu\text{mol N/l}$; large phytoplankton $0.4 \mu\text{mol N/l}$; small zooplankton $0.1 \mu\text{mol N/l}$, large zooplankton $0.2 \mu\text{mol N/l}$; detritus nitrogen $5.0 \mu\text{mol N/l}$; and detritus silicon $2.0 \mu\text{mol N/l}$. Since the water is well mixed during winter, the uniform initial values used for biological variables are good approximations of observed values with little influence on the seasonal simulation results. Initial values do not correspond to specific observational data. Instead, they are rough approximations extrapolated from multiple cruise data and empirical estimations.

The physical submodel provides the biological model with vertical profiles of temperature, salinity, velocity and diffusion coefficients. Short-wave radiation is used as the surface photosynthesis active radiance (PAR). Depth dependent light intensity is calculated by

$$I = I_0 e^{-k_{ext}d},$$

where I_0 is the incoming light intensity, I is the light intensity traveling a distance of d , and K_{ext} is the light attenuation coefficient.

Three basic experiments were performed with the model. First, the effects of variation in the light environment on the timing of the spring bloom were investigated; second, changes in nutrients conditions have been made to examine nutrient limitation of phytoplankton blooms; and finally, the zooplankton grazing pressure was examined to see the importance of the top-down control. Physical related parameters, such as vertical mixing coefficient, are not examined in 1-D model experiment. Biological responses are expected to be insensitive to vertical mixing coefficient in the well mixed site due to the strong tidal mixing, while they could be sensitive to this parameter in the seasonally stratified region. This issue will be discussed in the 2-D model experiments. Table 3.1 lists all the biological and physical elements being investigated for site A and B; the model runs are the combination of those elements as shown in Table 3.2.

3.5 MODEL RESULTS

The standard model run (run A1 and B1) results are presented in this section. The rest of model results are presented in the discussion section to explore the factors controlling the spring bloom and lower trophic food web dynamics.

3.5.1 SITE A

WATER TEMPERATURE

The water temperature was vertically homogeneous throughout the modeled time period, from the beginning of January to the end of June (Figure 3.7). The coldest water temperature was not reached until March, when the water temperature was about 4 °C. The water started warming up by April, when temperatures ranged from

Table 3.1: Definition of code used in Table 3.2 for site A.

<i>Group</i>	<i>parameter</i>	<i>setting</i>	<i>code</i>
Light related	Kext	variant	K1
		Constant 0.10	K2
		Constant 0.15	K3
	P-I	<i>Eilers and Peeters</i> [1988]	L1
		<i>Steele</i> [1962]	L2
		<i>Jassby and Platt</i> [1976]	L3
Nutrients related	[Si]	Initial [Si] = 5.0 μ M	S1
		Initial [Si] = 2.0 μ M	S2
	N:Si	1.5	NS1
		0.8	NS2
	Edn	0.06	E1
		0.1	E2
Zooplankton related	Rzl	0.3	R1
		0.2	R2
		0.4	R3

Table 3.2: Design of model run matrix for site A.

Run	K1	K2	K3	L1	L2	L3	S1	S2	NS1	NS2	E1	E2	R1	R2	R3
A1	-			-			-		-		-		-		
A2		-		-			-		-		-		-		
A3			-	-			-		-		-		-		
A4	-				-		-		-		-		-		
A5	-					-	-		-		-		-		
A6	-			-			-	-	-		-		-		
A7	-			-			-		-	-	-		-		
A8	-			-			-		-		-	-	-		
A9	-			-			-		-		-		-	-	
A10	-			-			-		-		-		-		-

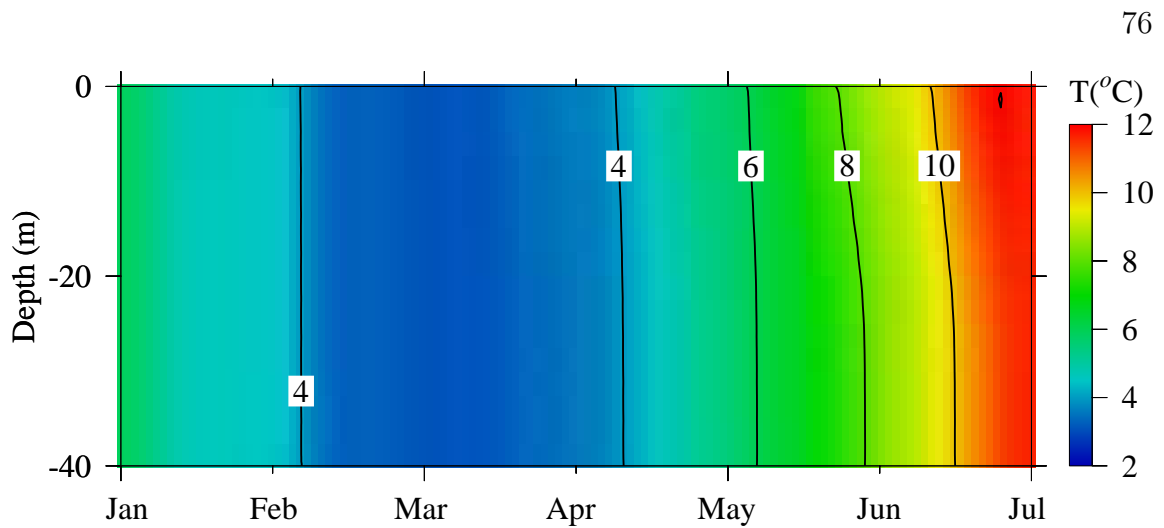


Figure 3.7: Time sequence of the vertical distribution of model-predicted temperature in Site A from January to June.

5 to 6 °C. The water temperature reached 12 °C at the end of June. Qualitatively, The model results agree well with observation of water temperature evolution over the top of GB, providing a good basic physical background for the biological model.

PHYTOPLANKTON

During the spring, the phytoplankton group is dominated by large phytoplankton (diatoms). It shows a significant bloom starting from March and ended in the middle of May (Figure 3.8). The biomass reaches 3.0-4.0 $\mu\text{mol N/l}$, equivalent to 6.0-8.0 $\mu\text{g Chl-}a/\text{l}$. Small phytoplankton show much less biomass compared with large phytoplankton, mainly due to their lower maximum growth rate. They start to grow during the end of May and their biomass can reach 1.0 $\mu\text{mol N/l}$.

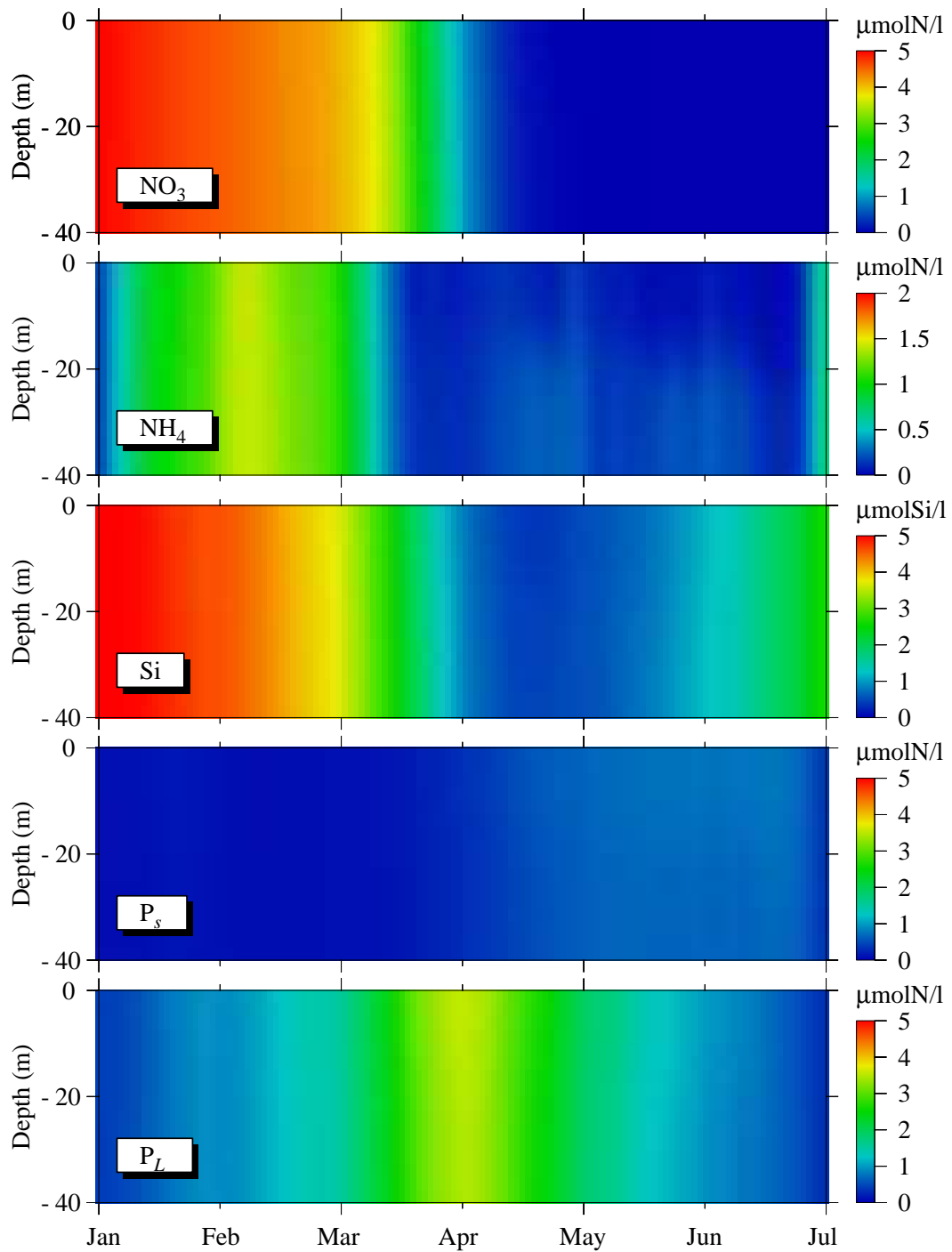


Figure 3.8: Time sequence of the vertical distribution of model-predicted nitrate (NO_3^-), ammonia (NH_4^+), silicate (Si), small phytoplankton (P_s), and large phytoplankton (P_L) in Site A from January to June.

NUTRIENTS

The temporal variation of nutrient concentrations is strongly related to phytoplankton growth. Nitrate concentration decreases from $5.0 \mu\text{mol N/l}$ in January to nearly undetectable in the beginning of April, and remains almost undetectable during the rest of the modeling period (Figure 3.8). Ammonia concentration changes more irregularly, due to the balance of decomposition of particulate organic nitrogen and phytoplankton uptake. It increases from January to February from 0.2 to about $1.5 \mu\text{mol N/l}$, and then gradually decreased to $1.0 \mu\text{mol N/l}$ in March. When diatoms start to bloom, ammonia is quickly consumed due to its preferential uptake over nitrate by phytoplankton. Silicate shows an interesting pattern. It decreases from January to May from $5.0 \mu\text{mol Si/l}$ to near undetectable due to the uptake by large phytoplankton. This is almost synchronized with the depletion of nitrate. During June, the silicate concentration increases again, partially due to the decrease of uptake by large phytoplankton during the post bloom period. More importantly, the dissolution of particulate organic silicon increases with the rise of seawater temperature. Unlike silicate, nitrate is not able to recover without supply from outside of the system.

ZOOPLANKTON

Large phytoplankton biomass increased one month after the increase of phytoplankton biomass (Figure 3.9). The peak appears during May with biomass over $0.5 \mu\text{mol N/l}$, then gradually decreases to $0.35 \mu\text{mol N/l}$. Compared with large zooplankton, small zooplankton are less abundant, mainly due to the lack of small phytoplankton as food support. The biomass remains less than $0.2 \mu\text{mol N/l}$ during the entire modeling period. Due to the grazing of large zooplankton, the biomass of

small zooplankton decreases to the lowest level ($<0.1 \mu\text{mol N/l}$) during May, even though the small phytoplankton start to pick up at that time.

PARTICULATE ORGANIC MATTER

Both particulate organic nitrogen and silica shows an increase from January to June (Figure 3.9). Particulate silica increased more significantly than particulate nitrogen due to its slower decomposition. This pattern of increase indicates that, in general, mass has been transferred from inorganic form to organic form due to the biological process.

3.5.2 SITE B

WATER TEMPERATURE

The water temperature is vertically homogeneous from the beginning of January to the middle of April (Figure 3.10). Weak stratification started to develop after the middle of April and intensified from May to June, when the surface water temperatures were about $9-10 \text{ }^\circ\text{C}$ and the water below 60 meter remained cold with temperature of $5-6 \text{ }^\circ\text{C}$. The model simulated the evolution of water temperature structure very well qualitatively, especially the timing of stratification. However, it is very hard for a 1-D model to get a perfect simulation of temperature because of its very simple tidal forcing scheme and heat flux input, as well as the lack of advection process.

PHYTOPLANKTON

In contrast with the well mixed site, large phytoplankton (diatoms) did not bloom during March and early April (Figure 3.11). Instead, a significant bloom occurred in the upper water column ($< 50 \text{ m}$) from the middle of April to the end of May. The

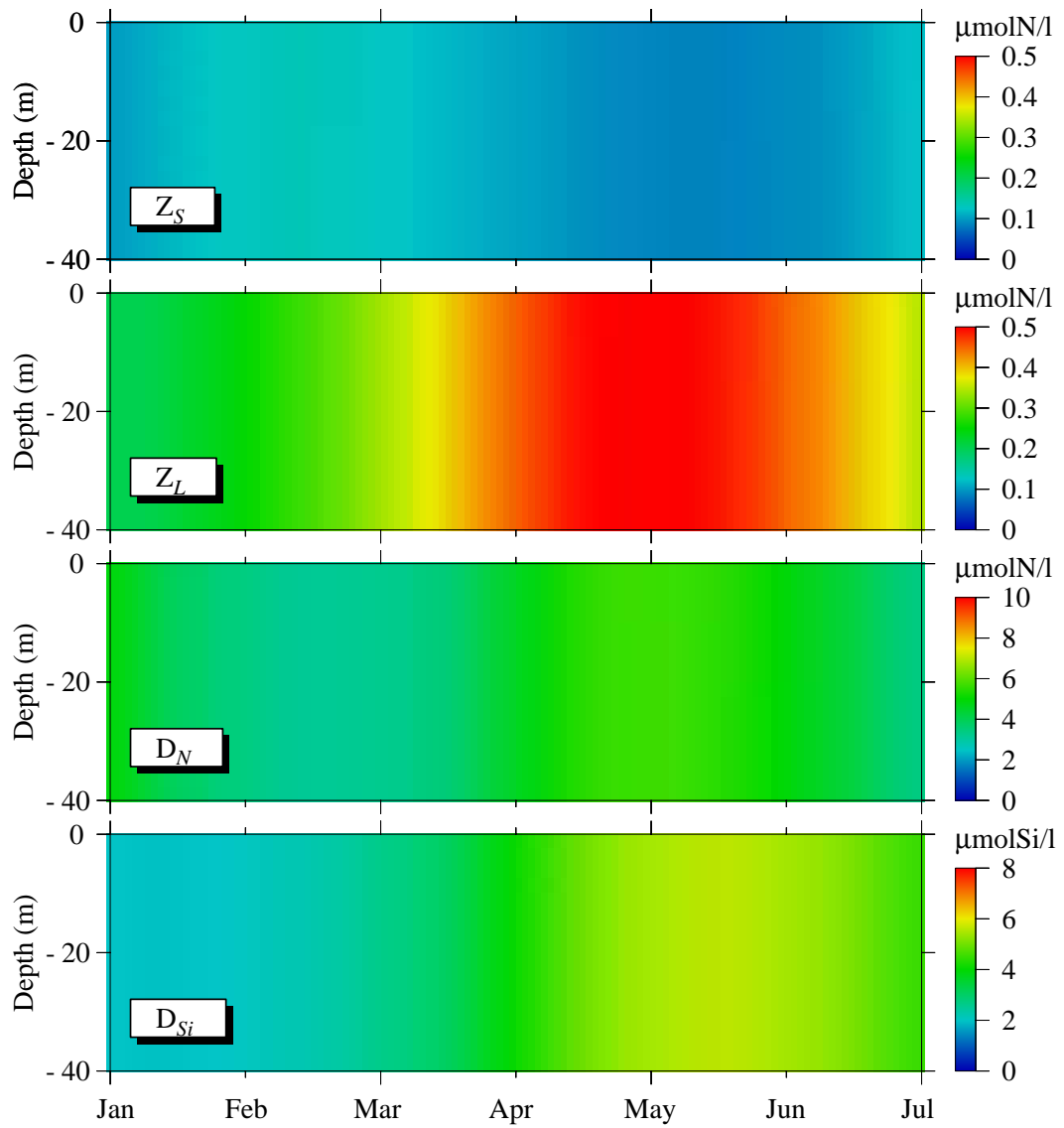


Figure 3.9: Time sequence of the vertical distribution of model-predicted small zooplankton (Z_S), large zooplankton (Z_L), detrital organic nitrogen (D_N) and detrital organic silicon (D_{Si}) in Site A from January to June.

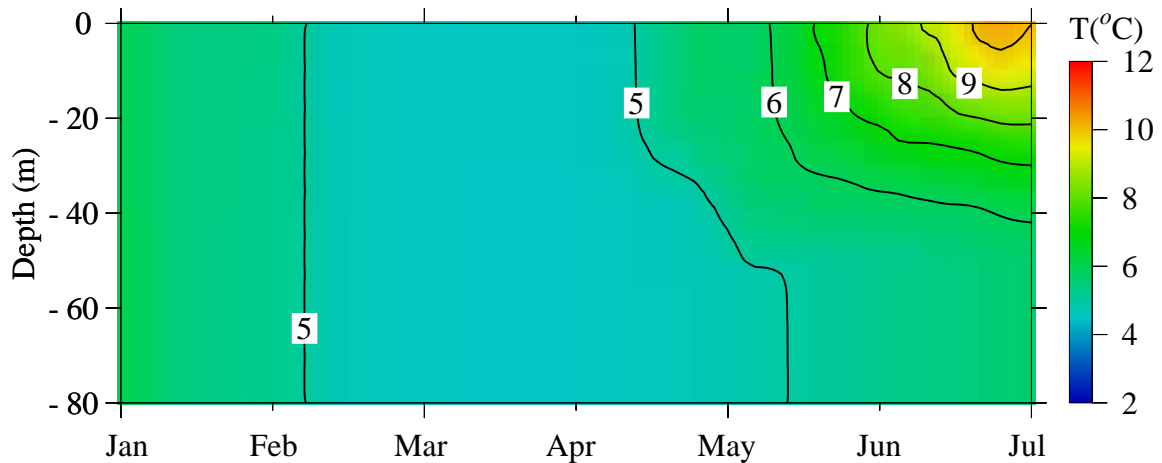


Figure 3.10: Time sequence of the vertical distribution of model-predicted temperature in Site B from January to June.

biomass reached above $5.0 \mu\text{mol N/l}$ during peak time, though the duration was very short, about 10 days. The bloom declined from the beginning of June. The biomass of large phytoplankton in the surface layer (above 20 m) during this time was less than $0.3 \mu\text{mol N/l}$, while in the subsurface (20 to 40 m deep), a weak phytoplankton band remained, probably due to the combination of two factors: sinking of diatoms and nutrient supply from deep water under the stratification layer. Small phytoplankton started to show a very weak sign of grow during the middle of May; their biomass reached ca. $1.0 \mu\text{mol N/l}$ by late June.

NUTRIENTS

Nitrate concentration remained high from January to the middle of April, then decreased from $5.0 \mu\text{mol N/l}$ to nearly undetectable in the upper water column (<40 m) in less than a week, corresponding to the significant diatom bloom in the stratified region (Figure 3.11). Ammonia concentration increased dramatically after January and remained very high ($>2 \mu\text{mol N/l}$) in the whole water column until

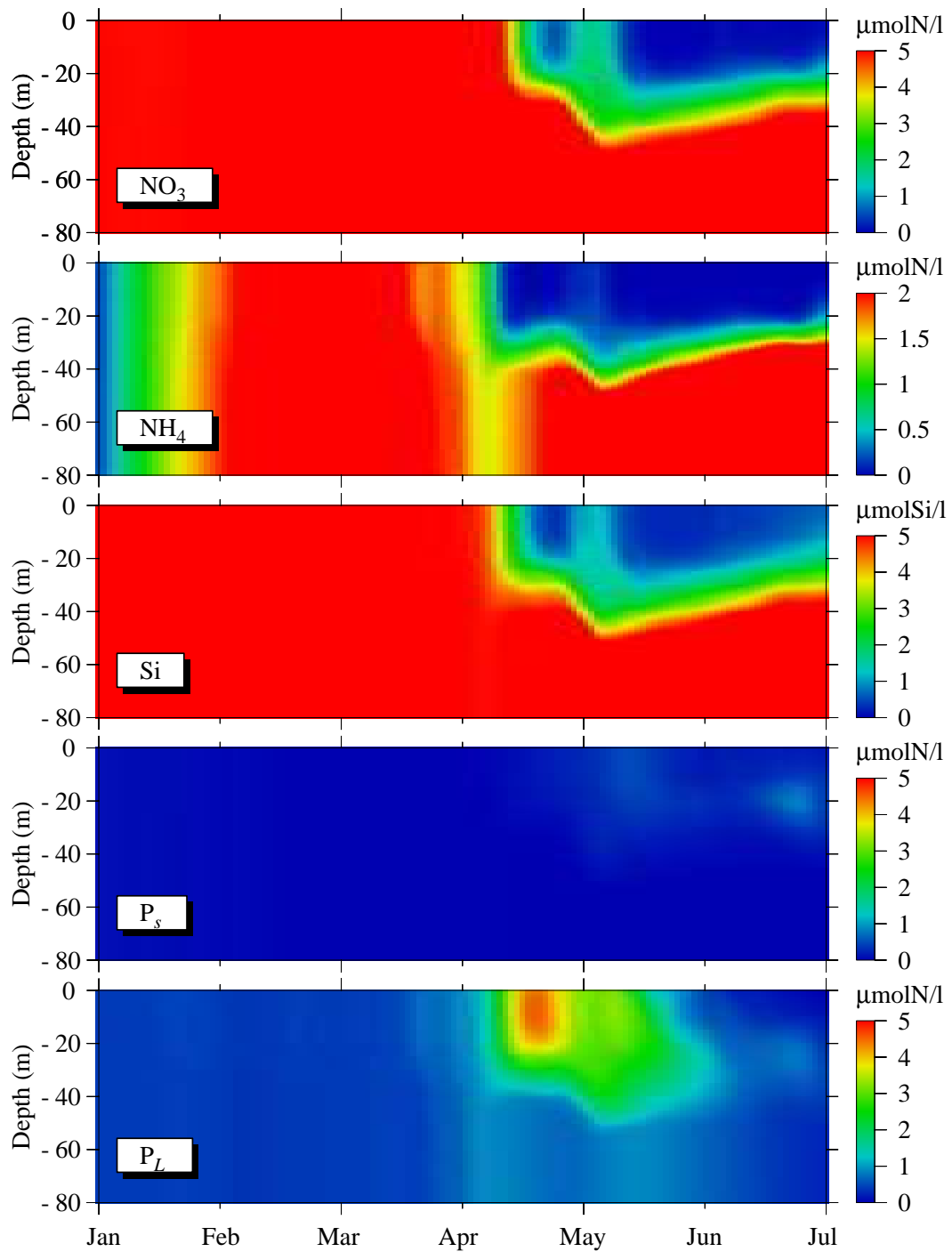


Figure 3.11: Time sequence of the vertical distribution of model-predicted nitrate (NO_3^-), ammonia (NH_4^+), silicate (Si), small phytoplankton (P_s), and large phytoplankton (P_L) in Site B from January to June.

middle April. The surface ammonia concentration decreased quickly from middle April and diminished during May and June, while deeper water (>40 m) kept a higher concentration of ammonia. The occurrence of high ammonia concentration in the model results is contradictory to the real situation where the concentration is rarely over $0.2 \mu\text{mol N/l}$ [Townsend and Thomas, 2002]. This is probably due to the lack of nitrification in this model. Concentration of silicate showed a similar pattern of spatial and temporal variation to that of nitrate and ammonia, corresponding to the diatom bloom starting from middle April.

ZOOPLANKTON

Large phytoplankton biomass increased as phytoplankton biomass increased with a time lag of about 1 month (Figure 3.12). Peak biomass occurred in May and early June with values of $0.4\text{-}0.5 \mu\text{mol N/l}$, then declined in the end of June. As observed in the well mixed site, small zooplankton were much less abundant due to grazing by large zooplankton and lower abundance of small phytoplankton prey.

PARTICULATE ORGANIC MATTER

Both particulate organic nitrogen and silica decreased from January to early April due to the decomposition process (Figure 3.12). After middle April, the stratification stimulated bloom increased the flux from inorganic matter to organic matter. A high particulate organic nitrogen and silica concentration in the lower water column was observed due to the sinking process.

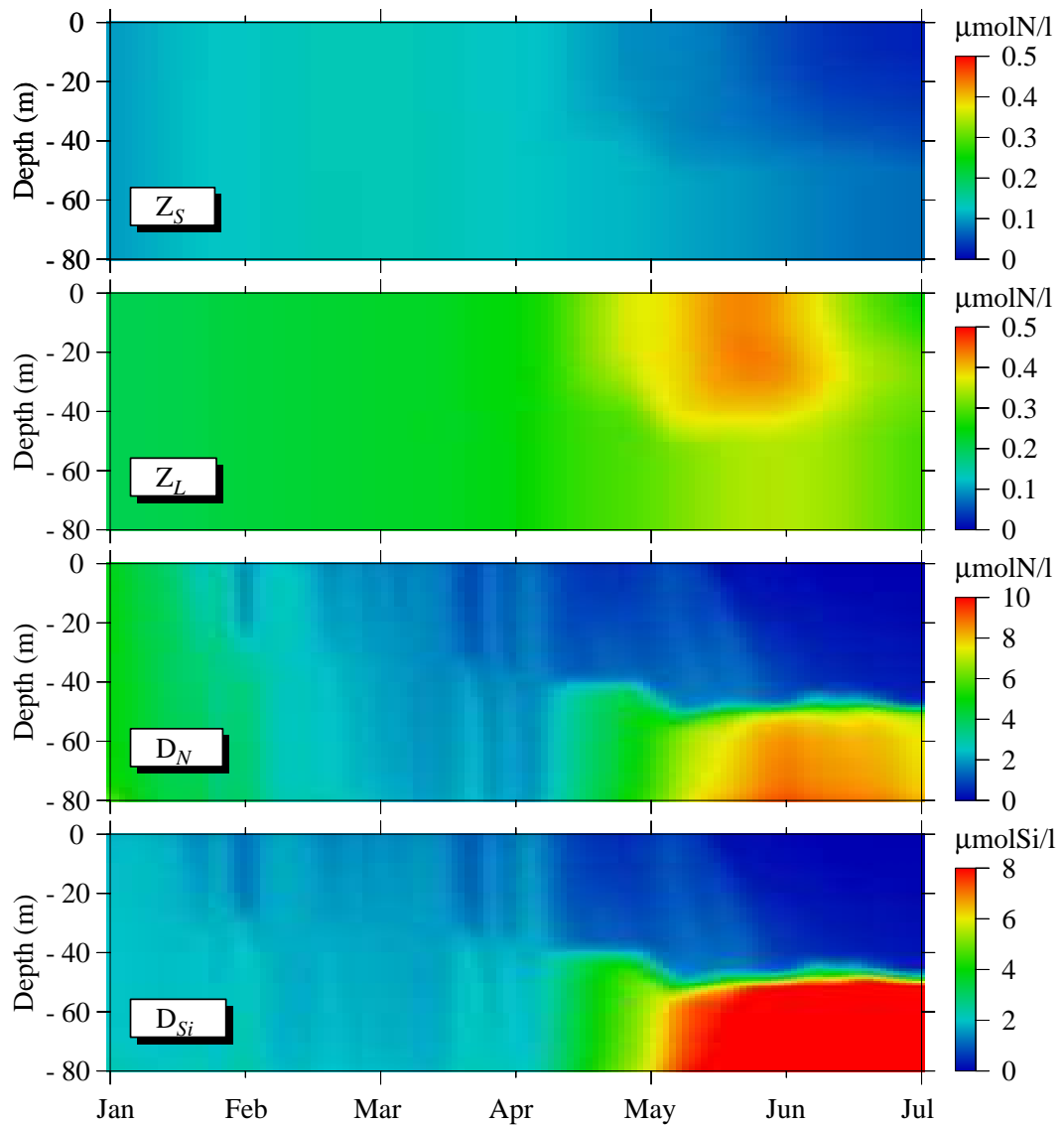


Figure 3.12: Time sequence of the vertical distribution of model-predicted small zooplankton (Z_S), large zooplankton (Z_L), detrital organic nitrogen (D_N) and detrital organic silicon (D_{Si}) in Site B from January to June.

3.6 DISCUSSION

3.6.1 GENERAL FEATURES OF MODELED SYSTEM

One of the major concerns of biological modelling is whether the model can capture the basic patterns of the system as understood from observational data. A direct comparison of the 1-D model results and the observed data is difficult for at least two reasons: first, it is difficult to find data taken with high temporal and spatial resolution; second, and perhaps more importantly, a 1-D model that does not consider advective process and uses simplified wind and tidal forcing scheme, cannot provide a realistic physical setting for the biological system. Due to these two reasons, the comparison is usually qualitative and focuses more on patterns in terms of the phase and magnitude of biological variables.

Station 12 in year 1999 can be used as an example. This station is a typical shallow mixing site, with water depth of about 41 m. A spring phytoplankton bloom in March and April with chlorophyll *a* concentration of ca. 6-7 $\mu\text{g}/\text{l}$ was observed. The model results reproduced the bloom with a good agreement of timing and magnitude (Figure 3.13 top panel). However, a relatively weaker bloom observed during June is not shown in the model results, although the recovery of silicate concentration can be found both in observation and model results (Figure 3.13 bottom panel). This second bloom was a puzzle in terms of 1-D modeling study, since nitrogen ($\text{NO}_3+\text{NO}_2+\text{NH}_4$) was very low as shown in both observation and model results (Figure 3.13 middle panel). How can the recovery of silicate alone trigger the second diatom bloom? Is this caused by advection? Is it a regular or episodic event? This should be explored in more detail with 2-D and 3-D models.

The 1-D model results are much less successful at capturing the basic pattern of spring nutrient and phytoplankton dynamics in the deeper flank area. Taking station 15, for example, unlike the observed weak spring time (in March) bloom, the model

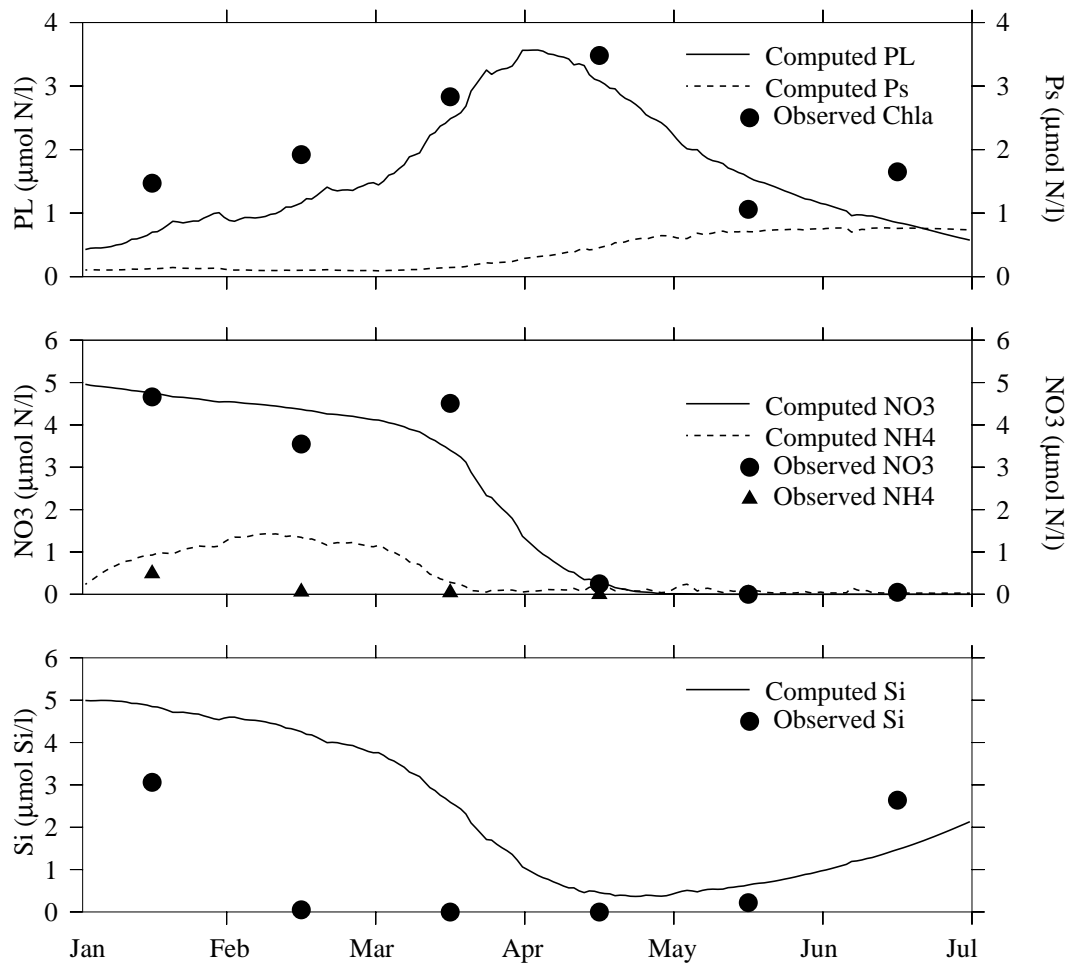


Figure 3.13: Comparisons between the model-predicted and observed depth-averaged phytoplankton (top), nitrate (NO_3) (middle), ammonia (NH_4) (middle), and silicate (Si) (bottom) in Site A from January to June.

shows a strong bloom starting from middle April that lasted for about 1 month, then declined. This bloom was even more significant than at the shallow mixing site, but with about a 1-month time lag (Figure 3.14, top panel). The timing of this significant bloom corresponds to the formation of weak stratification in middle April. This bloom is not observed in stations along the flank area during 1997, 1998 and 1999 (Figure 3.2). On the other hand, the model does not capture the weak bloom that was observed during March, with chlorophyll *a* concentration reaching over 3 $\mu\text{g}/\text{l}$. Also, the depletion of silicate during March shown by observational data is almost one month earlier than the model results (Figure 3.14 bottom panel). These significant differences between model results and observed data indicate that advective or other processes may play a much more significant role in the springtime phytoplankton bloom, which is not a surprise in the flank area of the bank due to the short residence time, clockwise recirculation, Scotian Shelf Water “cross over” and Slope Water intrusion. 3-D modeling study is required to explore the possible mechanisms of these dynamics.

3.6.2 EFFECTS OF LIGHT ON SPRING BLOOM

The spring diatom bloom is usually a consequence of increasing light intensity and nutrient supply during the spring. Assuming the initial nutrient concentration is sufficient due to supply from deeper water induced by winter mixing processes, the light environment becomes critical to the timing of the spring bloom. Three light related issues are considered here, the temporal variation of light intensity, the light attenuation coefficient, and the photosynthesis-light intensity relationship on GB during spring time.

The underwater light environment for phytoplankton is largely controlled by incoming short wave radiation from the sun and the downward light attenuation coefficient. Photosynthetically active radiation (PAR) with wave lengths of 400 - 700

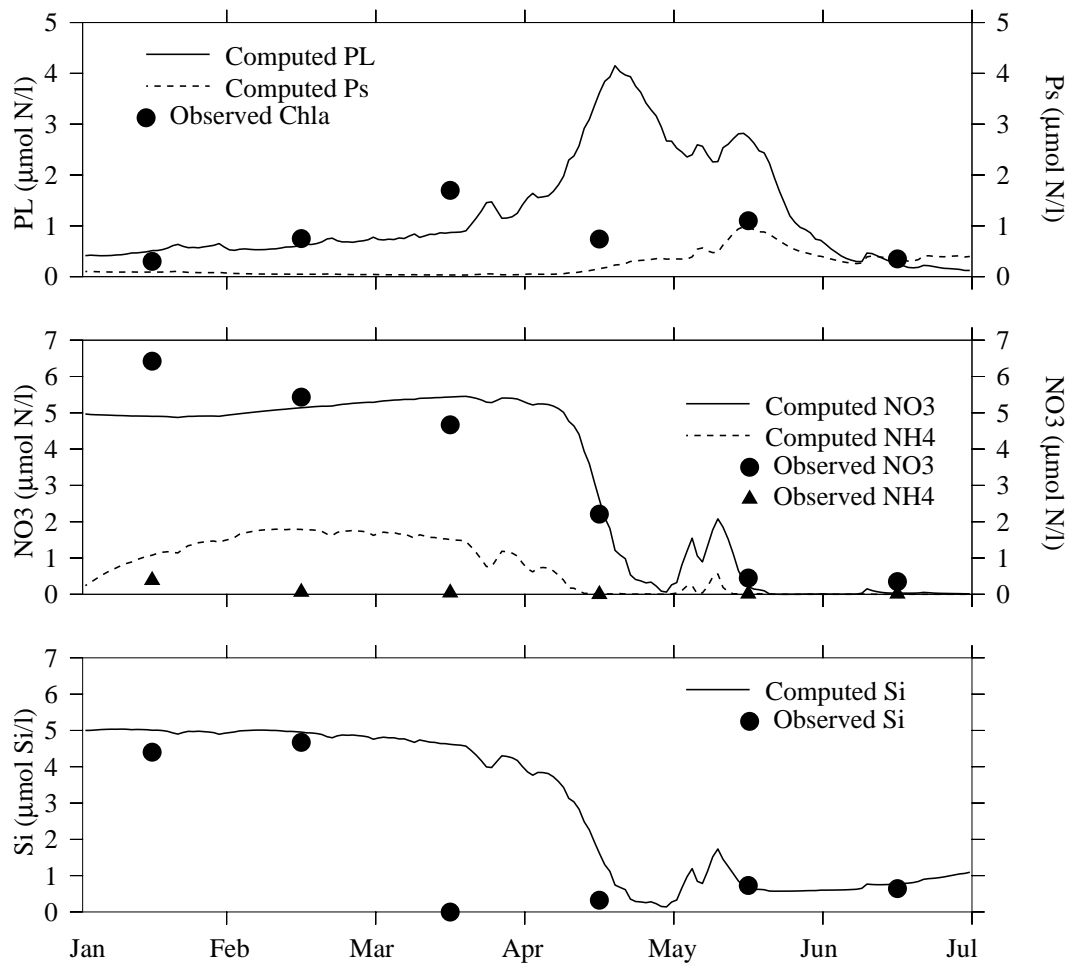


Figure 3.14: Comparisons between the model-predicted and observed depth-averaged phytoplankton (top), nitrate (NO_3) (middle), ammonia (NH_4) (middle), and silicate (Si) (bottom) in Site B from January to June.

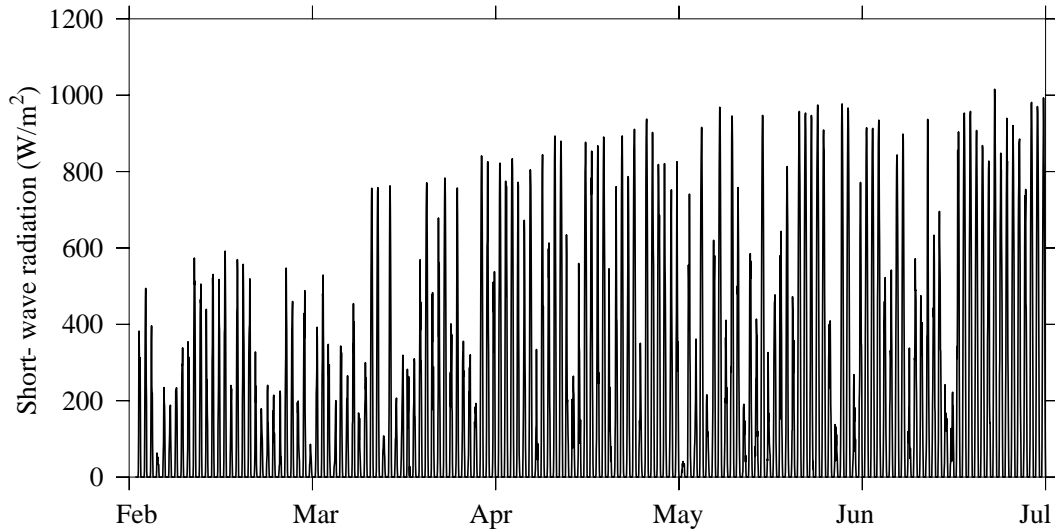


Figure 3.15: Time series of short-wave radiation from February 1 to June 30, 1995.

nm is a major component of short wave radiation (wave length 100 - 700 nm). Figure 3.15 shows the variation of short wave radiation from February to June 1995. The maximum radiation strength increased from ca. 400 W/m^2 in February to ca. 1000 W/m^2 in June. Also, the duration of day-light increased from ca. 10 hr in February to 14 hr in June, indicating an increasing duration of photosynthesis through the time period modeled.

Once light gets into the water column, its intensity is affected by water depth and the light attenuation coefficient (K_{ext}). K_{ext} is the rate at which light is attenuated as a result of all absorbing and scattering components of the water column. These components include a background rate (0.1 m^{-1} in clear water), and varying components of total suspended solids, phytoplankton, dissolved organic matter and colored dissolved organic matter. A higher value is usually observed on the shallow parts of the bank during winter and early spring due to the high suspended sediment concentration, caused by strong wind-induced mixing. The climatological wind data

summarized by *Manning and Strout* [2001] showed clearly the difference in wind stress between winter and spring time. Our analysis of wind data by calculating days with wind speed $>10\text{m/s}$ for each month support this conclusion (Figure 3.16). Figure 3.17 shows that if the water is clear enough, with low K_{ext} (0.1 m^{-1}) during the entire model run time (Run A2), the spring bloom occurs in late February, which is about two months earlier than the high K_{ext} case (0.15 m^{-1} during the whole modeling time). Considering the temporal variation of K_{ext} on the bank, a higher K_{ext} (0.15 m^{-1}) is applied for January to February, a middle value (0.12 m^{-1}) for March, and a lower K_{ext} (0.1 m^{-1}) for April to June. Such a parameterization is used in the standard model run. The peak of the bloom occurs in the end of April which seems to match the general pattern of timing of the spring bloom on the central portion of the bank better than both constant K_{ext} cases.

The above test on K_{ext} is based on the photosynthesis-light intensity relationship from *Eilers and Peeters* [1988]. Compared with other P-I relationship models, we can see that model from *Steele* [1962] shows an earlier bloom in the beginning of March and quickly declines afterwards; while the model from *Jassby and Platt* [1976] shows a result similar to the *Eilers and Peeters* [1988] model, with a slight time lag (Figure 3.18).

In summation, the modeling results indicate that the light environment is an important factor in determining the timing of the spring bloom. The selection of light related parameters and P-I relationships have a significant impact on the model output.

3.6.3 EFFECT OF NUTRIENTS ON SPRING BLOOM

The model results from the standard model run indicate that silicate is depleted almost at the same time as nitrate. This pattern is different from observation where silicate was believed to be a limiting nutrient for phytoplankton as early as February.

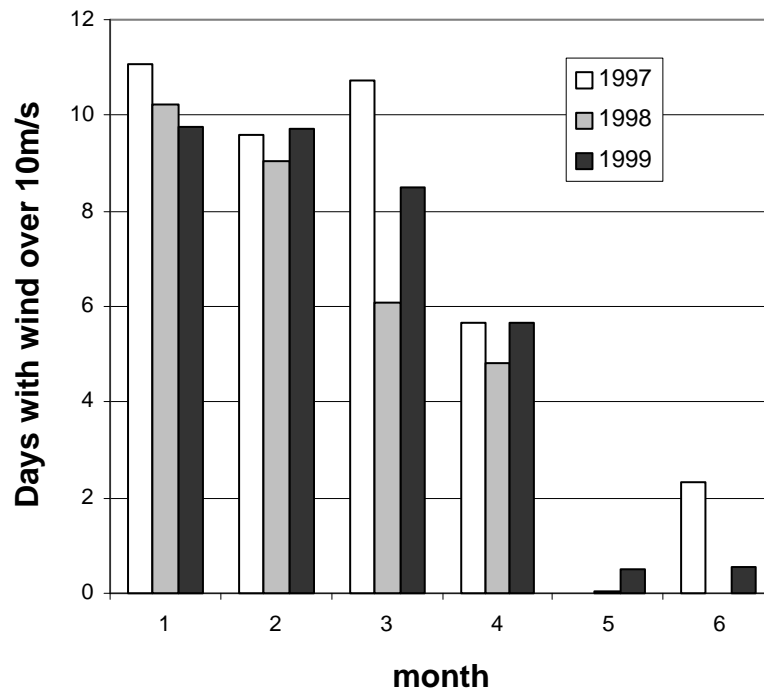


Figure 3.16: Comparison of days with wind speed over 10 m/s for each month in 1997, 1998 and 1999.

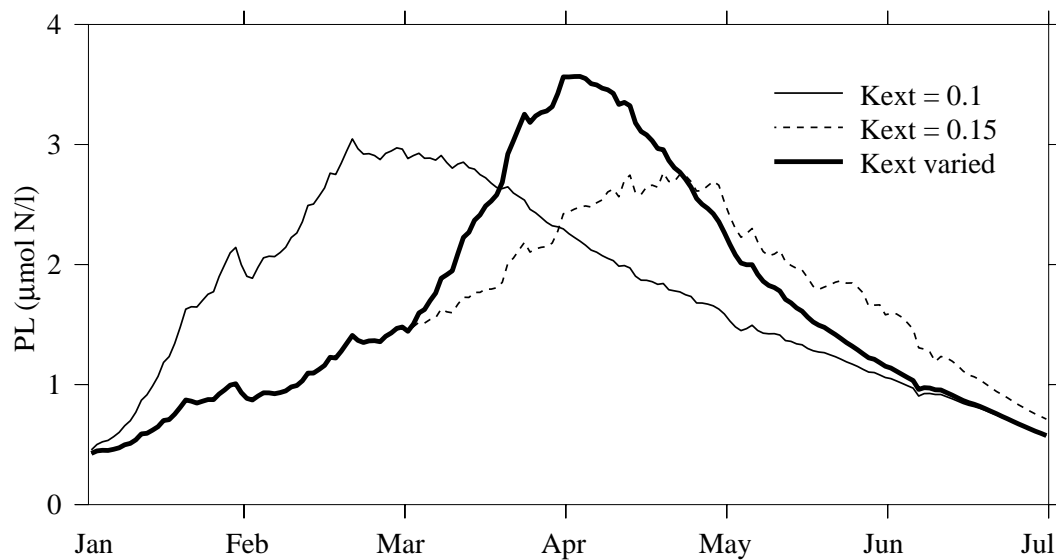


Figure 3.17: Effects of light attenuation coefficient (K_{ext}) on the seasonal variation of large phytoplankton (PL). The case labeled with “ K_{ext} varied” means K_{ext} is $0.15 m^{-1}$ for January, February and March, $0.12 m^{-1}$ for April, and $0.10 m^{-1}$ for May and June.

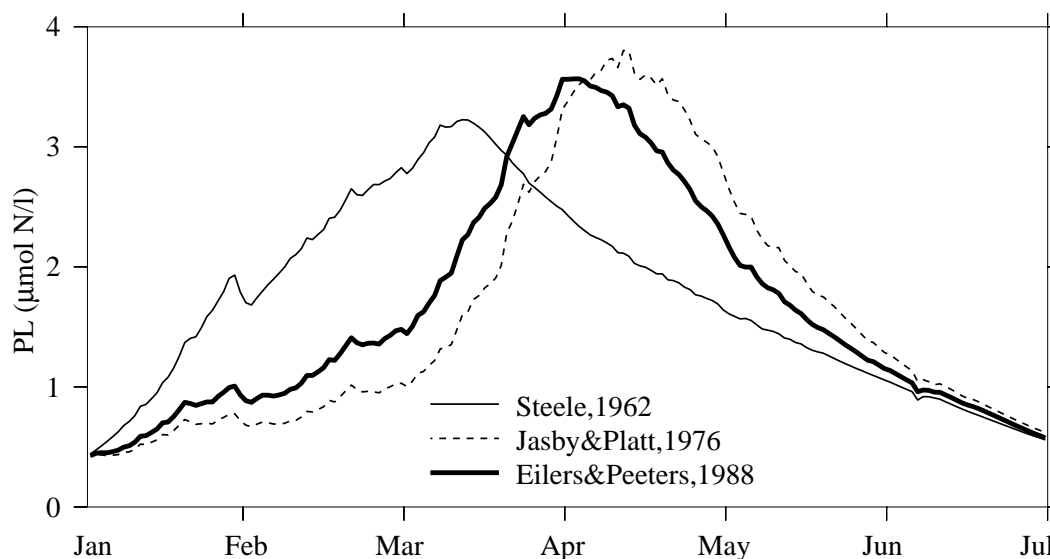


Figure 3.18: Effects of different P-I functions on the seasonal variation of large phytoplankton (PL).

Assuming the half saturation constant for large phytoplankton uptake of silicate is same through the whole modeling period, the spring diatom bloom is less significant if we set the initial silicate concentration to $2.0 \mu\text{mol Si/l}$ at the beginning of January (Figure 3.19). The biomass of the large phytoplankton group increased from $0.5 \mu\text{mol N/l}$ in January to $1.4 \mu\text{mol N/l}$ in April at low initial silicate concentrations. Although the peak time is similar to the case of high initial silicate concentration ($5.0 \mu\text{mol Si/l}$), the magnitude of the bloom is about 2 times lower, indicating a strong limitation from silicate.

By adjusting the N/Si ratio of large phytoplankton, the scenario of synchronized depletion of nitrate and silicate as shown in Figure 3.20 can be varied. If the N/Si ratio decreases to 0.8, meaning more silicate is needed when an equal amount of nitrogen is taken up, silicate is depleted much earlier than in the high N/Si ratio case (Figure 3.21). It is not surprising to see that a spring bloom is less likely to occur

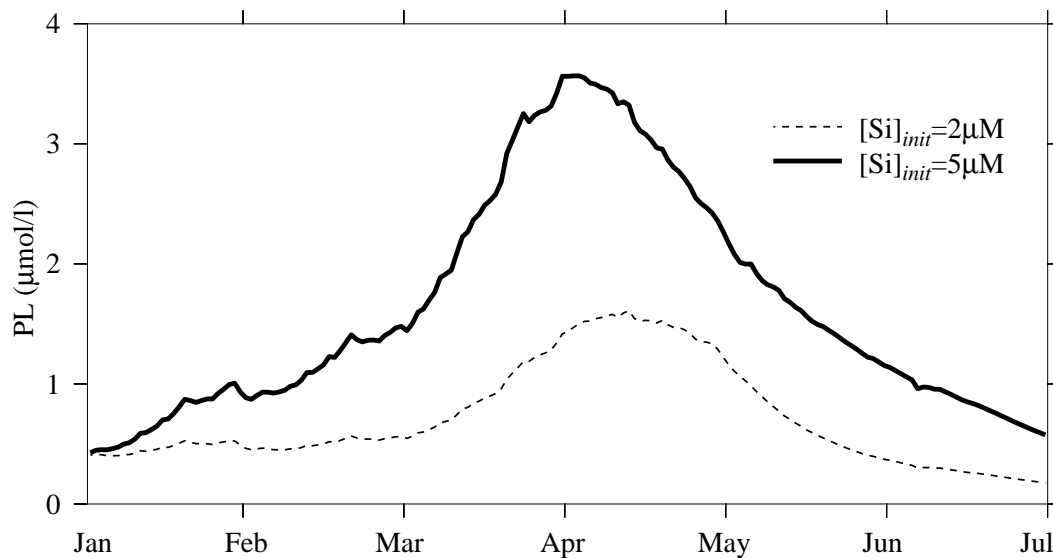


Figure 3.19: Effects of silicate initial concentration ($[\text{Si}]_{init}$) on the seasonal variation of large phytoplankton (PL).

in this situation with a fixed half saturation concentration due to the early limitation of silicate. The sensitivity analysis of the biological parameters (See Appendix B) indicates that the N/Si ratio is the most sensitive biological parameter in terms of the timing and magnitude of diatom blooms.

The failure of this model to reproduce significant spring blooms and early silicate depletion suggests that the silicate uptake and assimilation is more complex than this model represents. It is necessary to be aware of the different roles of nitrogen and silica within the cell. Nitrogen is a functional nutrient, a necessary constituent of amino acids and proteins that mediate photosynthesis and cell growth. The growth rate will decrease under conditions of stress. In contrast, silica can be considered as a structural nutrient since it is primarily required by the diatom to synthesize its frustules. Metabolically active silica pools constitute only a few percent of total cell silica [Werner, 1977]. When silica availability is limited, cells may sacrifice some

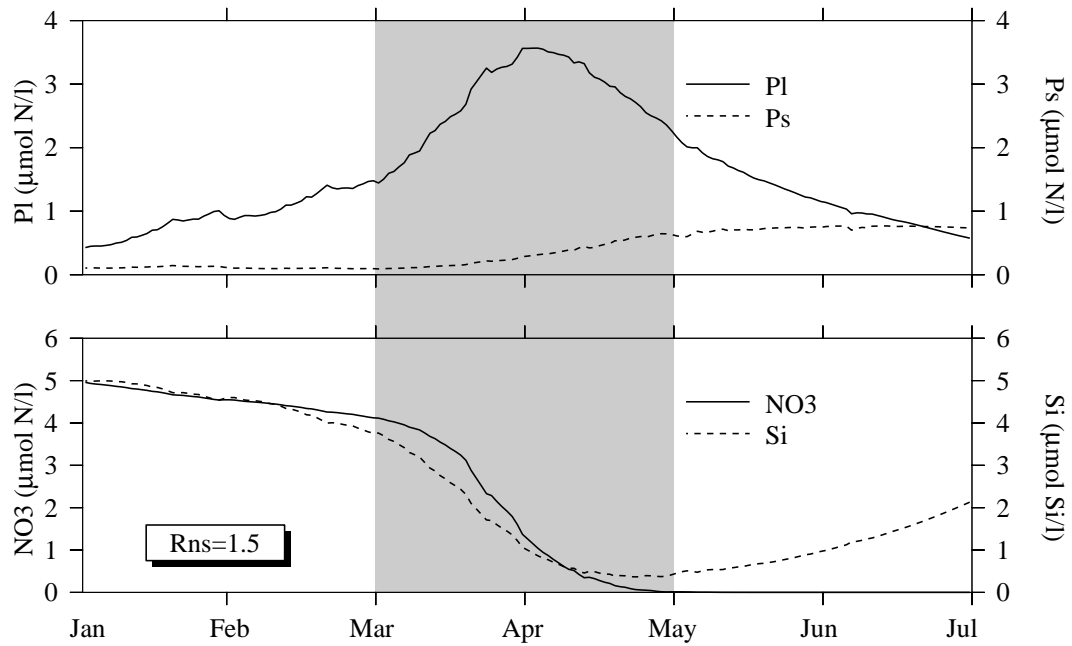


Figure 3.20: Seasonal variation of large phytoplankton (Pl) and small phytoplankton (Ps) (top) when ratio of nitrogen and silicon (Rns) in large phytoplankton is 1.5. Bottom shows a synchronized depletion of nitrate (NO_3) and silicate (Si) during later March.

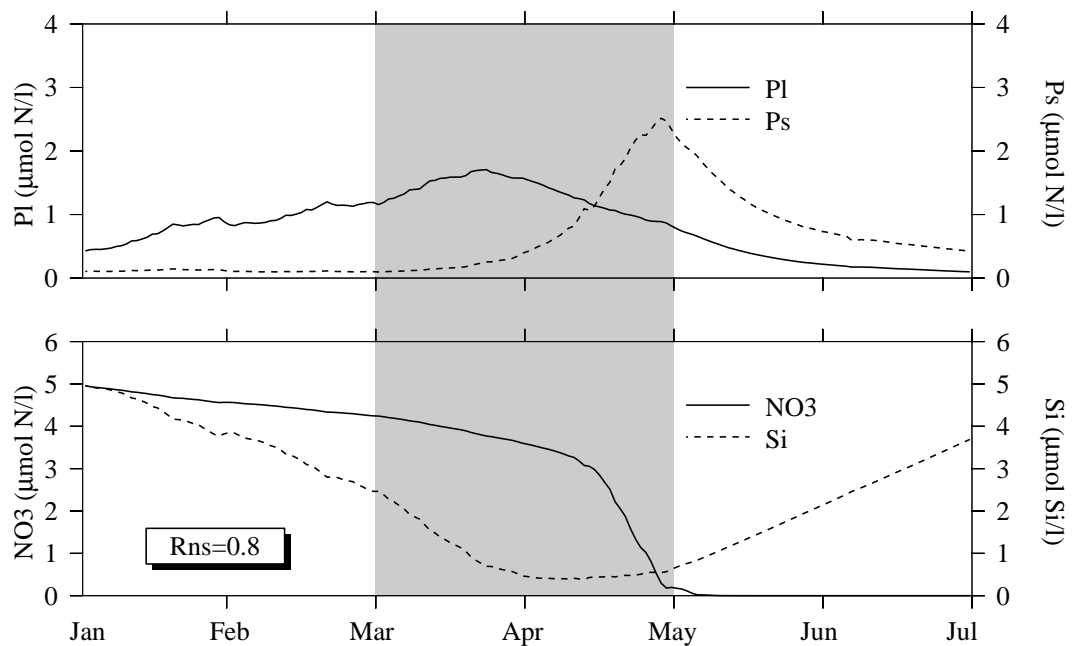


Figure 3.21: Seasonal variation of large phytoplankton (Pl) and small phytoplankton (Ps) (top) when ratio of nitrogen and silicon (Rns) in large phytoplankton is 0.8. Bottom shows an asynchronized depletion of nitrate (NO_3) and silicate (Si), with silicate being depleted about 1 month earlier than nitrate.

structural (cell wall) silica to meet metabolic needs [*Paasch, 1973*]. To some extent, nitrogen uptake by large phytoplankton may be unaffected by silicate availability within the cell [*Davidson and Gurney, 1999*]. These observations suggest that the N/Si ratio and half saturation constants in diatom are not constant, a fact that greatly compromises the modeling efforts. To simplify the model, a high constant N/Si ratio was used in order to obtain a better simulation of the spring bloom. As a result, the silica did not show depletion during February in this model.

Both the model and observations showed a constant low concentration of ammonia on the shallow area of the bank. “Early blooms” of large phytoplankton are less likely impacted by the ammonia availability since the nitrogen supply is sufficient before the bloom occurs. Increasing the decomposition rate of detritus nitrogen can increase the ammonia concentration between January to March (Figure 3.22, bottom panel), but does not change the diatom blooming process (Figure 3.22 middle panel). Concentration of ammonia almost doubled before the phytoplankton bloom due to the increased decomposition rate (Figure 3.22 bottom panel). During the post-bloom period, increase of ammonia regeneration stimulates the growth of small phytoplankton, and causes a bloom during May. In other words, the regeneration of nitrogen is more important to small phytoplankton than to large phytoplankton, especially during late spring.

3.6.4 ABOUT THE SECOND DIATOM BLOOM

The 1-D model failed to reproduce the second diatom bloom, which was observed in both the 1998 and 1999 surveys. With the recovery of silicate concentration, if recycled nitrogen is the only nitrogen source for phytoplankton, is that enough to support a diatom bloom without a net incoming nitrogen flux? Model results have suggested that ammonia as the nitrogen source of second diatom bloom is very weak,

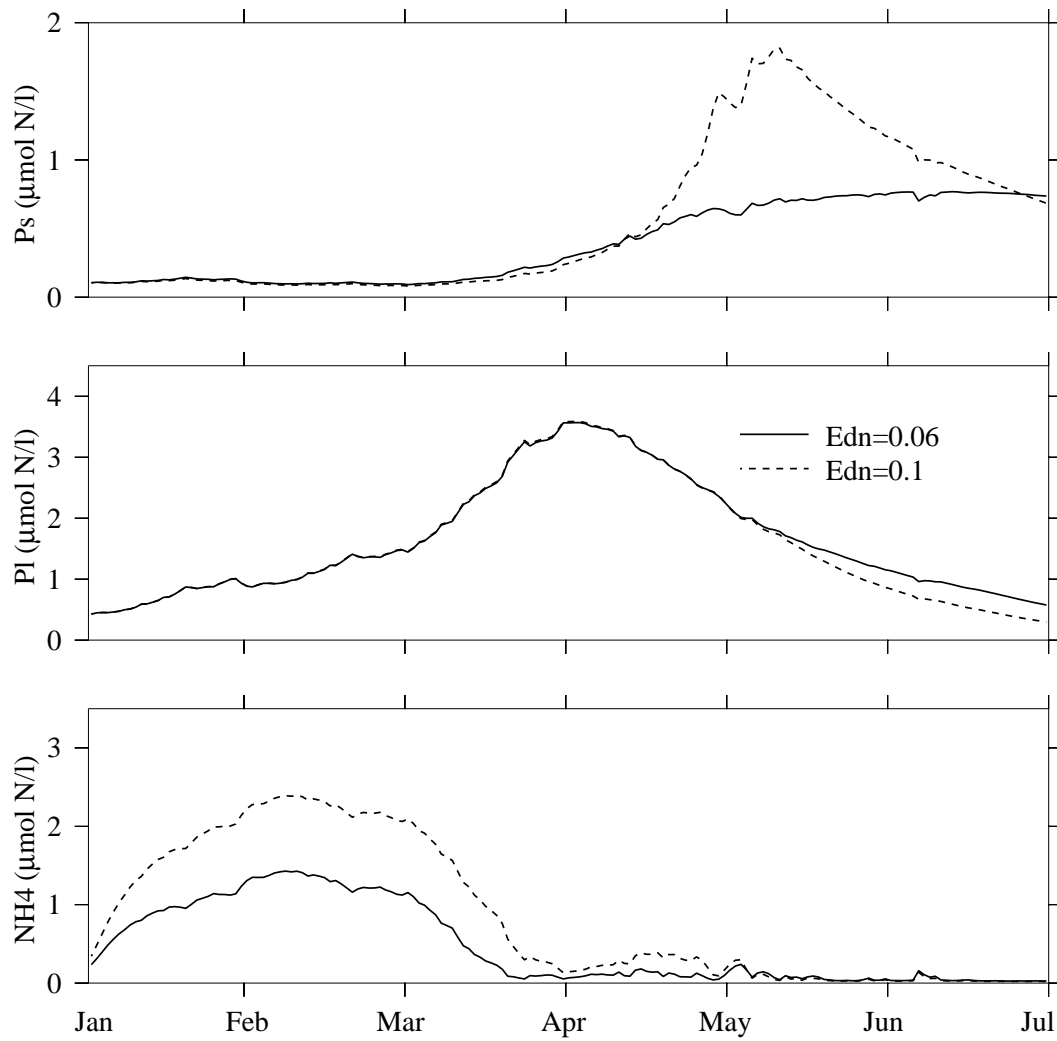


Figure 3.22: Effects of decomposition rate (E_{dn}) of detrital organic nitrogen on the seasonal variation of small phytoplankton (Ps) (top), large phytoplankton (Pl) (middle), and ammonia (NH_4) (bottom). The dashed line represents the case with E_{dn} of 0.1 and solid line with E_{dn} of 0.06.

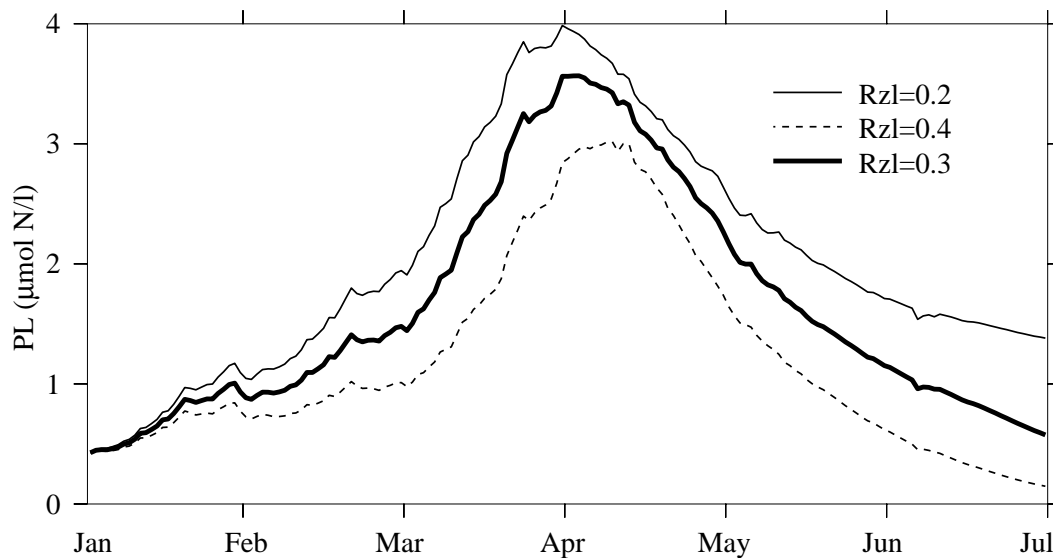


Figure 3.23: Effects of maximum grazing rate of large zooplankton on large phytoplankton (Rzl) on the seasonal variation of large phytoplankton (PL).

especially when the small phytoplankton are competing for the same nutrient with a lower half saturation constant.

As an alternative explanation, variation of zooplankton grazing pressure is tested in this model. The result (Figure 3.23) shows that the timing of bloom is insensitive to changes in grazing rate Rzl. Also, the second bloom does not occur when large zooplankton grazing rate is decreased, suggesting that top-down control is probably not a factor in the shallow mixed region.

Overall, the failure of the 1-D model to reproduce the second diatom bloom suggests that this may not be a local event. Advection of nutrients and phytoplankton from surrounding waters could play an important role. A model with a higher dimension may be necessary in order to obtain a better understanding of phytoplankton blooming dynamics on GB.

3.6.5 WHAT IS MISSING IN THE 1-D MODEL

In a system like GB with strong horizontal gradients, the average residence time is less than 2 months in the flanks and longer on the crest of the bank. The 1-D model is probably not ideal for long-term modeling. However, for the system in a well-mixed region, which is relatively homogenous and self-contained, the 1-D model can at least capture the basic pattern of the dynamics of the spring bloom as we can see from the modeling results. In the deeper flank area, the ability of the model to achieve an acceptable 6-month simulation is very weak, but the model still allow us to explore the impact of stratification and sinking to the dynamics of the spring bloom.

Overall, the purpose of the 1-D model on GB is to test the system behavior of the food web itself, capture the very basic seasonal pattern without advection process and identify the unresolved issues for further modeling.

3.7 SUMMARY

A one-dimensional coupled biological-physical model was tested based on observed features of lower trophic food web dynamics on GB. The biological and physical factors controlling the timing and magnitude of the spring bloom were examined using 1-D modeling experiments driven by observed meteorological forcings.

In the shallow and well-mixed central Bank, the timing of the spring bloom is mainly controlled by the light environment (including light intensity and light attenuation coefficient), while the magnitude is regulated by light, nutrient supply and zooplankton grazing pressure. In the relatively deeper flank area, the seasonally developed stratification processes mainly controls the timing of the spring bloom.

Both nitrogen and silicon could be limiting nutrients for diatom growth. Silicon may become limiting for diatom growth earlier than nitrogen. The contradiction

between early depletion of silicate and months-long diatom blooms indicates the complex role of silicon in diatom growth. A constant N/Si ratio and half saturation constant of silicate uptake is probably an over-simplification.

The model failed to capture the relatively weak “second” bloom in early summer, indicating that this may not be a local event. Advection of nutrients and phytoplankton from surrounding waters could play an important role. A model with a higher dimension is necessary in order to obtain a better understanding of phytoplankton bloom dynamics on GB.

3.8 REFERENCES

- Backus, R. H., and D. W. Bourne (Eds.), *Georges Bank*, 632 pp., MIT Press, Cambridge, Massachusetts, 1987.
- Beardsley, R. C., S. J. Lentz, R. A. Weller, R. Limeburner, J. D. Irish, and J. B. Edson, Surface forcing on the southern flank of Georges Bank, February-August 1995, *Journal of Geophysical Research*, p. In press, 2003.
- Brzezinski, M. A., The silicon:carbon:nitrogen ratio of marine diatoms: interspecific variability and the effect of some environmental variables, *Journal of Phycology*, 1985.
- Chen, C., and R. Beardsley, Tidal mixing and cross-frontal particle exchange over a finite amplitude asymmetric bank: A model study with application to Georges Bank, *Journal of Marine Research*, 56, 1163–1201, 1998.
- Chen, C., R. Ji, D. J. Schwab, D. Beletsky, G. L. Fahnenstiel, M. Jiang, T. H. Johengen, H. Vanderploeg, B. Eadie, J. W. Budd, M. H. Bundy, W. Gardner, J. Cotner, and P. J. Lavrentyev, A model study of the coupled biological and physical dynamics in Lake Michigan, *Ecological Modelling*, 152, 145–168, 2002.

- Chen, C., R. Beardsley, P. J. S. Franks, and J. V. Keuren, Influences of diurnal varying heat flux on circulation and stratification over Georges Bank: a 3-D prognostic model experiment, *Journal of Geophysical Research*, In press, 2003.
- Cura, J. J., Phytoplankton, in *Georges Bank*, edited by R. H. Backus and D. W. Bourne, pp. 213–218, MIT Press, Cambridge, Massachusetts, 1987.
- Davidson, K., and W. S. C. Gurney, An investigation of non-steady-state algal growth. II. Mathematical modeling of co-nutrient-limited algal growth, *Journal of Plankton Research*, *21*(5), 839–858, 1999.
- Dugdale, R. C., and J. J. Goering, Uptake of new and regenerated forms of nitrogen in primary productivity, *Limnology and Oceanography*, *12*, 196–206, 1967.
- Eilers, P. H. C., and J. C. H. Peeters, A model for the relationship between light intensity and the rate of photosynthesis in phytoplankton, *Ecological Modelling*, *42*, 199–215, 1988.
- Eppley, R. W., and B. J. Peterson, Particulate organic matter flux and planktonic new production in the deep ocean, *Nature*, *282*, 677–680, 1979.
- Franks, P. J. S., and C. Chen, Plankton production in tidal fronts: A model of Georges Bank in summer, *Journal of Marine Research*, *54*, 631–651, 1996.
- Franks, P. J. S., and C. Chen, A 3-d prognostic numerical model study of the Georges Bank ecosystem. Part II: biological-physical model, *Deep Sea Research II*, *48*, 457–482, 2001.
- Houghton, R. W., Diapycnal flow through a tidal front: a dye tracer study on Georges Bank, *Journal of Marine Systems*, *37*, 31–46, 2002.

- Jassby, A. D., and T. Platt, Mathematical formulation of the relationship between photosynthesis and light for phytoplankton, *Limnology and Oceanography*, *21*(4), 540–547, 1976.
- Klein, P., A simulation of some physical and biological interactions, in *Georges Bank*, edited by R. H. Backus and D. W. Bourne, pp. 395–402, MIT Press, Cambridge, Massachusetts, 1987.
- Lewis, C. V., C. S. Davis, and G. Gawarkiewicz, Wind-forced biological-physical interactions on an isolated off-shore bank, *Deep Sea Research II*, *41*, 51–73, 1994.
- Loder, J. W., and T. Platt, Physical controls on phytoplankton production at tidal fronts, in *Proceedings of the Nineteenth European Marine Biology Symposium*, edited by P. E. Gibbs, pp. 3–21, Cambridge University Press, 1985.
- Manning, J., and G. Strout, Georges Bank winds: 1975-1997, *Deep Sea Research II*, *48*(1-3), 115–135, 2001.
- Mellor, G. L., and T. Yamada, Development of a turbulence closure model for geophysical fluid problems, *Reviews of Geophysics and Space Physics*, *20*, 851–875, 1982.
- O'Reilly, J. E., C. E. Evans-Zetlin, and D. A. Busch, Primary production, in *Georges Bank*, edited by R. H. Backus and D. W. Bourne, pp. 220–233, MIT Press, Cambridge, Massachusetts, 1987.
- Paasch, E., Silicon and the ecology of marine plankton diatoms. II. Silicate uptake kinetics in five diatoms species, *Marine Biology*, *19*, 262–269, 1973.
- Pastuszak, M., W. R. Wright, and D. Patanjo, One year of nutrient distribution in the Georges Bank region in relation to hydrography, *Journal of Marine Research*, *14*, 525–542, 1982.

- Steele, J. H., Environmental control of photosynthesis in the sea, *Limnology and Oceanography*, 7, 137–150, 1962.
- Townsend, D. W., and N. R. Pettigrew, Nitrogen limitation of secondary production on Georges Bank, *Journal of Plankton Research*, 19(2), 221–235, 1997.
- Townsend, D. W., and A. C. Thomas, Winter-spring transition of phytoplankton chlorophyll and inorganic nutrients on Georges Bank, *Deep Sea Research II*, 48, 199–214, 2001.
- Townsend, D. W., and M. Thomas, Springtime nutrient and phytoplankton dynamics on Georges Bank, *Marine Ecology Progress Series*, 228, 57–74, 2002.
- Walsh, J. J., T. E. Whitledge, J. E. O'Reilly, W. C. Phoel, and A. F. Draxler, Nitrogen cycling on Georges Bank and the New York shelf: a comparison between well-mixed and seasonally stratified waters, in *Georges Bank*, edited by R. H. Backus and D. W. Bourne, pp. 234–246, MIT Press, Cambridge, Massachusetts, 1987.
- Werner, D., *The Biology of Diatoms*, 498 pp., University of California Press, California, 1977.

CHAPTER 4

EFFECTS OF STRATIFICATION AND FRONTAL SYSTEM ON SPRING BLOOM: 2-D MODEL EXPERIMENTS¹

¹R. Ji. Will be submitted to *Journal of Geophysical Research*. 2003.12.

4.1 ABSTRACT

The two-dimensional (2-D) coupled biological-physical model experiments were conducted in a transect across the southern Georges Bank (GB). The biological model is identical to the model used in the one-dimensional (1-D) model experiments. The temporal variation and sectional distribution of biological variables were examined. The biological and physical factors controlling the timing and magnitude of spring bloom were also explored. The model results showed a similar control mechanism for spring bloom dynamics in the central bank and the deep flank area as in the 1-D model experiments, except for the area between shallow and deep region. In this area, a phytoplankton maximum was observed in the model due to light availability and continuous nutrient support from the nutrient rich off-bank water through the tidal mixing process before the stratification develops. Once the tidal mixing front is established, a “second” bloom occurred as a result of the up-front nutrient flux driven by the secondary flow. The development of spring blooms in the deep flank area is sensitive to the development of stratification, especially during the transition time between vertical mixing and stratification, which usually occurs in later April or early May.

4.2 INTRODUCTION

The one-dimensional (1-D) modeling experiments conducted in Chapter 3 show basic patterns of the seasonal dynamics of nutrients and phytoplankton in both shallow and deeper sites. It suggests that in the well-mixed shallow site, changing of light environment (light intensity and light attenuation coefficient) is critical for the timing of spring bloom. Silicon may be limit on phytoplankton growth prior to nitrogen. The initial concentration and recycling of nutrients play important roles in controlling the magnitude of spring bloom. In the deep site, however, the stratification process

is the most important factor regarding the control of timing and magnitude of spring bloom. 1-D model experiments also suggest that the water in the shallow areas is more self-contained since the seasonal dynamics of biological system could be better reproduced in 1-D domain, while for the deep site the model failed to capture the basic pattern due to the significance of advective processes in the deeper flank area of Georges Bank (GB).

The 1-D model is not capable of examining the interaction between the shallow well-mixed central bank and the deep flank area, nor can it describe the cross-sectional distribution of biological variables. The dynamics in a two-dimensional domain is complex as shown in a schematic view of the interaction between biological and physical factors along the cross-bank section (Figure 4.1). For the “before stratification” case (Figure 4.1 upper panel) during winter and early spring, tidal mixing, cooling and strong wind induced mixing make the entire GB very well mixed. The critical depth for phytoplankton growth is expected to be relatively shallow due to the increase of light attenuation coefficient. In the shallower part of the bank, the critical depth is slightly shallower or similar to the vertical mixing depth, while in the deep area, the vertical mixing depth is much greater than the critical depth. Consequently, a bloom of phytoplankton can occur more easily in the shallower region [Sverdrup, 1953]. Correspondingly, the concentration of nutrients would decrease due to uptake of phytoplankton. On the other hand, in the deep region, the dilution caused by mixing processes decreases the overall growth in the whole water column. As a result, a quick increase of phytoplankton biomass is unlikely to happen in this case. Without considering the lateral advection, the concentration of nutrients can be maintained or even increased due to the recycling process. These two “extreme” situations should mirror the site A and B in the 1-D modeling experiments. The area in between, however, is unique regarding the critical depth/mixing depth ratio

(Rcm) and nutrients support, which in turn will affect the variation of phytoplankton growth.

The seasonally developed stratification would make the situation even more complex (Figure 4.1 lower panel) as summarized by *Mann and Lazier* [1996]. In the shallow area, the nutrient limitation of phytoplankton growth would be significant due to the depletion of nutrients by a continuous uptake of phytoplankton. In the deep area, stratification would make the surface mixing layer shallower than the critical depth, allowing a positive growth of phytoplankton and associated depletion of nutrients. The water below the stratification layer, however, should maintain a high nutrient concentration. Near the tidal mixing front, strong tidal mixing can result in a greater up-front flux of nutrients at the stratified side, and fuel the growth of phytoplankton in that region.

Physical forcings like heat flux and wind can have significant impacts on the stratification process and cross-frontal exchange of both nutrients and phytoplankton on GB [*Chen and Beardsley*, 2002; *Chen et al.*, 2003b,a]. During the transition time between mixing and stratification, usually in later April and/or early May on GB, the stratification is very weak and unstable. Without considering the external water advected into the system, a change in heat flux or wind is expected to affect the stratification, and therefore regulate both the timing and magnitude of phytoplankton blooms, as well as the nutrient dynamics. Irregular short-term declines or even breakdowns of stratification could have a longer-term effect on the physical and biological properties of the water column. The consequence of the timing of the onset and the extent of the stratification for the phytoplankton production, the succession and trophic interactions has been studied in the North Sea region using a three-layer model (a simplified 1-D version model), including surface mixed layer, bottom mixed layer and thermocline layer [*Ruardij et al.*, 1997]. In this model, the vertical transport in the water column is induced by the shifting of the layer boundaries.

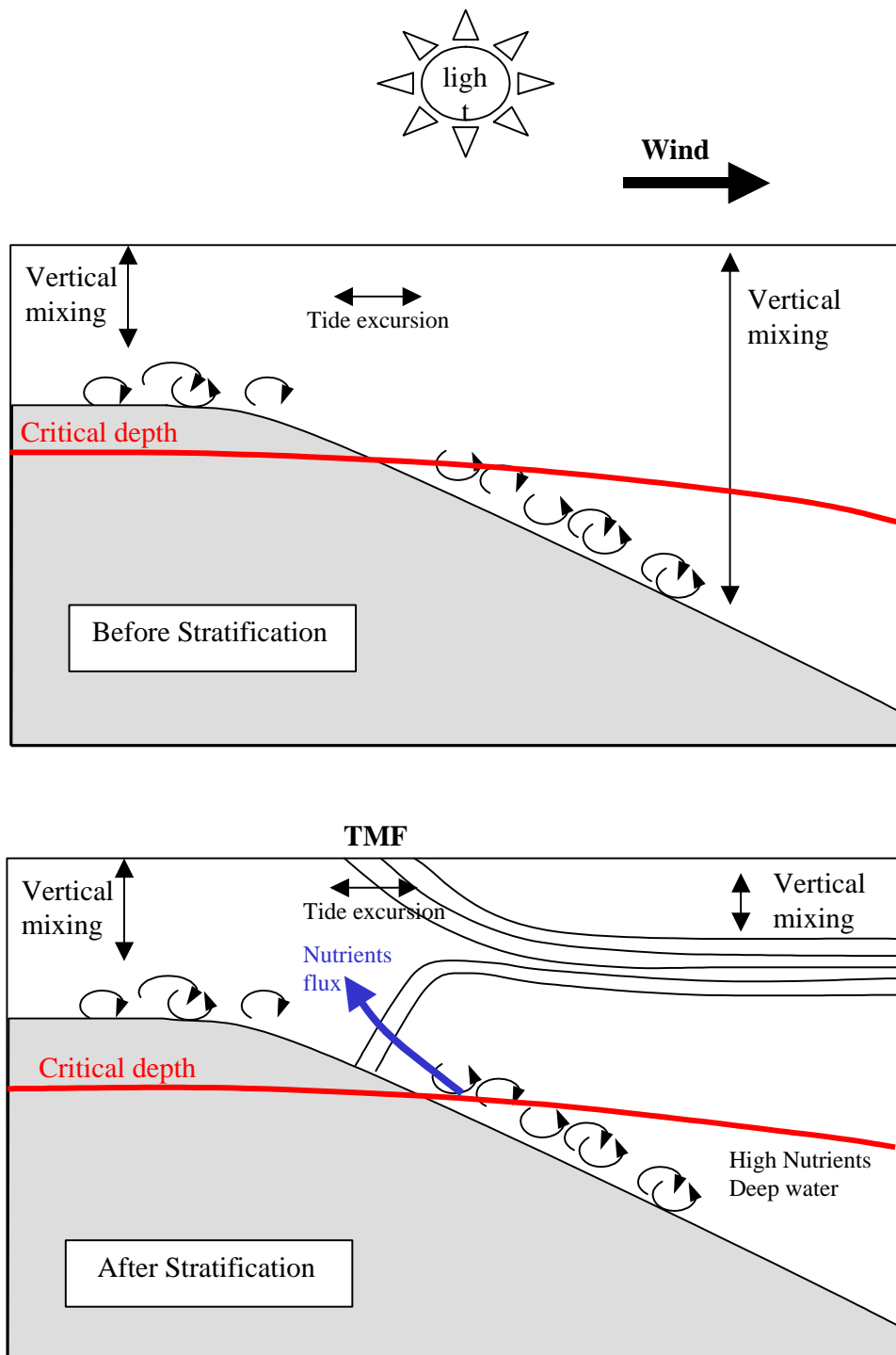


Figure 4.1: A schematic view of interaction between biological and physical factors along the section. Upper figure represents an un-stratified case and bottom one represents a stratified case. TMF stands for tidal mixing front. The critical depth changes with light intensity and water turbidity.

The results show that the onset of stratification has major consequences for the production and succession of phytoplankton and the structure of the food web during the entire growing season. *Eigenheer et al.* [1996] used an ecosystem box model to discuss the response of phytoplankton and nutrients for different types of stratification. They found that the influence of the definition and derivation of the mixed layer depth on the simulation results is significant. Temporal variability of the mixed-layer depth causes a variability of the onset of phytoplankton bloom of about two weeks. Both of the above models were one-dimensional, so the impact of heat on the water column with different water depths was not considered. The impact of wind induced divergence and convergence was also excluded.

The 2-D modeling approach has been applied on GB with various purposes. It has been used to study tidal mixing, internal wave generation, and cross-bank particle exchange [*Chen and Beardsley*, 1995; *Chen et al.*, 1995; *Chen and Beardsley*, 1998]. *Franks and Chen* [1996] coupled an NPZ model to a 2-D prognostic hydrodynamic model of a cross-section on GB. They used this model to explore the influence of tidally generated mixing and advection on the development of patterns in the summertime plankton community on GB and its surrounding fronts. More recently, the effects of wind and surface heating on the transport of water and particles through the tidal mixing front on the southern flank of GB has been examined using a 2-D primitive equation ocean model [*Chen et al.*, 2003a,b].

The modeling studies mentioned above focused on process study with short modeling time period, usually less than a month. The basic assumption in the 2-D model is that no along-isobath variation exists, which is acceptable if modeling time is relatively short. What will happen if the model runs over a month, or even longer, for example a half year? On GB, due to the recirculation along the flank area, it is expected that a 2-D model will less successfully capture the basic patterns of the biological system in the deep area than it will in the shallow central area. The

question is what kind of difference it would be in terms of temporal variation and spatial distribution of biological variables if no advection is included. Indirectly, the 2-D model results can give an indication of the importance of advective processes. On the other hand, the 2-D model is a convenient tool to test and analyze the cross-sectional interaction and cross-frontal exchange processes.

This work will (1) test if the biological model developed in the 1-D domain is valid under a 2-D domain; (2) examine the cross-sectional distribution and interaction between the shallow and deep region; (3) examine the stratification formation process and its impact on the timing of the spring bloom and succession of phytoplankton population in April; and (4) test the effects of tides and surface wind stress on the cross-frontal nutrient exchange.

4.3 MODELING APPROACH

The model experiments were conducted using the lower trophic level food web model developed in Chapter 2 coupled with ECOM-si.

The configuration of the 2-D model features a cross-isobath section with water depth varying from 100 m on the southern flank to 36 m on the top of the bank (Figure 4.2). This numerical domain is extended about 250 km northward and southward with depths of 36 and 100 m, respectively. As shown in Figure 4.2, a uniform grid is used in σ , with vertical resolution $\sigma = 0.0196$ (51 points in the vertical). This resolution corresponds to a maximum vertical depth of 2 m off the bank and <1 m on the top of the bank. A non-uniform horizontal grid is used in the cross-bank direction. The horizontal resolution is 500 m near and across the bank and increases linearly over an interval of 30 grid points to 11.96 km outside the immediate domain. The time step is 110.4 sec, corresponding to 405 time steps over an M_2 (12.42 hr)

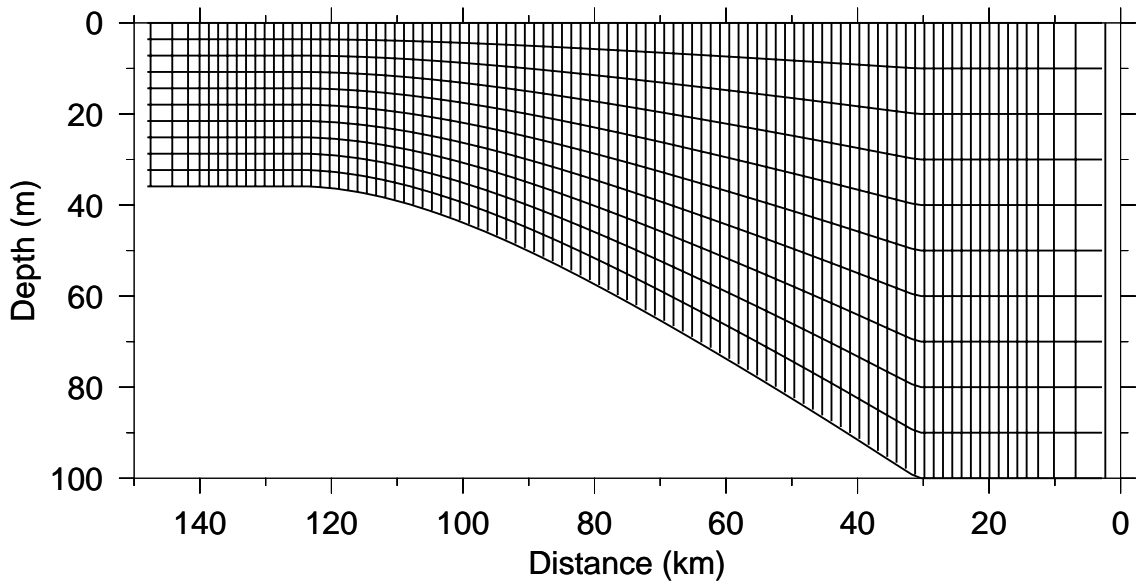


Figure 4.2: Numerical model grid, plotted every five points in the vertical and every three in the horizontal. Horizontal resolution is 500 m near and across the bank and increase linearly over an interval of 30 grid points to 11.96 km away from the region of interest. A uniform grid is used in σ , with vertical resolution $\Delta\sigma = 0.0196$.

tidal cycle. An M_2 tidal forcing is specified at the southern open boundary, and a gravity wave radiation condition is applied at the northern open boundary.

The measured wind and surface heat flux for 1995 was added into the model as a basic metrological forcing. The surface and bottom conditions for both momentum and biological equations are identical to 1-D model experiments as described in Appendix A.

Like the 1-D model, the standard model run starts from January 1, and ends on June 30. The biological model used in 2-D domain is exactly the same as in 1-D, with a vertically and horizontally homogenous initiation concentration for all the biological variables as follows: nitrate: $5.0 \mu\text{mol N/l}$; ammonia: $0.1 \mu\text{mol N/l}$; silicate: $5.0 \mu\text{mol Si/l}$; small phytoplankton: $0.1 \mu\text{mol N/l}$; large phytoplankton: $0.4 \mu\text{mol}$

N/l; small zooplankton: $0.1 \mu\text{mol N/l}$, large zooplankton: $0.2 \mu\text{mol N/l}$; detritus nitrogen $5.0 \mu\text{mol N/l}$; detritus silicon: $2.0 \mu\text{mol N/l}$. These initial values are also identical to the 1-D model experiments.

4.4 MODEL RESULTS

4.4.1 PHYSICAL FIELD

The water was vertically well mixed over the entire section of the bank before April. As represented by the February case (Figure 4.3), The cross-bank residual flow (U velocity) was relatively stronger in the surface than in deep water, mainly caused by surface wind stress. The vertical residual current (W velocity) was very weak with an order of less than $0.3 \times 10^{-2} \text{cm/s}$. The along-bank residual flow field (V velocity) showed a weak southwestward current jet near the 60-m isobath, with a maximum speed of about 5 cm/s. During April (Figure 4.4), the water started to show a weak stratification due to the increased surface heat flux. Along with this, the velocity field also showed a slight change, with an appearance of multiple circulation cells across the section and a vertically non-uniform distribution of V velocity. This change has been enhanced with the intensification of stratification during June (Figure 4.5). The residual flow field showed a strong southwestward current jet in the along-bank direction and double circulation cells in the cross-bank direction within the north of the tidal mixing front. The current jet had a maximum speed of about 12 cm/s at a subsurface depth of 10-15 m. Near the tidal mixing front zone, two secondary circulation cells existed with divergence near the surface and convergence near the bottom. The water tended to converge toward the bank edge of the tidal mixing front in the upper 10 m and then recirculate back in the deeper region. This depiction of secondary circulation is very similar to that suggested using the semi-analytical diagnostic frontal model of *Garrett and Loder* [1981] and *Chen and Beardsley* [2002].

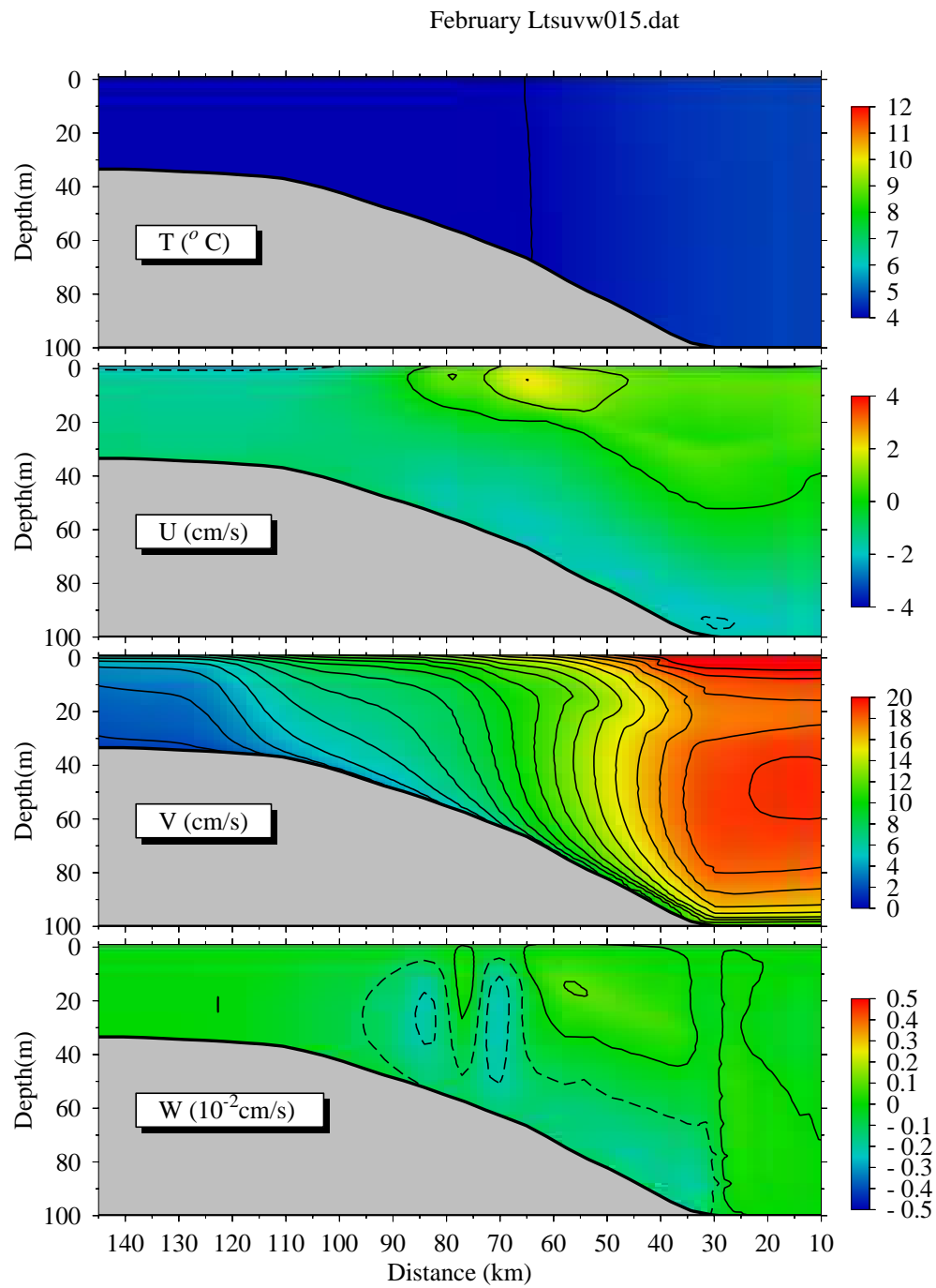


Figure 4.3: Model-computed cross-isobath distribution of tidally averaged temperature (T), and cross-bank (U : positive on-bank), along-bank (V : positive out of the paper) and vertical (W : positive upward) velocities on the southern flank of GB on February 15, 1995.

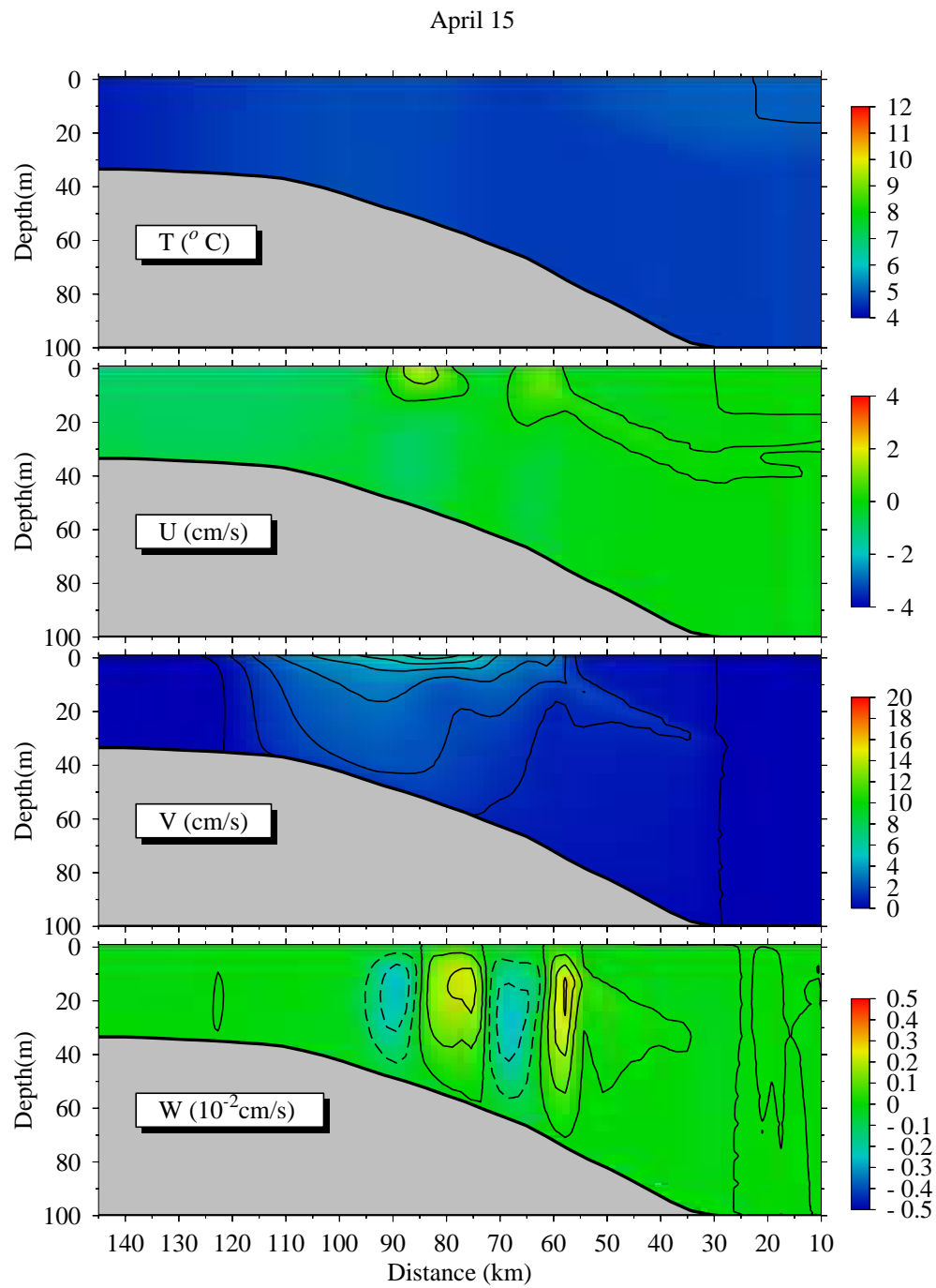


Figure 4.4: Model-computed cross-isobath distribution of tidally averaged temperature (T), and cross-bank (U : positive on-bank), along-bank (V : positive out of the paper) and vertical (W : positive upward) velocities on the southern flank of GB on April 15, 1995.

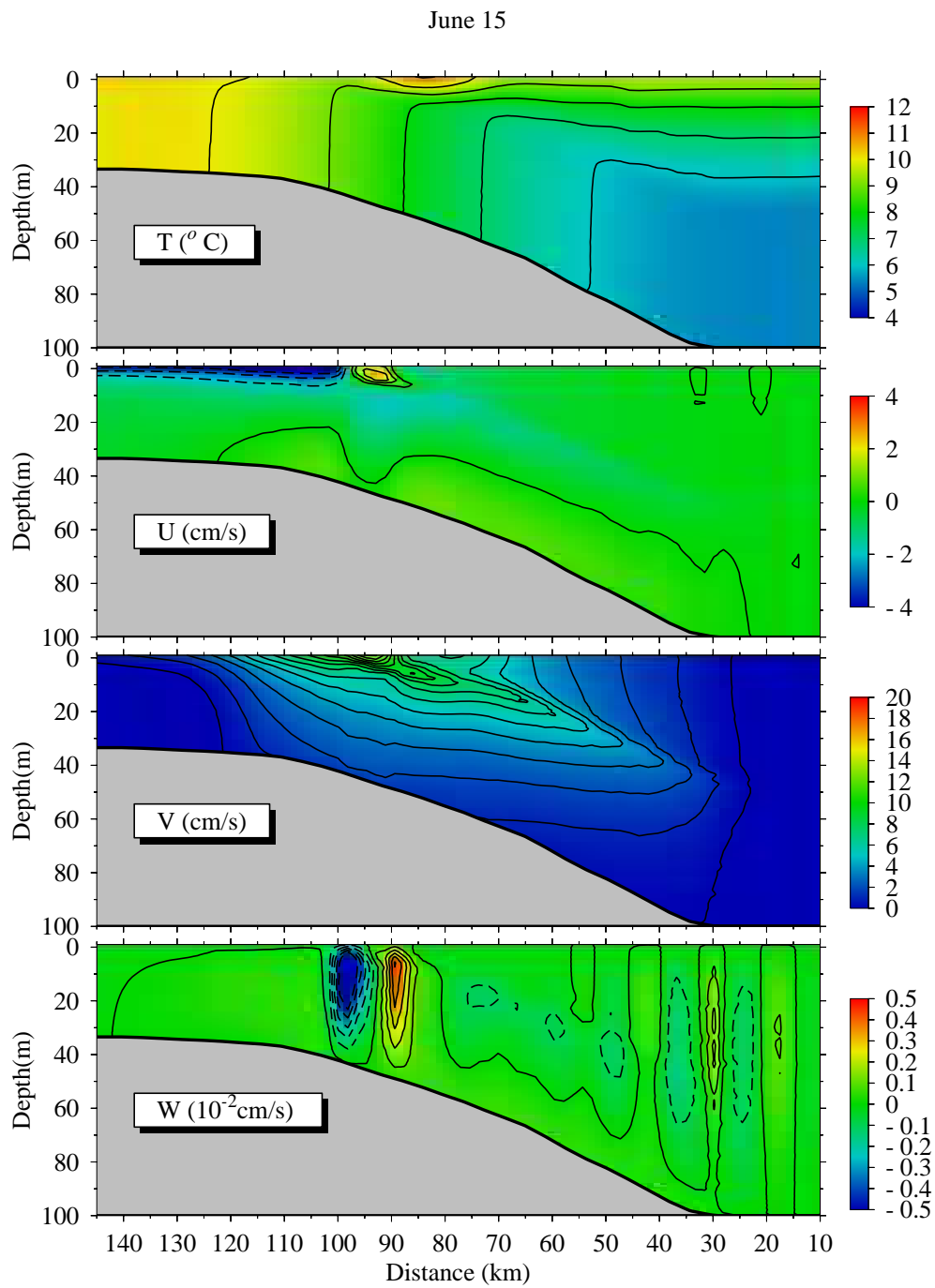


Figure 4.5: Model-computed cross-isobath distribution of tidally averaged temperature (T), and cross-bank (U: positive on-bank), along-bank (V: positive out of the paper) and vertical (W: positive upward) velocities on the southern flank of GB on June 15, 1995.

4.4.2 BIOLOGICAL COMPONENTS

Biological variables began to show sectional variation different from their original homogenous distribution quickly after the model started. The shallow and deep sites mirrored the 1D model results well. In February (Figure 4.6, Figure 4.7), the area shallower than 50 m showed an increase of large phytoplankton from initial $0.4 \mu\text{mol N/l}$ to about $2 \mu\text{mol N/l}$, while both nitrogen and silicate decreased from initial $5.0 \mu\text{mol N/l}$ to $4.0 \mu\text{mol N/l}$ and $5.0 \mu\text{mol Si/l}$ to $4.0 \mu\text{mol Si/l}$, respectively. No detectable change was shown for small phytoplankton, small zooplankton and large zooplankton. In contrast, the area deeper than 60 m did not show a noticeable change of nitrate, silicate, and phytoplankton, largely due to the mixing dilution limiting phytoplankton growth (as discussed in 1-D model). Detritus nitrogen and silicon slightly decreased due to the balance between sinking and mixing process.

The large phytoplankton showed an increase of biomass to a much larger extent, reaching the 70-80 m isobath in April (Figure 4.8, 4.9). The maximum biomass, about $3.0 \mu\text{mol N/l}$, occurred around 50 m isobath, as a consequence of light availability and nutrient support from the deep area (see discussion at section 3.5.3). By this time, small phytoplankton began to grow, their biomass reaching about $1.0 \mu\text{mol N/l}$ in the shallow area. Nitrate and nitrite showed signs of depletion over the area shallower than 50 m, while silicate was depleted to a slightly larger extent, reaching 60-m isobath. The depletion of ammonia was more severe due to the preference of phytoplankton uptake of ammonia over nitrate. Detritus nitrogen and silicon increased significantly due to mortality and rejected part of grazing process. In the deeper area, large phytoplankton began to show a very weak vertical structure corresponding to the weak stratification at that time (detailed description of this structure is described in next section). Ammonia concentration increased to near $3 \mu\text{mol N/l}$ in the deeper region lower than 90 m, due to the decomposition of detritus

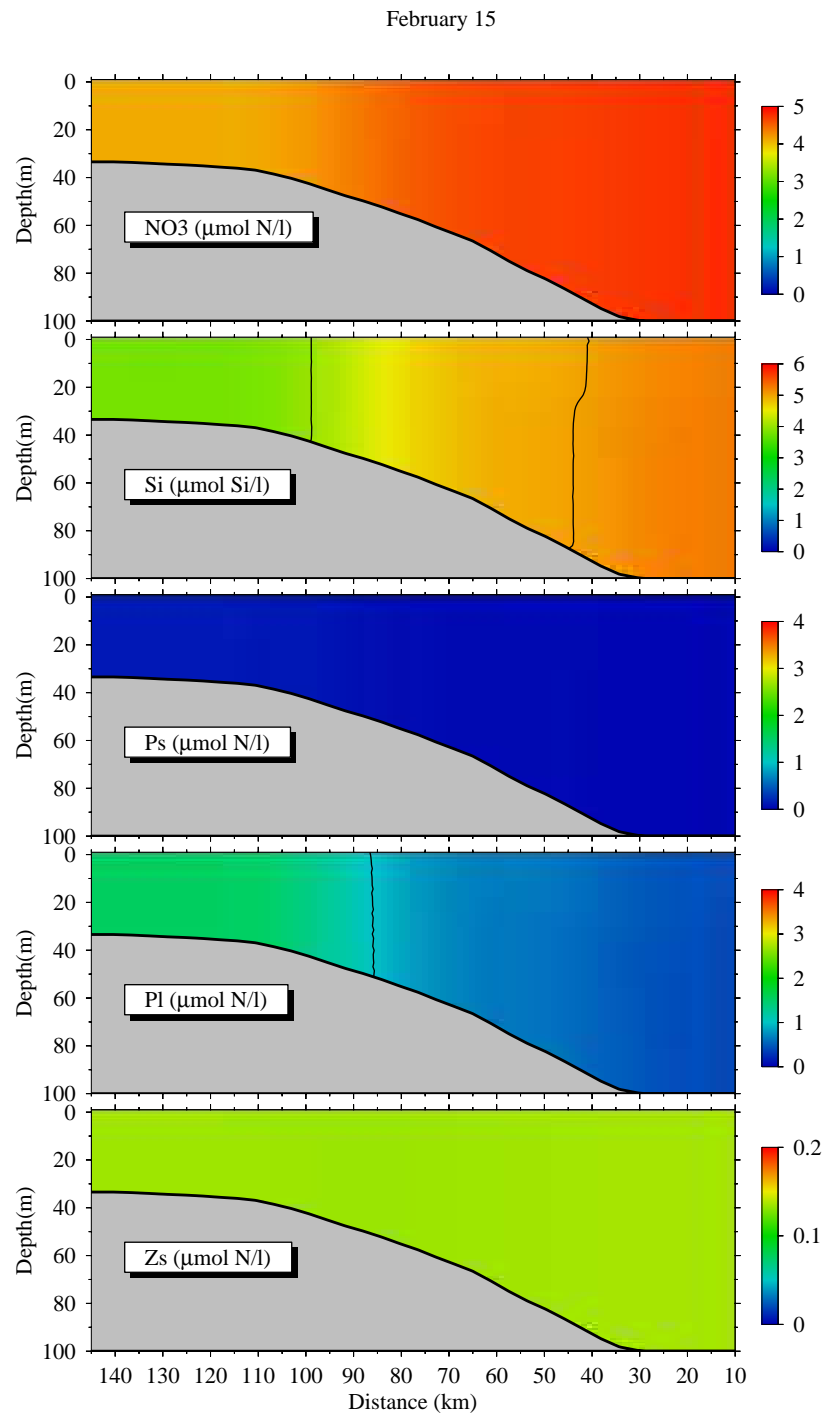


Figure 4.6: Model-computed cross-isobath distribution of tidally averaged nitrate (NO_3), silicate (Si), small phytoplankton (Ps), large phytoplankton (Pl), and small zooplankton (Zs) on the southern flank of GB on February 15, 1995.

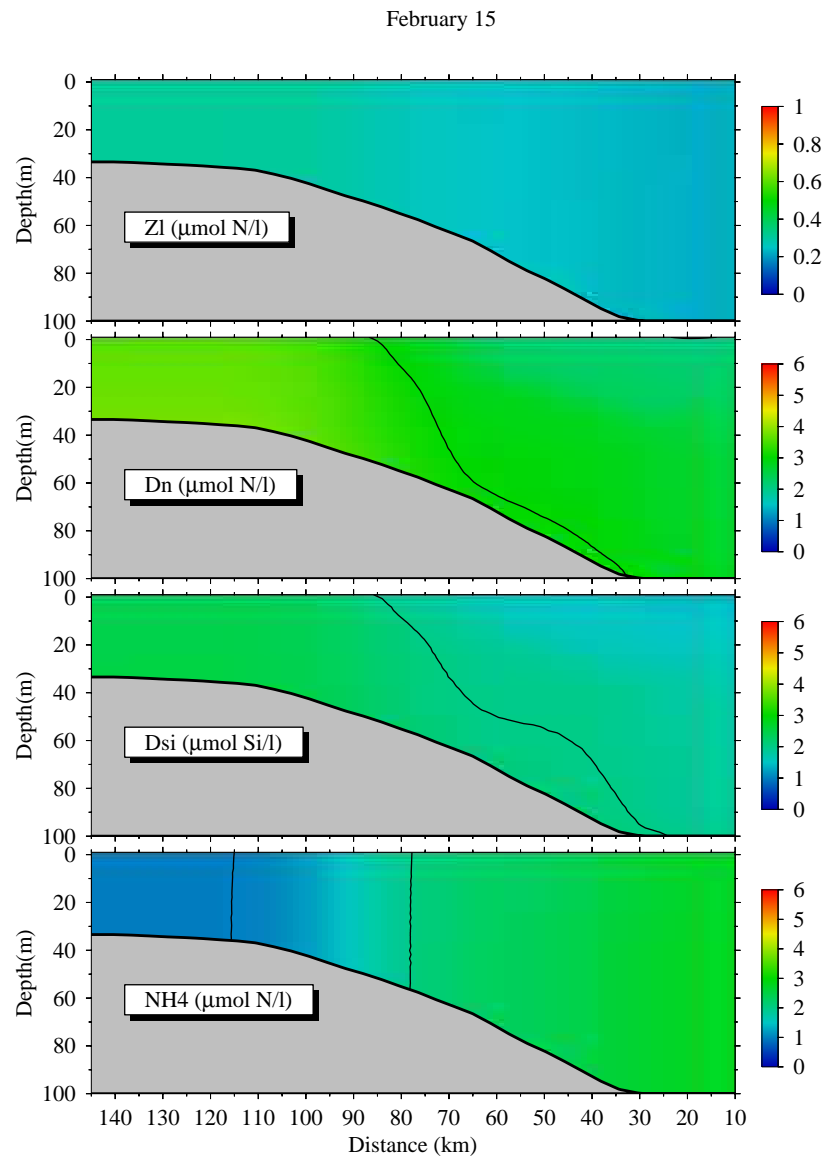


Figure 4.7: Model-computed cross-isobath distribution of tidally averaged large zooplankton (Zl), detrital organic nitrogen (Dn), detrital organic silicon (Dsi), and ammonia (NH4) on the southern flank of GB on February 15, 1995.

nitrogen and reduction in phytoplankton uptake. Sinking and weak stratification also caused the vertical gradients of detritus nitrogen and silicon in the deeper region.

After the stratification fully developed during June (Figure 4.10, Figure 4.11), the modeled large phytoplankton bloom declined with a concentration of near $1.0 \mu\text{mol N/l}$ in the shallow area. Near the frontal zone, the concentration was slightly higher due to nutrients from the deep nutrient-rich region, as indicated by the nitrate and silicate distribution. In the deep area, large phytoplankton showed a subsurface maximum layer as a consequence of growth and sinking from the surface mixing layer. Nitrate was depleted both in the shallow area and at the surface of the deep area, while an upward intrusion of deep nutrient rich water was observed near the frontal zone. Silicate and ammonia showed a similar dynamics as nitrate. During June, the modeled concentration of silicate in the shallow region recovered from an undetected level to ca. $1.5 \mu\text{mol Si/l}$, mainly due to the increase of detritus silicate decomposition as water temperature increased. The small phytoplankton concentration showed a steady increase after April and reached ca. $1.5 \mu\text{mol N/l}$ in the shallow area, with slightly higher concentration over the tidal mixing front. As expected, the detritus nitrogen and silicon showed a higher concentration over the shallow area and below the surface mixing area due to sinking.

4.5 DISCUSSION

4.5.1 EFFECT OF UNSTABLE STRATIFICATION

In the southern flank of the bank, the exact timing and magnitude of the development of stratification seems to be strongly dependent on the annual meteorological forcings, although the interannual pattern is similar. During later spring (around April), the net heat flux into GB water gradually becomes positive and surface waters heat up, allowing the development of stratification. In the meantime, the

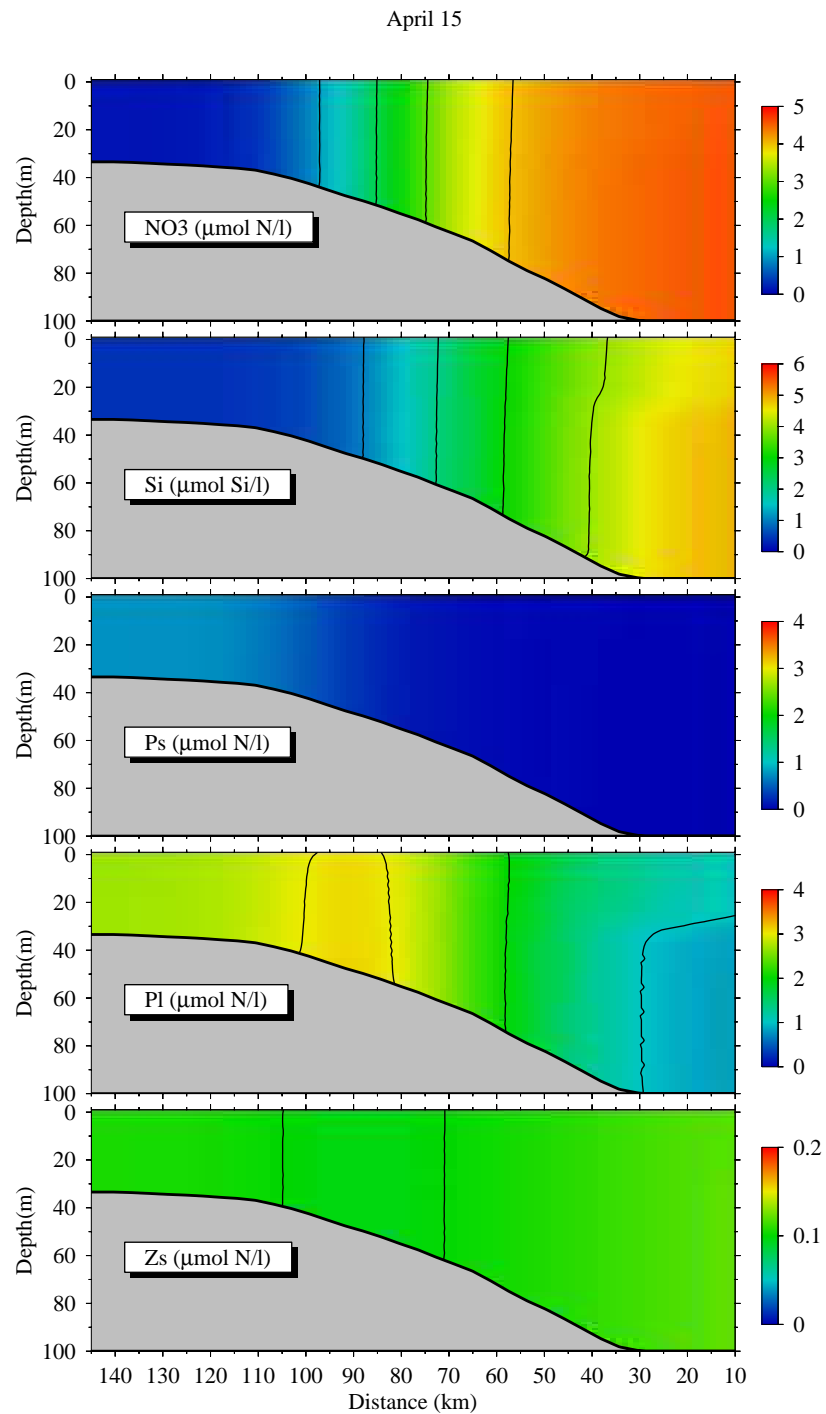


Figure 4.8: Model-computed cross-isobath distribution of tidally averaged nitrate (NO_3), silicate (Si), small phytoplankton (Ps), large phytoplankton (Pl), and small zooplankton (Zs) on the southern flank of GB on April 15, 1995.

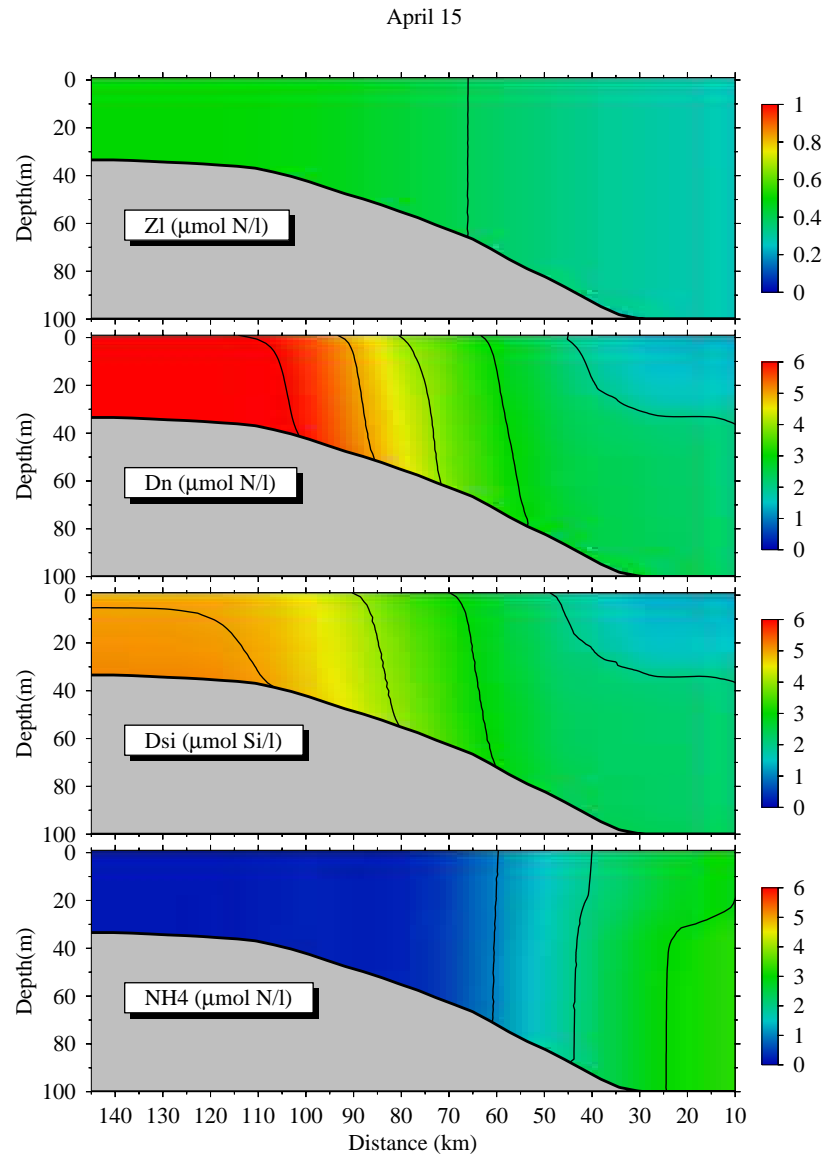


Figure 4.9: Model-computed cross-isobath distribution of tidally averaged large zooplankton (Zl), detrital organic nitrogen (Dn), detrital organic silicon (Dsi), and ammonia (NH₄) on the southern flank of GB on April 15, 1995.

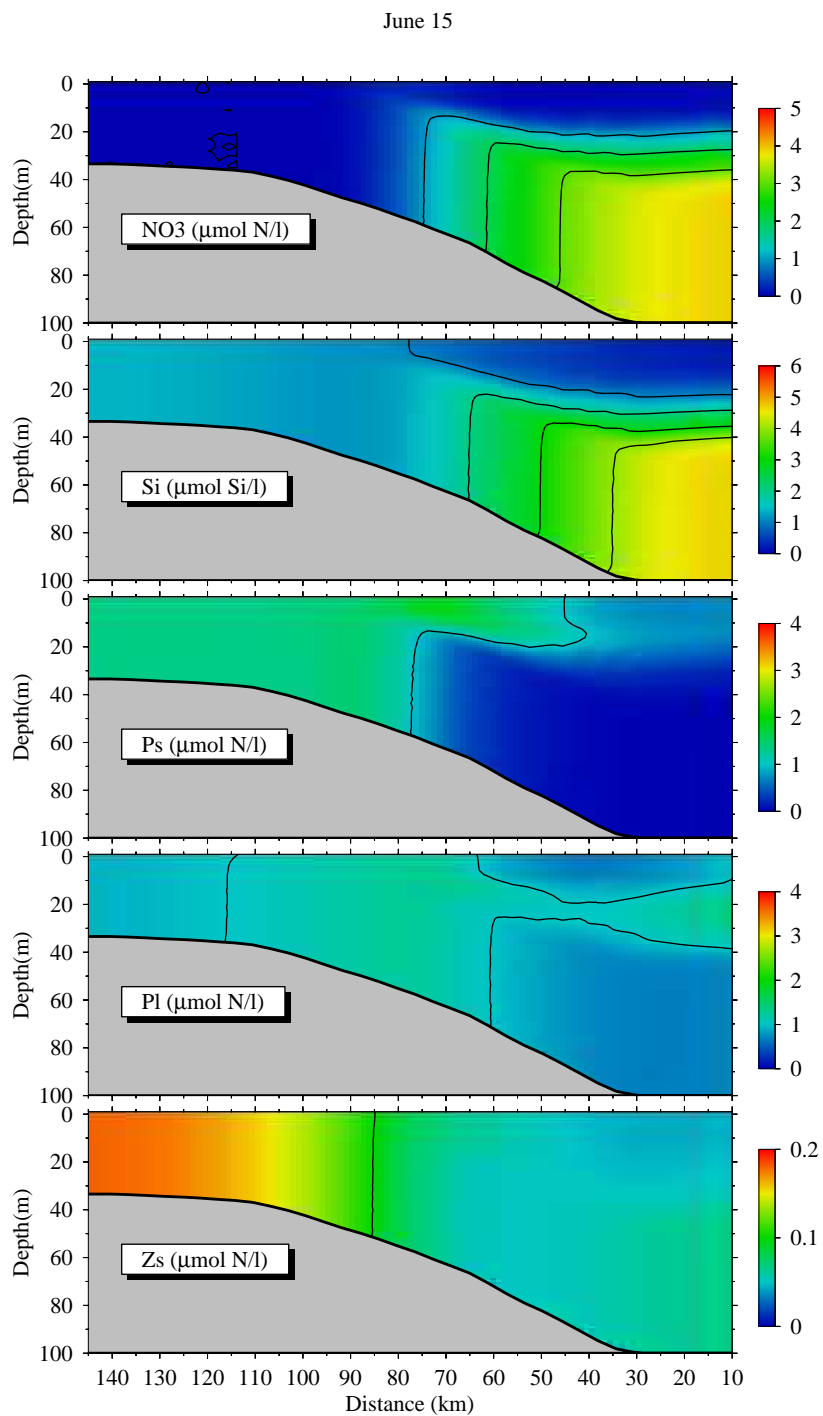


Figure 4.10: Model-computed cross-isobath distribution of tidally averaged nitrate (NO_3), silicate (Si), small phytoplankton (Ps), large phytoplankton (Pl), and small zooplankton (Zs) on the southern flank of GB on June 15, 1995.

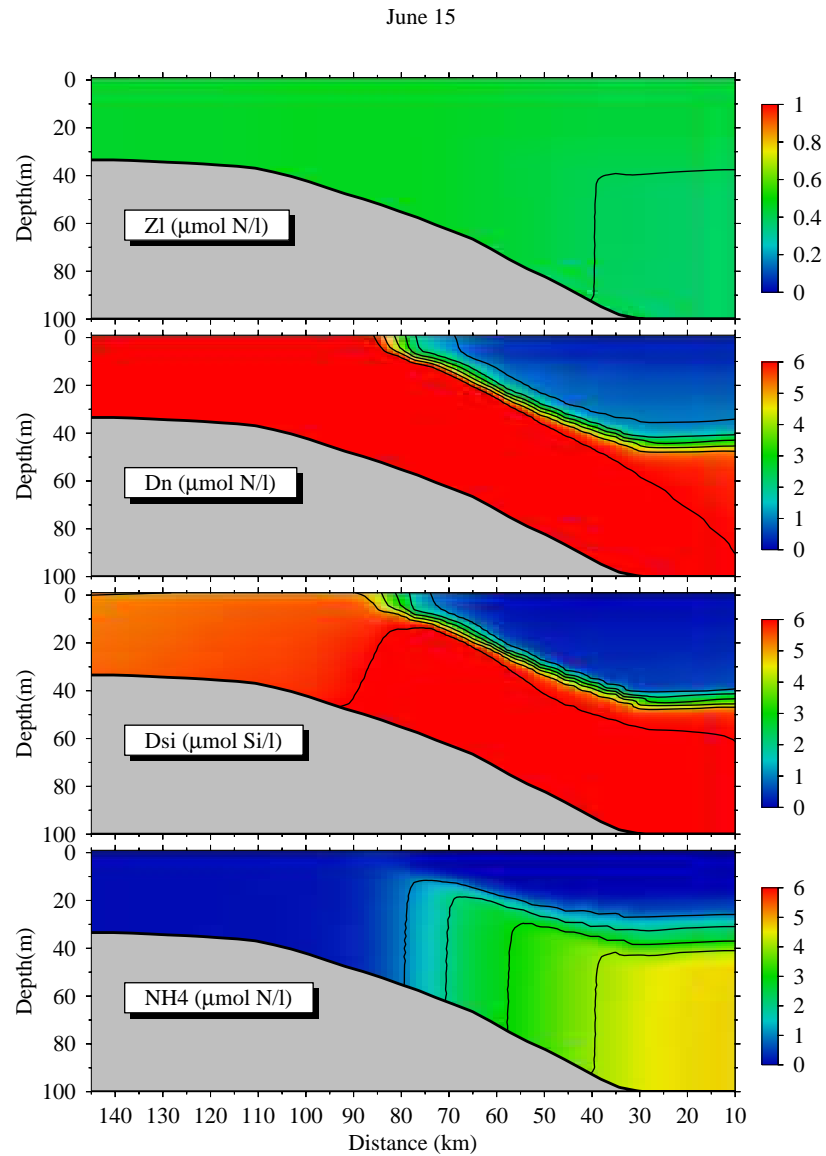


Figure 4.11: Model-computed cross-isobath distribution of tidally averaged large zooplankton (Zl), detrital organic nitrogen (Dn), detrital organic silicon (Dsi), and ammonia (NH4) on the southern flank of GB on June 15, 1995.

tide- and wind-driven turbulent mixing de-stabilizes stratification. Therefore, the stratification at that time is weak and unstable.

To have a “close-up” examination of the transition time between the well-mixed and stratification situation, a detailed structure of temperature and mixing coefficient (Km) distribution along the transect in three different times during April is shown in Figure 4.12, Figure 4.13 and Figure 4.14. In Figure 4.12, the water column in the deeper area started to show a sign of weak stratification. Correspondingly, phytoplankton showed a slightly higher concentration at the surface (< 40 m) of deeper area with a water depth of > 80 m (Figure 4.15 bottom panel). On April 29 (Figure 4.13), in the deeper area, water temperature above 40 m was about 0.5 °C different from water below, with a lower turbulence mixing coefficient (Km) near the 40 m. Correspondingly, large phytoplankton had a much higher concentration in the surface layer shallower than 40 m, with a value of near 3.0 $\mu\text{mol N/l}$ (Figure 4.16). Compared with 1.0 $\mu\text{mol N/l}$ in the water below, it is a significant vertical gradient. Both nitrate and silicate decreased as a consequence of phytoplankton uptake and reduced mixing exchange between the surface and bottom waters. This stratification was not stable at this time of the year, where strong wind and cooling could interrupt and breakdown the stratification. Figure 4.14 showed such an instance. With a strong southwestward wind and cooling, as occurred during the end of April, Km increased significantly, reaching 0.1 m^2/s . The water was totally mixed (as shown in the temperature field), as were the nutrient and large phytoplankton fields (Figure 4.17). As a result, the bloom disappeared due to the vertical dilution, and nutrients were re-supplied from the deep water to the surface.

Questions raised from above example are (1) what are the criteria of stratification for phytoplankton to show vertical structure? and (2) what is the response time of the phytoplankton to the development and decline of stratification? If we cut a section along the water column at the distance of 20 km in Figure 4.12 and plot the vertical

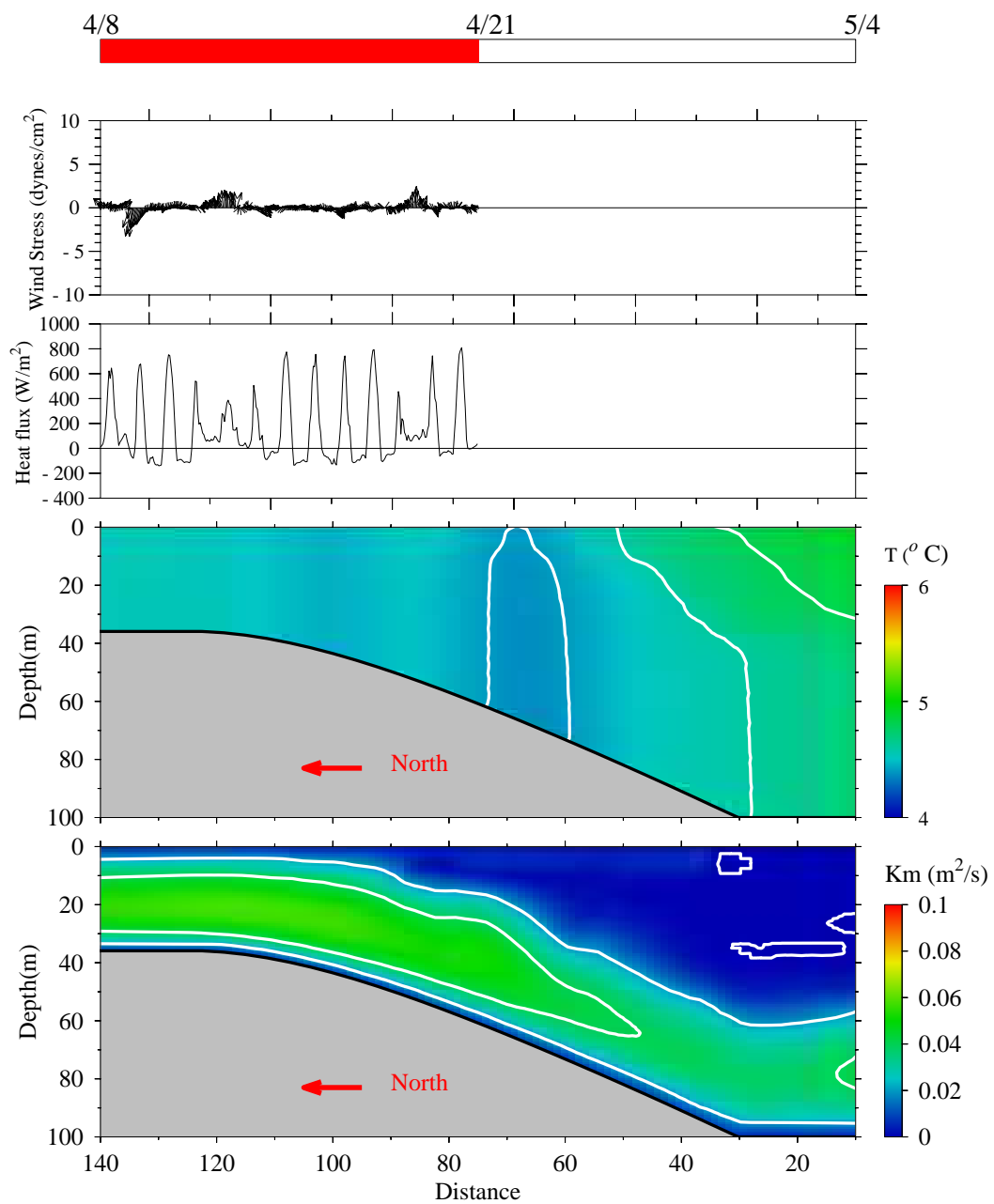


Figure 4.12: Time series of wind and surface heatflux for the 2-D model experiments (Top two), and model-computed cross-isobath distribution of tidally averaged temperature (T) and vertical turbulence mixing coefficient (K_m) on the southern flank of GB on April 21, 1995 (bottom two).

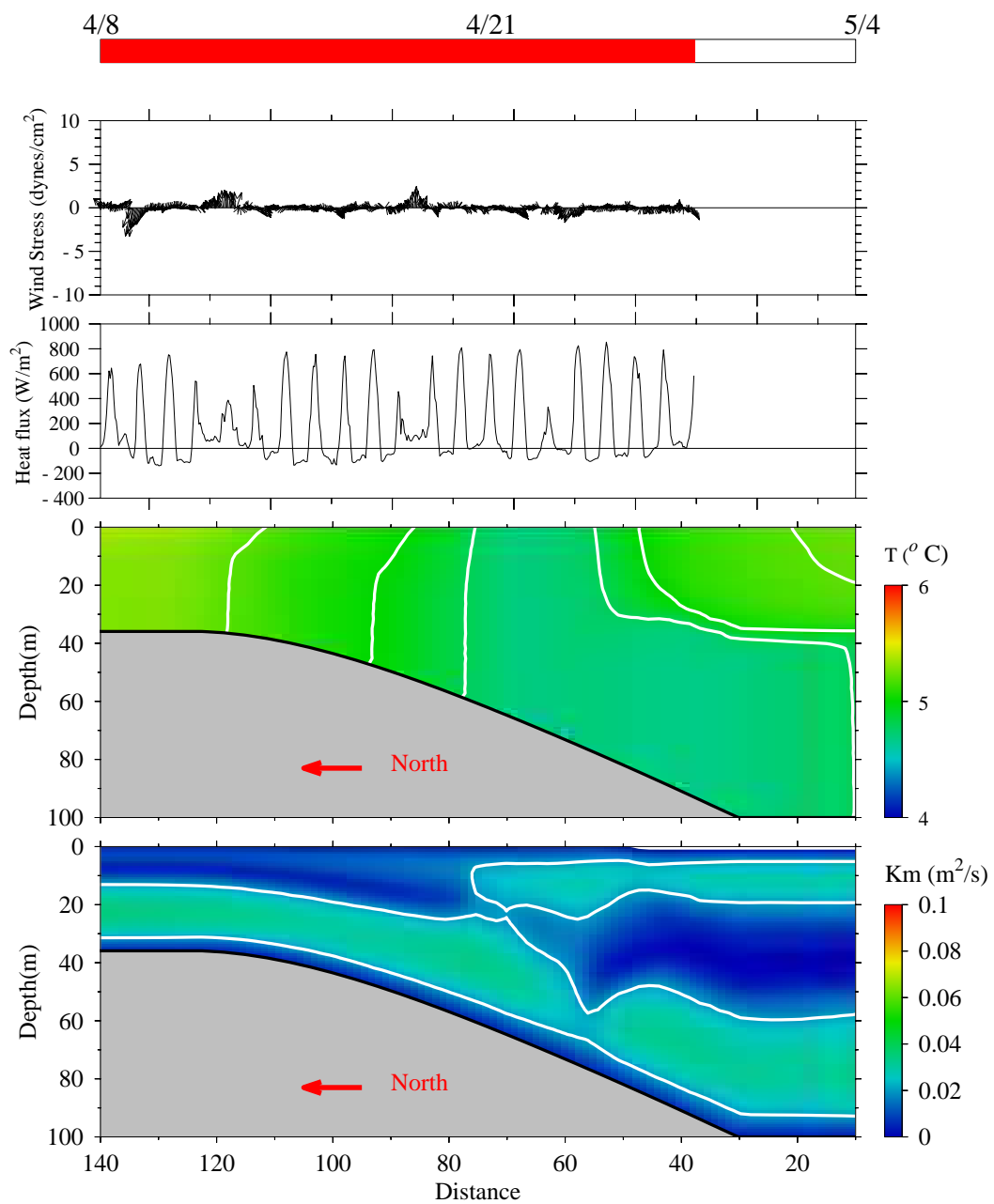


Figure 4.13: Time series of wind and surface heatflux for the 2-D model experiments (Top two), and model-computed cross-isobath distribution of tidally averaged temperature (T) and vertical turbulence mixing coefficient (K_m) on the southern flank of GB on April 29, 1995 (bottom two).

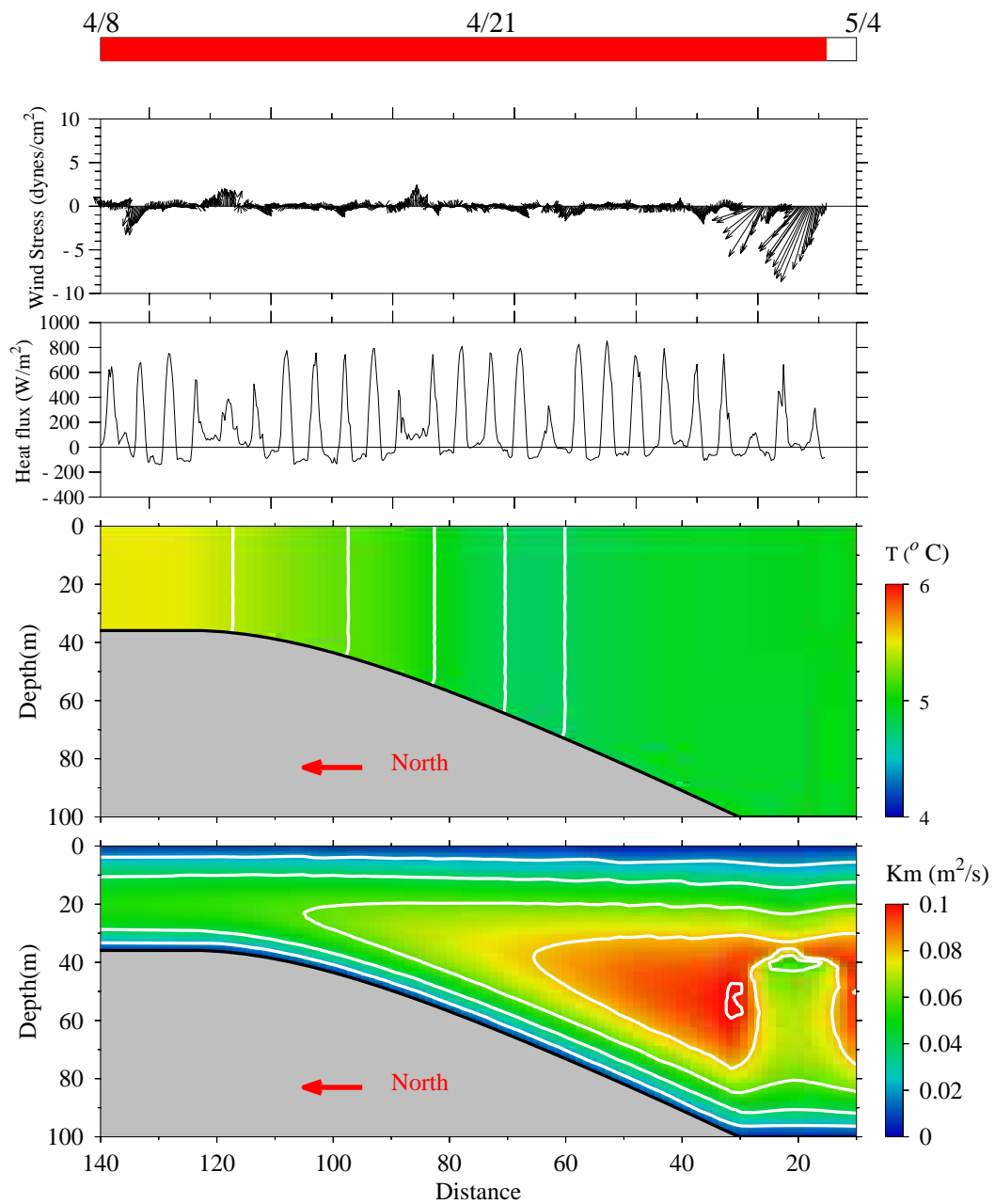


Figure 4.14: Time series of wind and surface heatflux for the 2-D model experiments (Top two), and model-computed cross-isobath distribution of tidally averaged temperature (T) and vertical turbulence mixing coefficient (K_m) on the southern flank of GB on May 2, 1995 (bottom two).

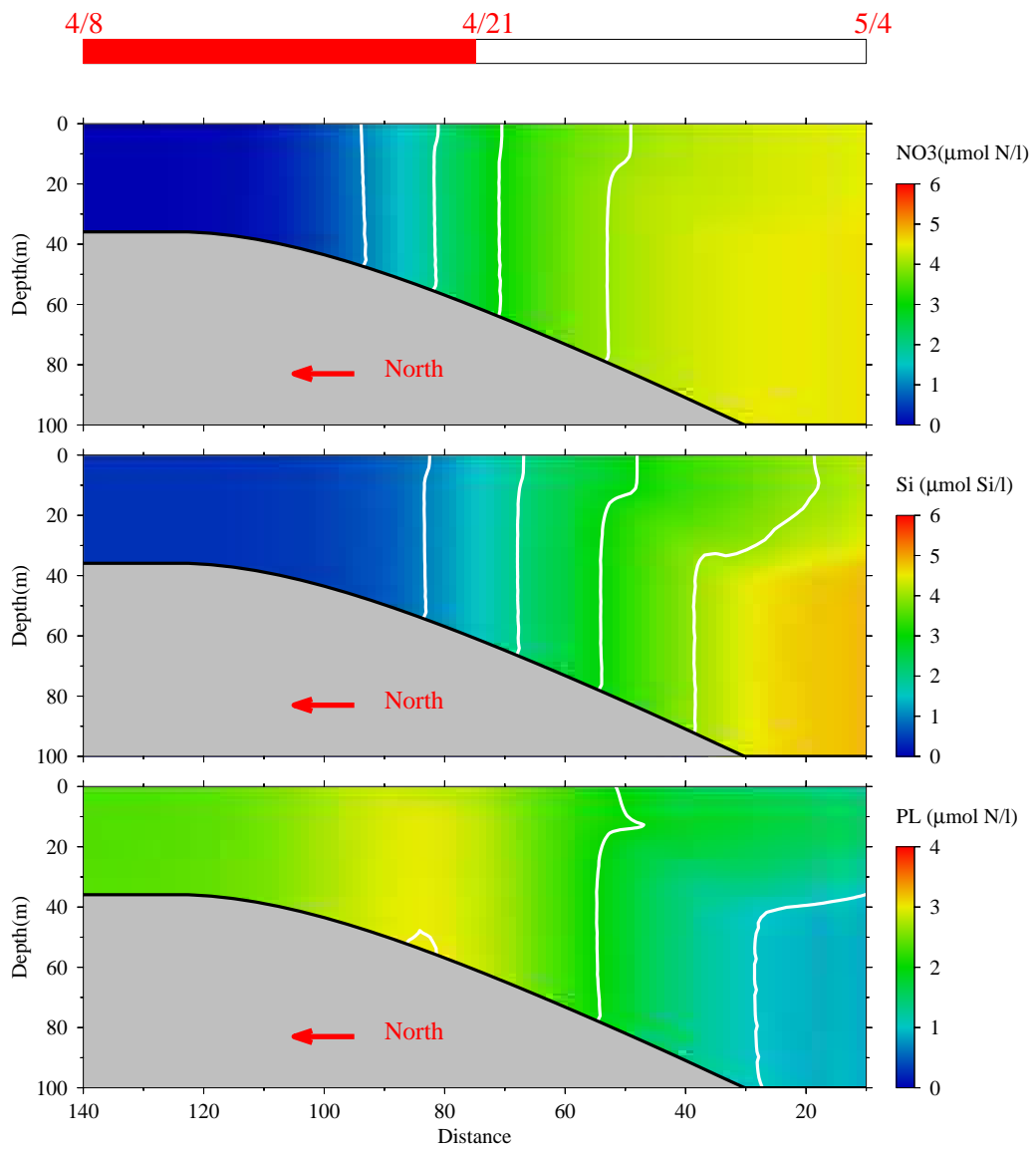


Figure 4.15: Model-computed cross-isobath distribution of tidally averaged nitrate (NO₃), silicate (Si) and large phytoplankton (PL) on the southern flank of GB on April 21, 1995.

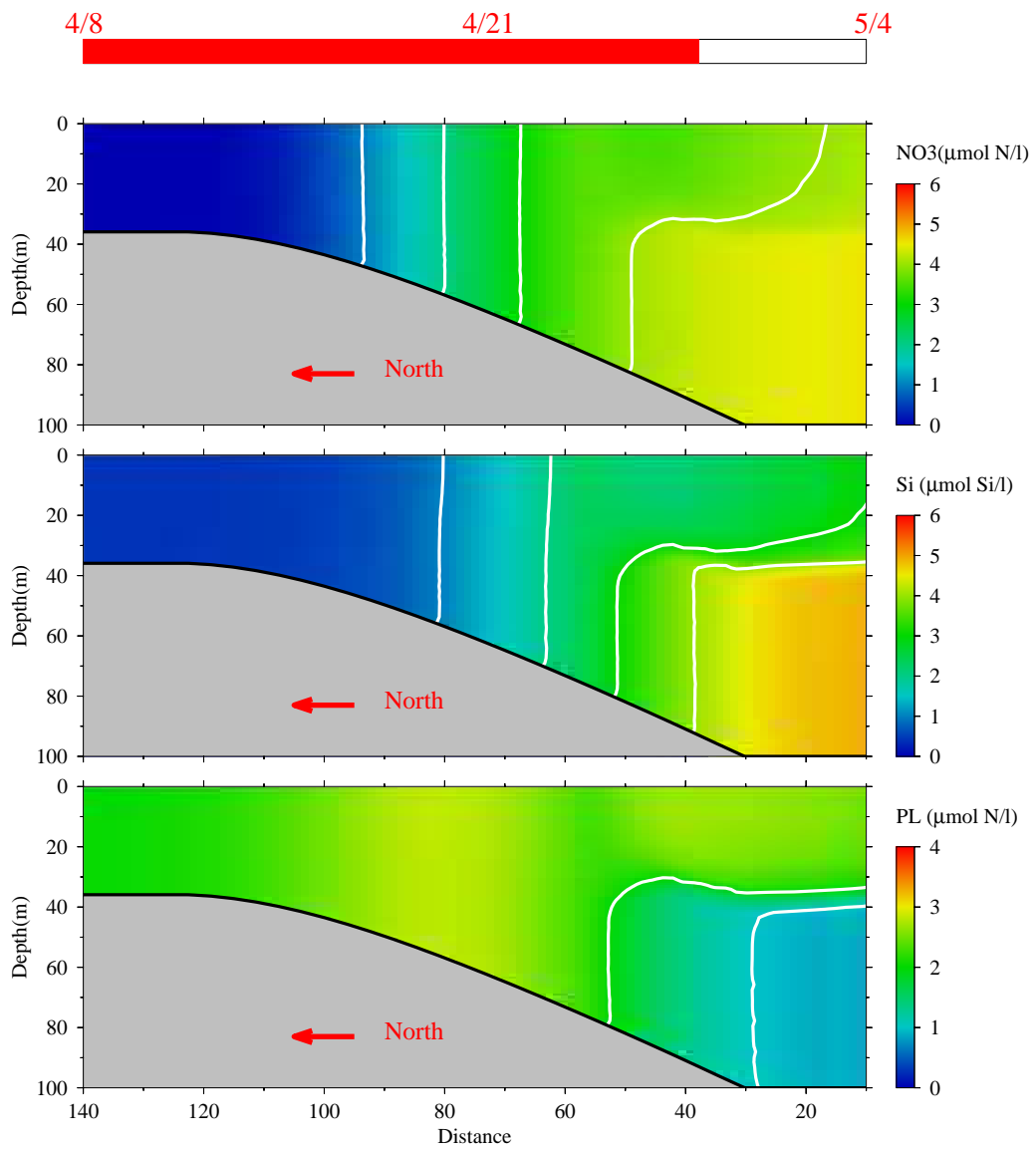


Figure 4.16: Model-computed cross-isobath distribution of tidally averaged nitrate (NO₃), silicate (Si) and large phytoplankton (PL) on the southern flank of GB on April 29, 1995.

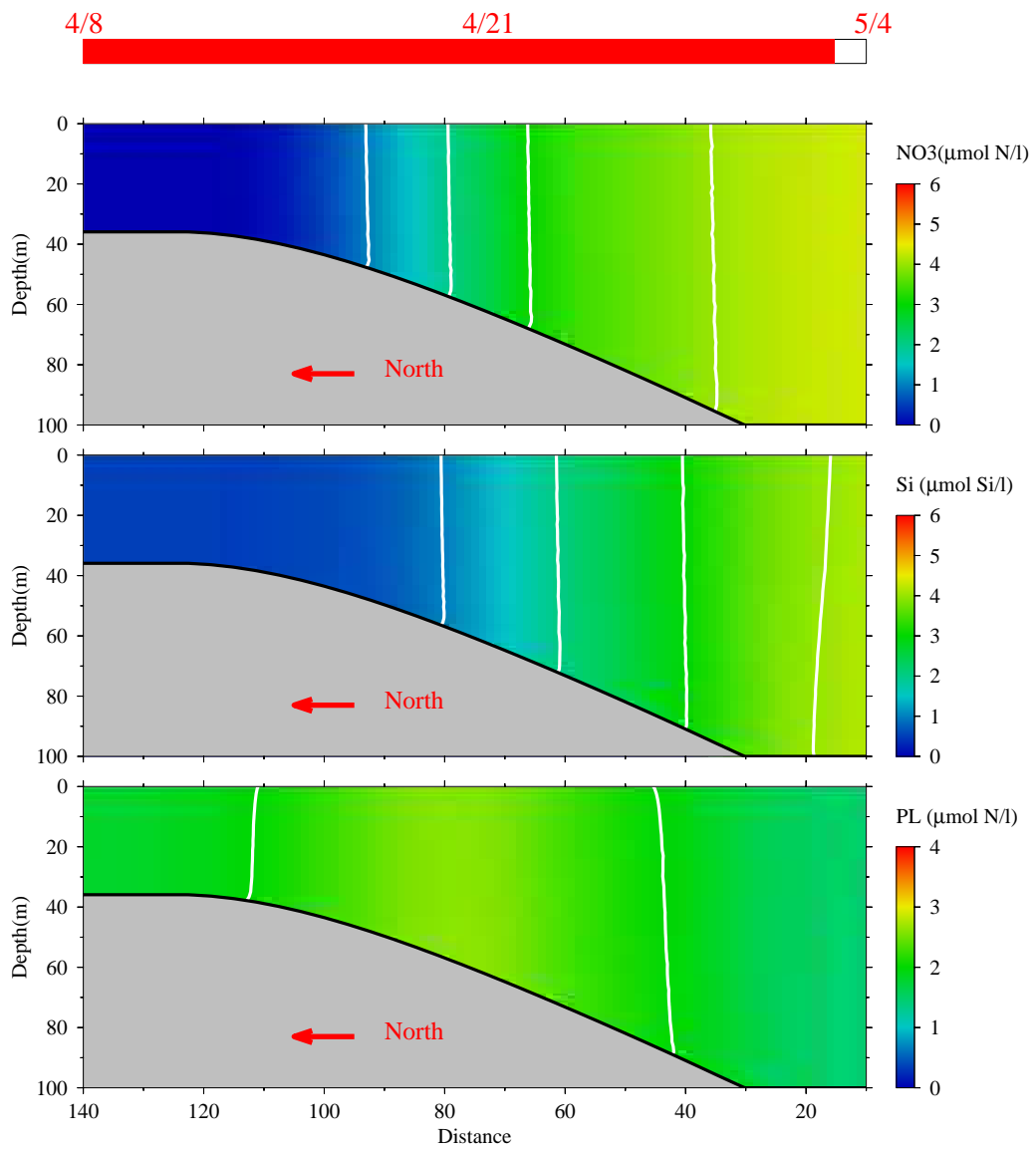


Figure 4.17: Model-computed cross-isobath distribution of tidally averaged nitrate (NO₃), silicate (Si) and large phytoplankton (PL) on the southern flank of GB on May 2, 1995.

distribution of temperature gradients (dT/dZ) and Km against time (Figure 4.18, top two panels), the development of stratification is shown in more detail. Generally, the critical temperature gradient criteria to define mixed-layer depth varies between 0.02 and 0.05 $^{\circ}C/m$ [Springtall and Cronin, 2001]. This criterion may be sensitive to the vertical depth interval over which the gradient is calculated. Assuming a temperature gradient of 0.02 $^{\circ}C/m$ is the criteria for the stratification, it can be seen that weak stratification with gradient slightly higher than 0.02 has been developed from April 25 to May 1. The positive growth of large phytoplankton occurred around April 20 and reached a peak value of 2.5 $\mu\text{mol N/l}$ before stratification broke down (Figure 4.18, bottom panel), indicating that real stratification is not necessarily limited by the 0.02 $^{\circ}C/m$ criteria in this case, but may be smaller. The response of phytoplankton to the development of weak stratification was fairly quick, since the concentration almost doubled in 10 days from April 20 to 30, reaching 2.5 $\mu\text{mol N/l}$. The decline of phytoplankton due to the breakdown of stratification was even faster, with time scale of 1 or 2 days. Such a fluid condition also indicates that patches of phytoplankton can form and decline on small temporal and spatial scales and therefore greatly compromise the observation efforts.

In model runs where less short-wave heat penetrated to the water column, stratification was weaker, as shown in Figure (4.19) using 30% percent less short-wave radiation. Consequently, the large phytoplankton bloom was much weaker, with a maximum concentration of less than 2.0 $\mu\text{mol N/l}$. This result indicates that during stratification transition time, biological processes are very sensitive to the surface heat flux. It is very difficult to get a reasonable simulation results without good meteorological forcings.

The stratification does not always cause a phytoplankton bloom. Figure (4.20) shows such an example that with a lower silicate concentration (1.0 $\mu\text{mol Si/l}$) in the deep area initiated in April 1, the large phytoplankton did not bloom in the

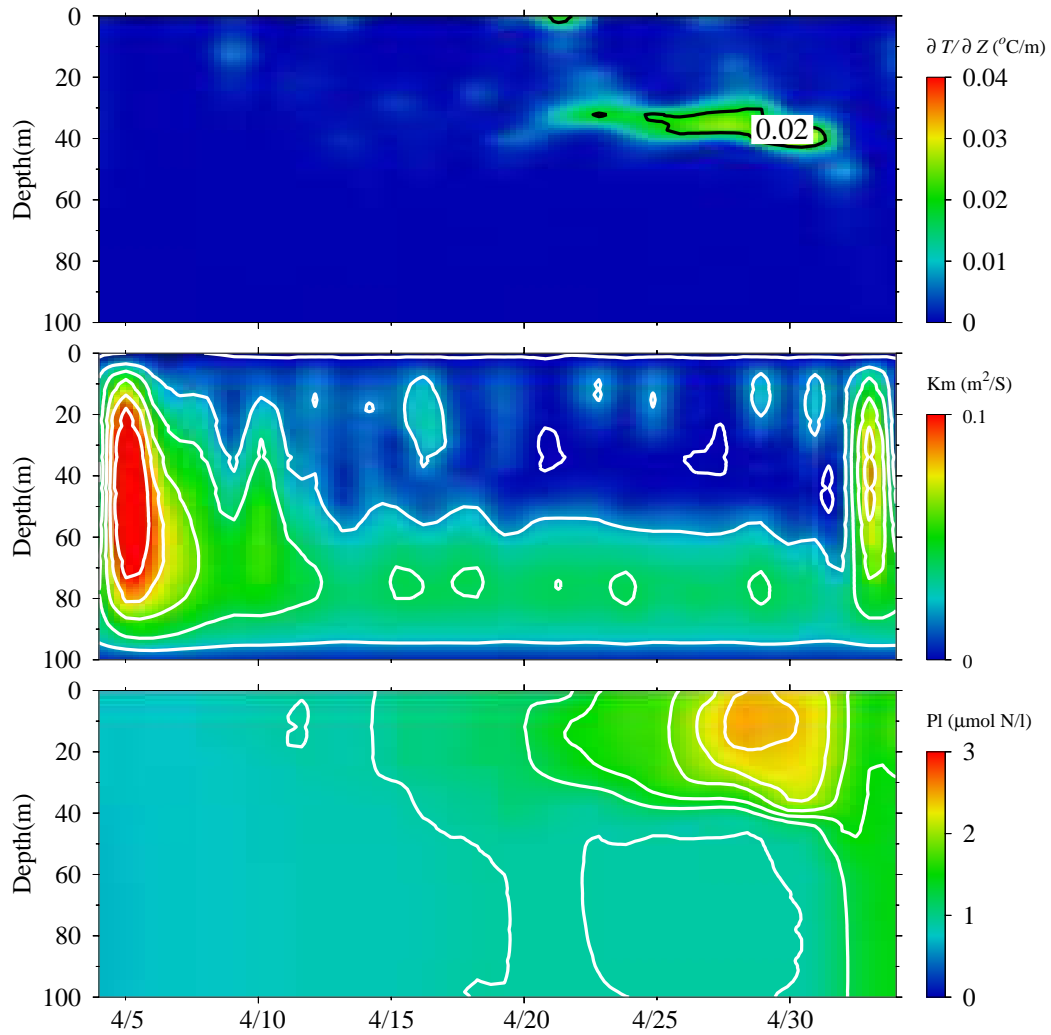


Figure 4.18: Time sequence of the vertical distribution of model-predicted temperature gradient ($\delta T / \delta Z$), vertical turbulence mixing coefficient (K_m), and large phytoplankton (PI). The vertical section is located in at the distance of 20 km in 2-D model domain.

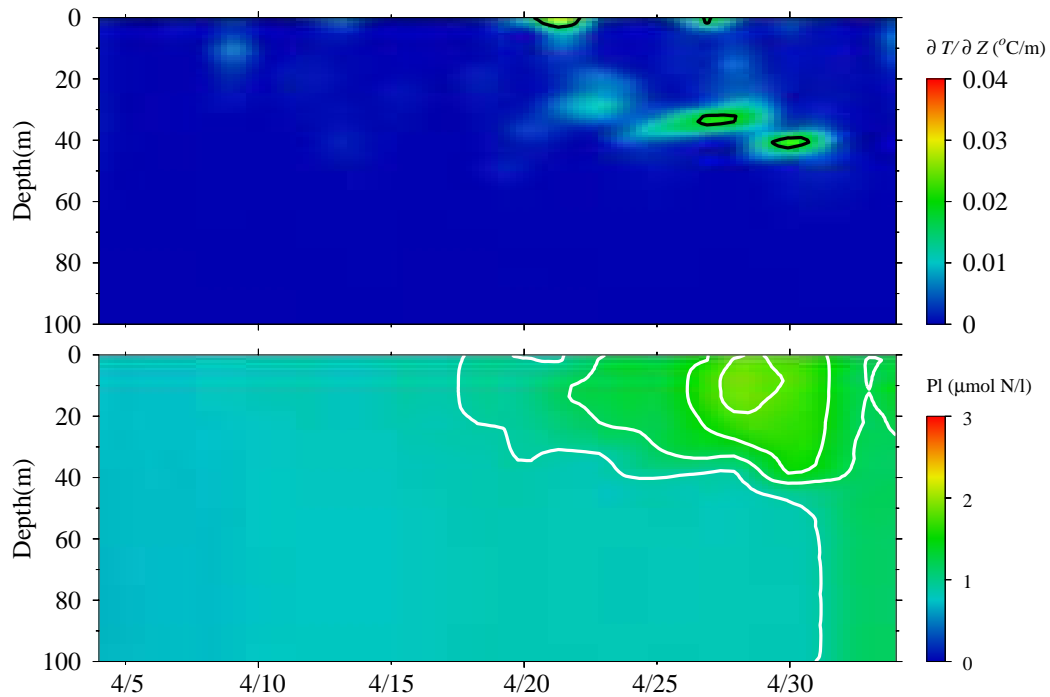


Figure 4.19: Time sequence of the vertical distribution of model-predicted temperature gradient ($\delta T/\delta Z$), and large phytoplankton (PI) with 30% less of surface heat flux. The vertical section is located in at the distance of 20 km in 2-D model domain.

deeper area through April. This condition is most likely to occur when upstream water flowing into the domain is already nutrient depleted, an situation which is hard to be incorporated into the 2-D model domain.

4.5.2 BIOLOGICAL SIGNIFICANCE OF STRATIFICATION AND TIDAL MIXING FRONT

Model results indicated that once the stratification is stabilized, usually after late May, nutrients in surface mixing layer will be quickly consumed by phytoplankton. Large phytoplankton gradually sink out of the surface mixing layer and accumulate in the subsurface area, between water depths of 10 and 40 m, where both

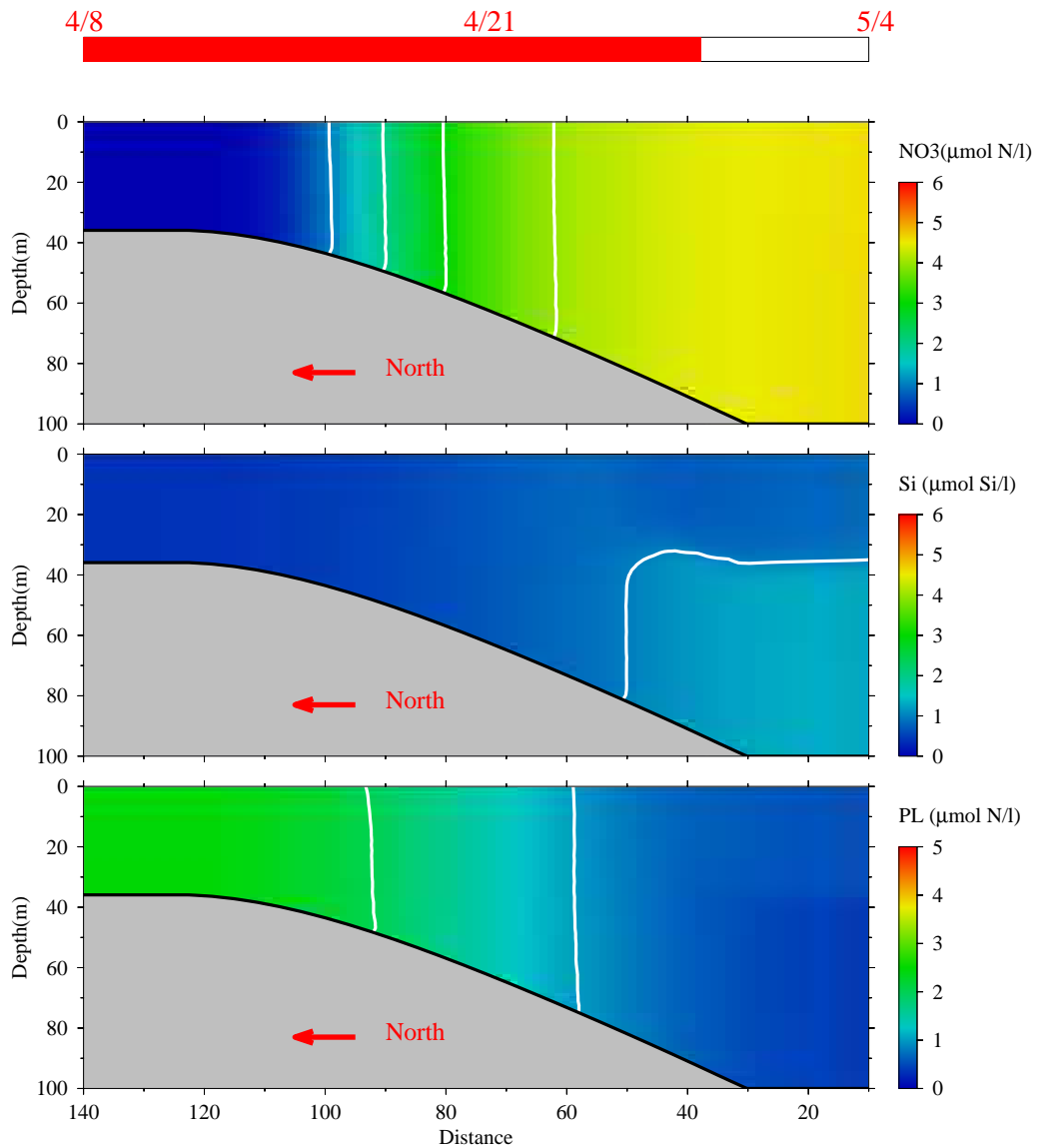


Figure 4.20: Model-computed cross-isobath distribution of tidally averaged nitrate (NO₃), silicate (Si) and large phytoplankton (PL) on the southern flank of GB on April 29, 1995 with low initial silicate concentration ($1 \mu\text{mol/l}$) in the deeper region (water depth >60 m).

nutrients from deep water and light availability kept large phytoplankton from declining (Figure 4.21). Subsurface phytoplankton maxima are not detectable by remote sensing, but have been detected on GB by *in situ* fluorometry (Figure 4.22, *Mountain and Taylor, 1996*) and direct chlorophyll measurement (Figure 4.23) conducted during early summer time.

A tidal mixing front is formed as the stratification is developed in the deeper flank area while water in the shallow central bank remains well-mixed. This seasonally developed tidal mixing front is an area associated with unique biological processes. Observational data indicates that in the frontal zone, the turbulence created by the strong tidal currents is most energetic at the bottom and stirs the water enough to mix some of the cold high- nutrient layer into the fully-mixed region where it is distributed throughout the water column. A tracer experiment with idealized front structure was carried out to examine the time scale of such a process and the effect of wind on this process. Figure (4.24) shows the initial distribution of the tracer. The initial concentration of tracer below the 10 °C isothermal line is 1.0 unit/l, while it is 0.0 unit/l in the rest of the model domain. In one tidal cycle the upward mixing process can bring the tracer up to the near surface (Figure 4.25), and in 5 days, the tracer is distributed in the whole water column near the front with a concentration of about 0.5 unit/l, decreasing shoreward (Figure 4.26). In the case without wind, the mixing of tracer seems to be slightly less extensive after 5 model days (Figure 4.27), but still shows significant mixing near the tidal mixing front area, indicating that tidal mixing is a major driving force to bring the high-nutrient water from deep water up into the surface.

As discussed in Chapter 3, the 1-D model did not capture the weak “second” diatom bloom along the 40- to 60-m isobath of GB, nitrogen limitation in the model simulation is one possible reason. The significant recovery of silicate due to enhanced remineralization processes alone is not able to stimulate the “second” bloom. How-

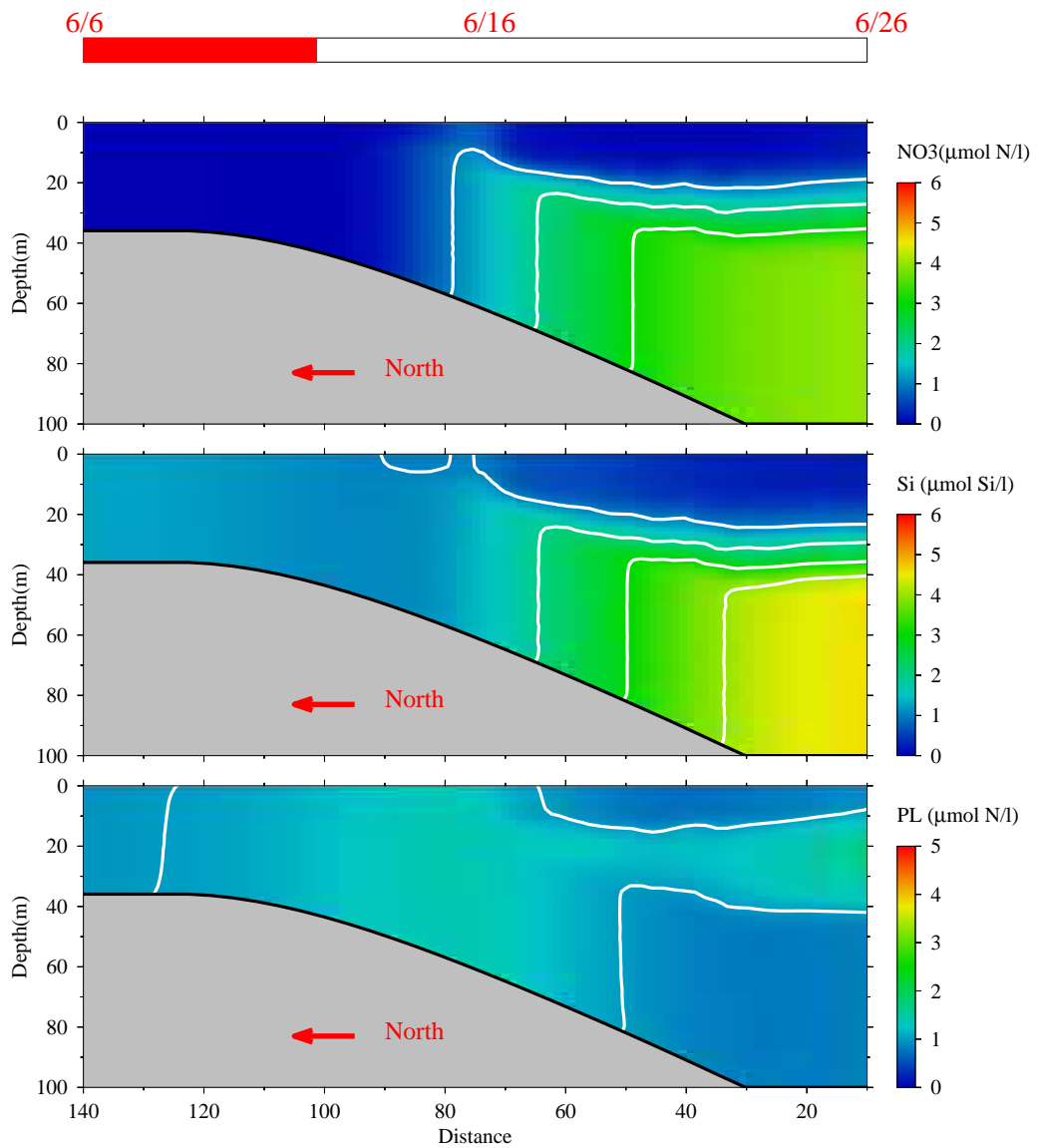


Figure 4.21: Model-computed cross-isobath distribution of tidally averaged nitrate (NO₃), silicate (Si) and large phytoplankton (PL) on the southern flank of GB on June 12, 1995, showing the stratification in the deeper region with nutrients being depleted in the surface layer (top two) and a subsurface maximum of large phytoplankton (bottom).

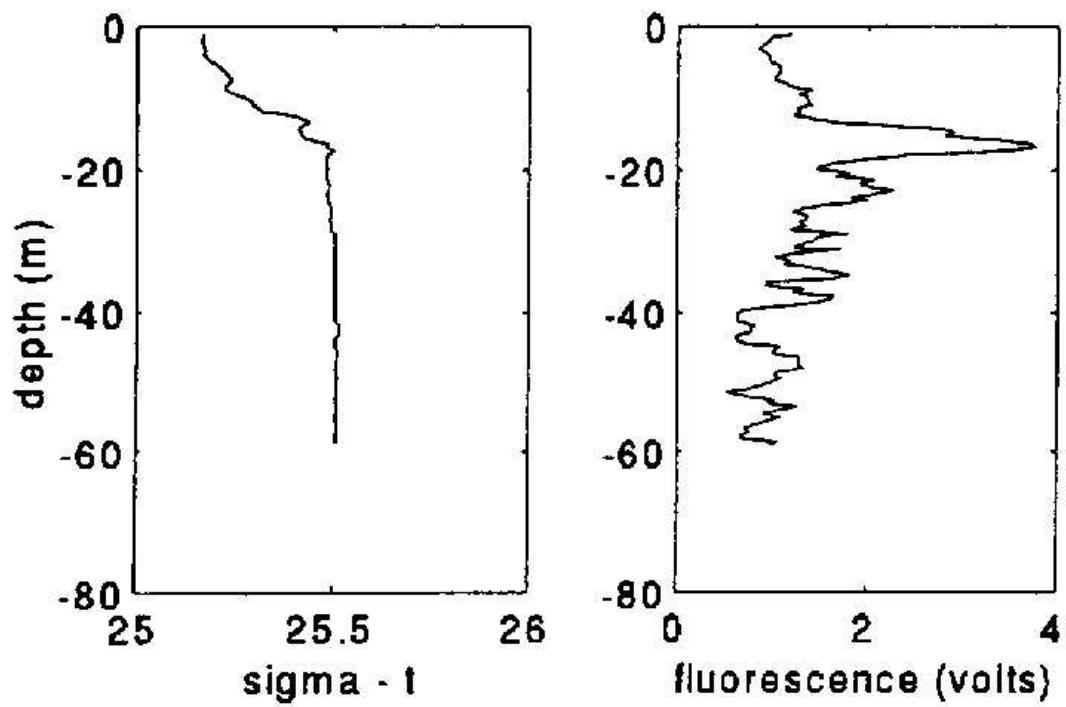


Figure 4.22: Fluorescence profile for representative station in the stratified areas of the southern flank of GB. This figure is from Mountain and Taylor (1996).

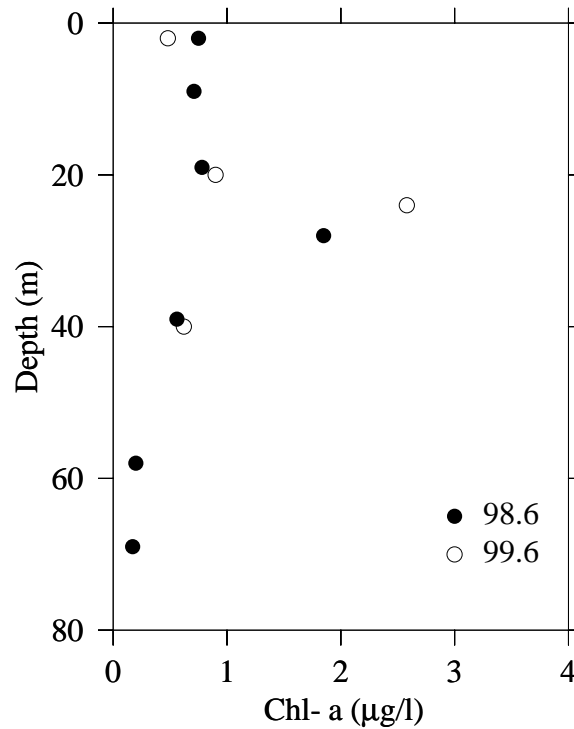


Figure 4.23: Chlorophyll *a* profile for station 15 during June of 1998 and 1999.

ever, in the 2-D model, a continuous nutrient support from deep nutrient-rich water is possible through tidal mixing processes. This, combined with episodic strong wind events which enhance the mixing and nutrient transport processes could support a “second” bloom near the tidal mixing front area. This model results indicate that this weak bloom is more likely to occur near the tidal mixing front area and is probably a re-occurring event controlled by both biological recycling process and the up-frontal nutrients transport.

4.5.3 PHYTOPLANKTON MAXIMUM AREA

As shown in the model results (Figure 4.8), a narrow band of high phytoplankton concentration at 40-60 m water depth area was observed. This area is coincident with

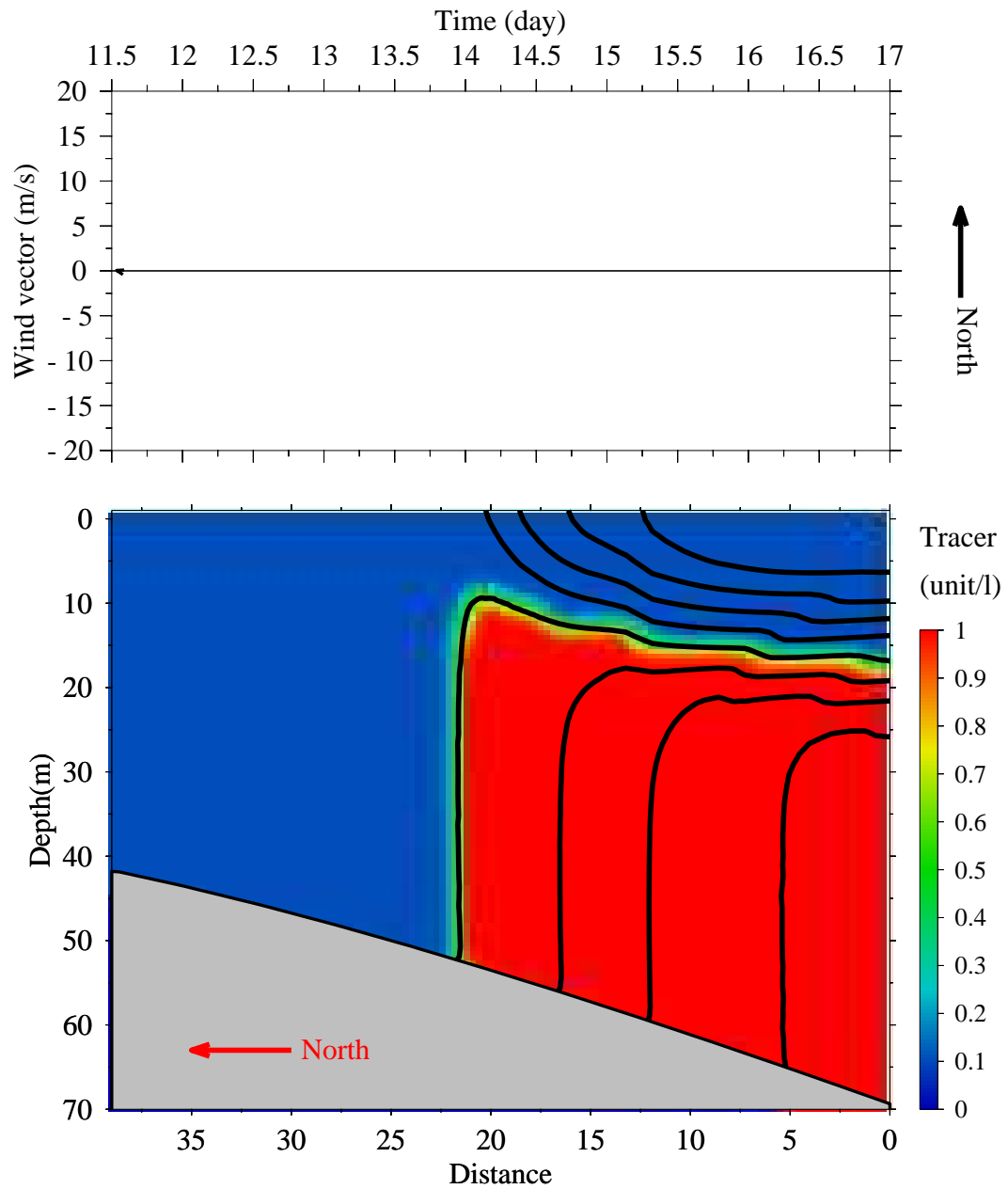


Figure 4.24: Initial distribution of tracer along the cross-isobath section, with concentration of tracer below the 10°C isothermal line is 1 unit/l and 0 unit/l in the rest of the area.

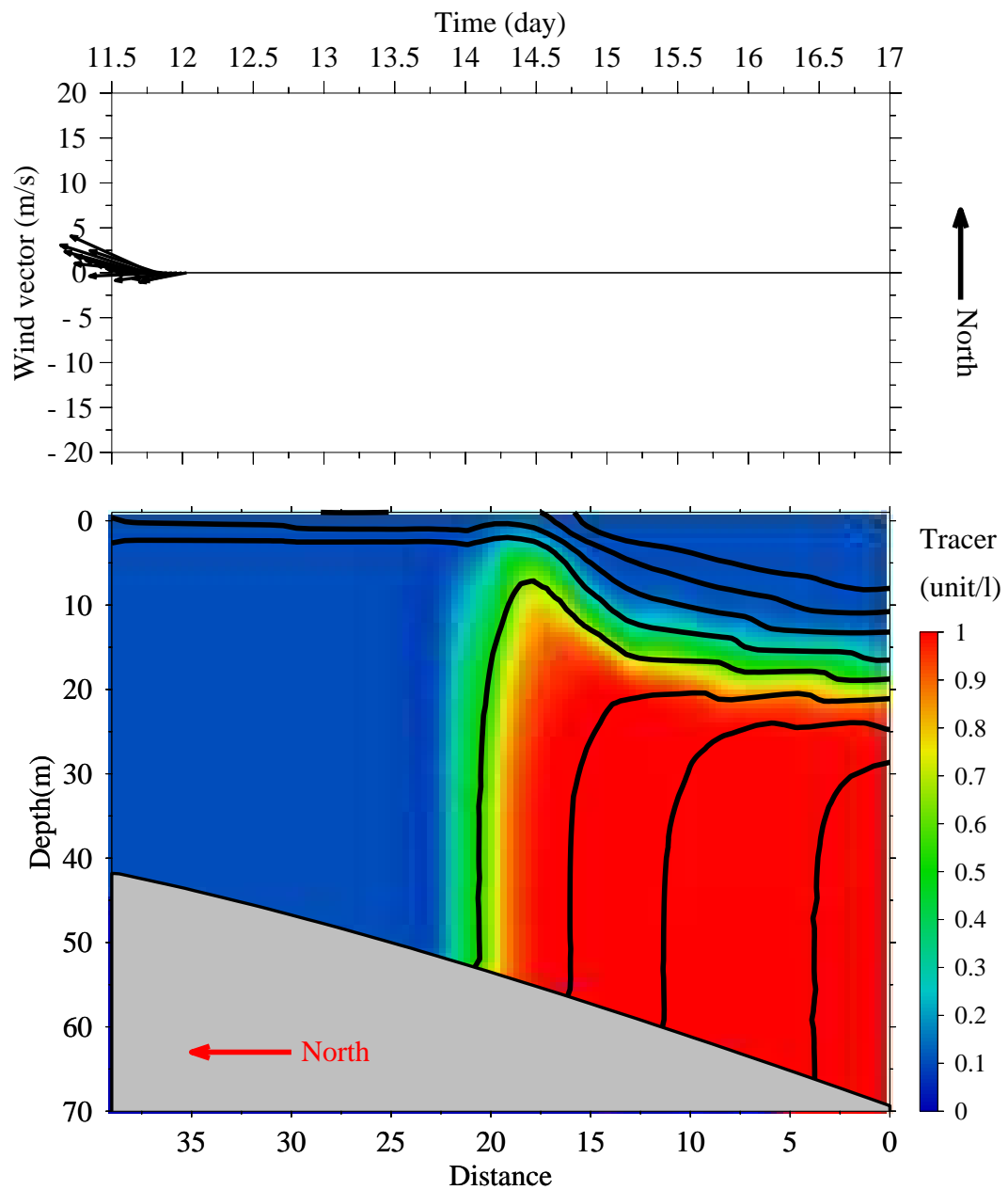


Figure 4.25: Model computed distribution of tracer along the cross-isobath section after one tidal cycle with tidal forcing plus realistic wind stress.

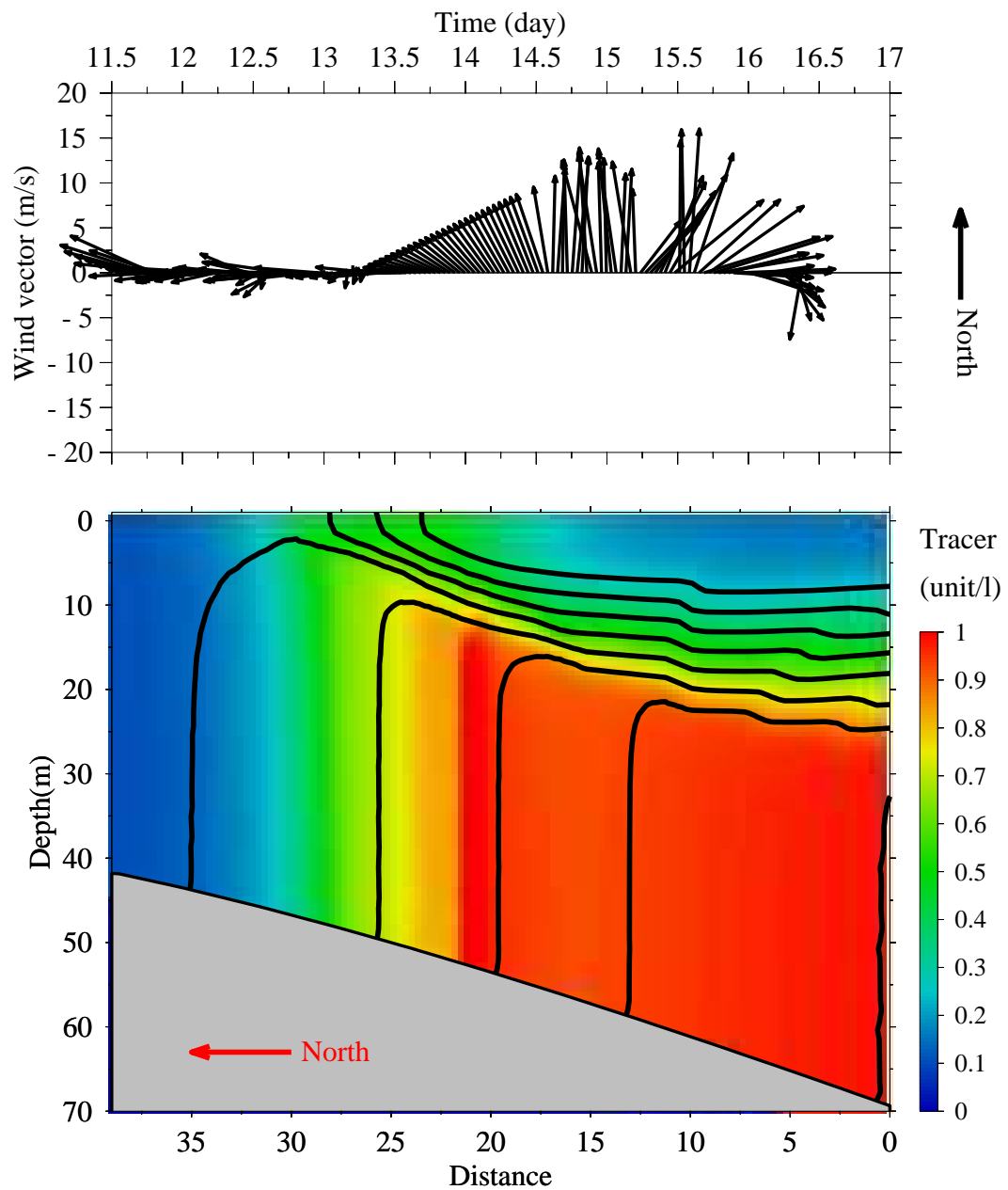


Figure 4.26: Model computed distribution of tracer along the cross-isobath section after ten tidal cycle with tidal forcing plus realistic wind stress.

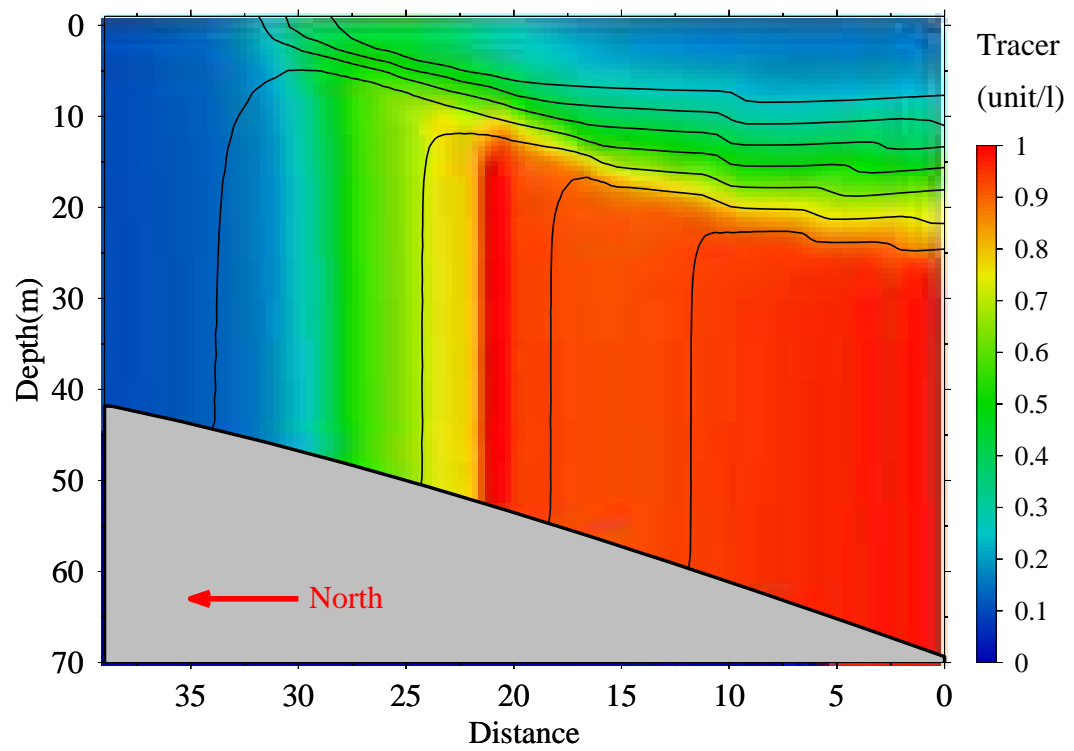


Figure 4.27: Model computed distribution of tracer along the cross-isobath section after ten tidal cycle with tidal only.

the tidal mixing front that occurs during stratification season. At that time however, no tidal mixing front exists since the water is completely mixed even in the deep flank area. Therefore the usual explanation for high phytoplankton concentration near a frontal area, such as water mass convergence, is not applicable.

Figure 4.28 illustrates a possible explanation for this phenomena. In the area shallower than 50 m, the biomass of phytoplankton starts to decline since nutrients are depleted during the end of spring bloom. Meanwhile, in the deep flank area, no phytoplankton bloom occurred because the vertical mixing dilutes the accumulation of phytoplankton biomass. As a result, a nutrient gradient can be found in the cross-bank section. As shown in the lower panel of Figure 4.28, during the flooding tide, high nutrient water mixes with low nutrient shallow water, causes a positive nutrient flux into the area with water depth of near 50 m. As a result, a phytoplankton maximum area (PMA) is formed. This influx of nutrients is utilized by phytoplankton and causes a net increase of biomass (the critical depth is less than mixing depth). During ebb tide, part of nutrients in the PMA has already been taken up by phytoplankton, therefore the loss of nutrients is less than the gain during flood time, and causes a net influx of nutrients into PMA.

Although theoretically the existence of PMA is possible, it is hard to observe in the field mainly due to the complicated topographic situation and possible effects from lateral advective processes. The wind-induced cross sectional advection may further complicate the situation. Figure 4.29 shows a weak PMA near the area with water depth of about 50 m in a transect across southern GB during April 1997. It remains unclear whether such phenomena recur each year and are observable bank-wide. Further field measurement with better spatial resolution may be needed to resolve this issue.

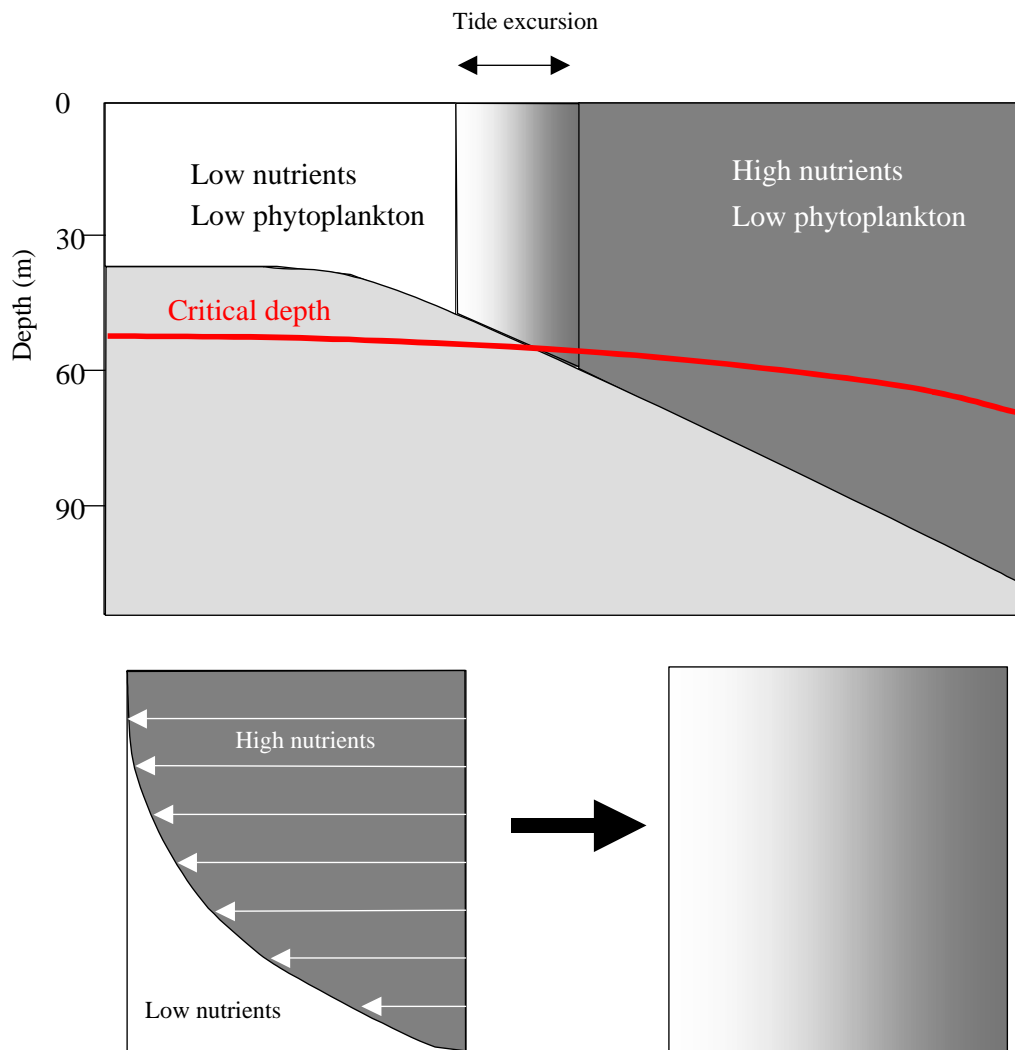


Figure 4.28: Schematic of formation of phytoplankton maximum area (PMA) in the transition between shallow and deep areas. See the text for detailed explanation.

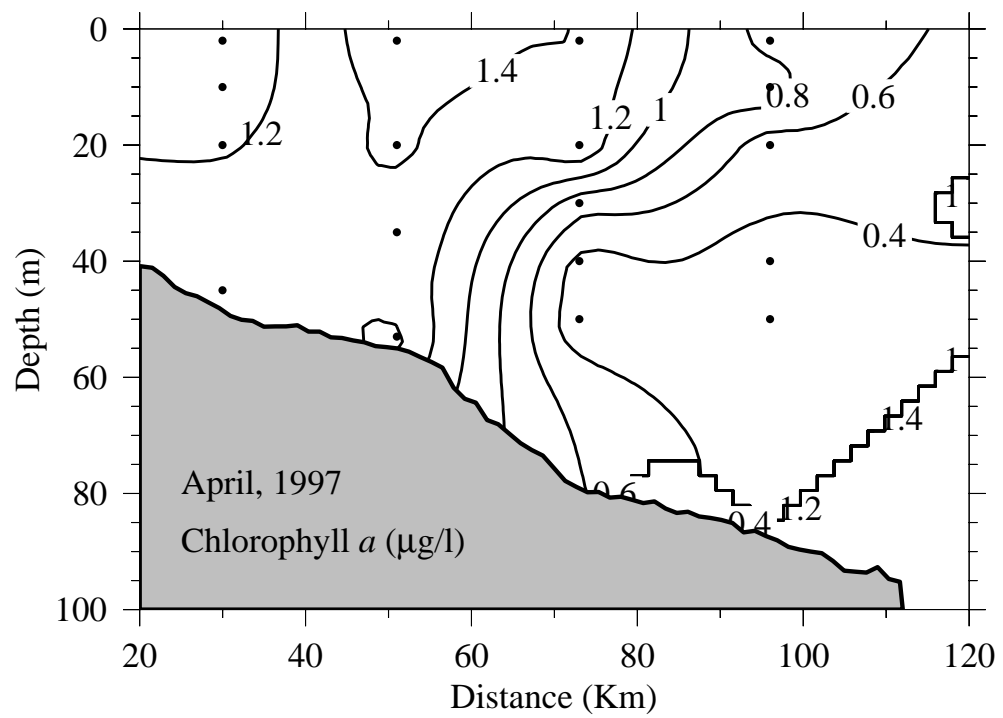


Figure 4.29: Example of a phytoplankton maximum area (PMA) in the transition between shallow and deep areas along the cross-isobath section during April 1997.

4.5.4 WHAT IS MISSING IN 2-D MODEL

In the model results, the phytoplankton bloom in the deep flank area corresponds to the development of stratification very well. This bloom occurred in April and declined as the nutrients were depleted in the surface mixing layer during late May. However, this dynamics is difficult to be observed in the field. Figure 4.30 shows the chlorophyll *a* concentration across a transect in the southern GB in 1999 (Figure 4.31). The sectional distribution is easy to understand for the January and February cases, with higher concentration in the shallow area and lower in the deep area. However, a higher value of chlorophyll *a* is observed during March, with concentrations reaching over 4 $\mu\text{g}/\text{l}$. This is not consistent with the model results. As we can also see from Figure 4.32, corresponding to the phytoplankton increase, the silicate concentration in the deep area is quickly reduced from 3-4 $\mu\text{mol}/\text{l}$ in February to 1-2 $\mu\text{mol}/\text{l}$ in March. Nitrate shows a similar decline, mainly in the surface layer above 60 m water depth (Figure 4.33). A vertical gradient of nitrate can also be observed, indicating that the water starts to show stratification as early as March, an impossible scenario in the model if only thermal-induced stratification was allowed to develop. Temperature gradient structure (Figure 4.34) verifies the existence of such stratification, but with lower temperature in the upper layer. Salinity structure (Figure 4.35) indicates that the water is less saline at the surface, which explains the existence of low temperature surface water. Thus it appears that the stratification structure in the southern flank of GB during March is mainly controlled by salinity.

The low-salinity water can inflow through the Northeast Channel on the eastern side [*Ramp et al.*, 1985; *Bisagni et al.*, 1996] and across the northern Great South Channel on the western side [*Chen et al.*, 1995]. This water can have a significant impact on the stratification processes on GB. The 2-D model is inherently unable to capture such dynamics. Therefore, the dynamics explored in this chapter are mainly

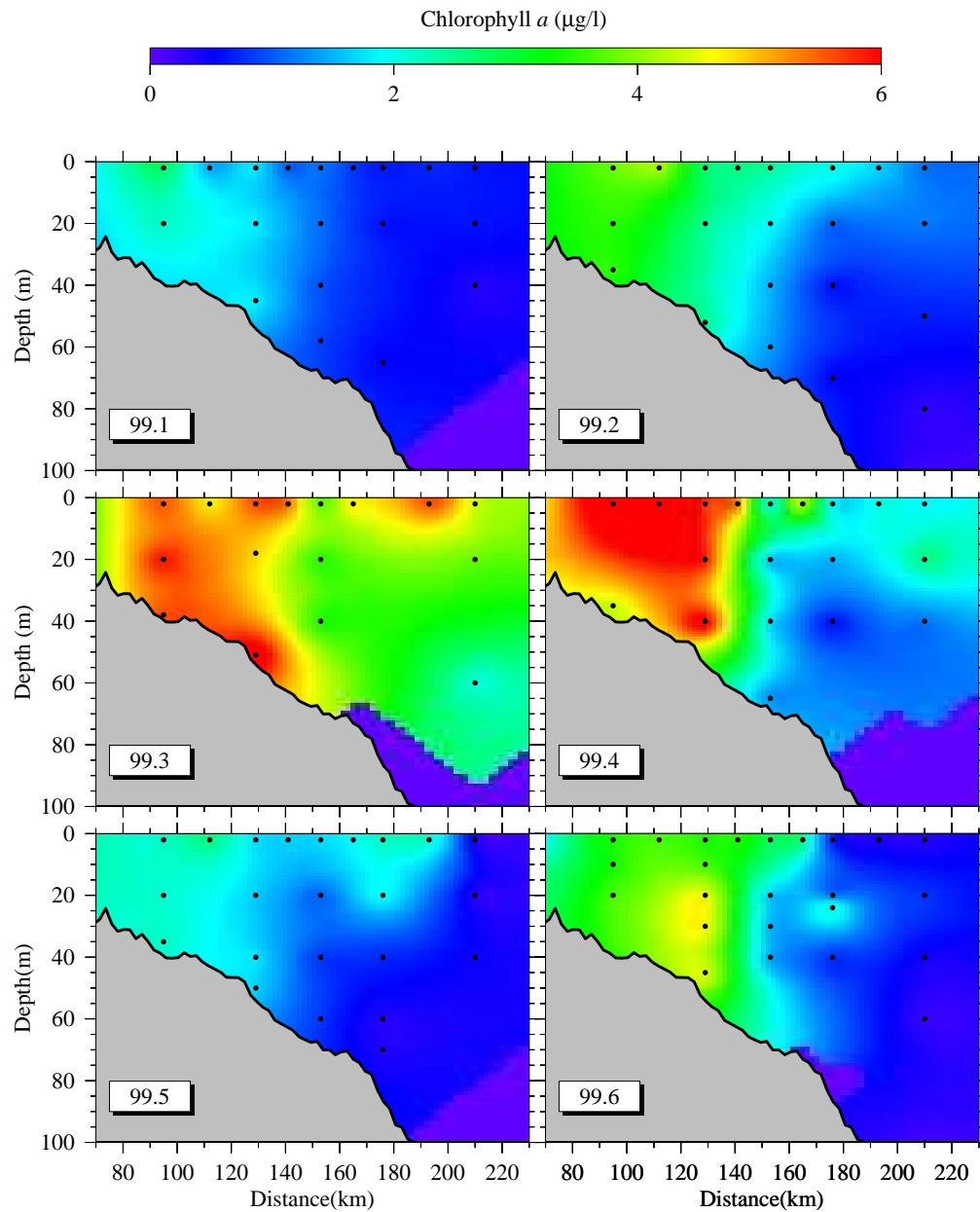


Figure 4.30: Cross-isobath distribution of chlorophyll *a* during the broad-scale survey for the U.S. GLOBEC/GB Program in 1999.

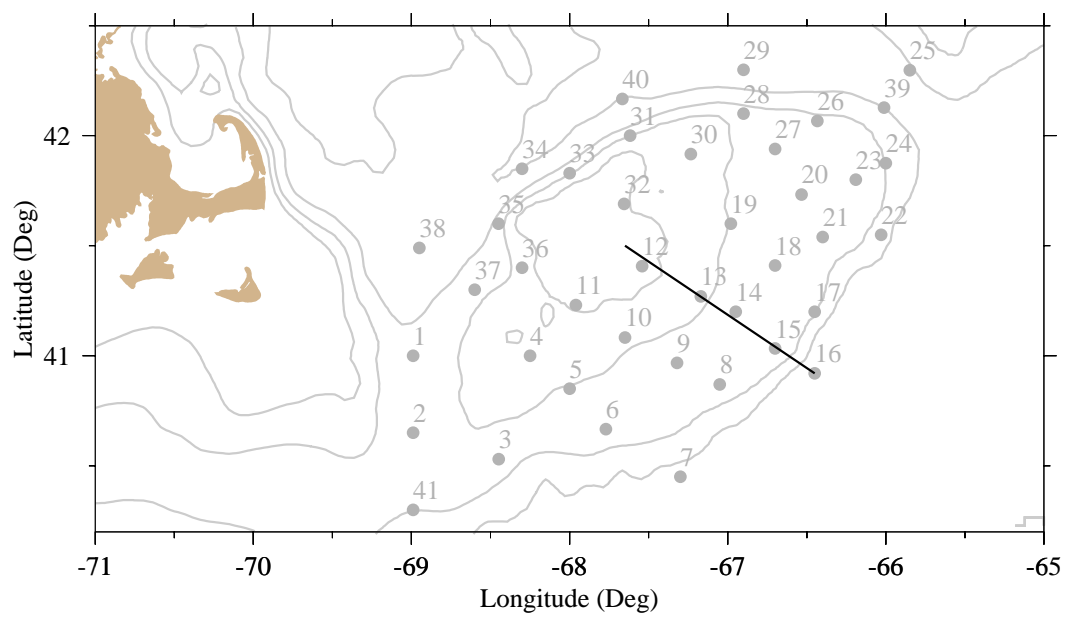


Figure 4.31: A cross-isobath section used to plot the vertical distribution of chlorophyll *a*, silicate, nitrate, temperature and salinity during the broad scale survey for the U.S. GLOBEC/GB Program in 1999.

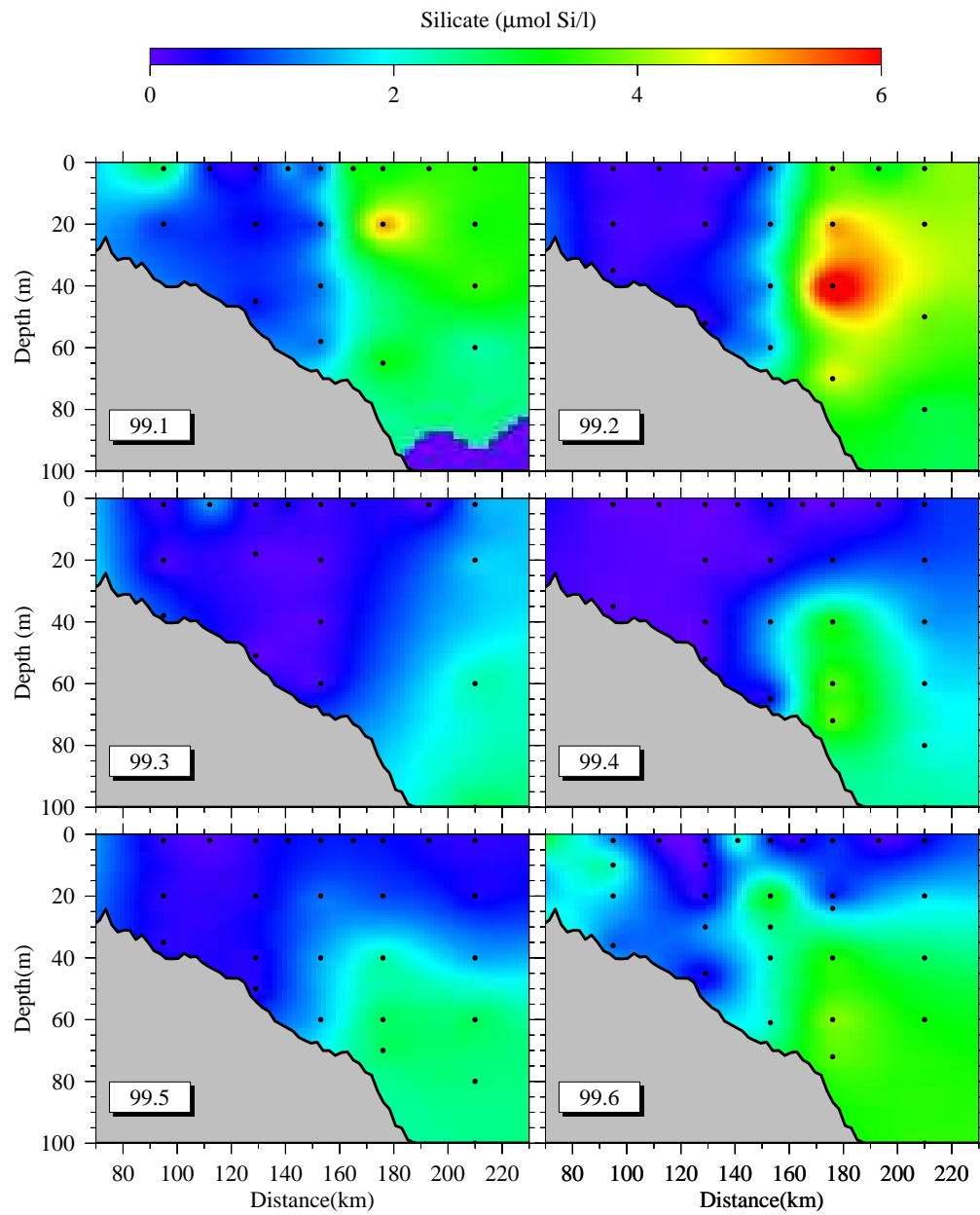


Figure 4.32: Cross-isobath distribution of silicate during the broad-scale survey for the U.S. GLOBEC/GB Program in 1999.

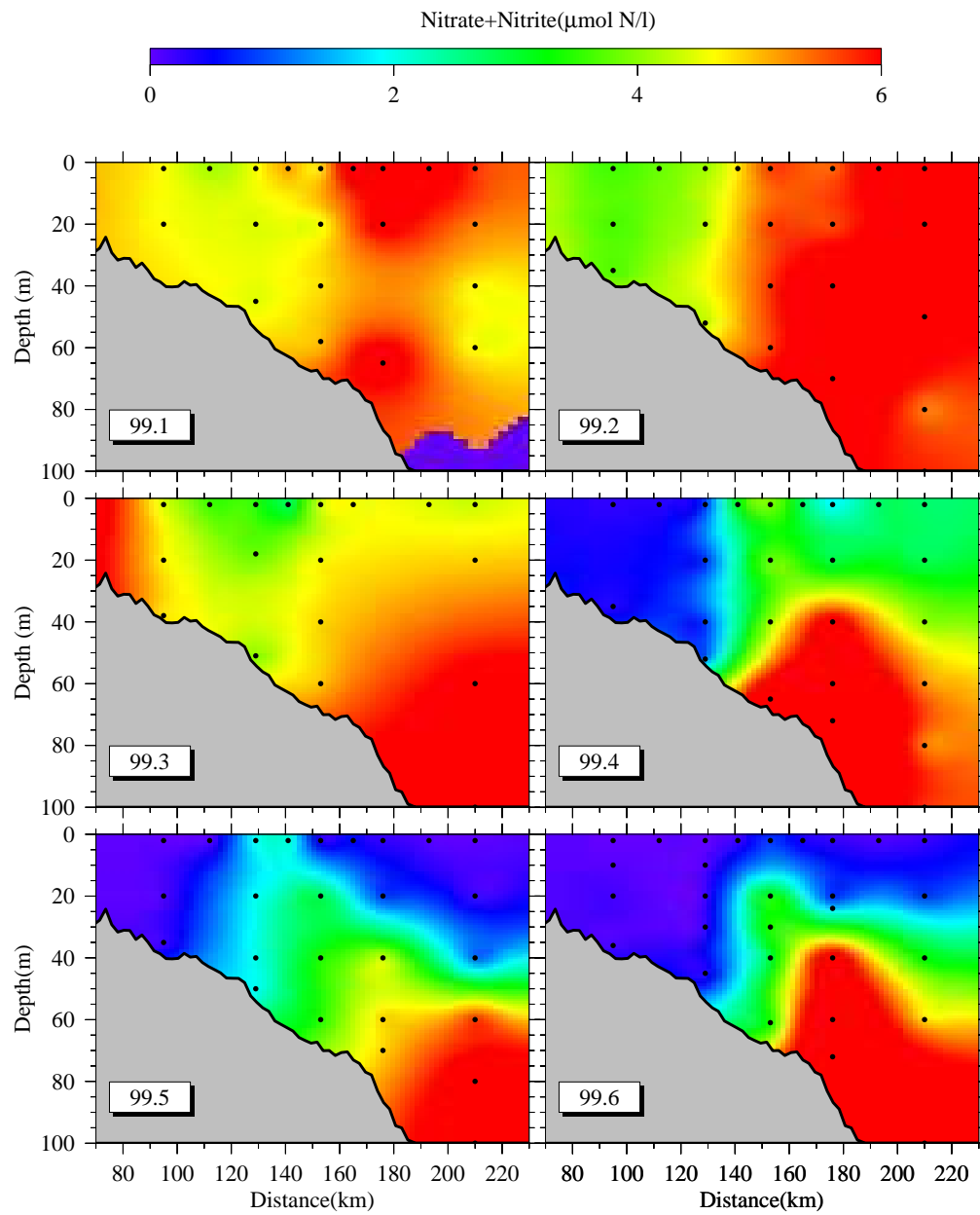


Figure 4.33: Cross-isobath distribution of nitrate during the broad-scale survey for the U.S. GLOBEC/GB Program in 1999.

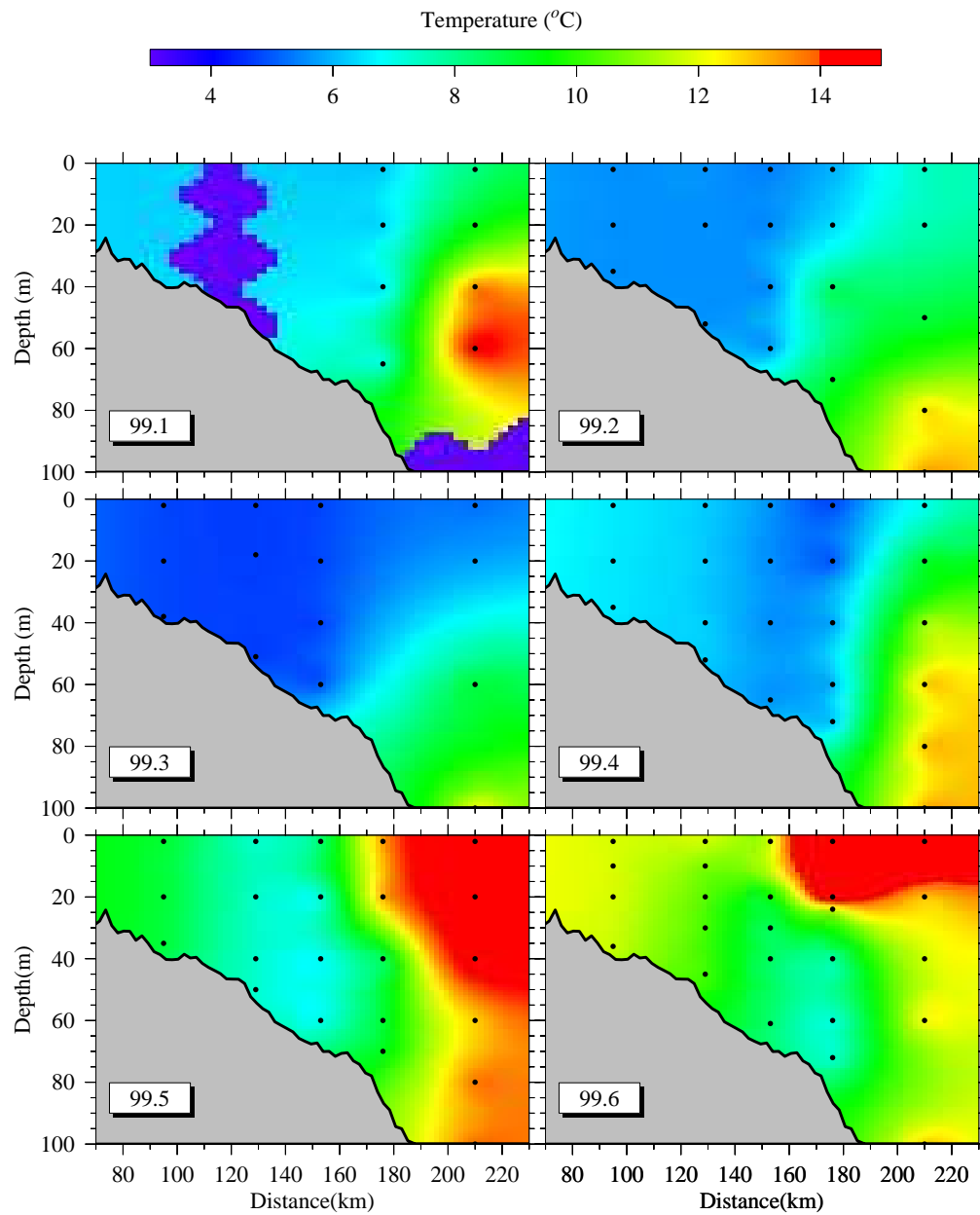


Figure 4.34: Cross-isobath distribution of temperature during the broad-scale survey for the U.S. GLOBEC/GB Program in 1999.

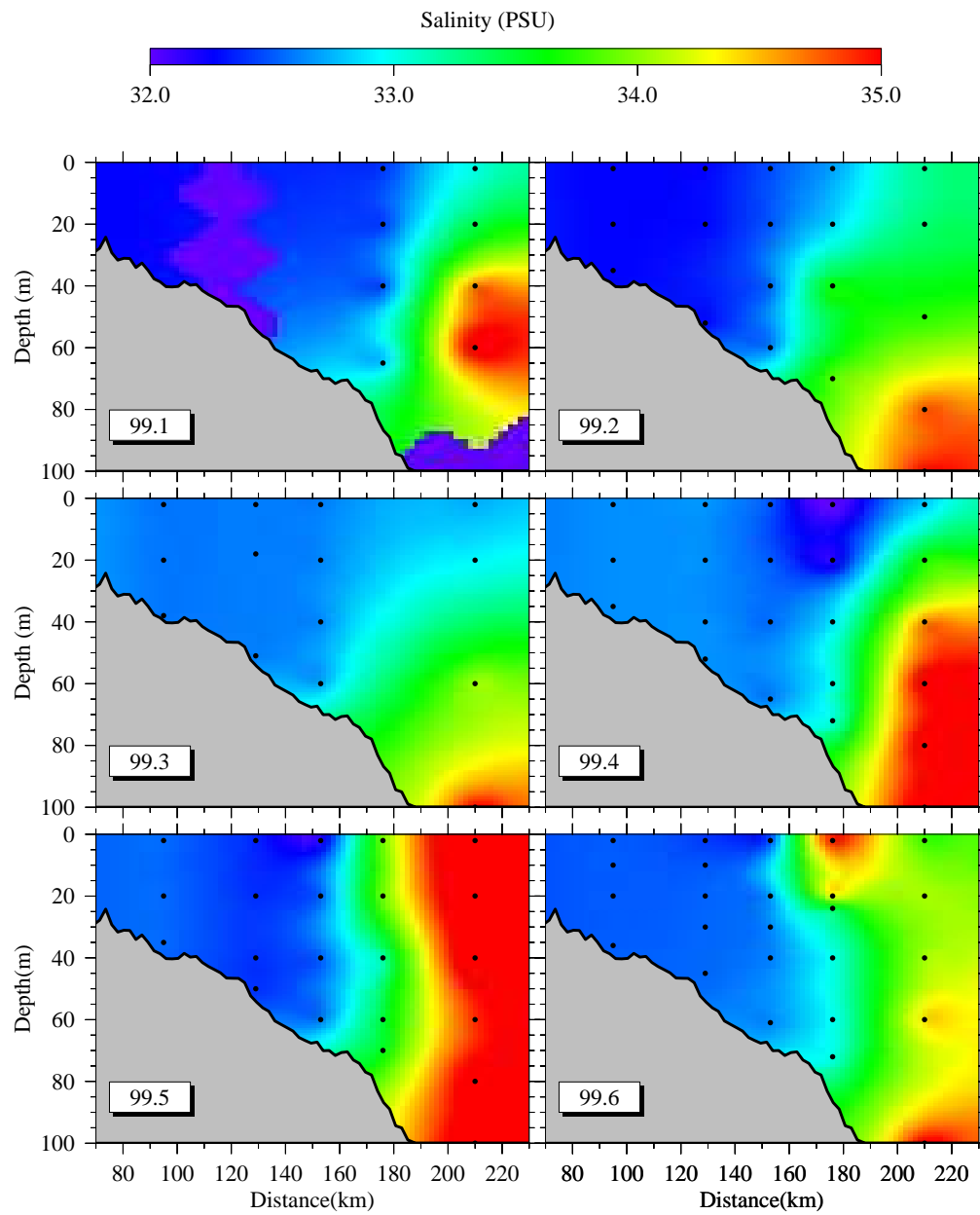


Figure 4.35: Cross-isobath distribution of salinity during the broad-scale survey for the U.S. GLOBEC/GB Program in 1999.

process-oriented and focus on the sensitivity of biological response to the fluctuation of physical environment. The impact of advection process is discussed in a three-dimensional model experiment featured with an “cross over” event as shown in next Chapter.

4.6 SUMMARY

The 2-D model experiments shown here demonstrate the spring bloom dynamics in a transect across the southern GB. The model shows that:

1. Timing and magnitude of the spring bloom in the shallow central bank and deep flank area mirrors the results in 1-D model experiments.
2. The phytoplankton maximum area that occurred between the shallow and deep area is a result of light availability and continuous nutrient support from nutrient rich off-bank water through tidal mixing processes.
3. Development of the spring bloom in the deep flank area is sensitive to the development of stratification, especially during the transition time between vertical mixing and stratification, usually in later April.
4. The development of a subsurface layer of high phytoplankton concentration after stratification is the result of phytoplankton growth and sinking in the surface mixing layer.

As with the 1-D model, the difference between model results and observed biological features indicate that the 2-D model is not able to capture the basic dynamics of the biological system in the deep flank area, mainly due to the lack of lateral advective processes. Also because of the sensitivity of the biological system to the hydrodynamic environment, the accuracy of the physical model is critical to obtain good model results of biological variables.

4.7 REFERENCES

- Bisagni, J. J., R. C. Beardsley, C. M. Ruhsam, J. P. Manning, and W. J. Williams, Historical and recent evidence of Scotian Shelf Water on southern Georges Bank, *Deep Sea Research II*, *43*, 1439–1472, 1996.
- Chen, C., and R. Beardsley, Tidal mixing and cross-frontal particle exchange over a finite amplitude asymmetric bank: A model study with application to Georges Bank, *Journal of Marine Research*, *56*, 1163–1201, 1998.
- Chen, C., and R. Beardsley, Cross-frontal water exchange on Georges Bank: modeling exploration of the US GLOBEC/Georges Bank phase III study, *Journal of Oceanography*, *58*, 403–420, 2002.
- Chen, C., and R. C. Beardsley, Numerical study of stratified tidal rectification over finite-amplitude banks. Part I: Symmetric Banks, *Journal of Physical Oceanography*, *25*, 2090–2210, 1995.
- Chen, C., R. C. Beardsley, and R. Limeburner, Numerical study of stratified tidal rectification over finite-amplitude banks. Part II: Georges Bank, *Journal of Physical Oceanography*, *25*, 2111–2128, 1995.
- Chen, C., R. Beardsley, P. J. S. Franks, and J. V. Keuren, Influences of diurnal varying heat flux on circulation and stratification over Georges Bank: a 3-D prognostic model experiment, *Journal of Geophysical Research*, In press, 2003a.
- Chen, C., R. Beardsley, P. J. S. Franks, and J. V. Keuren, Wind-induced cross-frontal water transport on the southern flank of Georges Bank: A physical mechanism for the cross-frontal fish larval transport in early summer, *Journal of Geophysical Research*, In press, 2003b.

- Eigenheer, A., W. Kühn, and G. Radach, On the sensitivity of ecosystem box model simulations on mixed-layer depth estimates, *Deep Sea Research I*, 43(7), 1011–1027, 1996.
- Eilers, P. H. C., and J. C. H. Peeters, A model for the relationship between light intensity and the rate of photosynthesis in phytoplankton, *Ecological Modelling*, 42, 199–215, 1988.
- Franks, P. J. S., and C. Chen, Plankton production in tidal fronts: A model of Georges Bank in summer, *Journal of Marine Research*, 54, 631–651, 1996.
- Garrett, C. J. R., and J. W. Loder, Dynamical aspects of shallow sea fronts, *Philosophical Transactions of the Royal Society of London*, A302, 563–581, 1981.
- Jassby, A. D., and T. Platt, Mathematical formulation of the relationship between photosynthesis and light for phytoplankton, *Limnology and Oceanography*, 21(4), 540–547, 1976.
- Mann, K. H., and J. R. N. Lazier, *Dynamics of Marine Ecosystems: Biological-Physical Interactions in the Oceans*, second ed., 400 pp., Blackwell Science, Cambridge, Massachusetts and Oxford, U.K., 1996.
- Mountain, D. G., and M. H. Taylor, Fluorescence structure in the region of the tidal mixing front on the southern flank of Georges Bank, *Deep Sea Research II*, 43(7-8), 1831–1853, 1996.
- Ramp, S., R. Schlitz, and W. Wright, The deep flow through the Northeast Channel, Gulf of Maine, *Journal of Physical Oceanography*, 15, 1790–1808, 1985.
- Ruardij, P., H. V. Haren, and H. Ridderiokhof, The impact of thermal stratification on phytoplankton and nutrient dynamics in shelf seas: a model study, *Journal of Sea Research*, 38, 311–331, 1997.

Springtall, J., and M. F. Cronin, Upper ocean vertical structure, in *Encyclopedia of Ocean Sciences*, vol. 6, edited by J. Steele, S. Thorpe, and K. Turekian, pp. 3120–3129, Academic Press, London, UK, 2001.

Steele, J. H., Environmental control of photosynthesis in the sea, *Limnology and Oceanography*, 7, 137–150, 1962.

Sverdrup, H. U., On conditions for the vernal blooming of phytoplankton, *Journal du Conseil International pour l'Exploration de la Mer*, 18, 287–295, 1953.

Townsend, D. W., and M. Thomas, Springtime nutrient and phytoplankton dynamics on Georges Bank, *Marine Ecology Progress Series*, 228, 57–74, 2002.

CHAPTER 5

THE IMPACT OF SCOTIAN SHELF WATER “CROSS-OVER” ON THE PLANKTON DYNAMICS ON GEORGES BANK: A 3-D EXPERIMENT FOR THE 1999 SPRING BLOOM¹

¹R. Ji. Will be submitted to *Journal of Geophysical Research*. 2003.12.

5.1 ABSTRACT

The 1999 March SeaWiFS images detected an intensive bloom on the southern flank of Georges Bank (GB). The bloom covered a large portion of the southern flank between 60- and 200-m isobaths, and later extended to and connected with an even larger patch near the North-East Peak and Browns Bank during later March. A three-dimensional (3-D) model experiment was conducted to examine the cause of the bloom and the impact of Scotian Shelf Water on spring phytoplankton bloom dynamics. The Finite Volume Coastal Ocean Model (FVCOM) provided the hydrodynamic field for the Lagrange particle trajectory, tracer and biological model experiments.

Process-oriented modeling experiments showed that the formation of the phytoplankton bloom on the southeastern flank of GB is related to (1) transport of the Scotian Shelf Water, (2) wind- and tidal-induced vertical mixing and surface cooling, and (3) the location of the salinity front. With sufficient nutrients from the slope, the bloom can be the result of *in situ* growth of phytoplankton near the slope where the stabilized salinity front is located. The model results suggested that an accurate simulation of the spatial distribution of temperature and salinity on GB, as well as the flow field across the Northeast Channel is a prerequisite for modeling the spring bloom over GB.

5.2 INTRODUCTION

The springtime phytoplankton bloom in the Gulf of Maine (GOM) and Georges Bank (GB) is a recurrent seasonal event that persists over periods of weeks. It usually occurs in March and April over a large area, and can be easily detected from satellite images. The spring bloom is important in modifying the elemental composition of surface waters, providing a food source for upper trophic levels and potentially having

a long term (in the scale of months) impact on lower trophic food web dynamics [Cloern, 1996]. For instance, the Northeast Peak (NEP) and the southern flank of GB are critical areas for the recruitment of *Calanus finmarchicus*, the dominant zooplankton species during springtime on GB (Chapter 1). The temporal variation and spatial distribution of phytoplankton over these areas have a direct impact on the zooplankton population dynamics. Food limitation on zooplankton is observed on the southern flank of the bank in April 1997 [Campbell *et al.*, 2001]. The timing and magnitude of the spring bloom is a critical factor affecting the spatial and temporal scale of food limitation on zooplankton population.

In a natural system, the bloom usually shows “patchiness”, which is mainly controlled by (1) spatial variability in population dynamics (i.e. the local balance between phytoplankton production and loss), and (2) spatially and temporally variable transports of water and phytoplankton [Lucas *et al.*, 1999]. Local change of phytoplankton biomass depends on transport (advection and diffusion) as well as spatially and temporally variable local growth, which can be summarized by the following equation:

$$\frac{\partial C}{\partial t} = B - \nabla \cdot (VC) + \nabla \cdot (K\nabla C),$$

where $C(x, y, z, t)$ is the concentration of phytoplankton at position (x, y, z) at time t ; $V(u, v, w)$ represents the advective fluid velocities in x, y, z directions; K_x, K_y, K_z are diffusivities in x, y, z direction; $\nabla = (\partial/\partial x, \partial/\partial y, \partial/\partial z)$ is the Laplacian operator; and B is the biological source and sink term. On the left side of equation is the local change of C . On the right side, the first term is the biological source and sink term B ; the second term is the advection term; and the third term is the diffusion term. B varies significantly horizontally due to variations in water column height, as well as differences in turbidity, nutrient concentrations, grazing pressure and so on.

As suggested in 1D and 2D model studies (chapter 3 and 4), in the absence of advection, the spring bloom in the deep area of GB could occur only when thermally-induced stratification developed, usually after later April. As shown in Figure 5.1, this appears to be not true in March 1999, when a significant bloom was observed on the southern flank of the bank, indicating the importance of horizontal transport on the spring bloom dynamics in this area. Water in NEP and the southern flank could be advected from many sources, including GOM, Southern Scotian Shelf, the central Bank and continental slope (Figure 5.2). Flow from GOM onto the bank is a major pathway of water and has been described in various studies; while the direct “cross-over” of Scotian Shelf Water (SSW) appears to be an episodic event as suggested by the historical data [Bigelow, 1927; Hopkins and Garfield, 1981; Flagg, 1987] and recent satellite-derived sea surface temperature (SST) and hydrographic data [Bisagni *et al.*, 1996]. Using the low-salinity (< 32 PSU) signature of SSW, Bisagni and Smith [1998] showed that “cross-over” events could be related to the passage of cyclonic eddies and recur with a 3-5 yr time scale. Water exchange between the central bank and the surrounding area is mainly controlled by wind-driven transport process. Both modeling studies [e.g., Lewis *et al.*, 2001] and drifter experiments [Naimie *et al.*, 2001] indicate that the displacement of plankton from the central bank to the NEP and the southern flank could occur in 10 days with strong winds in a favorable direction. The last potential source is from the slope water in the form of warm-core rings (WCR) as suggested by Ryan *et al.* [1999, 2001]. Interaction of WCRs with the surrounding hydrography can enhance phytoplankton biomass within the core and along the shelf break of GB. However, this process usually occurs during late spring.

Once the water flows onto NEP and the southern flank, it follows a clockwise circulation along the isobath between about 60 m and 100 m with maximum speeds of about 3-5 cm/s [Chen *et al.*, 2001]. The occurrence of blooms upstream has a

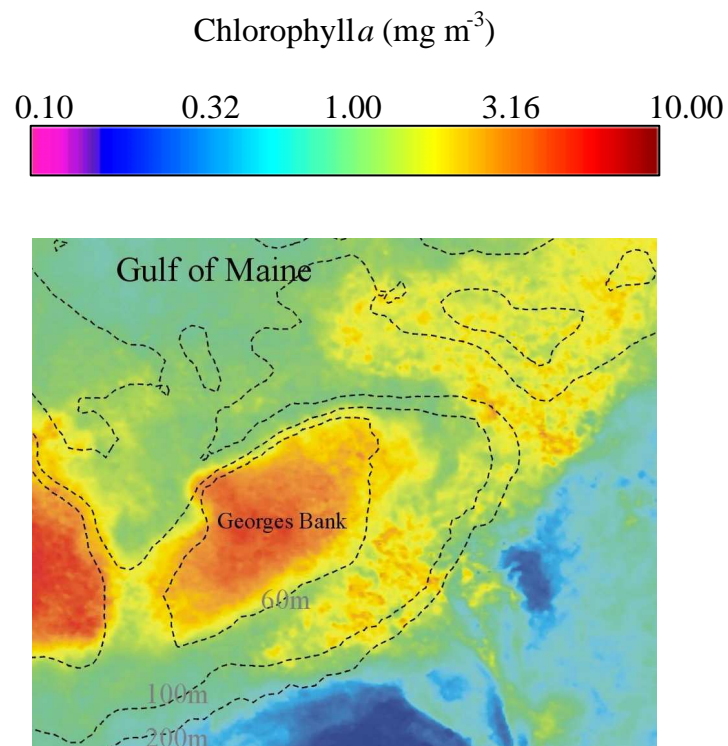


Figure 5.1: Monthly composite SeaWiFS image of GB and surrounding area during March 1999. Image is adapted from Dr. Andrew Thomas's website at the School of Marine Sciences, University of Maine.

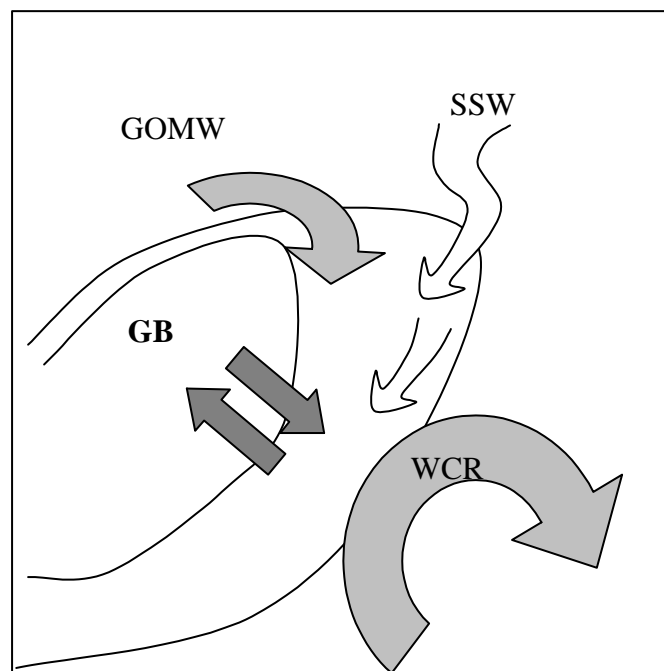


Figure 5.2: Schematic of possible source of water on the southern flank of GB. GOMW: Gulf of Maine Water; SSW: Scotian Shelf Water; GB: Georges Bank; WCR: Warm Core Ring.

significant influence on the ecosystem dynamics downstream, since the post-bloom water is usually nutrient depleted at the surface, and phytoplankton community structure may be altered significantly.

In this study, the focus is on the effect of SSW “cross-over” on the spring bloom dynamics with a case study in March 1999. The remaining sections of this chapter are organized as follows. In Section 5.3, the observed features of nutrients and phytoplankton dynamics in NEP and the southern flank are described. In Section 5.4, the modeling approach and design of numerical experiments is presented. The model results are given in Section 5.5, followed by the discussion in Section 5.6. Finally, the conclusions are summarized in Section 5.7.

5.3 OBSERVED BIOLOGICAL FEATURES ASSOCIATED WITH SSW “CROSS-OVER”

5.3.1 VIEWS FROM THE SATELLITE

The 1999 March SeaWiFS data clearly shows a spatially extensive bloom occurred near The Northeast Channel (NEC) and Browns Bank from julian day 73 to day 80 (Figure 5.3, upper panel, Area 1). The concentration of chlorophyll *a* in this area was higher than $3.0 \mu\text{g}/\text{l}$ and reached about $8.0 \mu\text{g}/\text{l}$ in some patches. Meanwhile, an equally intense bloom was observed on the southern flank (Figure 5.3, upper panel, Area 2). This blooming patch was disconnected from the patches over NEC and Browns Bank areas. It extended on-bank reaching the 60 m isobath, and off-bank, reaching the 200 m isobath. Between day 81 and day 88, this relatively small patch in Area 2 seems to be extended and connected with the larger patch in Area 1 along the northeast edge of the bank (Figure 5.3, middle panel). The bloom declined afterward, with only some sporadic patches remained in NEP and the southern edge of the bank (Figure 5.3, bottom panel).

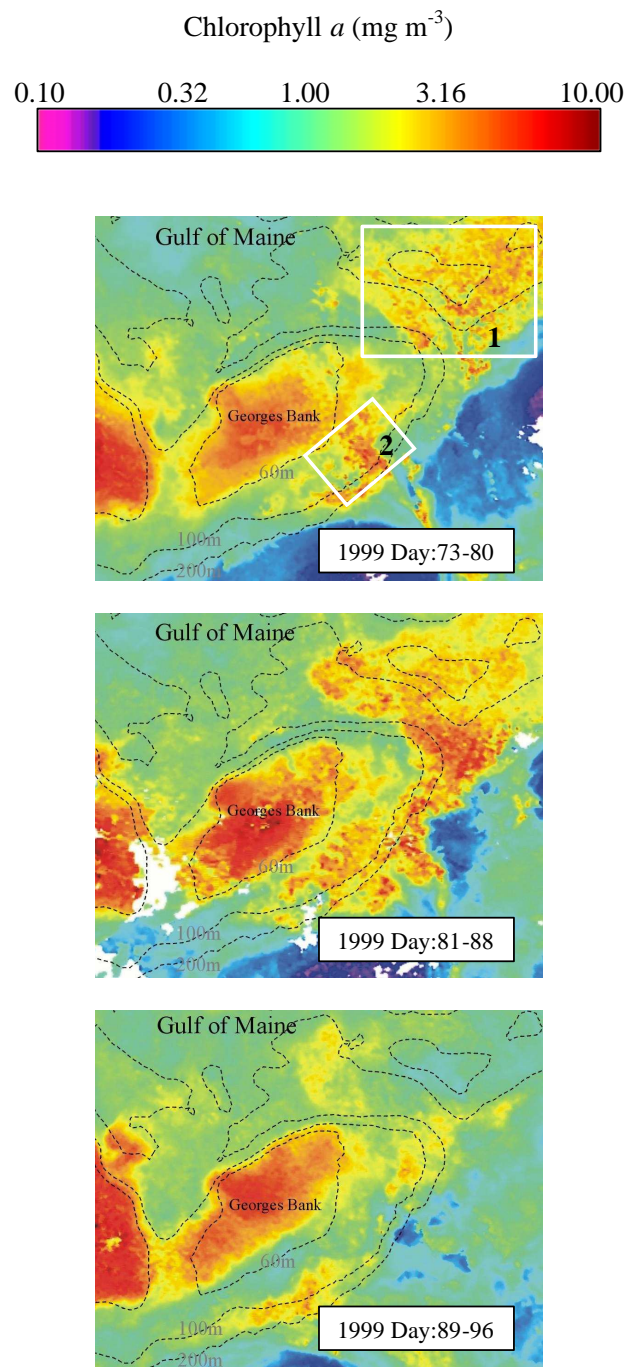


Figure 5.3: Eight-day composite SeaWiFS image of GB and surrounding area during March 1999. Image is adapted from Dr. Andrew Thomas's website at the School of Marine Sciences, University of Maine.

The water mass in Area 1 carried a clear signature of cold surface water temperature, as seen in Figure 5.4. The intrusion of water from the Browns Bank area across NEP occurred as early as February 16 (image labeled with “day 47” in upper left panel of Figure 5.4). The signal of cold water band “cross-over” was not stable during March. In day 62 and 65, the “cross-over” was weak. The cold SSW moved along the northeast edge of the bank between 100- and 200-m isobaths, with a small stream crossing the 100-m isobath and flowing to NEP. In day 76, the “cross-over” became significant and can be clearly observed from SST data. Two days later, the cold- water patch covered almost half of NEP area. This cold water patch seems to disappear at the end of March, as shown in the SST image of day 89.

5.3.2 CTD PROFILES

Unlike satellite images, which can only report the surface concentration of chlorophyll *a* and water temperature, CTD measurements are able to detect vertical profiles of physical and biological components in the water column. During the GLOBEC/GB broad-scale survey, CTD measurements were conducted in the stations covering the whole GB as shown in Figure 5.5. Here we briefly present the temperature, salinity, and fluorescence structure in March 1999 at the stations along a path from NEC to the southern flank of the bank as indicated by the connected arrows in Figure 5.5.

Figure 5.6 shows that the surface water (less than 30 m depth) of the easternmost station (25) had a temperature of about 3 °C and a salinity of about 31.7 PSU. This low salinity (less than 32 PSU) is a distinct signature of SSW, which confirms the observed feature of SST data. The temperature and salinity quickly increased at water depths below 30 m. The water below 60 m at this location had a high temperature (over 10 °C) and salinity (over 34 PSU), making it most likely a slope water mass. Accompanied with such a T-S vertical structure, fluorescence data showed a higher value at the surface (above 30 m) and decreases sharply below.

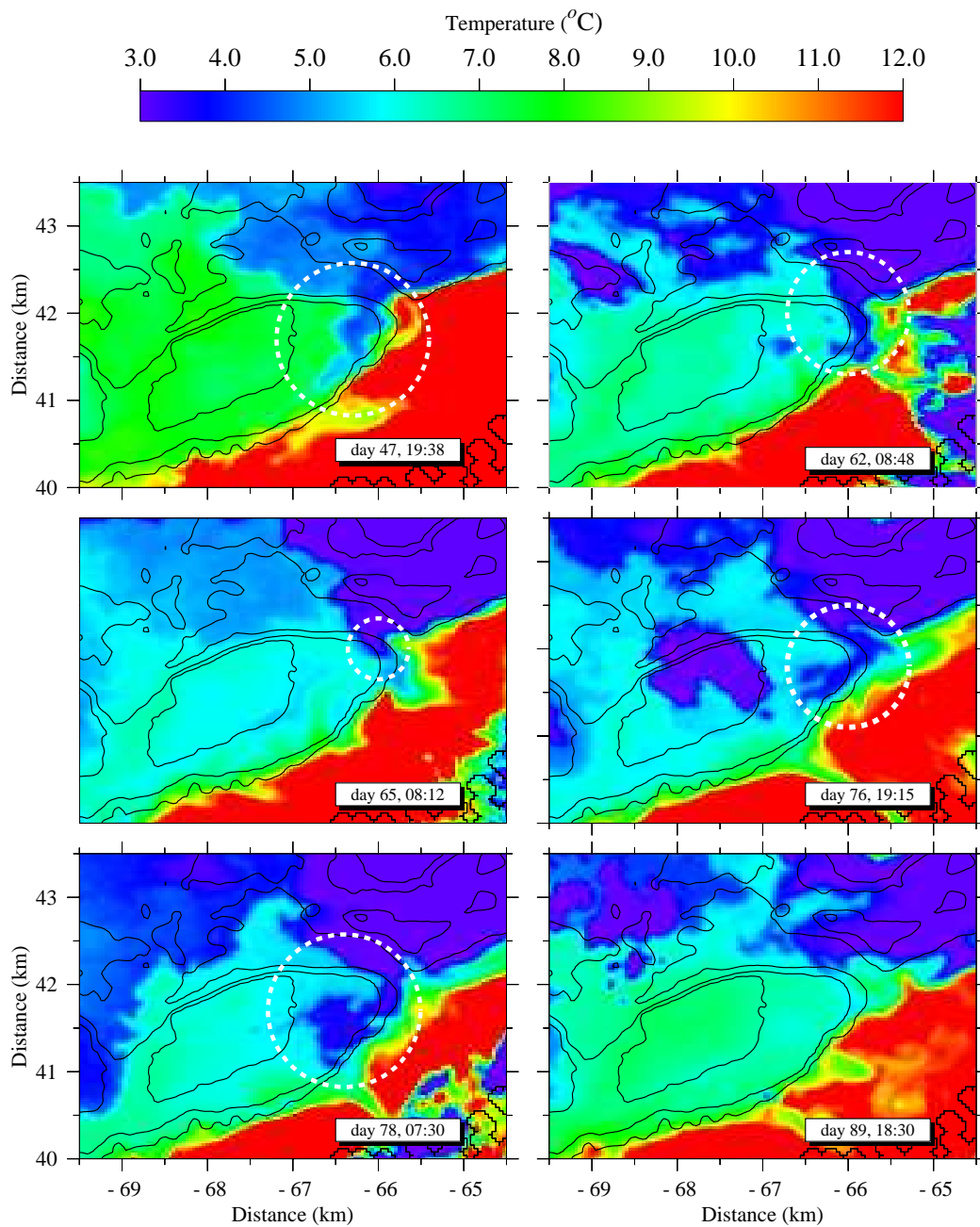


Figure 5.4: Selected Sea Surface Temperature (SST) images of GB and surrounding area during March 1999. Data is downloaded from NOAA's AVHRR (Advanced Very High Resolution Radiometer) website. White circles highlight SSW intrusion.

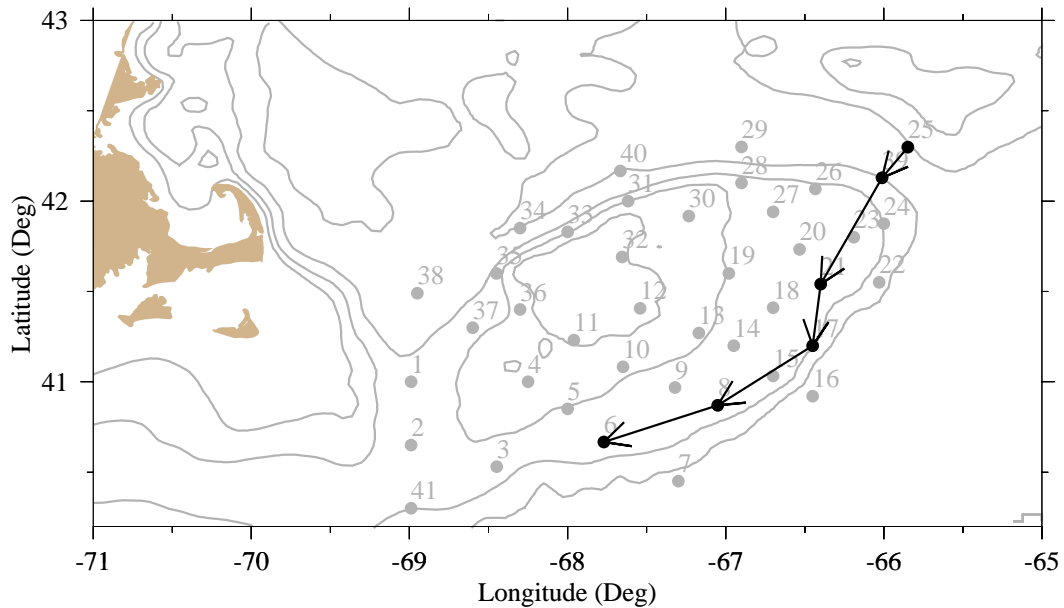


Figure 5.5: The U.S. GLOBEC/GB Program broad-scale sampling station plan for 1998 and 1999. CTD and water sample data at stations along the connected arrows are present later.

Across NEC, Station 39 showed that the surface salinity has increased to 32.4 PSU, and surface temperature was about 4 °C. Also the halocline has deepened from 30 m to about 50 m. Correspondingly, the fluorescence profile showed a lower value in the surface 50 m, hence a less significant vertical gradient.

Further inside the bank, Station 21 showed a weaker temperature and salinity cline at the water depth of about 30 m, although the fluorescence vertical gradient remained distinct. Station 17 is located in the outer edge of the bank. A weak halocline existed at a depth of 20 m, probably as a result of SSW intrusion. A much stronger halocline can be observed around a depth of 50 m. This halocline most likely reflects the boundary between the shelf water and slope water.

Continuing southward, the halocline and vertical gradient of fluorescence is evident at Station 8, although it has deepened to about 60 m. However, at Station 6, the

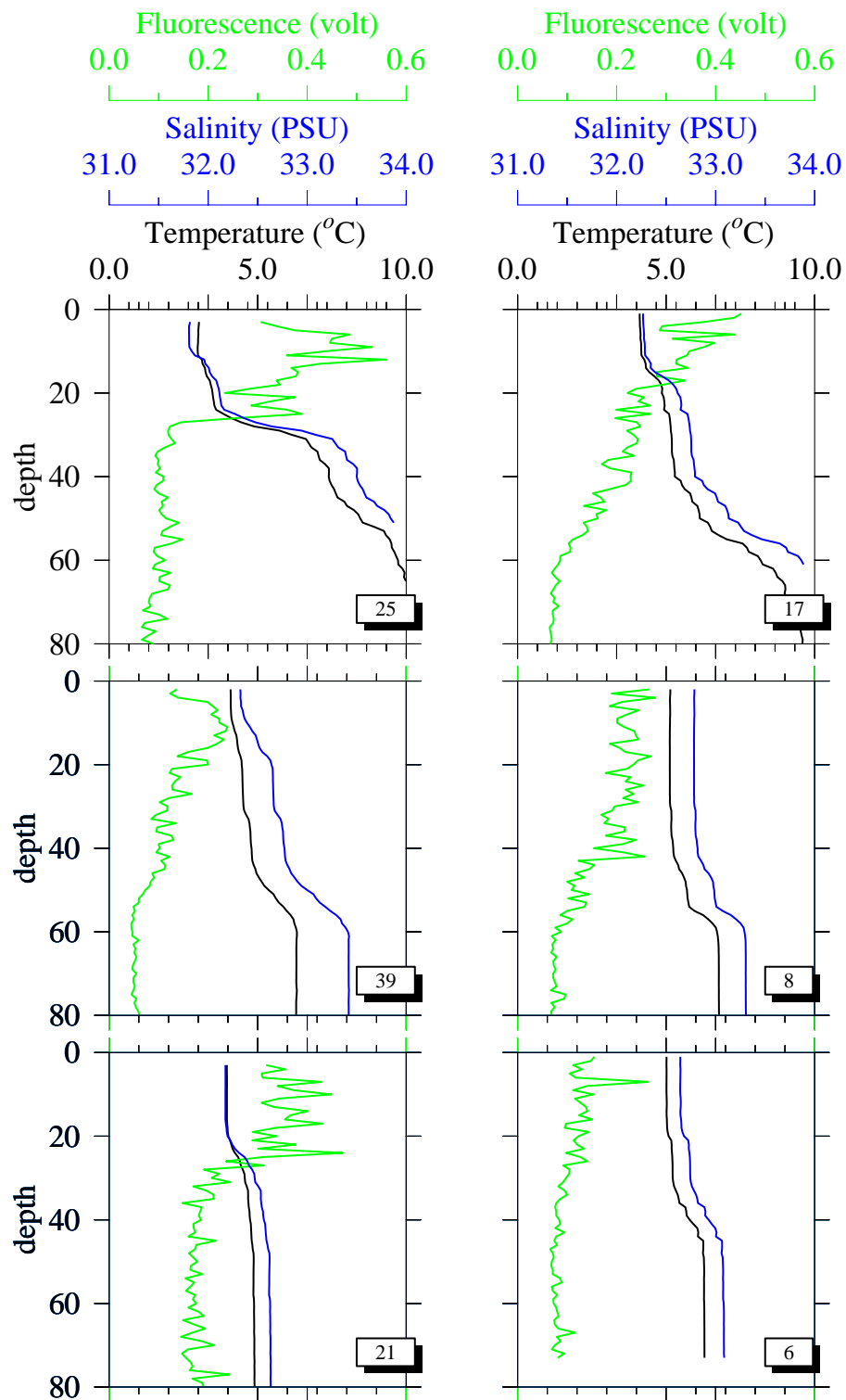


Figure 5.6: Vertical profile of fluorescence (green lines), salinity (blue lines) and temperature (black lines) along the stations as shown in Figure 5.5 during March 1999.

water column seems more vertically well mixed, and the vertical gradient structure of fluorescence disappeared.

5.3.3 WATER SAMPLES

Water samples were collected at the same time as the CTD measurements for each station during the broad-scale survey. Here we present the vertical structure of chlorophyll *a*, nitrate and silicate concentration as shown in Figure 5.7. The concentrations of chlorophyll *a* are consistent with the fluorescence data of the CTD measurements, except that the vertical resolution is much more coarse, with only 3 samples in the water column.

Corresponding to the high chlorophyll *a* concentrations, the concentrations of nitrate and silicate at the surface of Station 25 were nearly undetectable, and increased as the water become deeper. The concentrations of nitrate and silicate reached 8.0 and 3.7 $\mu\text{mol/l}$, respectively, at a water depth of 40 m. This vertical distribution indicates a significant phytoplankton bloom was ongoing at the surface.

The decrease in nutrient concentration at the surface layer was observable in Station 39, 21 and 17 to some extent. Stations 8 and 6 have no data at the very surface. It is hard to tell the vertical structure of the chlorophyll *a* and nutrients at those two stations.

5.4 MODELING APPROACH

5.4.1 PHYSICAL MODEL

The three-dimensional physical sub-model used in this study is Finite Volume Coastal Ocean Model (FVCOM), which was developed by *Chen et al.* [2003] and being applied to GB region. A general introduction of FVCOM can be found in Chapter 2. The numerical domain covers the entire GOM region and GB, enclosed

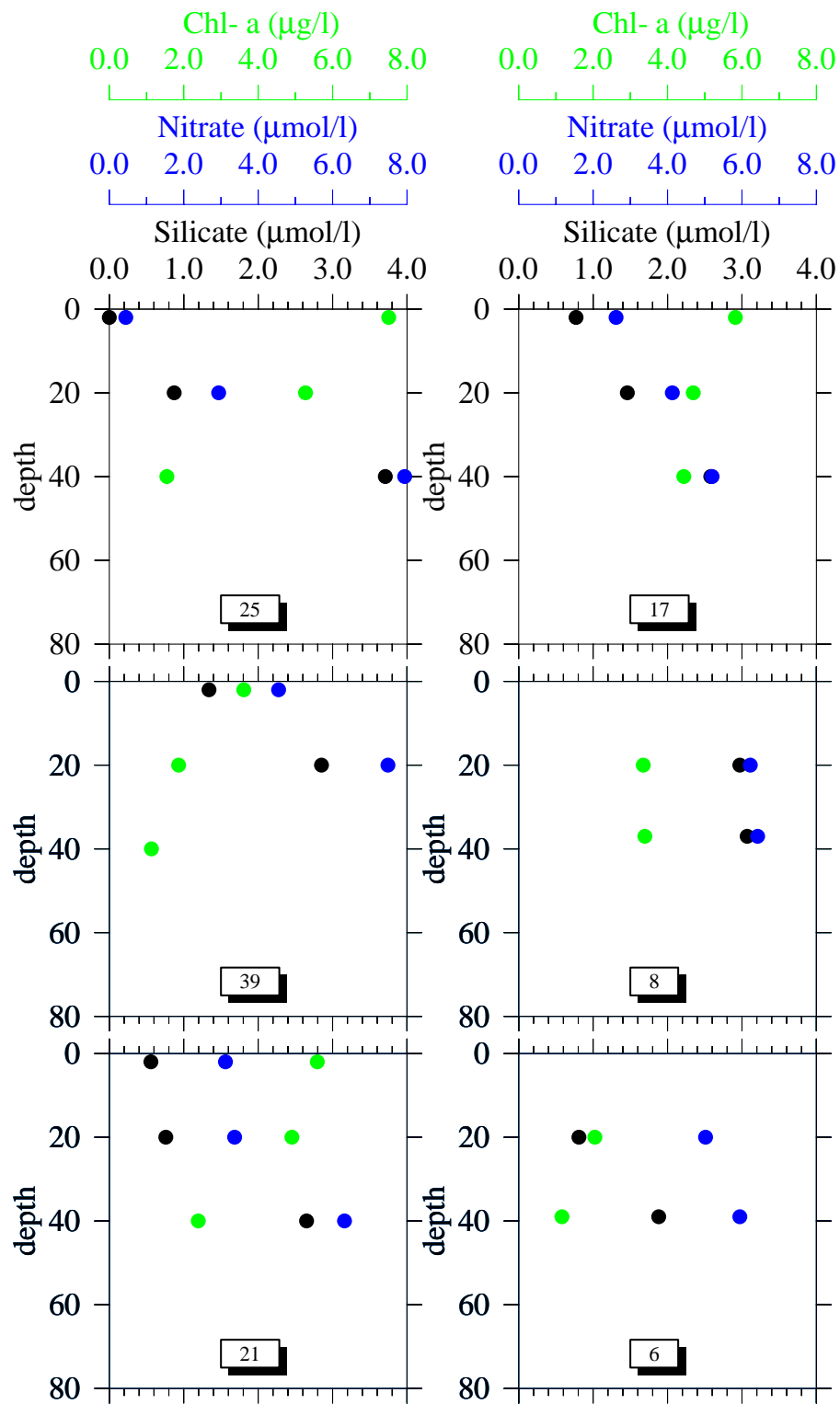


Figure 5.7: Vertical profile of chlorophyll *a* (green dots), nitrate (blue dots) and silicate (black dots) along the stations as shown in Figure 5.5 during March 1999.

by an open boundary running from the New Jersey shelf to the Nova Scotia shelf (Figure 5.8). The horizontal resolution of the model grid is about 3-4 km around the coast and edge of GB, and about 5-8 km in the interior and near the open boundary. Vertically, the uniform grid is used in σ coordinates, with vertical resolution $\sigma = 0.0323$ (31 points in the vertical). This resolution corresponds to 1.3-4 m vertical resolution over the depth range of 40-120 m on GB and a 10-m spacing over the off-bank depth of 300 m. *Mellor and Yamada* [1982]'s 2.5 turbulence closure scheme is used for the turbulent mixing of momentum and tracers. This is the same scheme used in the ECOM-si model.

The model was forced along the open boundary by the surface semidiurnal (M_2 , S_2 , N_2) and diurnal (O_1 and K_1) tide elevations and phases. The sea-level data used for tidal forcing were interpolated directly from observation data. A gravity-wave radiation condition on currents was applied at the open boundary to minimize energy reflection to the computational domain. The surface and bottom boundary conditions for both momentum and biological equations are the same as ECOM-si and described in Chapter 2. Surface heat and wind data is obtained from the mesoscale meteorological model MM5.

5.4.2 PARTICLE TRAJECTORY

In order to obtain a preliminary assessment of path and time scale of water parcel movement, a Lagrange particle trajectory program was incorporated into FVCOM. The technique was originally developed by *Chen and Beardsley* [1998] and was coupled with ECOM-si. It was subsequently modified by *Zheng* [1999]. In this program, particle trajectories are traced by solving the x , y , and σ velocity equations

$$\frac{dx}{dt} = u, \quad \frac{dy}{dt} = v, \quad \frac{d\sigma}{dt} = \frac{\omega}{h + \zeta}$$

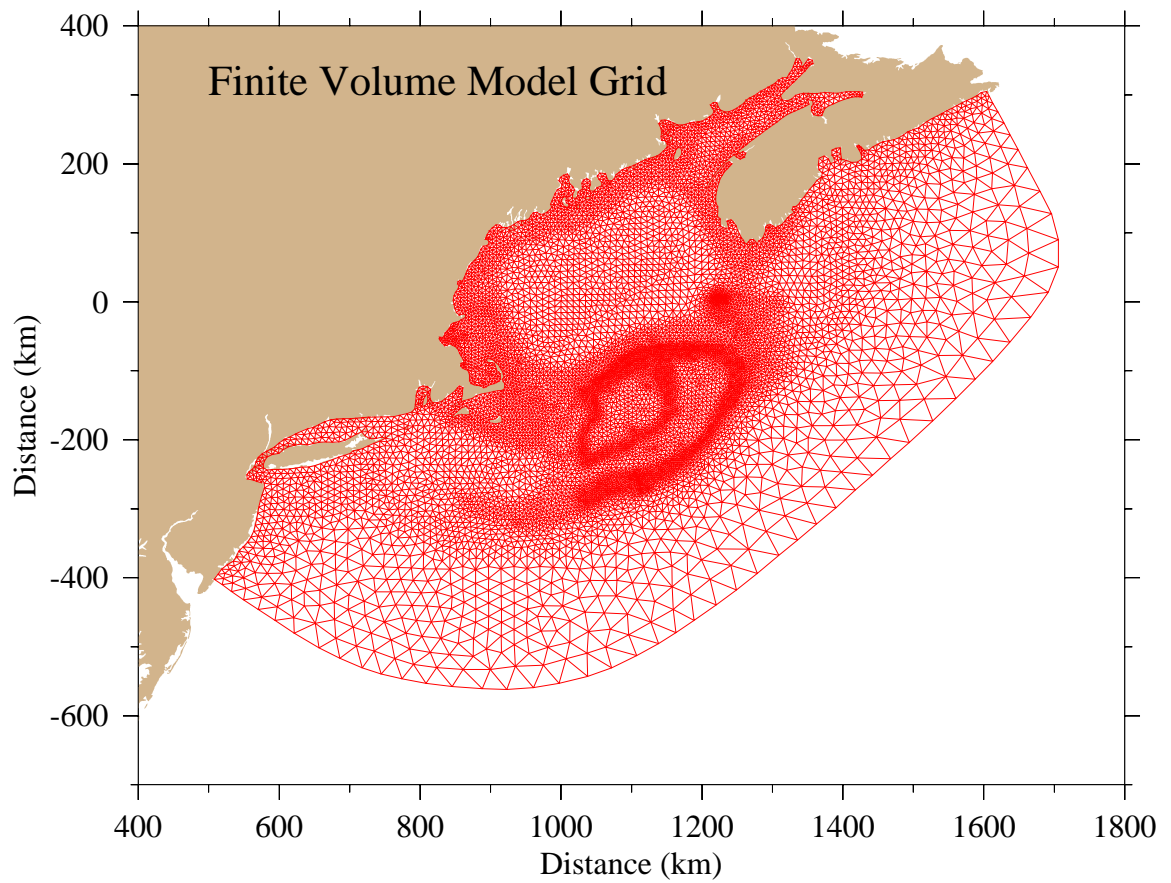


Figure 5.8: Unstructured numerical model grid for GOM/GB region.

where u , v , and ω are the x , y , and δ components of particle velocity, respectively. The kinematic equations for u , v , and w are calculated using a fourth-order Runge-Kuta integration method with a truncation error of the order $(\delta t)^5$. The particle velocity is determined by a bilinear interpolation from the eight nearest grid points. At each time step, each particle is checked to determine whether it is located inside the model domain. If a particle moves out of the numerical domain, it is no longer tracked. The time step δt is chosen to satisfy the criterion $\Delta t \cdot K < 0.05$, where K is an upper bounding of the spatial gradient of velocity. The particles are tracked in the model space (x, y, σ) and then their trajectories are converted to physical space (x, y, z) . This method avoids interpolation errors due to repeated transformation from the σ -coordinate and the z -coordinate.

5.4.3 TRACER STUDY

The particle trajectory experiments can provide an insight into the basic Lagrangian kinematics but do not include the effect of diffusion. To examine the influences of both pure motion (advection) and diffusion on the transport of phytoplankton, passive tracer experiments were conducted with tracer injected into two regions. One is in the central portion of the bank inside the 60-m isobath with a tracer concentration of 1 over the entire water column. The other is near the Browns Bank area with a tracer concentration of 1 in the surface 30 m.

5.4.4 BIOLOGICAL MODEL

The biological model is the same as the one used in 1-D and 2-D models (See Chapter 2). The coupled biological and physical model was started from the beginning of February with a horizontally and vertically homogenous distribution of biological variables as follows: nitrate: $5.0 \mu\text{mol N/l}$; ammonia: $0.1 \mu\text{mol N/l}$; silicate: $5.0 \mu\text{mol Si/l}$; small phytoplankton: $0.1 \mu\text{mol N/l}$; large phytoplankton: $1.0 \mu\text{mol N/l}$; small

zooplankton: $0.1 \mu\text{mol N/l}$, large zooplankton: $0.2 \mu\text{mol N/l}$; detritus nitrogen $5.0 \mu\text{mol N/l}$; detritus silicon: $2.0 \mu\text{mol N/l}$. The model results for February 28 served as the initial condition of the model run for March 1999.

5.5 MODEL RESULTS

5.5.1 PHYSICAL FIELD

Figure 5.9 shows the wind field of selected days in March 1999 as the MM5 model output. The wind velocity and direction changed constantly in the model domain. This wind forcing is used as an input for hydrodynamic model.

In this model, the subtidal currents are results of a combined effect of multiple components such as tides, wind, and baroclinic factors. It would be inappropriate to apply averaging currents over one tidal cycle to calculate the subtidal currents. Instead, a 40-h low pass filter is applied to filter out the tide component and obtain the subtidal currents.

The surface subtidal currents showed a strong relationship with wind forcing. For example, in day 66 (Figure 5.10, upper panel), the surface water in a major part of GOM and GB was dominated by the southward subtidal currents, corresponding well with the prevailing southeastward wind field during that time. The velocity of these subtidal currents reached 30 cm/s . Such a surface flow structure remained until day 76 (Figure 5.11, upper panel), when the wind field was showing an anticlockwise eddy structure. The surface subtidal current at that time was relatively weak in GOM region and the central portion of the bank, except for the northern and the southern flank of the bank. On day 81 (Figure 5.12), the surface subtidal currents shifted northeastward, and the jet current along the northern flank was intensified while the jet current on the southern flank was significantly weakened.

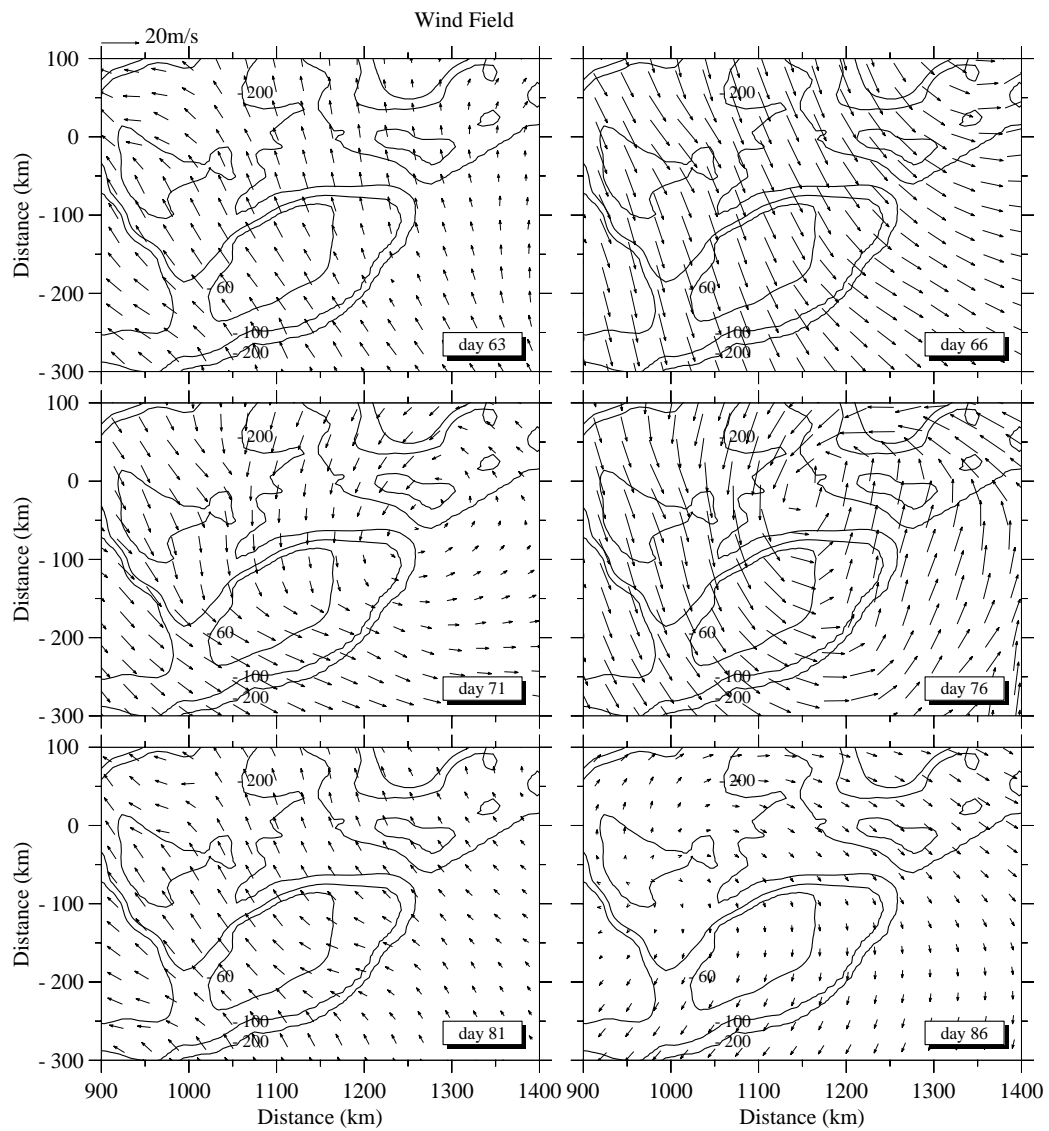


Figure 5.9: Wind field of selected days in March 1999 as the MM5 model output.

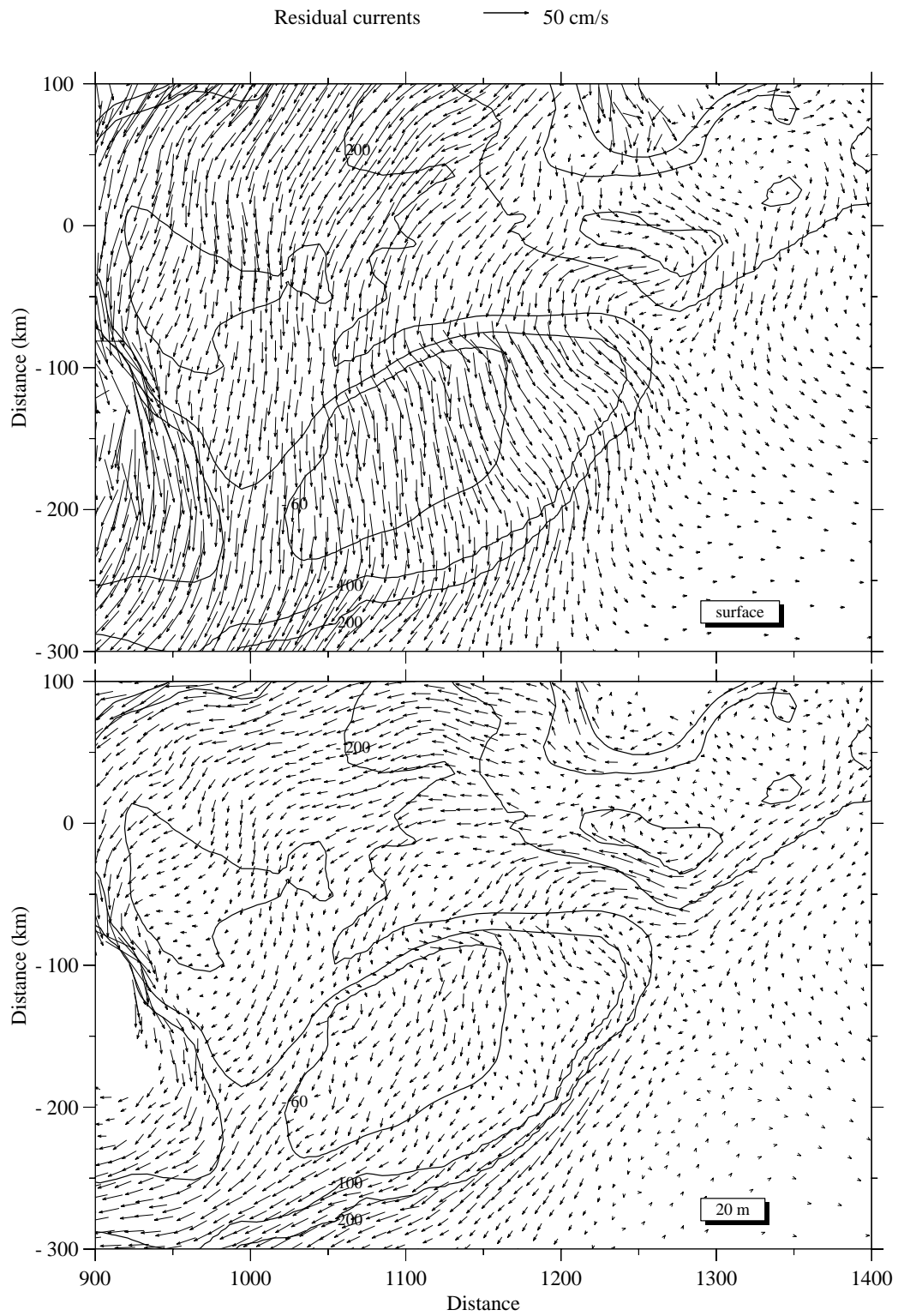


Figure 5.10: Model-computed subtidal currents on GB and surrounding region in day 66. upper: surface subtidal currents; bottom: subtidal currents at 20-m water depth.

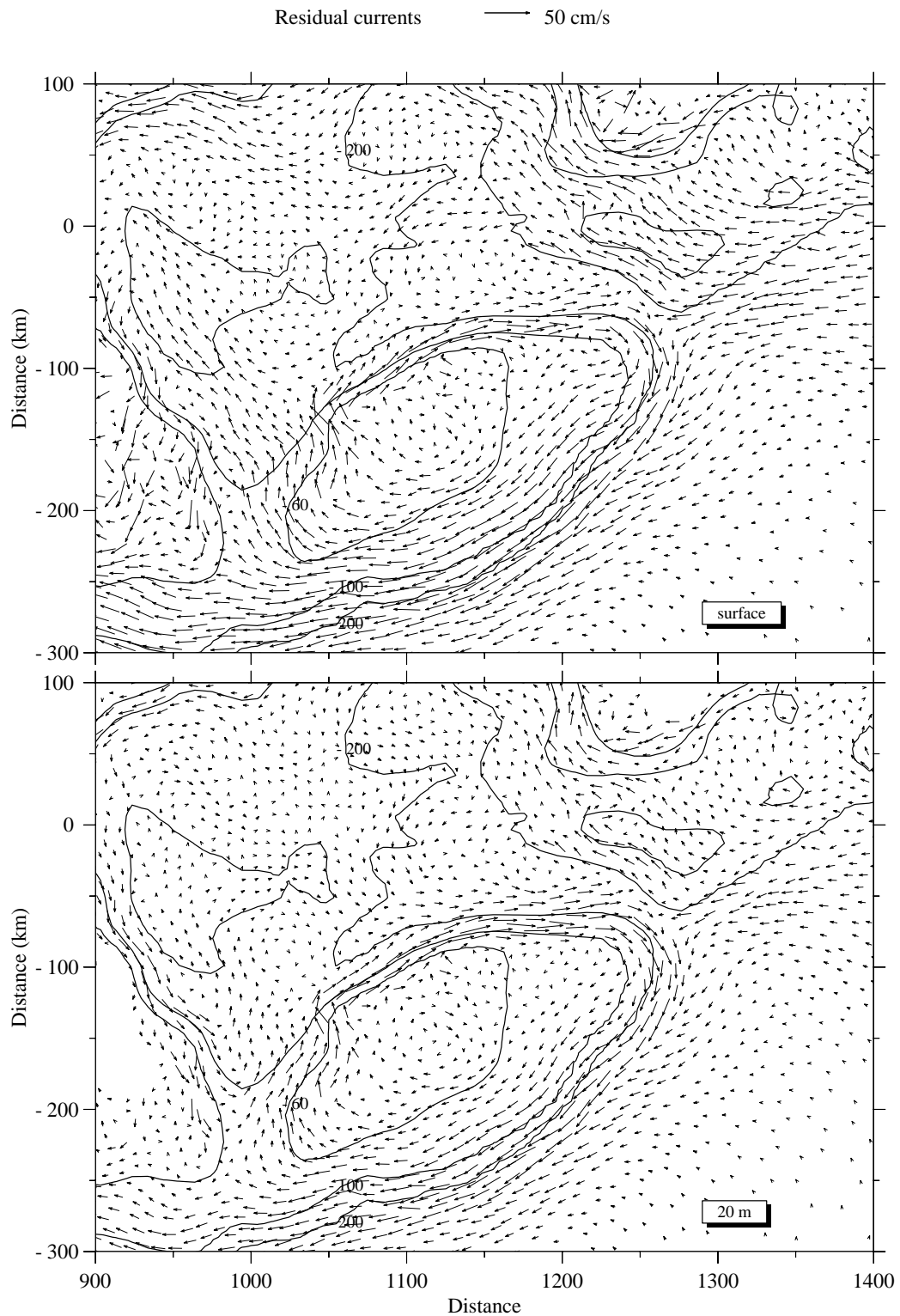


Figure 5.11: Model-computed subtidal currents on GB and surrounding region in day 76. upper: surface subtidal currents; bottom: subtidal currents at 20-m water depth.

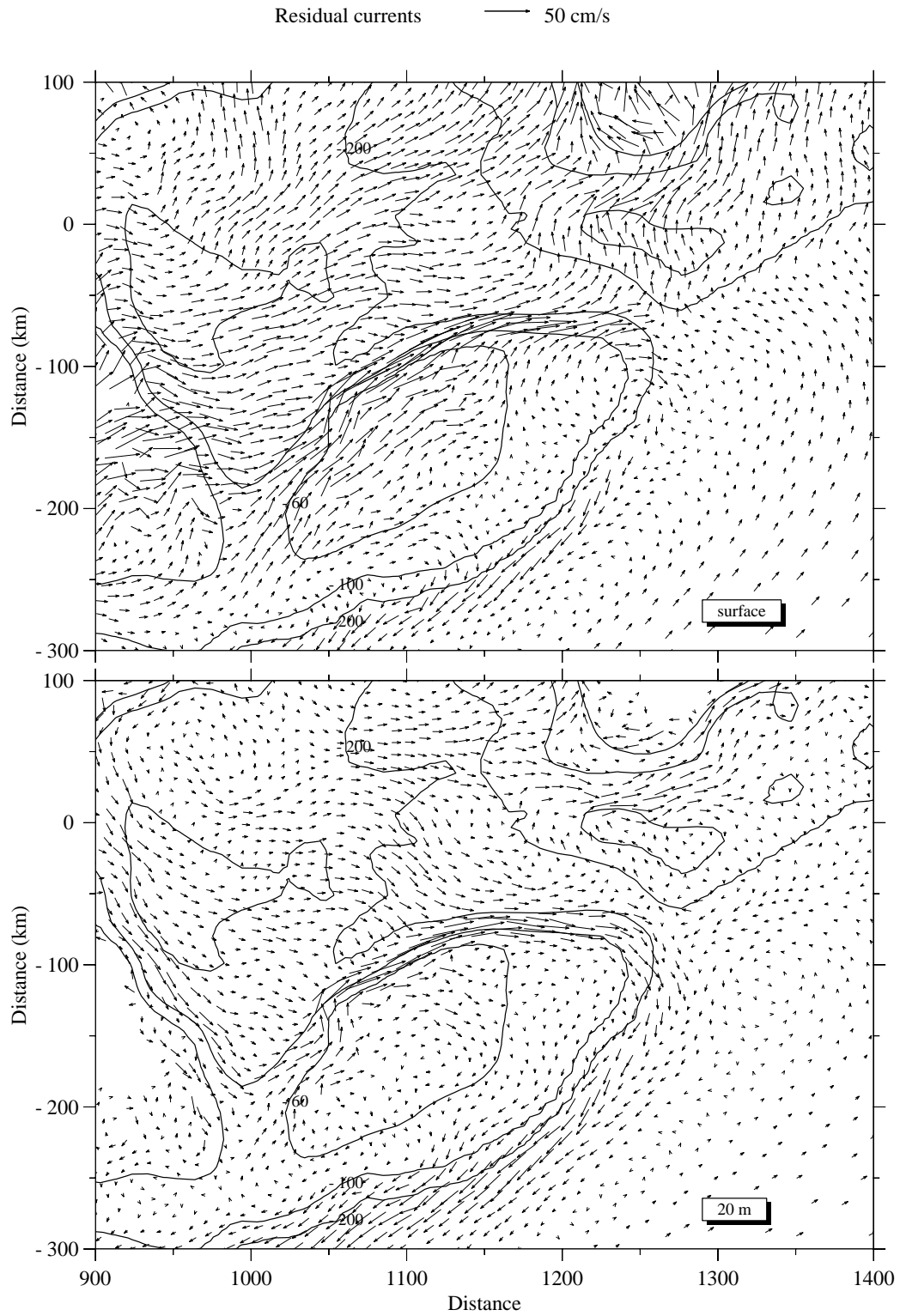


Figure 5.12: Model-computed subtidal currents on GB and surrounding region in day 81. upper: surface subtidal currents; bottom: subtidal currents at 20-m water depth.

The subtidal currents at the depth 20 m were less affected by wind forcing. The most significant feature of the circulation is the clockwise flow around the bank (Figure 5.10, 5.11, and 5.12, bottom panels). For example, on day 76, the jet current reached 20-30 cm/s along the edge of the northern flank, the flow turned southward in the edge of NEP and further turned southwestward and widened. The velocity was 20-30 cm/s near the 200-m isobath and decreased to 5-10 cm/s both shoreward and slopeward. This result is slightly different from that of *Chen et al.* [2003] using ECOM-si (which is initiated with a climatological temperature and salinity field, and driven by M_2 tidal components only), where two currents circulated around the bank. The first current is the tidally induced, topographically controlled clockwise subtidal circulation found around the crest of the bank, where a strong eastward/southeastward current jet of 15 to 18 cm/s forms along the edge of the northern flank and a relatively weaker and wider westward flow of 5 to 8 cm/s in the region shallower than 60 m on the southern flank. The second current is a buoyancy-induced, westward mean current located near the 100-m isobath at the shelf break of the southern flank. In the results of this FVCOM model, two flows on the southern flank are hard to separate, which could be caused by different wind forcing and initial condition of both temperature and salinity fields.

5.5.2 PASSIVE PARTICLE TRAJECTORY

Particles were released from a square area including Browns Bank and surroundings (Area A) or from the central portion of the bank inside the 60-m isobath (Area B). Trajectories were traced from day 63 through day 86. Figure 5.13 shows the trajectories of particles released at the surface of Area A. On day 66, only a few particles flowed onto the bank. By day 71, 25% of particles were inside the 200-m isobath. After the particles flowed to the bank, they moved southwestward following the clockwise circulation. More particles arrived on the bank in day 76, accounting

for 45% of the total. After that, particles seemed to separate into two groups as shown on days 81 and 86, with one group remaining in NEC and the other moving around the southern flank. The velocity of this movement was obviously decreased. Overall, 48% of total particles arrived inside 200-m isobath of the bank in 23 days. The movement of particles in the surface was strongly related to the surface subtidal current, which in turn related to the surface wind stress. The particles released in the subsurface (30-40 m below the surface) were less likely to be transported to the bank, as shown in Figure 5.14. Most of them moved northwestward, with only a few flowing onto the bank.

The particles released at the surface of Area B were quickly “washed out” (Figure 5.15), with only 11% of particles remained inside the 60-m isobath on day 71, and none on day 81. The particle trajectories corresponded well with wind stress. Most of the particles moved southward (Figure 5.15, day 66, 71), converge on the southern flank and then moved southwestward and out of the model domain (Figure 5.15, day 76, 81 and 86). The particles released in the subsurface (20-30 m below the surface) of Area B were less likely to leave the central portion of the bank (Figure 5.16). After 23 model days, only 21 percent of the total particles moved outside the 60-m isobath; these flowed either northward to the northern flank of the bank or southwestward to the Great South Channel. None of the particles arrived on the southeastern or southern flank of the bank.

The particle trajectories experiment indicates that particles at the surface of both Area A and B can move to the southern flank, but particles in the subsurface generally do not. To further quantify the water parcel movement including diffusion process, the results of tracer experiments are presented below.

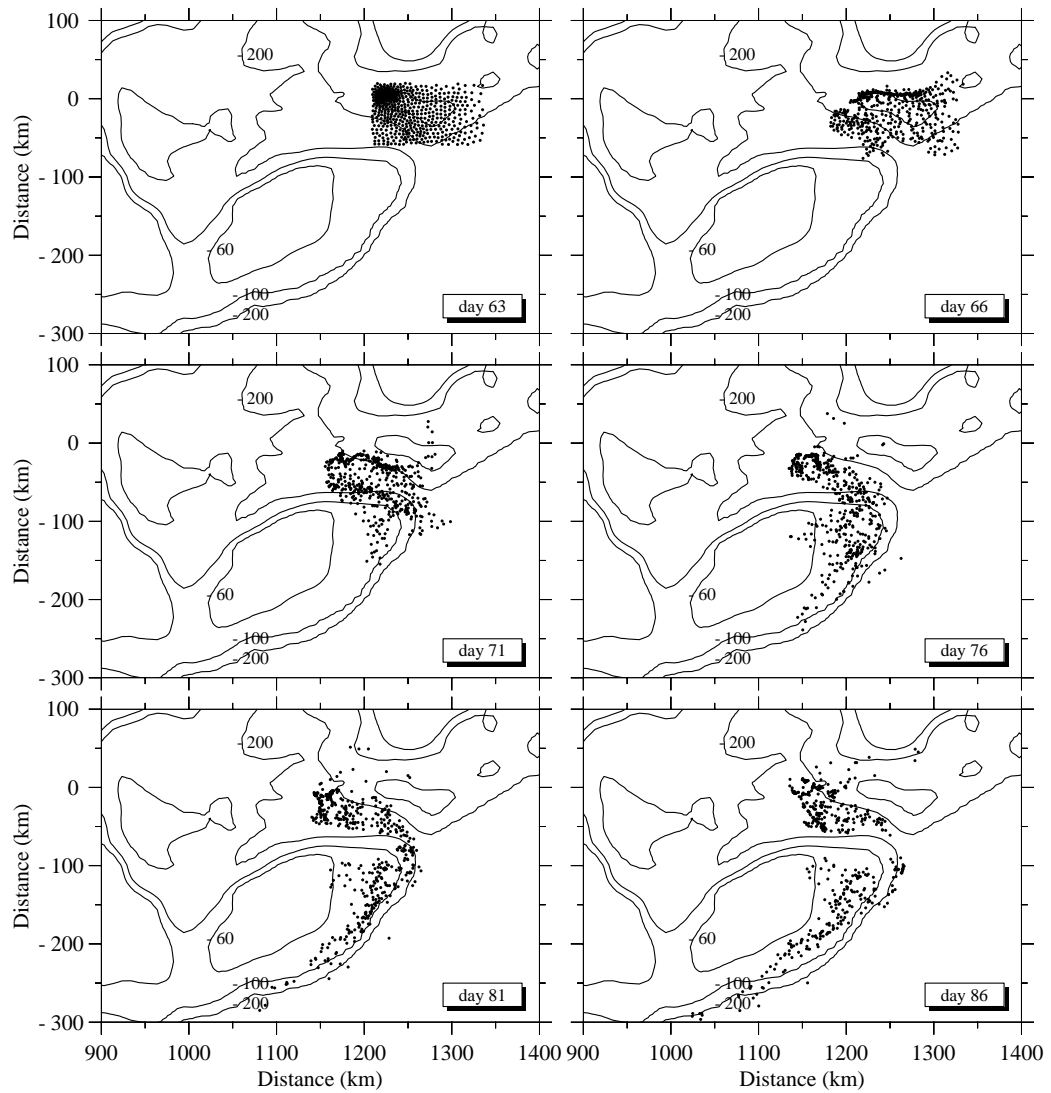


Figure 5.13: Selected snapshots of Lagrange particle trajectory. Particles were released at the surface near Browns Bank region at day 63.

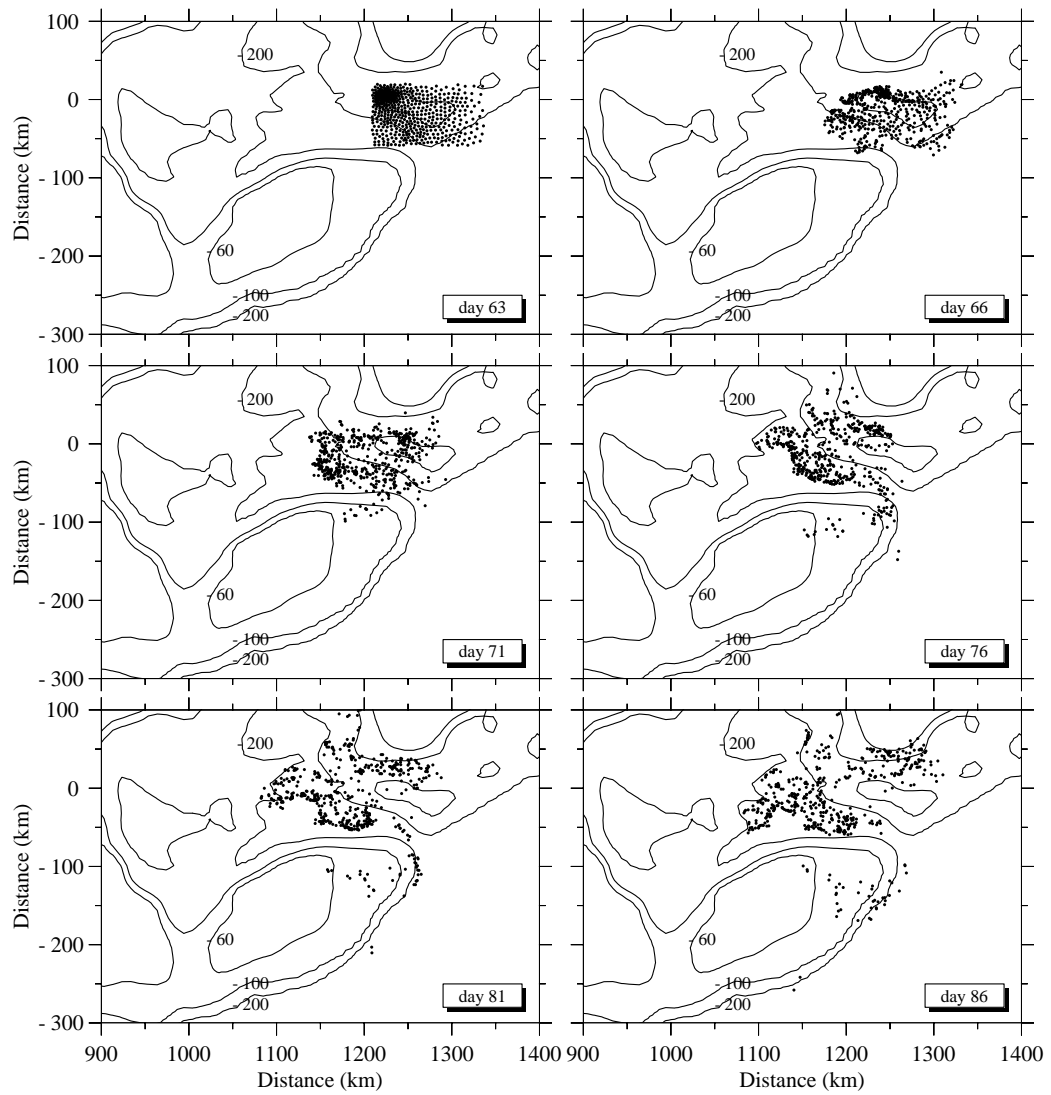


Figure 5.14: Selected snapshots of Lagrange particle trajectory. Particles were released at the sub-surface (30-40 m below the surface) near Browns Bank region at day 63.

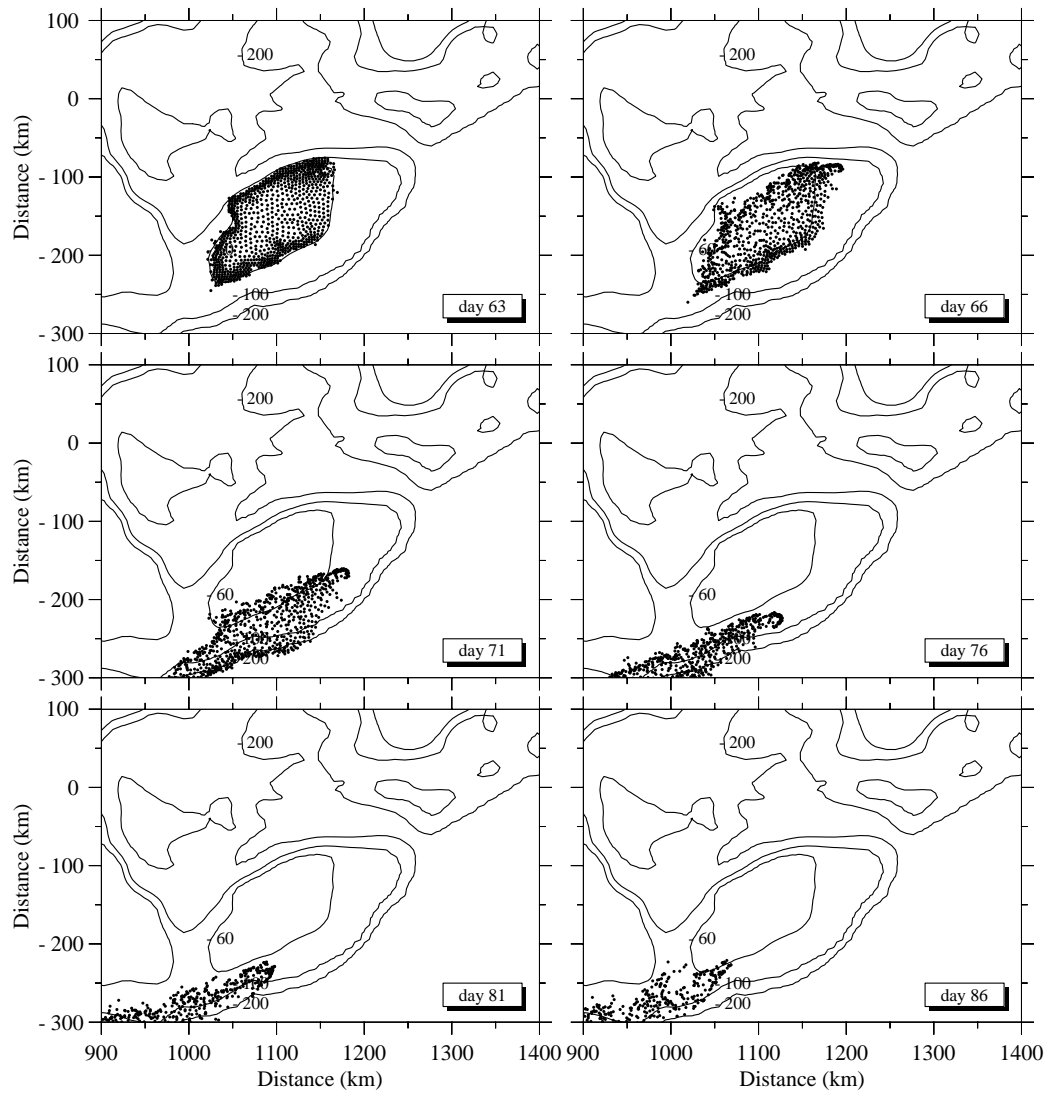


Figure 5.15: Selected snapshots of Lagrange particle trajectory. Particles were released at the surface on the central portion of GB at day 63.

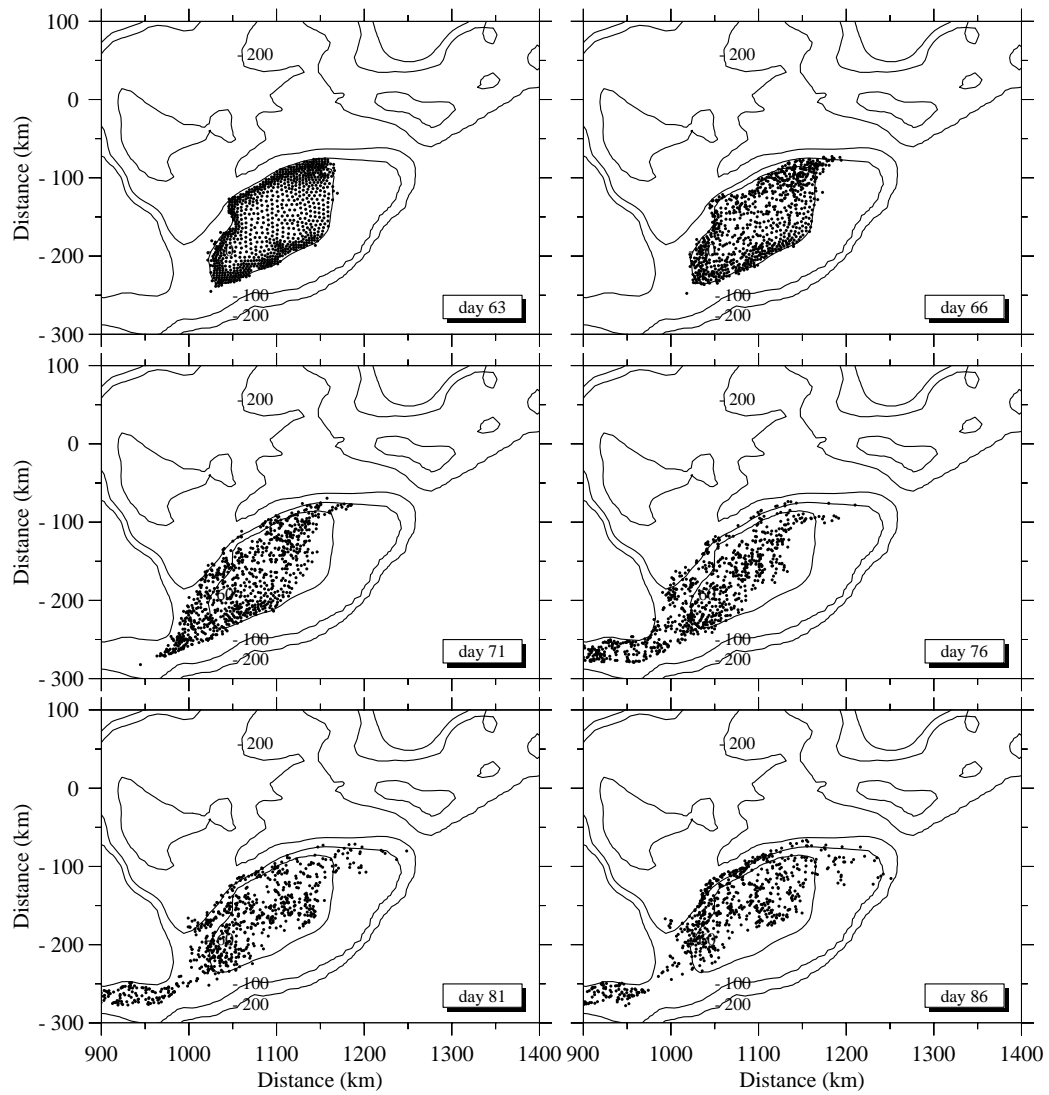


Figure 5.16: Selected snapshots of Lagrange particle trajectory. Particles were released at the sub-surface (20-30 m below the surface) on the central portion of GB at day 63.

5.5.3 TRACER MOVEMENT

Tracer was “injected” into the surface layer (< 30 m) of Area A homogenously and the whole water column in Area B. For Area A, a different vertical mixing coefficient was applied to test its effect on the “cross-over” events, with Case A1 representing the standard model run without changing the vertical mixing coefficient and Case A2 representing a smaller vertical mixing coefficient in the water column below 30 m depth.

Case A1: The surface tracer “injected” in Area A decayed very quickly (Figure 5.17). The initial concentration on day 63 was 1.0 unit/l. On day 76, the tracer “cross-over” towards NEP was detectable although the concentration had already declined to < 0.3 unit/l. On day 86, the tracer concentration on the bank was almost undetectable.

Case A2: If the tracer “injected” in Area A was subjected to less vertical mixing between surface water (to 30 m) and deep water (below 30 m), much more tracer “crossed-over” to the bank occurred. Figure 5.18 shows the results when the mixing coefficient in the water column below 30 m is one order smaller than the standard model run. In this case, the pattern of the tracer movement was much more similar to the particle trajectories, which showed a significant amount of particles “crossing-over” and flowing to the southeastern and southern flank of the bank.

Figure 5.19 shows that if the whole water column in the model domain was integrated, the total concentration was conservative except small perturbations caused by numerical error. The integration of tracer below 30 m water depth kept increasing with time, and reached over half of total concentration in Case A1 and much less in Case A2, suggesting that the vertical mixing loss of the tracer caused the difference in horizontal distribution shown above.

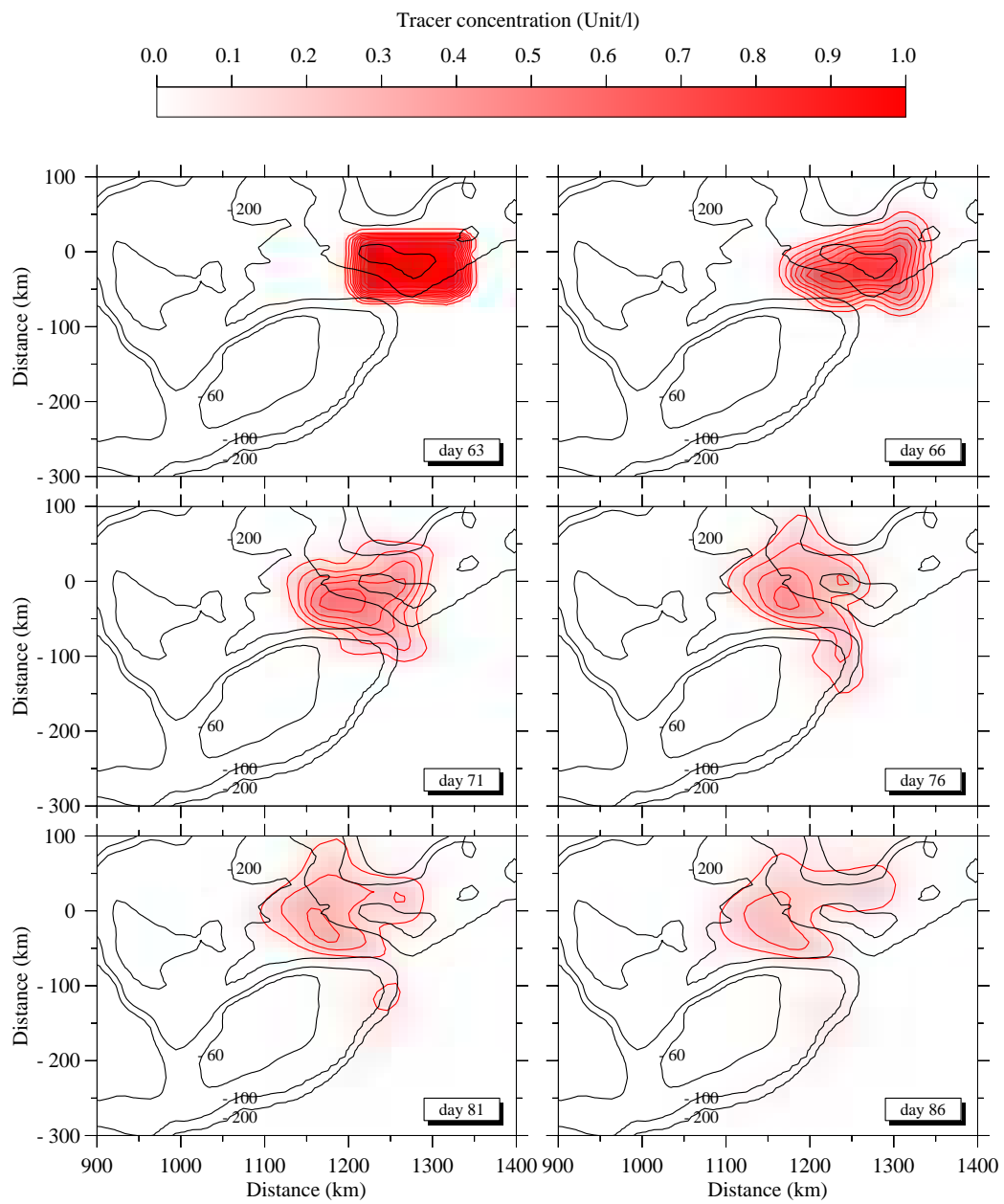


Figure 5.17: Selected snapshots of tracer experiment results. Tracer were released at the surface layer (<30 m) near the Browns Bank region at day 63.

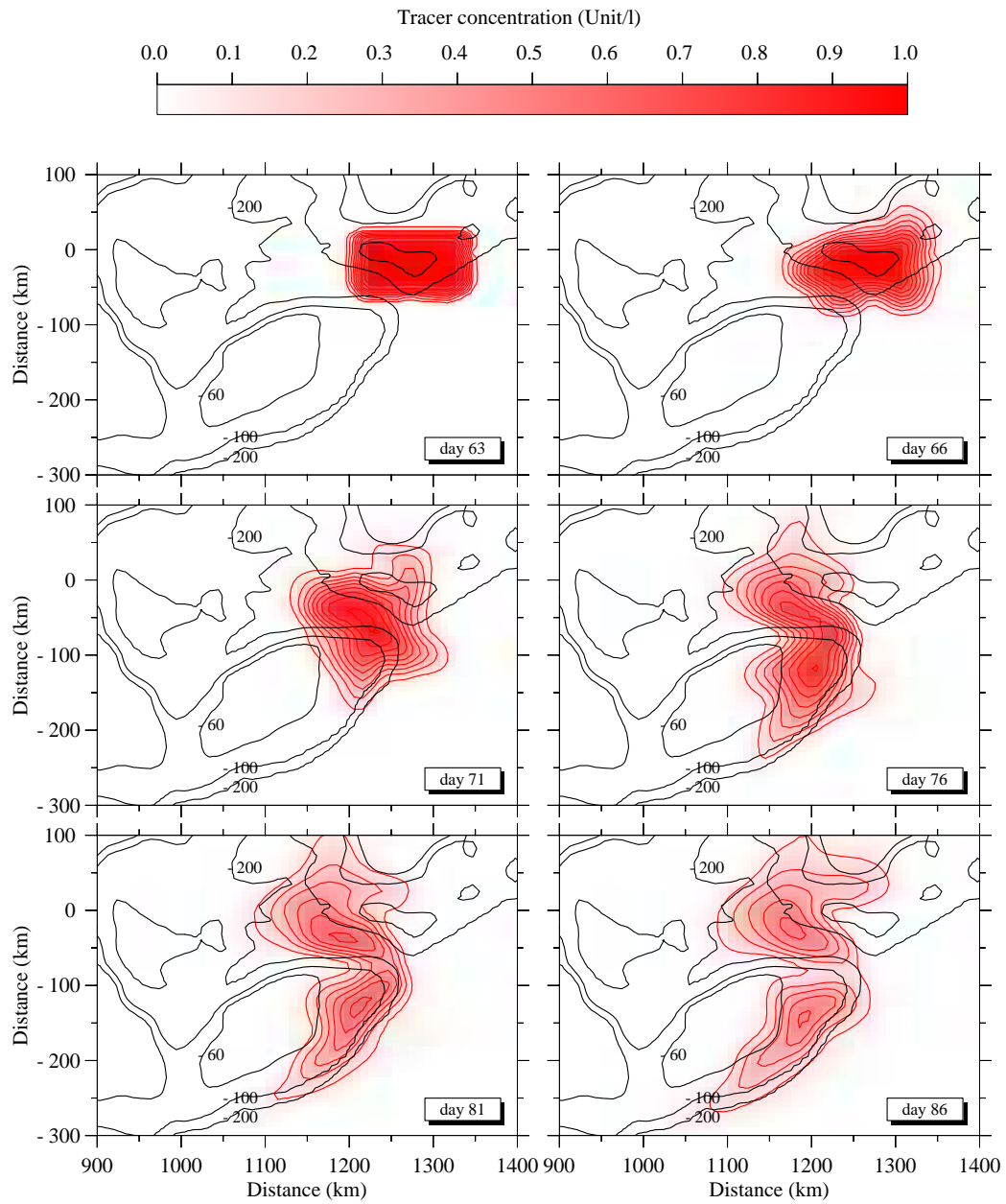


Figure 5.18: Selected snapshots of tracer experiment results. Tracer was released at the surface layer (<30 m) near the Browns Bank region at day 63. The vertical mixing coefficient in the water column below 30 m is one order smaller than the standard model run as shown in Figure 5.17

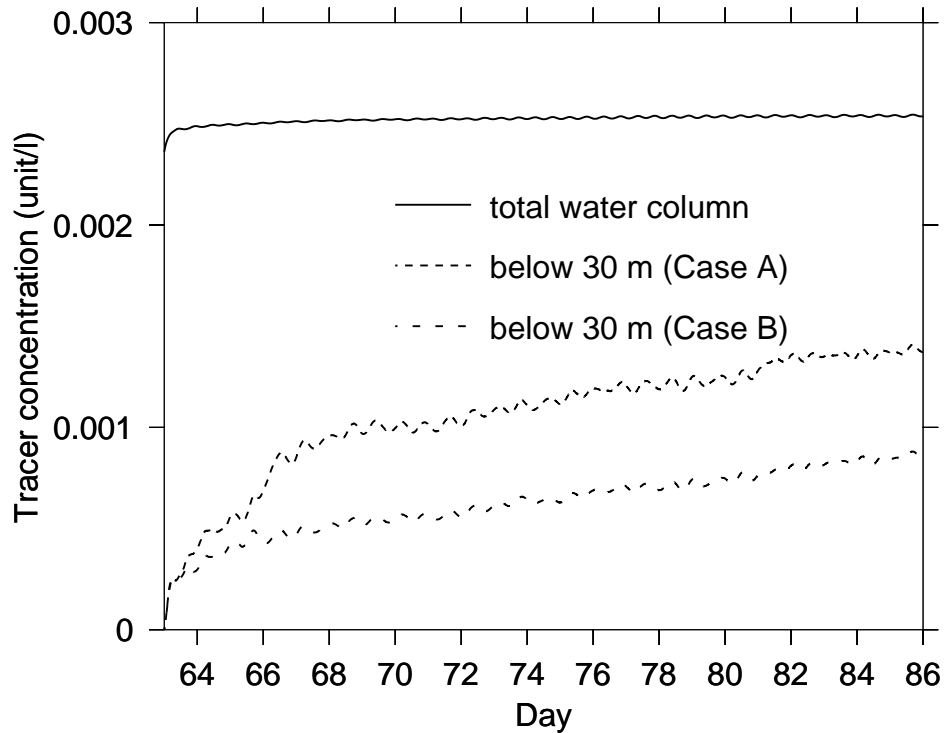


Figure 5.19: Time series of vertically integrated tracer concentration in the entire model domain.

The tracer “injected” in Area B (Figure 5.20) showed a relatively slower decay compared to Case A1. The maximum concentration on the top of the bank remained >0.8 unit/l after 20 model days. Most of the tracers “drifted” southwestward and left the model domain, without a detectable movement towards the southeastern and southern flanks.

5.5.4 COUPLED BIOLOGICAL MODELING RESULTS

Unlike the passive tracer, the coupled biological-physical model included biological source and sink terms. This model experiment was intended to examine whether the bloom can be extended from Area A to the southeastern and southern flank under

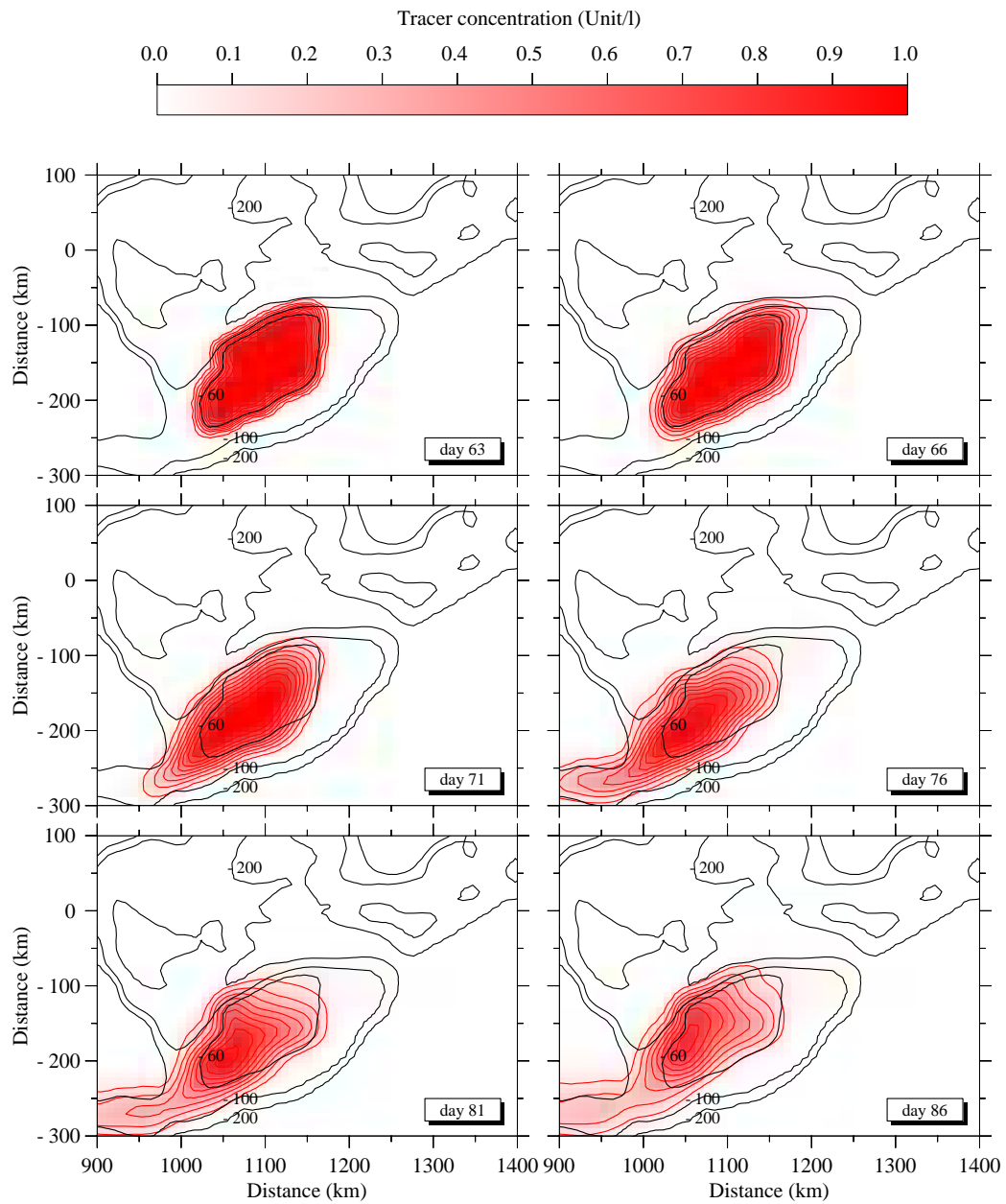


Figure 5.20: Selected snapshots of tracer experiment results. Tracer were released homogeneously in the entire water column of the central portion of GB at day 63.

the standard model configuration. In order to focus on bloom dynamics, only the results for large phytoplankton are presented here. The model was initiated with the biological field as specified in section 5.4.4. Such an initiation provides a basic background field, with a stabilized horizontal and vertical distribution of concentrations of biological variables. It is also assumed that there was an on-going phytoplankton (diatom) bloom in the Area A, with the concentration of large phytoplankton specified as $3 \mu\text{mol N/l}$ (equivalent to $6 \mu\text{g Chl-}a/l$ with $\text{N:Chl-}a = 2.0$).

Figure 5.21 shows that the movement of the bloom patch was similar to that in the tracer experiment, day 66 through day 76. An increase of large phytoplankton concentration at the surface was observable outside the 200-m isobath of southeastern flank from day 81 to 86. However, no bloom was observed on the southeastern and southern flank. This result indicates that with the same vertical mixing scheme as in the standard model run, blooms in SSW were not able to extend to the southern flank.

5.6 DISCUSSION

5.6.1 SOURCE OF THE PHYTOPLANKTON BLOOM ON THE SOUTHERN FLANK

The bloom that occurred on the southern flank of the bank in March 1999 as shown in satellite images was not likely a result of direct input from the central area of the bank or from SSW. Although the particle trajectory results show that a transport from both areas is possible, vertical mixing prevents a substantial replacement of water on the southern flank with surrounding water. Tracer experiments exclude the possibility of direct “washout” from the central portion of the bank to the southern flank. For SSW, the tracer can reach the southern flank and maintain $> 80\%$ of the initial concentration only if the vertical mixing between surface and deep water is weak.

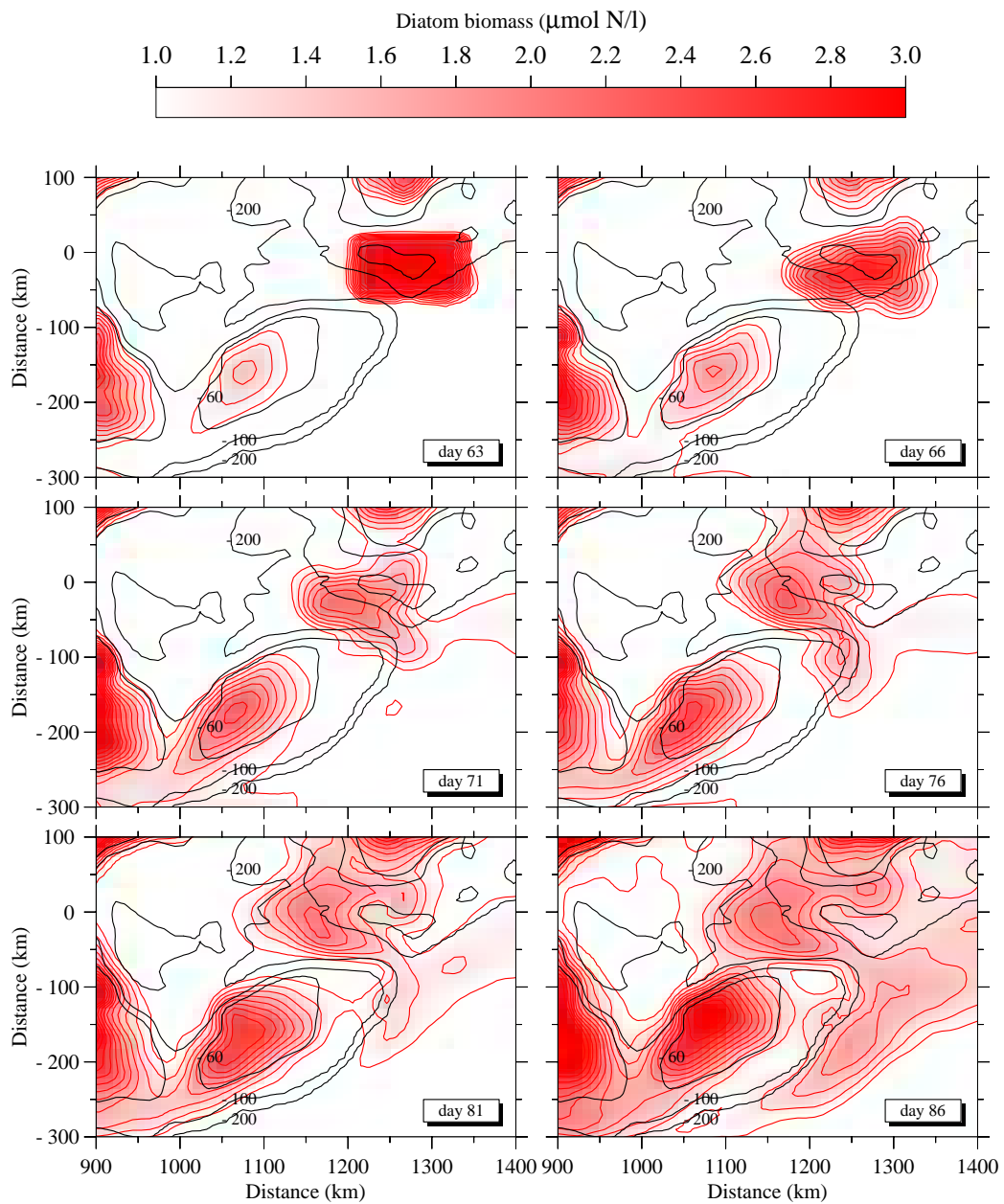


Figure 5.21: Selected snapshots of coupled biological-physical model experiment results. The large phytoplankton at the surface layer (< 30 m) near the Browns Bank region was set to be $3 \mu\text{mol/l}$ at day 63.

The separation of bloom patches shown in satellite images between the southern flank and NEC between days 73-80 suggests that the bloom on the southern flank is not likely an extension of the upstream bloom. Instead, the bloom may be triggered by the “in situ” growth of phytoplankton, with the help of stratification induced by SSW “cross over”. Figure 5.4 (upper left panel) shows that the “cross over” can occur in February. This suggests that there was a time window for SSW to arrive on the southern flank and set up a stratification condition that is favorable for phytoplankton to bloom. Such a widespread SSW influence over the southern flank between the 60-m isobath and the shelf break front was also observed in 1997 [*Ryan et al.*, 2001]. This SSW influence might significantly change the location of salinity front and hence the spring bloom dynamics.

In contrast to the 1999 case, no detectable bloom occurred on the southern flank in March 1998 as shown in Figure 5.22. One possible explanation is that SSW “cross- over” was relatively weak that year. Therefore, there was no “pre-setup” of stratification to allow an early spring bloom on the southern flank. The CTD data shown in Figure 5.23 indicates that the water is well mixed along the selected section, especially at Stations 21, 8 and 6, where water temperature and salinity is vertically homogenous. The fluorescence data at Station 8 also indicate that the phytoplankton did not show a higher concentration in the surface layer.

The influence of slope water from the southern edge of the bank remains unclear. Previous studies have shown that the phytoplankton bloom could occur early at the shelf break front where shoaling of the mixed layer by the front locally increases light exposure [*Marra et al.*, 1982; *Malone et al.*, 1983]. The interaction of warm core rings of the Gulf stream with shelf water masses is one of the factors that influence water column stability and vertical flow in the shelf break front area [*Smith and Baker*, 1985; *Yentsch and Phinney*, 1985; *Nelson et al.*, 1989; *Ryan et al.*, 1999, 2001]. However, this process is difficult to quantify, since it is intermittent in time

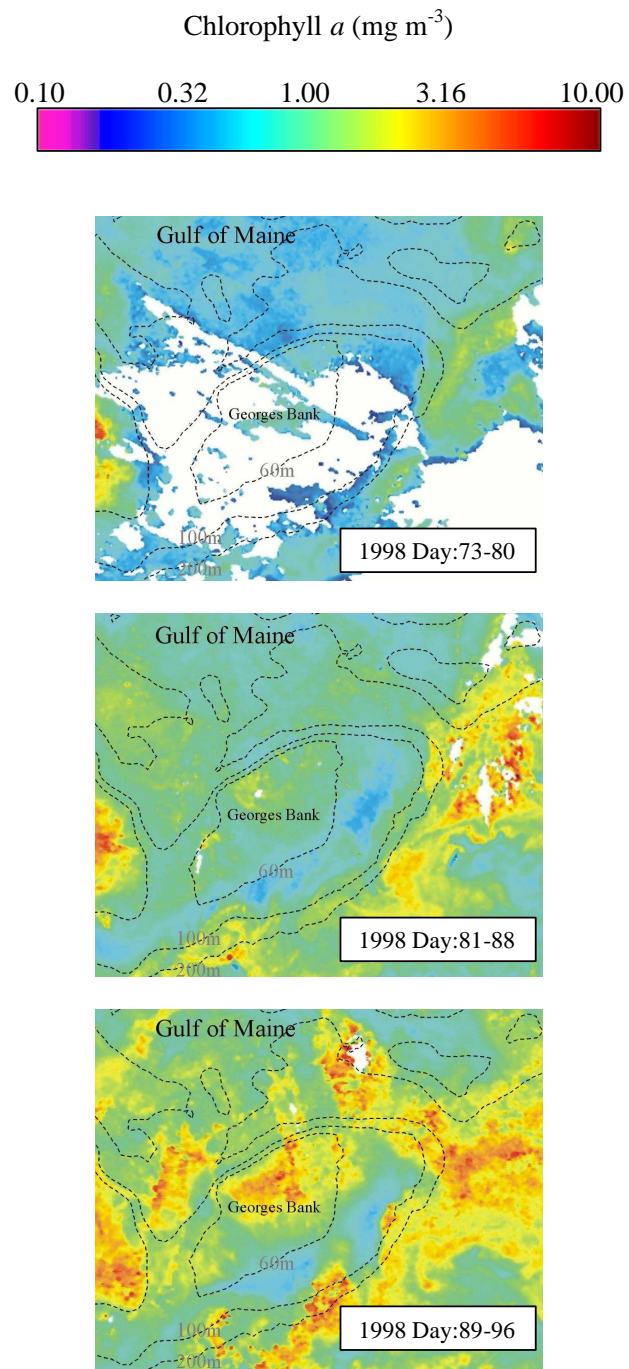


Figure 5.22: Eight-day composite SeaWiFS image of GB and surrounding area during March 1998. Image is adapted from Dr. Andrew Thomas's website at the School of Marine Sciences, University of Maine.

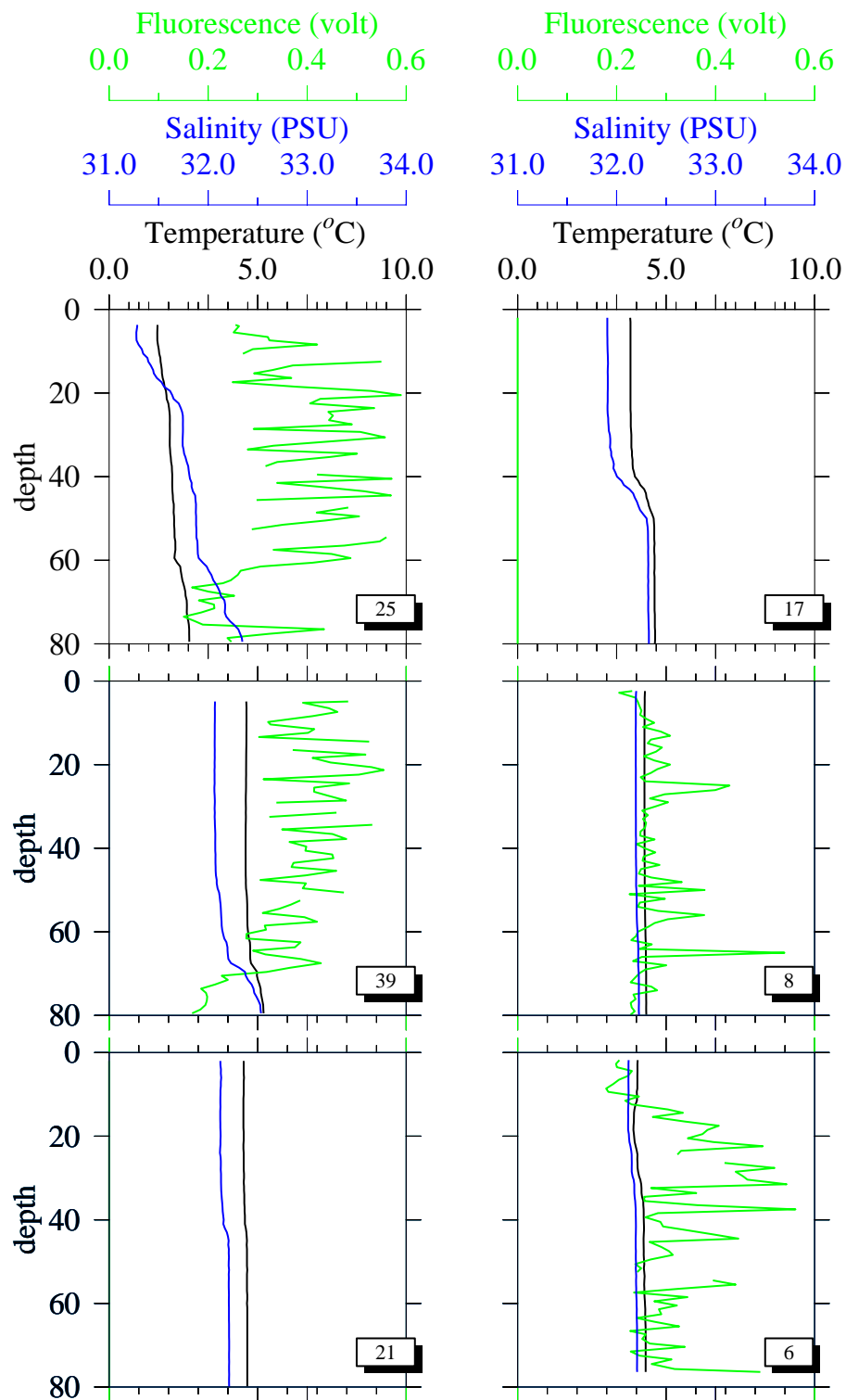


Figure 5.23: Vertical profile of fluorescence (green lines), salinity (blue lines) and temperature (black lines) along the stations as shown in Figure 5.5 during March 1998.

and space. A 3-D model with a better open boundary condition on the slope side is necessary to study such a process.

5.6.2 BIOLOGICAL IMPORTANCE OF SPRING BLOOM ON THE SOUTHERN FLANK

A lot of the previous GB studies focused on the productivity of central bank, stimulated by a dilemma of higher primary productivity and low new nutrient supply in that region. These studies addressed the cross-frontal exchange of the nutrients and associated phytoplankton production [Franks and Chen, 1996; Chen and Beardsley, 1998; Franks and Chen, 2001; Houghton and Ho, 2001; Houghton, 2002; Chen and Beardsley, 2002; Chen *et al.*, 2003]. Less attention has been paid on the dynamics of phytoplankton production on the southern flank, although this area is most important in terms of the dominant zooplankton species, like *Calanus finmarchicus*, during the spring and early summer [Meise and O'Reilly, 1996].

Food limitation in *Calanus finmarchicus* is most likely to occur on the southern flank of the bank [e.g., Campbell *et al.*, 2001]. Timing of the spring bloom is influenced by the advection from GOM and Scotian Shelf and can affect food availability. A mismatch of the spring bloom and peak of zooplankton reproduction may lead to reduced recruitment of zooplankton. For example, if the post-bloom SSW “cross-over” to the southern flank occurs during March, it usually brings only nutrient-depleted surface water. During April, the water from GOM could also be nutrient depleted, since the development of spring bloom in GOM usually occurs at this time (as a result of the stratification induced by the increased surface heat flux). A continuous lack of nutrient support is most likely the cause of the food limitation of zooplankton on the southern flank of the bank.

An early spring bloom which is mismatched with the *Calanus finmarchicus* cohort development may cause the “waste” of food. Under this situation, much of the spring bloom phytoplankton will settle to the bottom and enter benthic food chains

[Townsend and Cammen, 1988]. The observation in the southern GOM during 1988 and 1989 has proven the existence of this situation. Early bloom initiation usually corresponds with early termination of the bloom owing to the depletion of the nutrients, which may have an even more extended impact on the *Calanus finmarchicus* population. Under this scenario, the cohort receives less food before it goes to post-summer diapause. Animal size will be small, energy reserves low, and development retarded. Consequently, diapause survival will be reduced. Alternatively, if the spring bloom occurs too late, food limitation will be posed on the growth and reproduction of G1 population, and as a result, recruitment for this year will be less successful. Although there may be less food limitation for the later cohort, the small population size due to the early food limitation would mean less individuals go to diapause and less are available for next year's recruitment.

5.7 SUMMARY

The possible source of an intensive bloom that occurred on the southern flank of GB during March 1999 was investigated. 3-D model experiments were conducted to examine the cause of the bloom and impact of SSW on bloom dynamics. FVCOM provided the hydrodynamic field for the Lagrange particle trajectory, tracer and biological model experiments.

Surface particle released in the Browns Bank area “crossed-over” to the NEC, reached NEP of the bank in less than 10 days and followed the clock-wise circulation path over the Southern Flank of the bank. However, this experiment does not confirm that the phytoplankton bloom can “cross-over” and reach the southern flank, due to vertical mixing processes. The results of the coupled bio-physical model indicate that the maintenance of salinity-induced stratification, as well as *in situ* growth of phytoplankton, are essential for inducing a spring bloom over the southern flank

during March 1999. Tracer experiments also suggest that a direct “transport” of bloom water from the central bank to the southern flank is not likely.

The model results demonstrate that biological processes are sensitive to the hydrodynamic environment. This experiment also suggests that the simulation accuracy of the spatial distribution of water temperature and salinity (in particular, the location of the shelf break front) and “cross-over” water transport is a prerequisite to capture the spring bloom over the southeastern and southern edges of GB.

5.8 REFERENCES

- Bigelow, H. B., Physical oceanography of the Gulf of Maine, *Bulletin of the United States Bureau of Fisheries*, 40, 511–1027, 1927.
- Bisagni, J. J., and P. C. Smith, Eddy-induced flow of Scotian Shelf water across Northeast Channel, Gulf of Maine, *Continental Shelf Research*, 18, 515–539, 1998.
- Bisagni, J. J., R. C. Beardsley, C. M. Ruhsam, J. P. Manning, and W. J. Williams, Historical and recent evidence of Scotian Shelf Water on southern Georges Bank, *Deep Sea Research II*, 43, 1439–1472, 1996.
- Campbell, R. G., J. A. Runge, and E. G. Durbin, Evidence for food limitation of *Calanus finmarchicus* production rates on the southern flank of Georges Bank during April, 1997, *Deep Sea Research II*, 48, 531–550, 2001.
- Chen, C., and R. Beardsley, Tidal mixing and cross-frontal particle exchange over a finite amplitude asymmetric bank: A model study with application to Georges Bank, *Journal of Marine Research*, 56, 1163–1201, 1998.
- Chen, C., and R. Beardsley, Cross-frontal water exchange on Georges Bank: modeling exploration of the US GLOBEC/Georges Bank phase III study, *Journal of Oceanography*, 58, 403–420, 2002.

- Chen, C., R. C. Beardsley, and P. J. S. Franks, A 3-d prognostic model study of the ecosystem over Georges Bank and adjacent coastal regions. Part I: physical model, *Deep Sea Research II*, 48, 419–456, 2001.
- Chen, C., H. Liu, and R. C. Beardsley, An unstructured, finite-volume, three-dimensional, primitive equation ocean model: application to coastal ocean and estuaries, *Journal of Atmospheric and Oceanic Technology*, 20, 159–186, 2003.
- Chen, C., Q. Xu, R. C. Beardsley, and P. J. S. Franks, Model study of the cross-frontal water exchange on Georges Bank: A three-dimensional Lagrangian experiment, *Journal of Geophysical Research*, In press, 2003.
- Cloern, J. E., Phytoplankton bloom dynamics in coastal systems: A review with some general lessons from sustained investigation of San Francisco Bay, California, *Reviews of Geophysics*, 34(2), 127–168, 1996.
- Flagg, C. N., Hydrographic structure and variability, in *Georges Bank*, edited by R. H. Backus and D. W. Bourne, pp. 108–124, MIT Press, Cambridge, Massachusetts, 1987.
- Franks, P. J. S., and C. Chen, Plankton production in tidal fronts: A model of Georges Bank in summer, *Journal of Marine Research*, 54, 631–651, 1996.
- Franks, P. J. S., and C. Chen, A 3-d prognostic numerical model study of the Georges Bank ecosystem. Part II: biological-physical model, *Deep Sea Research II*, 48, 457–482, 2001.
- Hopkins, T. S., and N. Garfield, Physical origins of Georges Bank water, *Journal of Marine Research*, 39, 465–500, 1981.
- Houghton, R. W., Diapycnal flow through a tidal front: a dye tracer study on Georges Bank, *Journal of Marine Systems*, 37, 31–46, 2002.

- Houghton, R. W., and C. Ho, Diapycnal flow through the Georges Bank tidal front: A dye tracer study, *Geophysical Research Letter*, 28(1), 33–36, 2001.
- Lewis, C. V. W., C. Chen, and C. S. Davis, Effect of winter wind variability on plankton transport over Georges Bank, *Deep Sea Research II*, 48, 137–158, 2001.
- Lucas, L. V., J. R. Koseff, G. Monismith, J. E. Cloern, and J. K. Thompson, Processes governing phytoplankton blooms in estuaries. II: The role of horizontal transport, *Marine Ecology Progress Series*, 187, 17–30, 1999.
- Malone, T. C., T. S. Hopkins, P. G. Falkowski, and T. E. Whitledge, Production and transport of phytoplankton biomass over the continental shelf of the New York Bight, *Continental Shelf Research*, 1, 305–337, 1983.
- Marra, J., R. W. Houghton, D. C. Boardman, and P. J. Neale, Variability in surface chlorophyll *a* at a shelf-break front, *Journal of Marine Research*, 40, 575–591, 1982.
- Meise, C., and J. E. O'Reilly, Spatial and seasonal patterns in abundance and age-composition of *Calanus finmarchicus* in the Gulf of Maine and on Georges Bank: 1977-1987, *Deep Sea Research II*, 43, 1473–1501, 1996.
- Mellor, G. L., and T. Yamada, Development of a turbulence closure model for geophysical fluid problems, *Reviews of Geophysics and Space Physics*, 20, 851–875, 1982.
- Naimie, C. E., R. Limeburner, C. G. Hannah, and R. C. Beardsley, On the geographic and seasonal patterns of the near-surface circulation on Georges Bank - from real and simulated drifters, *Deep Sea Research II*, 48, 501–518, 2001.

- Nelson, D. M., J. J. McCarthy, T. M. Joyce, and H. W. Ducklow, Enhanced near-surface nutrient availability and new production resulting from frictional decay of a Gulf Stream warm-core ring, *Deep Sea Research I*, 36, 705–714, 1989.
- Ryan, J. P., J. a. Yoder, and P. C. Cornillon, Enhanced chlorophyll at the shelf-break of the Mid-Atlantic Bight and Georges Bank during the spring transition, *Limnology and Oceanography*, 44(1), 1–11, 1999.
- Ryan, J. P., J. A. Yoder, and D. W. Townsend, Influence of a Gulf Stream warm-core ring on water mass and chlorophyll distributions along the southern flank of Georges Bank, *Deep Sea Research II*, 48, 159–178, 2001.
- Smith, R. C., and K. S. Baker, Spatial and temporal patterns in pigment biomass in Gulf Stream warm-core ring 82B and its environs, *Journal of Geophysical Research*, 90, 8859–8870, 1985.
- Townsend, D. W., and L. M. Cammen, Potential importance of the timing of spring plankton blooms to benthic pelagic coupling and recruitment of juvenile demersal fishes, *Biological Oceanography*, 5, 215–229, 1988.
- Yentsch, C. S., and D. A. Phinney, Rotary motions and convection as a means of regulating primary production in warm core rings, *Journal of Geophysical Research*, 90, 3237–3284, 1985.
- Zheng, L. Y., A three-dimensional modeling study of estuarine system: An application to Satilla River, Georgia, M.Sc. thesis, University of Georgia, Athens, Georgia, 1999.

CHAPTER 6

SUMMARY AND SUGGESTIONS FOR FUTURE STUDY

In Chapter 2, a biological model was built based on the observed biological features on Georges Bank. The biological model consisted of 9 compartments, including nutrients (nitrate, ammonia and silicate), phytoplankton (large and small size group), zooplankton (large and small size group), detrital organic nitrogen and silicon. Physical models including ECOM-si and FVCOM were also introduced in this Chapter.

In Chapter 3, the biological and physical factors controlling the timing and magnitude of the spring bloom were examined using 1-D modeling experiments driven by observed meteorological forcings. In the shallow and well-mixed central Bank, the timing of the spring bloom was mainly controlled by the light environment (including light intensity and light attenuation coefficient), while the magnitude was regulated by light, nutrient supply, and zooplankton grazing pressure. In the relatively deep flank area, the seasonally-developed stratification processes controlled the timing of spring bloom predominantly. Both nitrogen and silicon may limit diatom growth. Silicon may become limiting for diatom growth earlier in the year than nitrogen. The contradiction between early depletion of silicate and the months-long diatom bloom indicates the complex role of silicon in diatom growth. The constant N/Si ratio and half saturation constant used for modeling silicate uptake is probably an oversimplification. The 1-D model failed to capture the relatively weak “second” bloom in early summer, indicating that this may not be a local event. Instead, advection of nutrients and phytoplankton from surrounding waters, as well as the tidal mixing

front could play an important role. A model with a higher dimension is necessary in order to obtain a better understanding of phytoplankton bloom dynamics on GB.

In Chapter 4, 2-D model experiments were conducted to describe the spring bloom dynamics in a transect across southern GB. The model results showed that the timing and magnitude of the spring bloom in the shallow central bank and deep flank areas mirrors the results of the 1-D model experiments. The phytoplankton maximum occurred between the shallow and deep area as a result of light availability and continuous nutrient support from nutrient rich off-bank water through tidal mixing processes. The model suggested that the development of the spring bloom in the deep flank area is sensitive to the development of stratification, especially during the transition time between vertical mixing and stratification, usually in late April. Furthermore, the development of a subsurface phytoplankton concentration maximum after stratification is the result of phytoplankton growth and sinking from the surface mixing layer. The 2-D model was not able to capture the basic dynamics of the biological system in the deep flank area, mainly due to the lack of lateral advective processes. Also because of the sensitivity of the biological system to the hydrodynamic environment, the accuracy of the physical model is critical for exploring biological dynamics.

In Chapter 5, the possible source of an intense bloom that occurred in the southern flank of GB during March 1999 was investigated. A 3-D model experiment was conducted to examine the cause of the bloom and the impact of Scotian Shelf Water on bloom dynamics. The Finite Volume Coastal Ocean Model provided the hydrodynamic field for the Lagrange particle trajectory, tracer and biological model experiments. Process-oriented modeling experiments showed that the formation of the phytoplankton bloom on the southeastern flank of GB was related to (1) transport of the Scotian Shelf Water, (2) wind- and tide-induced vertical mixing and surface cooling, and 3) the location of the salinity front. With sufficient supplies

of nutrients from the slope, the bloom could occur due to *in situ* growth of phytoplankton near the slope, where the stabilized salinity front is located. The model results suggest that an accurate simulation of the spatial distribution of temperature and salinity on GB and the flow field across the Northeast Channel is a prerequisite for accurately modeling the spring bloom over GB.

The work described above tested the hypotheses raised in Chapter 1. As expected, a strong coupling between the biological and physical systems was demonstrated. The dynamics of the biological system are very sensitive to variation of physical environment. Like most studies, this study generates as many new questions as answers to old ones. Suggestions for further modeling efforts include:

1. Since the biological model is sensitive to the N:Si ratio, it is important to understand the dynamics of silicate uptake and assimilation processes in diatoms on GB.
2. Light is critical to the timing of the spring bloom on the GB. Model studies require better resolution on the temporal and spatial scales of surface photosynthetically active radiation and light extinction coefficient. A better approximation of the P-I relationship on GB would also be helpful.
3. Without an understanding of the dynamics of the biological system in the Gulf of Maine and Scotian Shelf water, it would be difficult to understand the system in GB as demonstrated in Chapter 4. Attention should be paid in further modeling efforts to the boundary conditions in the northern section near Nova Scotia and in the southern slope region.
4. It would be premature to simulate the seasonal variation and spatial distribution of biological components without an accurate simulation of hydrodynamic features in GOM/GB region. Application of data assimilation techniques

to hydrodynamic modeling is necessary to provide a better physical field for the biological model. Focus should be not only on thermal-induced but also salinity-induced stratification.

5. Zooplankton population models can be improved by coupling to the lower trophic food web model. The food web model provides a prey field for the zooplankton individual based model. This will allow us to examine the impacts of food limitation on zooplankton populations.

APPENDIX A

BIOLOGICAL MODEL

Mathematical equations for each flux term described in Chapter 2 and parameters for biological model is given here.

A.1 EQUATIONS FOR EACH FLUX TERM

$$F1 = \frac{L_{NH4}^{PL}}{L_{NO3}^{PL} + L_{NH4}^{PL}} \min\{(L_{NO3}^{PL} + L_{NH4}^{PL}), L_{Si}^{PL}\} V_{\max}^{PL} L_I^{PL} PL \quad (A.1)$$

$$F2 = \frac{L_{NO3}^{PL}}{L_{NO3}^{PL} + L_{NH4}^{PL}} \min\{(L_{NO3}^{PL} + L_{NH4}^{PL}), L_{Si}^{PL}\} V_{\max}^{PL} L_I^{PL} PL \quad (A.2)$$

$$F3 = V_{\max}^{PS} L_{NO3}^{PS} L_I^{PS} PS \quad (A.3)$$

$$F4 = V_{\max}^{PS} L_{NH4}^{PS} L_I^{PS} PS \quad (A.4)$$

$$F5 = G_{\max}^{ZS} \left(1 - e^{(-k^{PS} PS)}\right) ZS \quad (A.5)$$

$$F5a = \varepsilon^{ZS} F5 \quad (A.6)$$

$$F5b = (1 - \varepsilon^{ZS}) F5 \quad (A.7)$$

$$F6 = \alpha^{PS} PS \quad (A.8)$$

$$F7 = \alpha^{ZS} ZS^2 \quad (A.9)$$

$$F8 = G_{\max}^{ZLS} \left(1 - e^{(-k^{ZLS} ZS)}\right) ZL \quad (A.10)$$

$$F8a = \varepsilon^{ZLS} F8 \quad (A.11)$$

$$F8b = (1 - \varepsilon^{ZLS}) F8 \quad (A.12)$$

$$F9 = G_{\max}^{ZSD} \left(1 - e^{(-k^{ZSD} DN)}\right) ZS \quad (A.13)$$

$$F10 = e_N DN \quad (A.14)$$

$$F11 = \alpha^{PL} PL \quad (A.15)$$

$$F12 = \alpha^{ZL} ZL^2 \quad (A.16)$$

$$F13 = \lambda_{Si:N}^{PL} (F1 + F2) \quad (A.17)$$

$$F14 = G_{\max}^{ZL} \left(1 - e^{(-k^{PL} PL)}\right) ZL \quad (A.18)$$

$$F14a = \varepsilon^{ZL} F14 \quad (A.19)$$

$$F14b = (1 - \varepsilon^{ZL}) F14 \quad (A.20)$$

$$F15 = \lambda_{Si:N}^{PL} F11 \quad (A.21)$$

$$F16 = \lambda_{Si:N}^{PL} F14 \quad (A.22)$$

$$F17 = e_{Si} D Si \quad (A.23)$$

where,

$$L_{NO_3}^{PL} = \frac{NO_3}{k_{NO_3}^{PL} + NO_3} \cdot \frac{1}{1 + \frac{NH_4}{\beta_{PL}}} \quad (\text{A.24})$$

$$L_{NH_4}^{PL} = \frac{NH_4}{k_{NH_4}^{PL} + NH_4} \quad (\text{A.25})$$

$$L_I^{PL} = \tanh(\alpha I / V_{\max}^{PL}) \quad (\text{A.26})$$

$$L_{NO_3}^{PS} = \frac{NO_3}{k_{NO_3}^{PS} + NO_3} \cdot \frac{1}{1 + \frac{NH_4}{\beta_{PS}}} \quad (\text{A.27})$$

$$L_I^{PS} = I / (aI^2 + bI + c) \quad (\text{A.28})$$

$$L_{NH_4}^{PS} = \frac{NH_4}{k_{NH_4}^{PS} + NH_4} \quad (\text{A.29})$$

A.2 MODEL PARAMETERS

Table A.1: Parameters used for the biological model

<i>Parameters</i>	<i>Definition</i>	<i>Value</i>
V_{max}^{PL} (Vpl)	Maximum growth rate for PL	3.0 day^{-1}
V_{max}^{PS} (Vps)	Maximum growth rate for PS	2.4 day^{-1}
$k_{NO_3}^{PL}$ (Kpl1)	Half-saturation constant for the NO3 uptake by PL	$1.0 \mu\text{mol N l}^{-1}$
$k_{NH_4}^{PL}$ (Kpl2)	Half-saturation constant for the NH4 uptake by PL	$0.2 \mu\text{mol N l}^{-1}$
$k_{NO_3}^{PS}$ (Kps1)	Half-saturation constant for the NO3 uptake by PS	$0.5 \mu\text{mol N l}^{-1}$
$k_{NH_4}^{PS}$ (Kps2)	Half-saturation constant for the NH4 uptake by PL	$0.05 \mu\text{mol N l}^{-1}$
k_{Si}^{PL} (Ksl)	Half-saturation constant the Si uptake by PL	$2.0 \mu\text{mol Si l}^{-1}$
G_{max}^{ZL} (Rzl)	Maximum grazing rate of ZL on PL	0.3 day^{-1}
G_{max}^{ZS} (Rzs)	Maximum grazing rate of ZS on PS	0.5 day^{-1}
G_{max}^{ZLS} (Rls)	Maximum grazing rate of ZL on ZS	0.3 day^{-1}
G_{max}^{ZSD} (Szl)	Maximum grazing rate of ZS on DN	0.5 day^{-1}
k^{PL} (Szl)	Ivlev constant for ZL grazing on PL	$1.0 (\mu\text{mol N l}^{-1})^{-1}$
k^{PS} (Szs)	Ivlev constant for ZS grazing on PS	$0.5 (\mu\text{mol N l}^{-1})^{-1}$
k^{ZSD} (Ssd)	Ivlev constant for ZS grazing on DN	$1.0 (\mu\text{mol N l}^{-1})^{-1}$
k^{ZLS} (Sls)	Ivlev constant for ZL grazing on ZS	$1.0 (\mu\text{mol N l}^{-1})^{-1}$
ε^{ZL} (Gzl)	Assimilation efficiency of ZL grazing on PL	0.35
ε^{ZS} (Gzs)	Assimilation efficiency of ZS grazing on PS	0.4
ε^{ZSD} (Gsd)	Assimilation efficiency of Zs grazing on DN	0.2
ε^{ZLS} (Gls)	Assimilation efficiency of ZL on ZS	0.4
α^{PL} (Epl)	Mortality rate of PL	0.1 day^{-1}
α^{PS} (Eps)	Mortality rate of PS	0.2 day^{-1}
α^{ZL} (Ezl)	Mortality rate of ZL	0.2 day^{-1}
α^{ZS} (Ezs)	Mortality rate of ZS	0.2 day^{-1}
e_{DN} (Edn)	Remineralization rate of DN	0.05 day^{-1}
e_{DS} (Eds)	Dissolution rate of Dsi	0.03 day^{-1}
$\lambda_{Si:N}^{PL}$ (Rns)	Ratio of Si versus N in PL	0.67
K_{ext}	light attenuation coefficient	0.1 m^{-1}
β_{PL} (Betal)	NH4 inhibition on NO3 uptaking for PL	$0.4 \mu\text{mol N l}^{-1}$
β_{PS} (Betas)	NH4 inhibition on NO3 uptaking for PS	$0.2 \mu\text{mol N l}^{-1}$

APPENDIX B

SENSITIVITY OF BIOLOGICAL PARAMETER

Sensitivity analysis of biological parameter is important to judge the reliability of the model. More importantly, it may indicate the necessity of improving the estimation of sensitive parameters. In this model, the sensitivity of biological parameters was estimated by

$$\hat{S} = \left| \frac{\Delta F / F}{\Delta \text{Parameter} / \text{Parameter}} \right|,$$

where \hat{S} is a measure index of sensitivity, F is the concentration of a biological variable in the model run with a standard set of biological parameters, and ΔF is the change of F caused by varying the model parameter. $\Delta \text{Parameter}$ is varied by 1% from the standard value. This method was the exact same as that used in *Franks et al.* [1986], *Fasham et al.* [1990] and *Chen et al.* [1999]. According to the definition used in those previous studies, one parameter is determined to be sensitive as its sensitivity index \hat{S} is equal or larger than 0.5.

Figure B.1 shows that the most sensitive parameter in terms of diatom bloom is the ratio between nitrogen and silicon in diatom (Rns). The temperature dependent coefficient (Afa) for biological processes, including growth, mortality and grazing, is also sensitive. Other than that, the sinking term of diatom, such as mortality (Epl) and grazing rate (Rzl) by large zooplankton are relatively sensitive. Overall, only 2 of 27 biological parameters is significantly sensitive in this model, indicating the spring bloom is not affected significantly with most of the parameters. Therefore, the model is qualitatively meaningful.

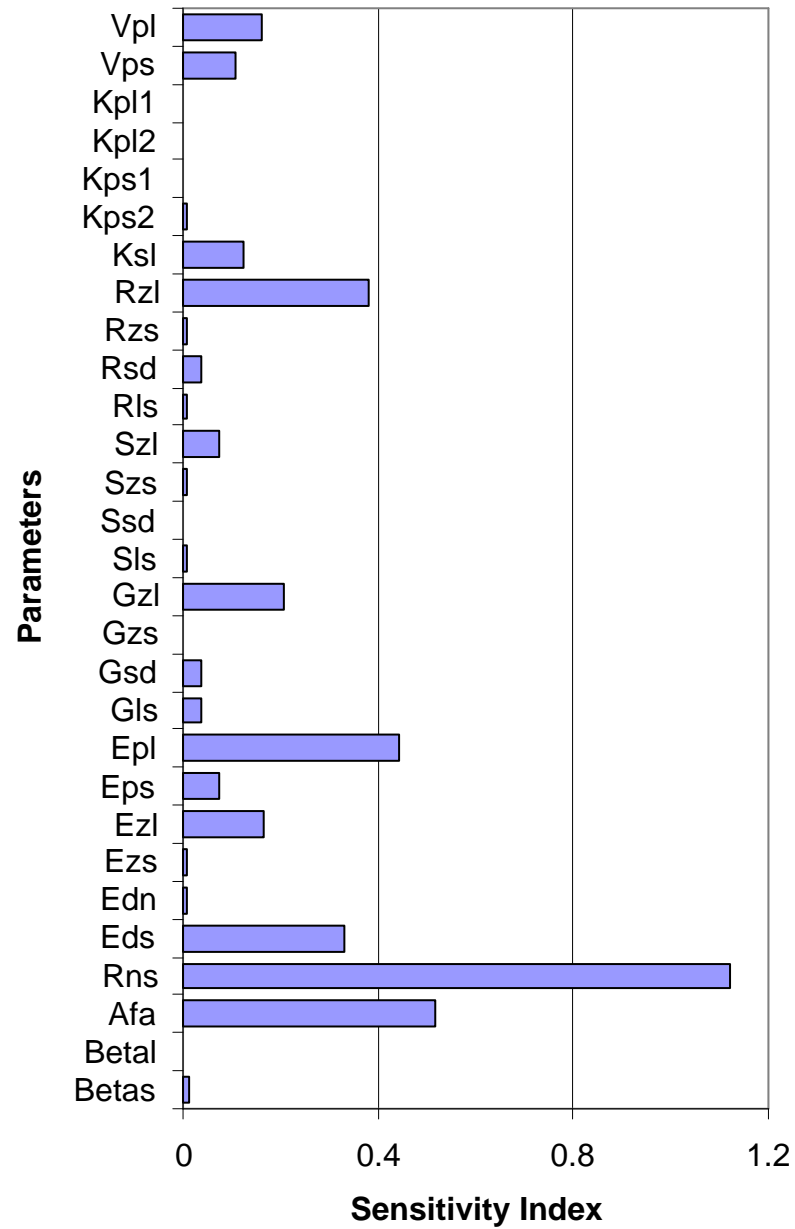


Figure B.1: Result of sensitivity analysis for 1-D model experiment as described in Chapter 3.

B.1 REFERENCES

- Chen, C., R. Ji, L. Zheng, M. Rawson, and M. Zhu, Influences of physical processes on the ecosystem in jiaozhou bay: a coupled physical and biological model experiment, *Journal of Geophysical Research*, 104(C12), 29,925–29,949, 1999.
- Fasham, M. J. R., H. W. Duklow, and S. M. McKelvie, A nitrogen-based model of plankton dynamics in the oceanic mixed layer, *Journal of Marine Research*, 48, 591–639, 1990.
- Franks, P. J. S., J. S. Wroblewski, and G. R. Flierl, Behavior of a simple plankton model with food-level acclimation by herbivores, *Marine Biology*, 91, 121–129, 1986.

APPENDIX C

TIME SERIES DATA OF SURFACE WIND AND HEAT FLUX IN 1995

Time series of wind stress and surface heat flux data from February to June of 1995 were plotted as follows.

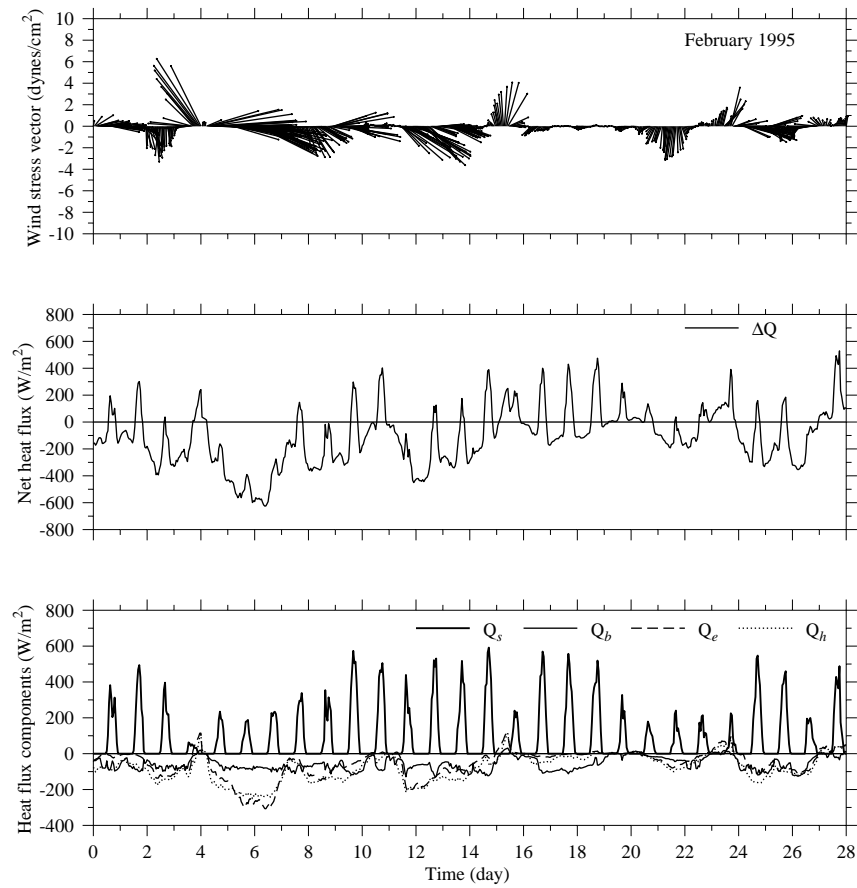


Figure C.1: Time series of wind stress and surface heat flux on the southern Georges Bank in February 1995

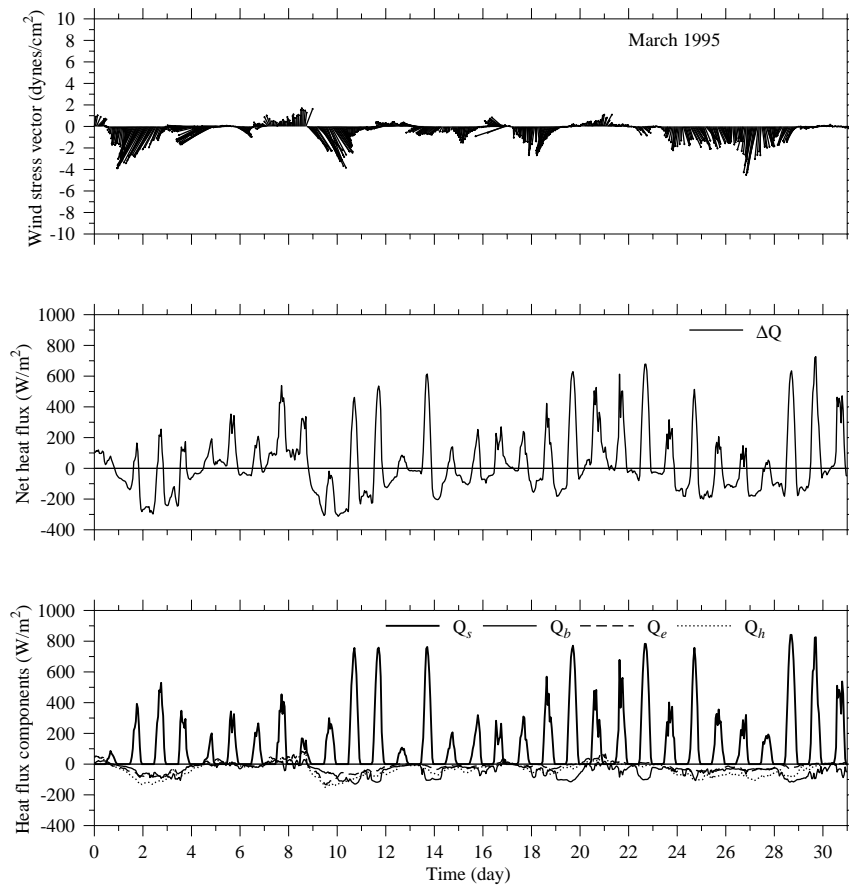


Figure C.2: Time series of wind stress and surface heat flux on the southern Georges Bank in March 1995

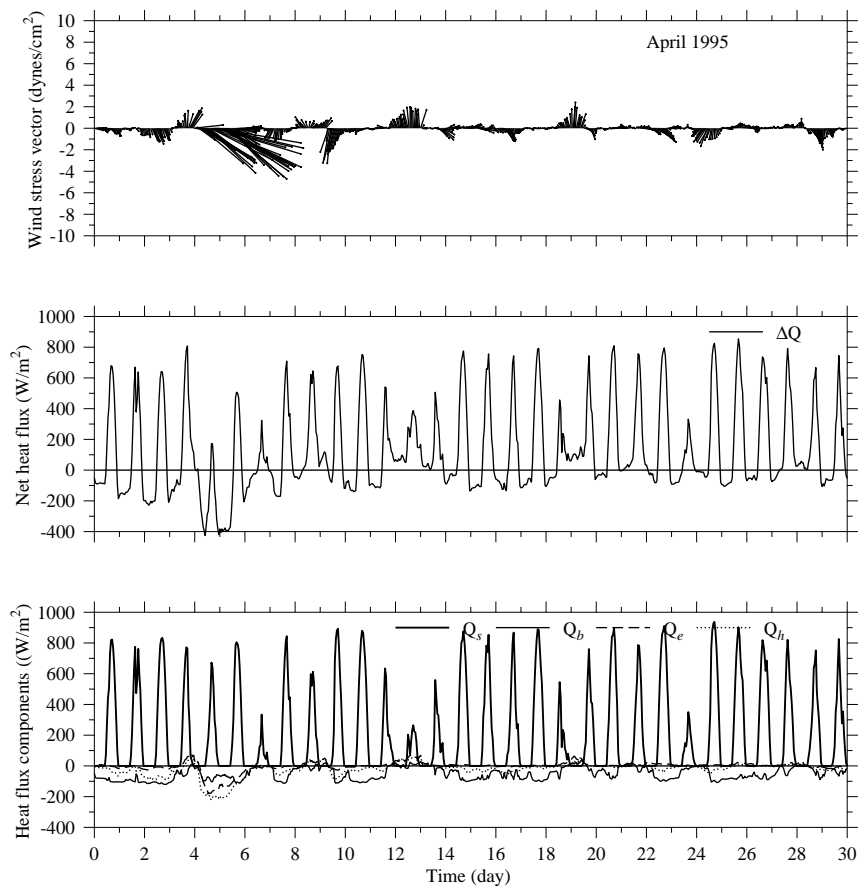


Figure C.3: Time series of wind stress and surface heat flux on the southern Georges Bank in April 1995

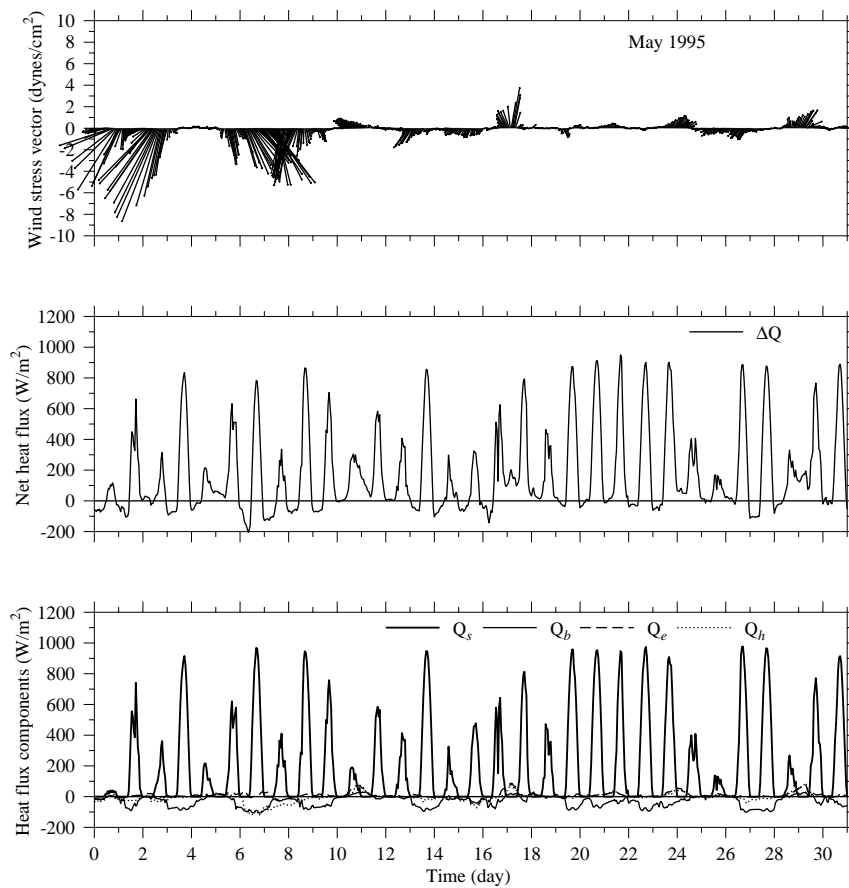


Figure C.4: Time series of wind stress and surface heat flux on the southern Georges Bank in May 1995

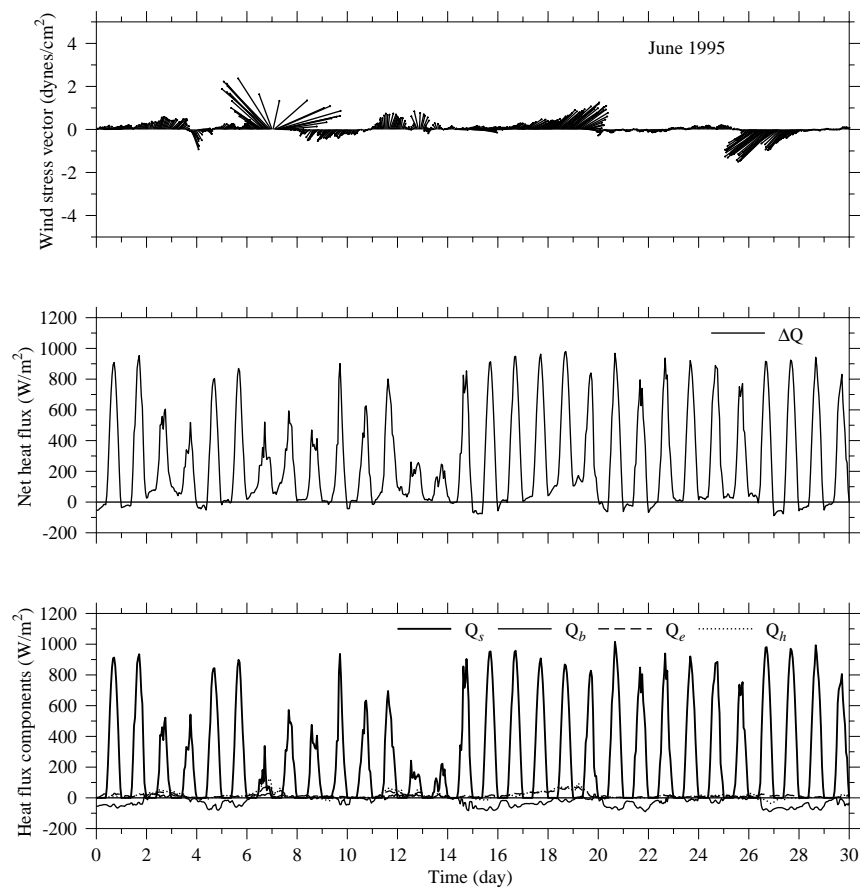


Figure C.5: Time series of wind stress and surface heat flux on the southern Georges Bank in June 1995